Dublin City University
Ollscoil Chathair Bhaile Átha Cliath

Magnetic Polymer Nanocomposite Materials for Biomedical Applications

Kevin Behan, M.Sc.

Thesis submitted for the Award of
Doctor of Philosophy

School of Chemical Sciences

Supervisors:
Dr. Kieran Nolan
Prof. Dermot Brougham (UCD)

September 2019

Declaration

I hereby certify that this material, which I now submit for assessment on the programme of study leading to the award of Doctor of Philosophy, is entirely my own work, that I have exercised reasonable care to ensure that the work is original, and does not to the best of my knowledge breach any law of copyright, and has not been taken from the work of others save and to the extent that such work has been cited and acknowledged within the text of my work.

Signed: ___________________________ (Candidate)

ID No.: ______________ Date: ____________

I dedicate this thesis to

The Behans and the Haydens

Lily and Chereen

Rosemarie

Forever and always

Acknowledgements

I would first like to offer my deepest thanks to my PhD advisor, Prof. Dermot Brougham, for his support, encouragement, loyalty, enthusiasm, and patience. I am eternally grateful to him.

I would also like to thank Dr. Kieran Nolan for agreeing to be my DCU supervisor when Dermot moved to UCD, and for his help during the latter stages of the writing process.

I would like to thank everyone involved in the Neogel project – Prof Andreas Heise, Dr. Aylvin Dias, and my fellow PhD students Saltuk, Timo, and Bing.

During my time at DSM, and a long time after it, I benefited from an untold number of discussions with Dr. Chris Duxbury. I will always appreciate the time he took to consider my questions and answer as thoroughly as is possible.

I am grateful to my other colleagues at DSM, especially Ruud de Groot for introducing me to the Picoliq; to Eric Arts and Llewellyn Rijk for the introduction to PTMC synthesis and functionalisation. To everyone else at DSM for their help, friendship, and vlaai.

Thanks to Bastiaan in TMO for help with 3D printing of the samples for tensile testing.

My colleagues, old and new, at DCU and UCD. Orla, Sarah, Cara, Trish, Eoghan, Sameer, and the guys from the Keane and Quinn groups.

A huge thanks to the DCU technical staff. You're all amazing. Also to Brenton at RCSI for the microscopy and Clémence at UCD for running my samples on the DSC.

Finally to the fireman Michel, the medical staff at the VU University Medical Center Amsterdam, and the staff in Tallaght Hospital: thank you for looking after me and making possible this journey.

Table of Contents

List of abbreviations

Abbreviation	Description
Fe_3O_4	Magnetite
γ-Fe_2O_3	Maghemite
NP	Superparamagnetic iron oxide nanoparticle
AC	Alternating current
DC	Direct current
DLS	Dynamic light scattering
TEM	Transmission electron microscopy
DSC	Differential scanning calorimetry
FAA	Flame atomic absorption
MFH	AC-magnetic field hyperthermia
VSM	Vibrating sample magnetometry
DLP	Digital light processing
YM	Young’s modulus
M_s	Saturation magnetisation
M_r	Remanent magnetisation
H_c	Coercivity field
XRD	X-ray diffraction
D_{crit}	Critical diameter
SAR	Specific absorption rate
MPNC	Magnetic polymer nanocomposite
MHNC	Magnetic hydrogel nanocomposite

VPTT	Volume phase transition temperature
LCST	Lower critical solution temperature
NIPAAm	*N*-Isopropylacrylamide
AAm	Acrylamide
PEGDA	Polyethyleneglycol diacrylate
TEMED	Tetramethylethylenediamine
APS	Ammonium persulfate
PTMC	Poly(trimethylene carbonate)
dhyd	Hydrodynamic diameter
D_{TEM}	Core diameter
D	Diffusion coefficient
PDI	Polydispersity index
STEM	Scanning transmission electron microscopy
NMR	Nuclear magnetic resonance spectroscopy
FID	Free induction decay
ATR	Attenuated Total Reflectance
FTIR	Fourier Transform Infrared Spectroscopy
GPC	Gel permeation chromatography
THF	Tetrahydrofuran
OAc	Oleic acid
OAm	Oleylamine
DMF	Dimethylformamide
DCC	Dicyclocarbodiimide
DMAP	Dimethylaminopyridine
3,4-DHBA	3,4-Dihydroxybenzoic acid

3,4,5-THBA	3,4,5-Trihydroxybenzoic acid (gallic acid)
PEA	Polyetheramine
Fe(acac)$_3$	Iron(III) acetylacetonate
[Fe]	Iron concentration
D_{XRD}	Scherrer diameter
PEA-3,4	Catechol-functionalised polyetheramine
NCH	Nanocomposite hydrogel
GRAS	Generally recognised as safe
HEBM	High energy ball milling
SMM	Stirred media milling
YSZ	Yttria-stabilised zirconia
Oe	Oersted
cP	Centipoise
FeO	Iron oxide
C_d	Cure depth
E_c	Critical light irradiation dose
D_p	Penetration depth
PI	Photoinitiator
2-Iso	2-Isocyanatoethyl methacrylate
MeHQ	2-Methoxyphenol
SLA	Stereolithography
$CDCl_3$	Deuterated chloroform
PTMC-MAc	Poly(trimethylenecarbonate) dimethacrylate
TFAA	Trifluoroacetic anhydride
M_n	Number average molecular weight

M_w	Molecular weight
Đ	Dispersity
TEGDMA	Triethyleneglycol dimethacrylate

Abstract

Kevin Behan

Magnetic Polymer Nanocomposite Materials for Biomedical Applications

Stimuli-responsive polymers have potential in drug delivery and tissue engineering applications, as heating can induce separation and shape memory change within a polymer network. Superparamagnetic iron oxide nanoparticles (NPs) can be heated remotely using AC magnetic field stimulation. With a suitable surface coating, NPs can be combined with monomers and polymerised to form nanocomposite hydrogels that can be remotely heated by externally applied AC fields.

The aim of this thesis was to progress nanoparticle synthesis, compositing, gel formulation and printing capabilities towards these goals. The first part of the work focused on the synthesis of size controlled NPs, with hydrophilic surface catechol-functional ligands. The nanoparticle surface coverage and effect of the ligands on the particle magnetisation were investigated.

The behaviour of magnetic hydrogels in AC fields, specifically their ability to de-swell as a function of the induced temperature change, was investigated. Temperature changes were studied as a function of nanoparticle concentration. Finally, stimulated de-swelling was studied for different formulations; *i.e.* as a function of the co-monomer and crosslinker content.

Using the catechol ligands as excipients for mechanical milling of micron-sized iron-oxide, it was shown that NPs can be generated and their surfaces coated *in situ*. This process removed the need for a ligand exchange step. The performance of these nano-materials for stimulated de-swelling was also evaluated.

NPs prepared by milling were used as additives in 3D printing of nanocomposites. It was shown that the nature of the iron oxide, either bulk or colloidal, affects the penetration of light into the resin formulation and hence the curing depth and spatial resolution that can be achieved. It also has implications for the mechanical behaviour of the printed object. Finally, the effect of build orientation on mechanical properties was studied.

Chapter 1 - Introduction

1.1. Thesis Overview

The central theme of the thesis is the magnetic polymer nanocomposite and the utility of doping polymer networks with responsive nanoparticles such as magnetite (Fe_3O_4) and maghemite (γ-Fe_2O_3).

Chapter 1 introduces magnetic polymer nanocomposites and the classification of magnetic materials. The properties of superparamagnetic iron oxide nanoparticles (NPs), including their behaviour in alternating current (AC) magnetic fields, is described. The potential biomedical applications are discussed, with a focus on magnetic hyperthermia. The role of crosslinked thermoresponsive polymers and the effect of NP incorporation into functional nanocomposites forms the foundation of the thesis.

Chapter 2 describes the key experimental techniques used in this work, including dynamic light scattering (DLS), transmission electron microscopy (TEM), differential scanning calorimetry (DSC), and AC-magnetic field hyperthermia (MFH).

Chapter 3 presents the synthesis of superparamagnetic iron oxide nanoparticles and their modification with catechol-based ligands for phase transfer (PT). Starting with nanoparticle seeds it was possible to generate larger sizes from the previous generation. Based on TEM measurements of core size and step yield, an effort was made to understand the nature of the losses that occur as the multi-step synthesis proceeds. The size-related properties and ligand effects on magnetic properties are also described. The outcome is a reproducible route to strongly heating particles with full water dispersion that are suitable for processing into nanocomposites.

Chapter 4 presents a study of magnetic nanocomposite hydrogels, wherein the effect of the polymer network and NP load on AC-field induced deswelling was assessed. This is a necessary first step in the understanding of the loss of hydrophilic drugs following AC-field exposure. The fifth generation of nanoparticles synthesised and presented in Chapter 3 was used as the magnetic nanomaterial. It was shown that the catechol ligand facilitated dispersion in pre-polymer solutions and, following polymerisation, the nanoparticles remained dispersed in the hydrogel. The magnetothermal response of the hydrogels as a function of nanoparticle concentration and co-monomer content was studied, showing that the hydrophilicity of the co-monomers largely determines the response, and that the crosslink density also controls the deswelling behaviour. Differential scanning calorimetry confirmed that the major events induced by AC field- and thermal-heating occur at the same bulk temperature, suggesting the NPs act as heat reservoirs and the properties of the bulk polymer determines the outcome.

Chapter 5 presents a method to generate monodisperse superparamagnetic iron oxide nanoparticles from bulk ferromagnetic iron oxide powders, using a technique called stirred media milling. It was shown that the milling of these ferromagnetic iron oxides generated superparamagnetic nanoparticles (as shown by vibrating sample magnetometry, VSM). VSM also showed that the transition from ferromagnetic acicular crystallites to superparamagnetic spherical nanoparticles resulted in a significant drop in the saturation magnetisation. X-ray diffraction showed that the maghemite phase was conserved post-milling, and precipitated nanoparticles were sensitive to a neodymium magnet. These precipitates could be redispersed in suitable solvent.

Chapter 6 presents the synthesis and photocrosslinking of poly(trimethylene carbonate) oligomers using digital light processing (DLP). Nanoparticles generated in Chapter 5 were used as dyes and the effect of different nanoparticle concentrations on the photocuring properties was studied. It was found that the type of filler as well as the concentration had significant effects on the photocuring. Secondly, the effect of the build orientation on the mechanical properties, specifically on the Young's modulus (YM) of elasticity, was studied. It was found that the orientation affected the Young's modulus, and that building in the flat orientation gave the lowest Young's modulus, suggesting that the flat orientation is the optimal orientation for these builds.

1.2. Magnetisation of Materials

The thesis deals with the properties and applications of polymer nanocomposites containing magnetite or maghemite nanoparticles. To this end, the introduction must start with the magnetisation of materials, and how certain types of magnetism can be exploited in useful ways. Specific properties of magnetite and maghemite will be covered later in the introduction.

Magnetisation is a property arising from the motion of electrically charged particles. The presence of electrons in matter results in a net magnetic moment, presenting as familiar bulk magnetic properties [1]. The strength of the magnetic effect varies depending on the material and is quantified by the magnetic susceptibility χ [2]. The relationship between a material's magnetisation and applied field strength H is given in Equation 1-1.

Equation 1-1

$$\chi = \frac{Ms}{H}$$

It is useful to provide an explanation of the different types of magnetisation in materials, to better understand the role of superparamagnetic iron oxide nanoparticles as heat mediators.

1.2.1. Diamagnetic Materials

When an external magnetic field is applied to an electron, the electron experiences torque and results in a Larmor precession, in which there is a change in the orientation of the rotational axis of the electron [3]. For paired electrons this rotation creates a magnetic moment opposite to the applied field (Fig 1-1). Diamagnetic materials possess no unpaired electrons in orbitals and are characterised by a weak and negative magnetic susceptibility χ, resulting in weak magnetisation opposing an applied field [4].

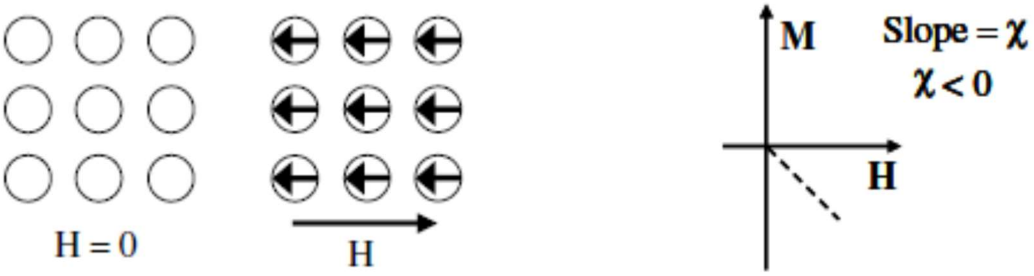

Figure 1-1: Schematic representation of the spin ordering of diamagnetic materials and the negative magnetic susceptibility [5].

1.2.2. Paramagnetic Materials

Paramagnetic materials contain unpaired electrons in partially filled orbitals, for which there is no coupling between neighbouring magnetic moments [4]. In the absence of an applied external field, the magnetic moments are randomly oriented due to thermal fluctuations (Fig 1-2). When an external field is applied the magnetic moments align parallel to the field, resulting in a bulk magnetisation. Paramagnetic materials are weakly attracted to an external applied field and are characterised by a positive χ. Upon removal of the field, ordering of the moments is lost [6].

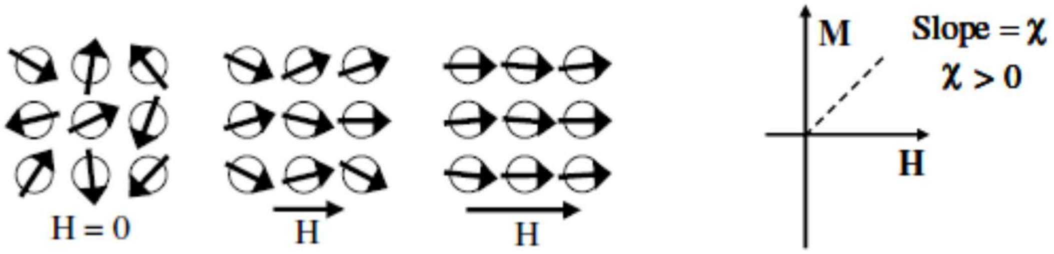

Figure 1-2: Schematic representation of the dipole ordering in paramagnetic materials and the positive magnetic susceptibility typically associated with these materials [5].

1.2.3. Ferromagnetic Materials

Ferromagnetic materials possess unpaired electrons in partially filled orbitals [4]. They differ from paramagnetic materials in that coupling between neighbouring moments results in a permanent magnetisation. In ferromagnetic materials orbitals containing unpaired electrons from different nuclei overlap, resulting in the coupling of moments in parallel. (Fig 1-3). This overlap allows electrons to be located further apart whilst retaining the same spin. This is known as the exchange interaction and is energetically favoured. The energy difference between an anti-parallel aligned spin system and an exchange interaction parallel aligned spin system is referred to as the exchange energy. When an external magnetic field is applied to a ferromagnetic material, the exchange interaction will drive the magnetic moments to align parallel to the field, inducing a strong magnetisation. Ferromagnetic materials are characterised by a large positive magnetic susceptibility, χ [7].

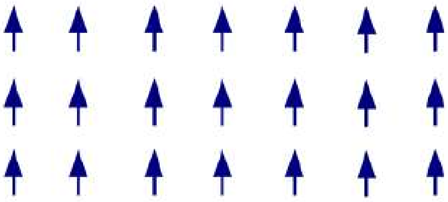

Figure 1-3: Representation of the parallel spin coupling found in ferromagnetic materials

A schematic of the response of a ferromagnetic material is shown in Fig 1-4, as described by Furlani *et al.* [8]. Starting at zero magnetic field there is no magnetisation, but on application of a magnetic field the sample magnetises according to χ. The magnetisation eventually reaches a maximum when all moments are aligned and this is known as the saturation magnetisation, M_s, occurring at saturation field B_s. If the applied field is reduced the magnetisation decreases accordingly. If the applied field is reduced to zero and there is still a remanent magnetisation (M_r) in the sample, the sample is ferromagnetic. As the applied field is reversed, the field at which the sample magnetisation reaches zero is known as the coercivity field (H_c).

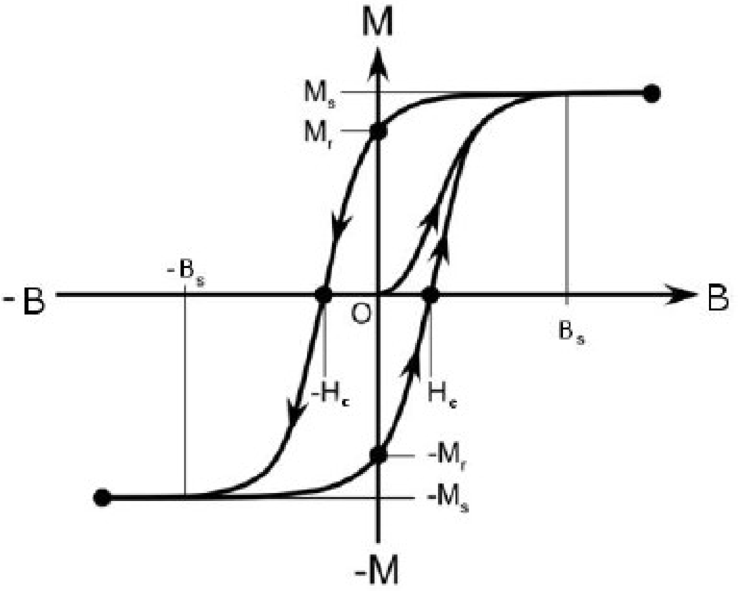

Figure 1-4: Magnetic hysteresis curve showing the evolution of magnetisation along with important magnetic parameters; saturation magnetisation, M_s; the coercivity, H_c; and the remnant magnetisation, M_r, adapted from Furlani *et al.* [8].

1.2.4. Antiferromagnetic Materials

Ferromagnetic and antiferromagnetic materials both have unpaired electrons in partially filled orbitals [4]. However, in antiferromagnetic materials the neighbouring magnetic moments are aligned antiparallel and the exchange interaction has a negative value, resulting in a net magnetic moment of zero [9] (Fig 1-5).

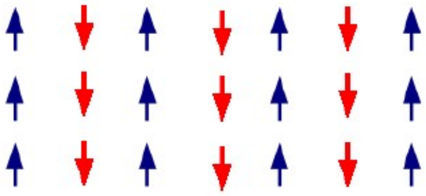

Figure 1-5: Anti-parallel spin ordering of anti-ferromagnetic materials

1.2.5. Ferrimagnetic Materials

Ferrimagnetic materials and antiferromagnetic materials both have unpaired electrons in partially filled orbitals and the neighbouring moments align antiparallel [4]. However, unlike antiferromagnetic materials, the opposing spins are of unequal magnitude and magnetisation is reduced in an applied field (Fig 1-6). Ferrimagnetic materials retain their magnetism in the absence of an external magnetic field and behave like weak ferromagnets [10]. Ferrimagnetism is common in iron oxides and is the type of magnetisation present in magnetite and maghemite.

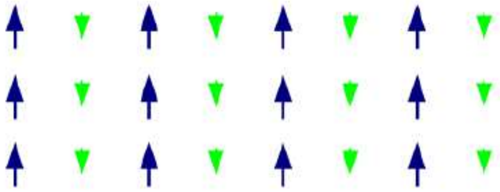

Figure 1-6: Unequal anti-parallel spin ordering of ferrimagnetic materials

Both magnetite and maghemite have a similar cubic structure [11] which cannot be resolved by X-ray diffraction (XRD) [12]. Magnetite has a spinel structure where a unit cell comprises eight cubic units where the lattice spacing is 8.39 Å. The unit cell is composed of 32 oxygen atoms, 16 Fe^{3+} atoms, and 8 Fe^{2+} atoms. There are 32 octahedral (B) and 64 tetrahedral (A) sites in the unit cell (Fig 1-7a) [13]. One in four of the octahedral interstitial sites are occupied by Fe^{2+} cations, and the Fe^{3+} cations are split between 1/4 of the octahedral sites and 1/8 of the tetrahedral sites. It follows that magnetite's unit cell can be represented as $(Fe^{3+})_8[Fe^{2.5+}]_{16}O_{32}$, where the parentheses () designate tetrahedral sites and the brackets [] designate octahedral sites. This crystallographic configuration is denoted as "inverse spinel". Maghemite attains a similar cubic spinel structure with a tetragonal supercell and lattice spacing of 8.33 Å (Fig 1-7b)

[13]. The major difference between magnetite and maghemite is that iron exists in the trivalent oxidation state (Fe^{3+}) and the cations are distributed in 16 octahedral and 8 tetrahedral interstitial sites [13]. The maghemite structure is obtained by creating 8/3 vacancies out of the 24 iron sites in the cubic cell of magnetite. The vacancies distribute in the octahedral sites which minimises the electrostatic energy of the crystal. The composition is written as $(Fe^{3+})_8[Fe^{3+}_{5/6}\ \square_{1/6}]_{16}O_{32}$, where "□" represents a vacancy.

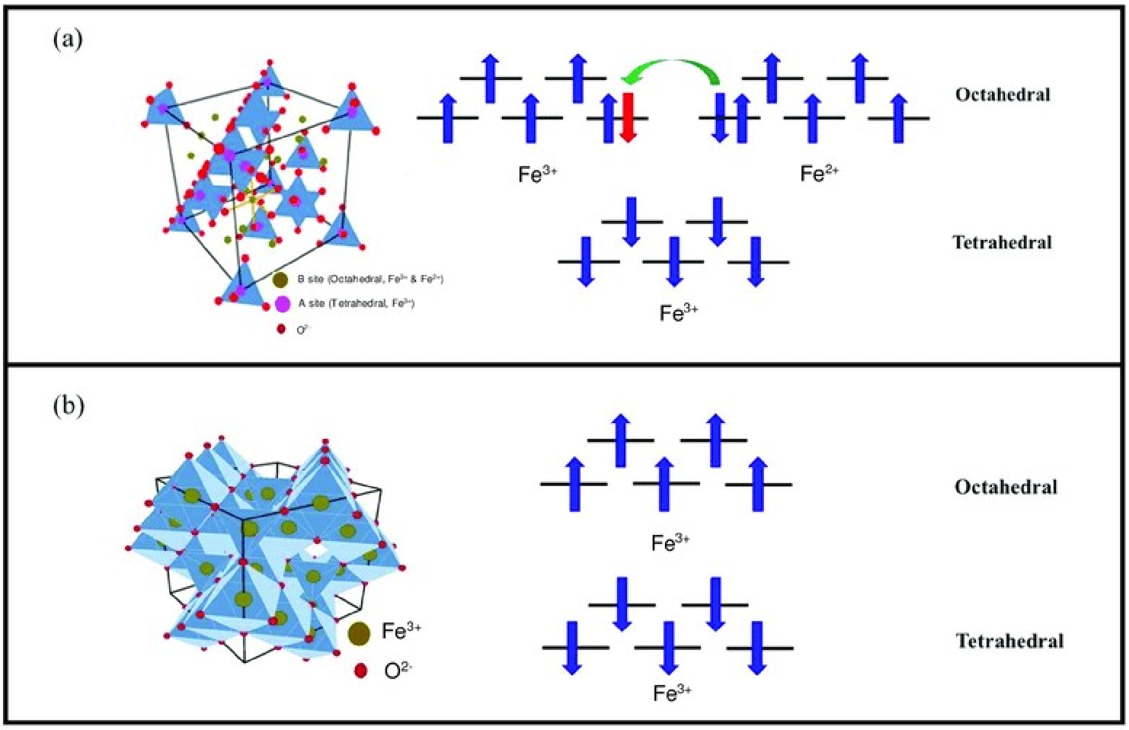

Figure 1-7: Crystal structures and spin configurations of (a) magnetite and (b) maghemite. Reproduced from [13].

1.2.6. Superparamagnetic Materials

Superparamagnetism is a phenomenon present in both ferro- and ferrimagnetic materials [4]. In both ferro- and ferrimagnetic materials discreet crystallites known as Weiss domains are thermodynamically favoured [14]. The individual magnetic moments are coupled and behave as one larger magnetic moment. In the case of larger ferromagnetic and ferrimagnetic objects, multiple domains are present and these domains are separated by grain boundaries. These domains (depending on the nature of the interface) are coupled by exchange interaction and/or by dipole-dipole interactions. As ferromagnetic materials and ferrimagnetic materials approach smaller sizes, the materials reach a size known as the critical diameter, d_{crit} [15]. Below d_{crit}, the surface area to volume relationship makes it thermodynamically disfavoured for grain boundaries to exist, resulting in single domain materials (Fig 1-8).

Table 1-1: Typical d_{crit} and d_{spm} values for a range of common magnetic materials [15].

Material	**d_{crit} (nm)**	**d_{spm} (nm)**
Fe_3O_4	128-85	25
γ-Fe_2O_3	166-90	30
$CoFe_2O_4$	100	10

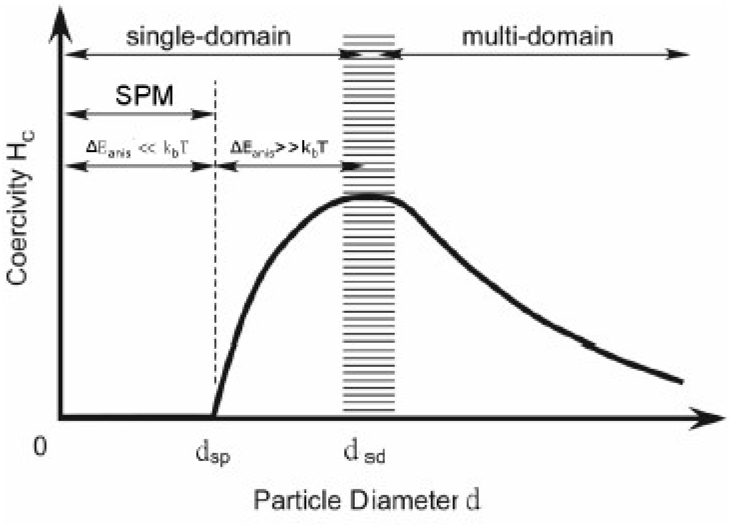

Figure 1-8: Schematic overview of the effect of nanoparticle size on coercivity (H_c); identifying the relationship between ΔE_{anis} and the superparamagnetic size limit, d_{sp}, and the single domain limit, d_{sd} adapted from Furlani *et al.* [8].

As the particle size of ferrimagnetic and ferromagnetic materials decreases below d_{crit}, the particle approaches a size known as the superparamagnetic diameter, d_{sp}. Below d_{sp}, the thermal energy k_BT available in the system at that temperature is comparable to the energy required to reverse the magnetic orientation of the domain, ΔE_{anis} (surface anisotropy energy) [2] which is proportional to the volume of the particle, V, and k_{eff} (Equation 1-3). This results in a spontaneous flipping of the magnetic moment about the preferred axis of magnetisation, known as the easy axis. Superparamagnetic materials are characterised by a near zero remanent magnetisation.

Equation 1-2

$$\Delta E_{anis} = k_{eff}V$$

1.3. Superparamagnetic Iron Oxide Nanoparticles

Superparamagnetic iron oxide nanoparticles such as magnetite and maghemite are ferrimagnetic materials. They have applications in several areas, including as adsorbents in separation processes [16, 17], enzyme immobilisation [18], catalysis [19], energy storage [20, 21] and biomedicine [22, 23]. Applications of these oxides in biomedicine have received considerable attention because NPs offer unique advantage over other materials. Iron oxide NPs are inexpensive to produce, physically and chemically stable, biocompatible, and environmentally safe [15]. The scheme in Fig 1-9 shows the biomedical applications and surface interactions of iron oxide nanoparticles. The breadth of applications is due to a versatile surface chemistry. NPs can be functionalised with small molecules and polymers, which allow the NPs to disperse in biological media [24]; when coated with precious metals such as silver and gold, these core-shell nanoparticles allow a tuning of plasmonic properties and increased stabilisation [25]; when conjugated to antibodies and proteins, specificity and selectivity to biological targets is conferred on the NPs [26].

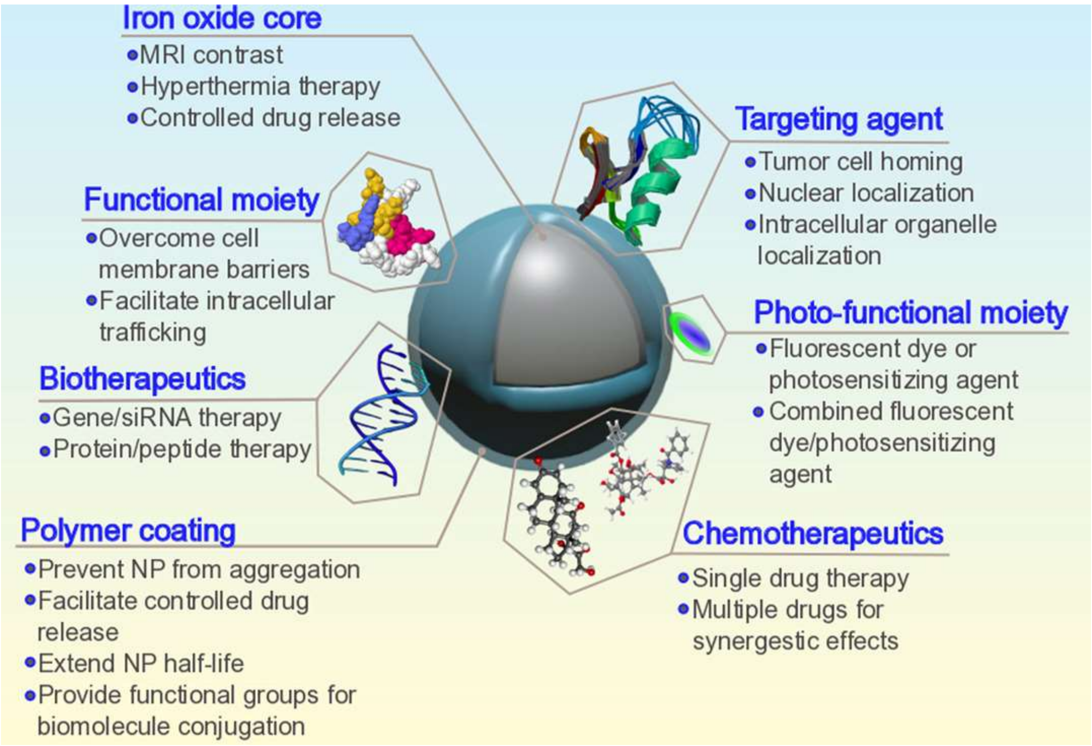

Figure 1-9: Schematic illustration of iron oxide nanoparticle surface properties and biomedical applications. Reproduced from [27].

NPs can be synthesised in a variety of ways: vapour phase, liquid phase and solid phase [28]. In the liquid phase, one of the simplest routes to NPs is Massart's method for co-precipitation of ferric and ferrous iron compounds in alkaline aqueous solution, published in 1981 [29]. NPs made using this approach tend to be polydisperse, which can affect the magnetic properties of the suspensions, due to their size dependence [30]. Several parameters must be controlled carefully, including pH, method of mixing, temperature, the nature and concentration of the anions. To overcome such limitations, non-aqueous approaches have been developed. The reaction of $FeCup_3$ with trioctylamine at 300 °C leads to 6-7 nm maghemite nanocrystals [31]. In 2002 and 2004, two seminal papers were published by Shouheng Sun, Hao Zeng and co-workers, describing the size-controlled synthesis of monodisperse nanoparticles by thermal decomposition of iron(III) acetylacetonate in benzyl ether [32, 33]. This technique allows the operator to synthesise monodisperse seeds (4 or 6 nm) and grow them in subsequent steps using additional amounts of precursor. Iron oxide nanoparticles can also be generated using top-down techniques which are either in the vapour phase (e.g. laser ablation) or the solid phase (e.g. mechanical milling) [28]. In Chapter 5 a type of mechanical milling known as stirred media milling is described which can generate nanoparticles < 10 nm, starting with micron-scale precursors. The relevant literature is reviewed in the introduction to this chapter.

1.4. AC-Magnetic Field Hyperthermia

AC-magnetic field hyperthermia (MFH) is a technique used to generate heat by irradiating superparamagnetic materials such as iron oxide nanoparticles. At sizes ≈ d_{crit}, ferrites such as magnetite and maghemite become single domain in character, having uniaxial anisotropy, which allows a continuous random flipping of magnetisation [34]. The magnetic energy has two minima separated by the energy barrier E, comprising the anisotropy energy E_A and the Zeeman energy E_Z,

Equation 1-3

$$E = E_A + E_Z = KV \sin \theta - HVM_s \cos (\theta - \varphi)$$

The energy input during magnetisation is expended as heat during each field cycle. Hysteresis, Brownian relaxation and Néel relaxation are the three possible mechanisms of nanoparticle heating and are described in detail by Rosensweig [35]. The schematic in Fig 1-10 shows the nature of each relaxation. The rotation of the particle magnetic moment in its local crystal field gives rise to Néel relaxation, whilst the rotation of the particle itself gives rise to Brownian relaxation. The hysteresis behaviour shown in Fig 1-5 tends to be negligible or absent for superparamagnetic iron oxide nanoparticles, and hence the total relaxation time is usually written as in Equation 1-4 [2],

Equation 1-4

$$\frac{1}{\tau} = \frac{1}{\tau_B} + \frac{1}{\tau_N}$$

where τ_B and τ_N are the Brownian and Néel relaxation times, respectively. The Néel relaxation time can be described using the Néel-Arrhenius equation,

Equation 1-5

$$\tau_N = \tau_0 \exp\left(\frac{\mathrm{KV}}{\mathrm{k_B T}}\right)$$

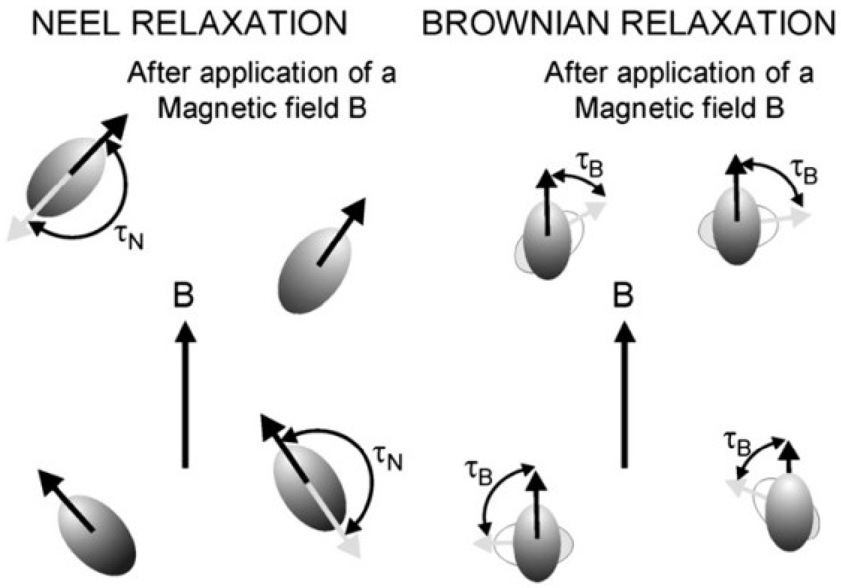

Figure 1-10: Schematic of relaxation processes associated with ferrimagnetic (Brownian) and superparamagnetic (Néel) nanoparticles. Reproduced from [36].

where KV is the height of the energy barrier (a product of the magnetic anisotropy energy density K and volume V); k_B is the Boltzmann constant, T is the temperature and the product k_BT is the thermal energy; τ_0 is a length of time characteristic of the material, called the attempt time or attempt period. Typical values for τ_0 are between 10^{-9} and 10^{-10} s.

The biomedical applications of AC-magnetic field hyperthermia are illustrated in Fig 1-11. These are biofilm eradication, magnetic imaging-guided hyperthermia, thermal cancer therapy, and magnetically-actuated drug delivery [37]. This thesis focuses on magnetically-actuated drug delivery, where the heat generated by the NPs is transferred to a surrounding thermoresponsive polymer network. The energy absorbed by the polymer network breaks hydrogen bonds, increasing hydrophobic interactions which result in macroscopic deformations.

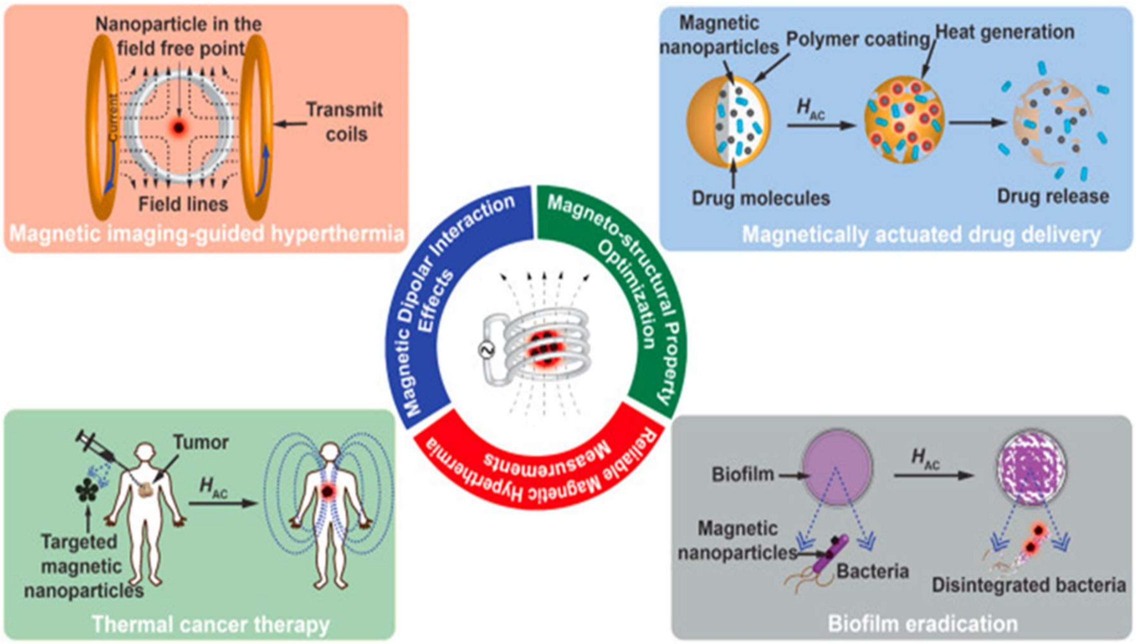

Figure 1-11: Illustrated biomedical applications of AC-magnetic field hyperthermia. Reproduced from [37].

For very small particles $\tau_N << \tau_B$ [38] and therefore the effective relaxation time for superparamagnetic iron oxide nanoparticles can be attributed to Néel relaxation. Furthermore, for superparamagnetic nanoparticles in suspensions and gels, only the Néel mechanism is expected to apply. This is due to particle diffusion being suppressed. The traditional application of magnetic hyperthermia has been thermally-mediated ablation of cancer cells. If the local temperature reaches 42 – 45 °C, cancer cells are more susceptible to these changes in temperature, compared with healthy cells, which are still functional up to 45 °C [39, 40]. One report states that mesenchymal stem cells are functional and possessing integrity up to 48 ºC [41]. Being able to create and maintain these temperatures in a mass of cancer cells would be advantageous for cancer treatment. As will be seen later, this is challenging.

The heat generated during a magnetic hyperthermia experiment or procedure is expressed in terms of the Specific Absorption Rate (SAR) [42] (Equation 1-6) and is reported in W/g of magnetic material.

Equation 1-6

$$SAR = \frac{1}{m_e}\left(\sum_i c_i m_{i\frac{dT}{dt}}\right)$$

where m_e is the total mass of the iron, c_i is the specific heat, and m_i is the weight of the different species in solution; finally, dT/dt is taken as the initial slope of the T(t) curve. This initial slope can be considered within a linear range, before heat transfer effects become significant. For a typical experimental set-up, the system is non-adiabatic, i.e. heat transfer occurs between sample and surroundings. The heating curve which develops has an initial slope of dT/dt which is used to calculate the SAR. As the experiment progresses, the slope decreases, eventually plateauing at thermal equilibrium. The linear response theory (LRT) [43] states that the SAR is at its maximum when the relaxation time of the NP approaches the period of the AC-magnetic field [44]. Until recently it was accepted that the NP size was 14 – 15 nm, but it has since been shown that nanoparticles in the ferromagnetic range (ca. 40 nm) have SAR values approaching a theoretical limit at clinically relevant frequencies [45].

Magnetic hyperthermia has been shown to be useful in drug delivery [46] and tissue engineering applications [47]. Perhaps the earliest report on magnetic hyperthermia was in 1957, when Gilchrist *et al.* investigated the use of magnetic nanoparticles subject to an externally applied magnetic field (the report does not state whether the field was AC or DC) [48]. The work was inspired by a clinical need to successfully clear lymph node metastases. A proof-of-principle was established: the application of a magnetic field to an aqueous suspension of maghemite particles led to a greater temperature differential, as compared with an equivalent volume of beef liver. In 1959 the same authors demonstrated magnetothermally localised tissue necrosis [49] and were the first to describe a typical instrumental setup for magnetic hyperthermia. Bryan, Jr. *et al.* were the first to suggest that magnetic hyperthermia may reduce the chemotherapeutic burden through targeted therapy [50]. Eight years after the first publication, Gilchrist and workers reported safety limits for use of this technique in animal models. They concluded that a finer particle would hopefully lead the way to testing in humans [51]. There are no significant papers until 1981, when a team from UCLA reported the use of “thermomagnetic surgery” for cancer treatment, albeit with no significant developments [52]. However, the following year the same authors suggested that human trials were feasible [53]. In 1996 the term “magnetic fluid hyperthermia” was coined by Jordan *et al.* [54], and this perhaps signified a step change in the development of the technique. Then, in 2003, Jones, along with Pankhurst, Connolly and Dobson, published the review “Applications of magnetic nanoparticles in biomedicine” (Web of Science – 5832 citations). This review firmly established magnetic hyperthermia as a technique, 46 years after Gilchrist’s paper. Since then, the focus has been on clinical translation, the most significant development being the approval of magnetic fluid hyperthermia for the treatment of glioblastoma multiforme, in which the NPs were delivered directly to the cancer site [55]. Even today there have been very few trials using magnetic hyperthermia, mainly due to challenges such as accurate thermometry within the tumour mass and precise tumour heating, which preclude its widespread application. The future of magnetic fluid hyperthermia as a serious treatment option rests on ensuring that it is a safe technique.

Superparamagnetic iron oxide nanoparticles have also been employed in the field of tissue engineering. Antman-Passig *et al.* were able to align collagen fibers for neuronal tissue engineering. By actuating an external magnetic field, the magnetic elements aggregated into magnetic particle strings along the magnetic lines within the gel [56]. A similar approach has allowed the fabrication of alginate-based macroporous scaffolds, showing morphological anisotropy on the nanoscale, and alignment of the scaffold's pores [57]. NPs have been employed as cellular magnetic tags, which allows construction of cell spheroids using magnetic fields [58]. A more detailed review of the literature relevant to the use of magnetically-responsive NPs in tissue engineering will be given in Chapter 6.

1.5. Magnetic Nanocomposites

Magnetic nanocomposites are composites in which at least one of the phases is magnetic, and shows dimensions in the nanometre range [59]. There are four main types of magnetic nanocomposites: core–shell inorganic nanocomposites, self-assembled nanocomposites, silica-based magnetic nanocomposites, and organic–inorganic nanocomposites [60]. The nanocomposites described in this work can be classed as organic-inorganic nanocomposites: typically, the inorganic phase is dispersed or blended within an organic phase such as a polymer blend and/or a polymer network. This is typically described as a magnetic polymer nanocomposite (MPNC) [61]. Magnetic polymer nanocomposites can be powders/suspensions, fibers, films/multilayers, or three dimensional solids. Iron oxides such as magnetite and maghemite are commonly used as the MNPC's magnetic component. In this thesis, the final nanocomposites are formed are bulk objects, typically a few cm across.

Magnetic hyperthermia can be applied to magnetic polymer nanocomposites, where the magnetic properties of the NPs are coupled to the properties of the polymer matrix. Hence, the response is modulated. Polymer matrices are crosslinked networks; either chemically, physically, or ionically bound together [62]. Chemical (or covalent) crosslinking involves the creation of junctions where (usually) smaller molecules with reactive end-groups link longer polymer chains together, forming the crosslinked network. Physical crosslinking can occur through physical entanglements [63], hydrogen bonding [64], and micelle formation [65]. Ionic crosslinking can occur via bridging of units by metal ions (Na^+, Ca^{2+}) [66]. The major advantage physical crosslinking has over chemical crosslinking is in relation to network formation *in vivo*. The monomers typically used for chemical crosslinking are toxic and therefore not suitable for generation of networks *in vivo*. However, it has also been shown that chemical crosslinking, and especially photocrosslinking, has advantages with respect to the *in vivo* stability of cell-seeded [67] and/or cell-laden scaffolds [68]. One of the earliest works describing a magnetic polymer nanocomposite which contains magnetic material for controlled release was that by Langer *et al.* They described a process of magnetothermally-mediated drug delivery. To test the process in vivo, they designed a polymer system with a 2-year supply of insulin and a small magnet, implanted subcutaneously in diabetic rats. The rats were placed in small cages on a stationary top disk, while a bottom disk rotated, giving the rats 20-min exposures to an oscillating magnetic field. Blood sugars were lowered to a near-normal level, when the magnetic field was applied. Four control groups exposed showed no such effect [69]. This is also described in "Biomaterials in drug delivery and tissue engineering: one laboratory's experience.", an account summarising the work in Langer's lab, dating back to 1974 [70]. This account probably has the first use of the umbrella term “drug delivery and tissue engineering”.

One of the first reports of magnetically-mediated release not to emerge from Langer’s lab was in 2005, when Lu and co-workers demonstrated magnetically-mediated tuning of permeability by rotation of ferromagnetic 3 nm Co@Au nanoparticles. The NPs had been embedded inside the walls of a drug capsule. During application of AC field, the rotating NPs generated distortions in the surroundings, creating channels capable of transporting macromolecules out of the capsule [71]. In 2006 De Paoli *et al.* reported the effect of an alternating magnetic field on the release properties of NP-loaded collagen gels. The AC field affected the magnitude of the initial burst release in gels containing nanoparticles. The AC field also increased the amount of released Dex-R from gels containing magnetic microparticles [72]. That same year, the biomedical applications of hydrogels were reviewed by Peppas, Hilt, Khademhosseini, and

Langer, "Hydrogels in biology and medicine: from molecular principles to bionanotechnology" [73]. In 2007 Hu *et al.* reported controlled pulsatile release from a "ferrogel" under applied AC-magnetic field. Under cyclic exposures of high-frequency magnetic stimuli, a tunable and reproducible burst release from the ferrogel was achieved [74]. In 2008, the same group reported accelerated drug release from magnetically-sensitive silica nanospheres. Controlled burst release by a high-frequency magnetic field was employed to deliver a therapeutically effective concentration of a model drug (ibuprofen) [75]. Again, they propose that the physical rotation of the nanoparticles in the AC field generated porous channels through which the drug molecules can migrate. They were able to quantify a change in specific surface area of the nanospheres and total pore volume, yet the exact release mechanism was not fully elucidated. During the same period, researchers were starting to experiment with magnetically-driven thermoresponsive hydrogel systems, using the heat generated by the magnetic nanoparticles to effect deformations in the polymer network. These will be discussed in the following sections.

1.6. Magnetic Hydrogel Nanocomposites

Magnetic hydrogel nanocomposites (MHNCs) are a sub-class of magnetic polymer nanocomposites that swell in the presence of water. Several terms to describe these systems have been used: (1) Magnetic hydrogel nanocomposites (Web of Science – 22 results), (2) Magnetic nanocomposite hydrogels (Web of Science – 16 results), (3) magnetic hydrogels (Web of Science – 90 results). In all cases, these are bulk gels, where the nanoparticles are dispersed in a monomer solution and the magnetic hydrogel nanocomposite is formed *in situ*. These macroscopic gel networks should not be confused with nanogels, where nanoparticles are composed of a hydrogel, albeit these can be prepared in a similar manner to the hydrogel nanocomposites described in this thesis, i.e. dispersion polymerisation [76].

The most highly cited publications on the use of materials for drug delivery and controlled release have come from the Hilt group in the University of Kentucky, under the search term "magnetic nanocomposite hydrogels". Along with Robert Langer and Nicholas Peppas, Hilt co-authored a seminal review in 2006 which currently has 2773 citations [73]. One of his students, Nitin Satarkar, published a paper in 2008 which currently has 378 citations. The title of the paper was "Magnetic hydrogel nanocomposites for remote controlled pulsatile drug release", published in the Journal of Controlled Release [77]. The work explores the use of MHNCs as vehicles for pulsatile drug release, demonstrating reversibility of the swelling response and increased rate of model drug release between magnetic pulses. A breakdown of the formulation used in ref [20] can be seen in the footnote. [1] The purpose of this is to compare with our own formulations, which are detailed in Chapter 4.

A variety of applications of these materials have been reported: drug delivery/release [77, 78], removal of toxic metal ions [79], valves [80], dual hyperthermia and cancer drug therapy [81], remote melting [82], infection control [83], and growth factor delivery for tissue engineering [84]. In 2008, Satarkar and Hilt described the application of magnetic hydrogel nanocomposites as valves in microfluidic devices. It was shown that the application of a magnetic field caused the valve to open, due to magnetically-mediated shrinking of the nanocomposite. When the field was switched off the nanocomposite recovered to equilibrium, and it was shown that the kinetics of recovery depended on the dimensions of the nanocomposite. Recovery was faster in those nanocomposites with smaller dimensions, due to faster heat transfer and diffusion of water molecules. In 2009, the same group issued a paper on nanocomposite degradable hydrogels, demonstrating magnetothermal remote control of the degradation process [46]. That same year, Le Renard *et al.* published a paper describing "The *in vivo* performance of magnetic particle-loaded injectable, *in situ* gelling, carriers for the delivery of local hyperthermia" [85]. This was an interesting alternative to the solid gels described by Satarkar, in that the gel formulations were liquid at room temperature, undergoing a gelling event at body temperature, allowing the formulation to take the shape of its target (in this case the internal microenvironment of a tumour). An insightful conclusion of this paper was that the need for high amounts of iron oxides compromised the sol-gel transition temperature and the mechanical properties of the hydrogel network, rendering hydrogels unsuitable for the application. As an alternative, an organogel was employed which could be tuned with respect to mechanical and microstructural properties. The work continued with a separate study of the heating characteristics of the organogels *in vivo*. They found that the

---

[1] Magnetite nanoparticles with an average size of 25 nm were used at 5 wt% relative to monomers *N*-Isopropylacrylamide (NIPAAm) and tetraethyleneglycol dimethacrylate (TEGDMA). The molar ratio of NIPAAm/TEGDMA was 95:5, dissolved in an equivalent mass of ethanol. Assuming a total of 1 mmol monomers, the mass of ethanol and Fe_3O_4 is 0.13 g and 6.35 mg, respectively. The mass of magnetite is comparable to that used in our own formulations (6 – 25 mg Fe_3O_4).

magnetic properties of the NP-doped silica-based microparticles were conserved during formulation and implant [86].

Meenach *et al.* reported a PEG-based MHNC which was employed for hyperthermic cancer therapy. It was shown that the composite had LCST behaviour (see page 21 for a description of LCST) and could reach temperatures in the range 42 – 45 °C, resulting in the death of M059K glioblastoma cells. It was concluded that these composites could be useful in a dual-therapy scenario, whereby the heating of the composite allows hyperthermia of cancer cells, whilst releasing chemotherapeutics in a controlled manner. Hu *et al.* showed that the heating capability could be controlled by anisotropic alignment of magnetic nanomaterials inside the composite. "Thermogenesis" of the organised material was greater than that of the non-organised material [87]. It is desirable that nanocomposites are homogenous, i.e. monomers are well mixed and nanoparticles dispersed prior to the polymerisation event. This can be monitored using light scattering techniques and transmission electron microscopy [88]. Meenach and Satarkar published "Remote actuation of hydrogel nanocomposites: Heating analysis, modelling, and simulations". A heat transfer model was proposed for predicting temperature profiles of the hydrogel disc heated with AMF in laboratory conditions, and was in good agreement with observed nanocomposite temperature at different swelling ratios [89].

Clinical translation requires biomedical devices to be well defined, with reproducible behaviour for a given set of conditions. Drug release is dependent on the polymer architecture, hence the importance of a thorough understanding of the magnetic hydrogel nanocomposite as a network with dispersed nanoparticles trapped in the matrix. The most common way to characterise the polymer network is to conduct deswelling experiments. The deswelling of hydrogels is usually determined gravimetrically. For example, a hydrogel can be placed in a suitable aqueous medium at pre-defined volume and temperature, and the hydrogel weighed at different time points. The deswelling of magnetic hydrogel nanocomposites in AC-magnetic fields cannot be measured so easily, as they are dynamic systems containing concurrent thermodynamic processes [90]. This is a very interesting characteristic of crosslinked systems containing actuatable materials: temperature affects deswelling, and vice-versa.

The temperature at which phase separation occurs in hydrogels is known as the volume phase transition temperature (VPTT) [91], analogous to the lower critical solution temperature (LCST). The LCST is the critical temperature below which the components of a mixture are miscible for all compositions, and is used to describe free polymer chains which undergo conformational changes within the physiological temperature range, whilst the VPTT is used to describe similar response in crosslinked polymer chains. The most well known of the thermoresponsive polymers, poly(*N*-Isopropylacrylamide) (poly(NIPAAm)), typically undergoes changes in the temperature range 32 - 34 °C, where there is an entropy-driven shedding of water molecules from the polymer network (Fig 1-12), ultimately resulting in a hydrophobic collapse of the network [92].

The VPTT can be modified by adjusting various parameters, such as the amounts of hydrophilic co-monomer and crosslinker used in the formulation. We sought to further understand the physico-chemical basis of the VPTT, as it is likely that the properties of the network determines the cargo release.

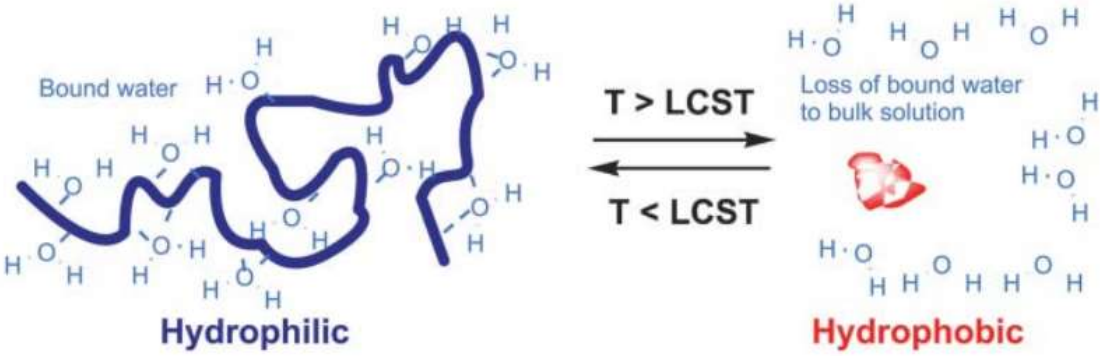

Figure 1-12: Schematic representation of water bound to the polymer chains separating at the LCST (VPTT for crosslinked systems). Reproduced from [92].

Nanocomposite hydrogels based on poly(NIPAAm) can trap a drug and release it *via* two mechanisms. The first mechanism is swelling-controlled release, where the drug diffuses out of the hydrogel as it swells [93]. The second mechanism is squeezing-controlled release, where a hydrated hydrogel collapses when heated to or beyond its VPTT, which results in water being lost from the gel. The embedded drug is also released during this process. Both systems are illustrated in Fig 1-13.

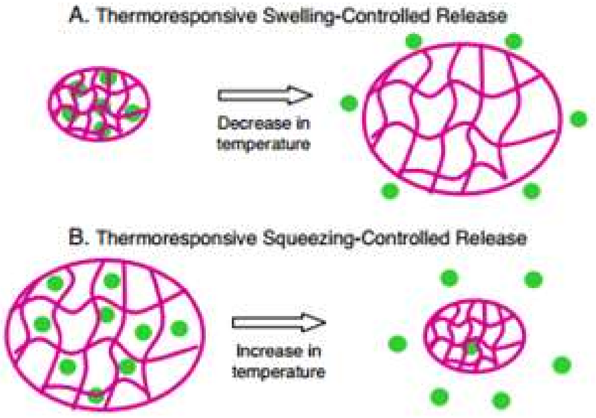

Figure 1-13: Schematic representation of the mechanisms of magnetothermally controlled release from thermoresponsive hydrogel networks. Reproduced from [94].

Ideally the system will have negligible drug diffusion at 37 °C with VPTT slightly above that temperature and resolved enough so that the triggering event controls subsequent release. Nanoparticles can be incorporated during the polymerisation step [95], but due to their small size they can diffuse throughout the hydrogel structure if not tightly bound to the polymer network. The solution to this problem is to coat the particles with a ligand that is either chemically or physically active, which can then interact with the polymer network. One such ligand is aminopropyltriethoxysilane (APTES), which can react with the acrylamide monomers by Michael Addition [96], acting as a crosslinker. However, this molecule can self-condense, leading to variability in the hydrodynamic size of the APTES-treated nanoparticles, which may also affect the magnetic properties of the suspension. Another way to incorporate the nanoparticles is to use polymeric ligands which are physically entrapped within the polymer network [63]. Therefore the initial goals of the study were to synthesise iron oxide nanoparticles, disperse these in monomer-containing solutions, and polymerise *in situ* whilst maintaining nanoparticle dispersion during and after polymerisation. The long term goals were a better understanding of the behaviour of crosslinked nanocomposite systems in AC-magnetic fields.

1.7. Nanocomposite Formulation Strategies used in this Work

When a magnetic hydrogel nanocomposite is placed in an AC-magnetic field, it begins to heat. The heat causes the breaking of hydrogen bonds, which increases the likelihood of hydrophobic interactions. The volume of the crosslinked network decreases as water is expelled, as will be described in Chapter 4. This in turn increases the effective concentration of nanoparticles for a given volume. [2] The volume expelled relates to the heat load and the network properties. The experimental set-up is described more fully in subsequent chapters, but the method for obtaining deswelling data of the magnetic hydrogel nanocomposites in AC-magnetic field, and the importance of sample equilibration, must be highlighted here. The polymer network architecture is quite sensitive to even small changes in temperature, hence equilibration is a prerequisite. Two approaches to controlled magnetic response are described in this thesis, requiring different formulation strategies.

The first approach is to synthesise by free radical polymerisation a thermoresponsive copolymer of *N*-Isopropylacrylamide (NIPAAm) and acrylamide (AAm), crosslinked with PEG700-diacrylate (Fig 1-14), and containing superparamagnetic iron oxide nanoparticles. *N*-Isopropylacrylamide is a type of acrylamide monomer which can form poly(NIPAAm), as well as form copolymers with other monomers. One of these is poly(*N*-Isopropylacrylamide-*co*-acrylamide), a thermoresponsive system with tunable behaviour [97].

This is a rational approach to producing a thermally responsive network by combining established chemistries. The first step in the acrylamide polymerization is a reaction between ammonium persulfate and tetramethylethylenediamine (TEMED) (see scheme, Fig 1-14) in which the TEMED molecule is left with an unpaired valence electron. The activated TEMED molecule can combine with an acrylamide (AAm or NIPAAm) or crosslinking monomer; in the process the unpaired electron is transferred to the acrylamide unit, so that it in turn becomes reactive. Another monomer can therefore be attached and activated in the same way. The polymer continues to grow until the supply of monomers is exhausted, with the active centre being continually shifted to the free end of the chain. If the solution included only acrylamide monomers, the chain would always be straight, or unbranched. A crosslinker molecule, however, can be incorporated into two chains simultaneously and forms a permanent link between them. As a result the polyacrylamide grows into a complex web of interconnected loops and branches.

---

[2] To measure deswelling kinetics accurately, the sample must be equilibrated at the defined temperature and the initial data point collected. For each subsequent data point, the sample must be re-equilibrated at the initial temperature, and the experiment restarted from t = 0, then stopped at a predetermined time. See Ch 4 for experimental set-up.

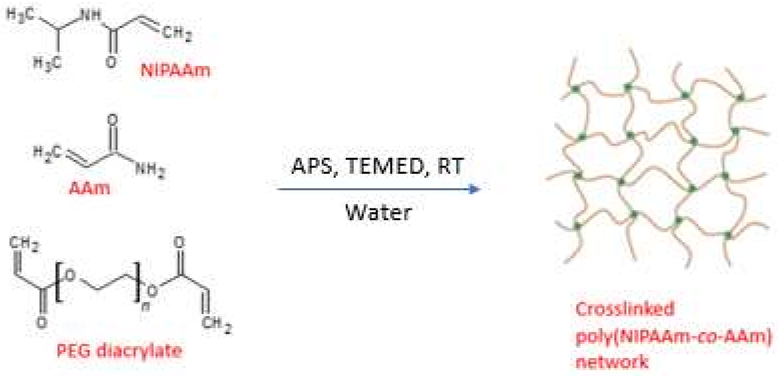

Figure 1-14: General scheme for the radical-initiated thermal copolymerisation of N-Isopropylacrylamide (NIPAAm) and acrylamide (AAm). The crosslinker PEG diacrylate has $M_n = 700$.

The addition of acrylamide monomer in place of the more hydrophobic *N*-Isopropylacrylamide results in a more hydrated network. In Chapter 4 of this thesis, we chose to study the effect of acrylamide comonomer on the deswelling of the copolymer networks, where the deswelling was effected magnetothermally.

The second approach described in this thesis was to fabricate superparamagnetic iron oxide nanoparticle-doped networks of a biodegradable elastomer known as poly(trimethylene carbonate) (PTMC), using DLP. The idea was that magnetically-accelerated resorption of the crosslinked PTMC networks could be induced locally, allowing the controlled release of a drug cargo. PTMC is an aliphatic polycarbonate, forming elastomeric networks when crosslinked. It has shown good biocompatibility as there are no acidic degradation products which have been observed for synthetic polymers based on lactide and glycolide [98].

It was hypothesised that PTMC networks could be prepared in the presence of superparamagnetic iron oxide nanoparticles, and the dispersion of NPs in the built network utilised to effect temperature changes locally, and perhaps allow fine tuning of the enzymatic degradation profile. A possible advantage of the PTMC network is that it is relatively hydrophobic, and perhaps more suitable for loading of hydrophobic drugs. There are few examples of magnetothermal degradation in the literature. The first report came from Hilt's group in 2009 [46]. In demonstrating remote control over drug release, several initial requirements had to be met: the gels had to display a temperature dependent degradation, the nanoparticles had to heat the gels, and finally the exposure to the field had to show some effect on the degradation and thus drug release of the nanocomposite. Knecht *et al.* described the use of a thermophilic enzyme which could be activated remotely using iron oxide nanoparticles and AC-magnetic fields [99]. Since its publication in 2012, there have been only 21 citations of this article, suggesting that this area has not been fully explored. It will be seen in Chapter 6 that the attempt to produce magnetothermally-active MPNCs using DLP was frustrated by the relatively low power of the light source (6 W/m^2). It should be noted here that there are DLP machines with significantly greater outputs (250 W/m^2), capable of generating MPNCs of sufficient iron oxide loads for magnetothermally-driven applications. Ji *et al.* used DLP to generate actuators made from formulation containing iron oxide nanoparticles, which could be manipulated remotely using AC-magnetic fields [100]. An excellent review of printing modalities for generating magnetic constructs can be found in Advanced Materials Interfaces [101].

Optimising the mechanical properties of the PTMC-based nanocomposites is an important step, therefore it was decided to study effects of filler types, filler concentration, and build orientation on the mechanical properties of the successfully-fabricated constructs. These are studies are reported in Chapter 6. Insights into the mechanical properties are useful, as these properties could then be tuned towards biomedical applications.

Chapter 2 – Experimental

2.1 Introduction

The purpose of this chapter is to introduce the main experimental techniques used to acquire data. The following techniques were used during the course of the work described in this thesis: dynamic light scattering; electron microscopy; differential scanning calorimetry; AC field magnetic hyperthermia; vibrating sample magnetometry; attenuated total reflectance-infrared spectroscopy; X-ray diffraction; and gel permeation chromatography. The background theory, principles of operation and experimental conditions are included in each description.

2.2. Dynamic Light Scattering

Dynamic light scattering (DLS) is a non-destructive analytical technique which can provide information on the hydrodynamic size of particles, calculated using the intensity of light scattered by suspended particles as a function of time. The theories of light scattering have not changed significantly since their publication (Rayleigh in 1871 [102] and Mie in 1908 [103]. The scattering theory developed by Rayleigh can be demonstrated during a DLS experiment. When light encounters small particles, the light is scattered in all directions, as long as the particles are small compared to the wavelength used. Even if the light source is a laser (monochromatic and coherent), the scattering intensity fluctuates over time. This fluctuation is due to small molecules in solutions undergoing Brownian motion, and so the distance between the scattering species in the solution is constantly changing with time. This scattered light then undergoes either constructive or destructive interference by the surrounding particles, and within this intensity fluctuation, information is contained about the time scale of movement of the scattering species. Sample preparation either by filtration or centrifugation is critical to remove dust and artefacts from the solution. The dynamic information of the particles is derived from an autocorrelation of the intensity trace recorded during the experiment. Figure 2-1 shows a typical DLS set-up, comprising three parts: a monochromatic light source which produces very uniform light, the sample (placed inside a cuvette), and a detector which consists of a photodiode array to count scattered photons.

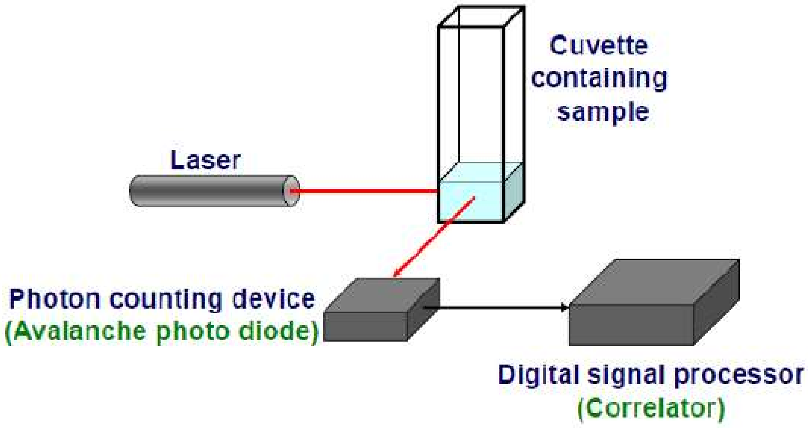

Figure 2-1: Schematic representation of a dynamic light scattering (DLS) instrument set-up, adapted from Malvern technical notes [104].

The fluctuations in scattered light intensity are related to the particles' translational diffusion coefficient (D) which is then related to the hydrodynamic size, dhyd, as described in Equation 2-1. η is viscosity of the solvent, T is temperature (in Kelvin), and k is the Boltzmann constant.

Equation 2-1

$$d_{HYD} = \frac{kT}{3\pi\eta D}$$

For a truly random fluctuation due to one size of dispersed particles, the intensity of a signal compared with itself at a later time interval will have no correlation. However, when comparing the signal with itself at a very small interval, τ, there will be a strong correlation. At longer time intervals the signal still correlates, but not as much (Fig 2-2). With increasing time, the fluctuations correlate less until such a time as correlation is lost. The rate at which the correlation decays from 1 (perfect correlation) to 0 (no correlation) is determined by D. For smaller particles, the correlation will decay over a shorter time scale, in the order of micro- or nanoseconds.

Equation 2-2

$$G(\tau) = \left\langle \frac{nI(t)*I(t+\tau)}{I(t)^2} \right\rangle$$

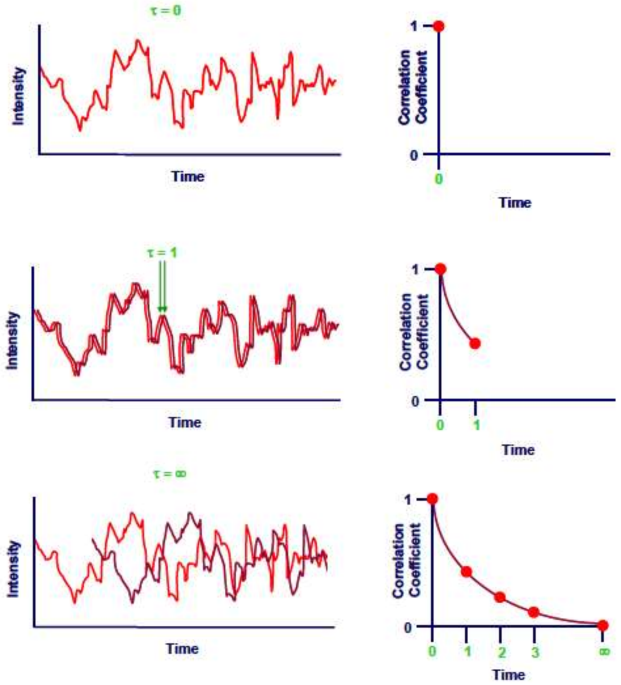

Figure 2-2: Schematic representation showing how the correlation function is constructed. Reproduced from [104].

The DLS result as seen in Fig 2-3 shows the correlation coefficient as a function of time. The correlation begins to decay and the data is fit using the cumulants analysis, in the form

Equation 2-3

$$\ln[G(t)] = a + bt + ct^2 + dt^3 + \ldots$$

Where b is the z-average diffusion coefficient, providing the z-average diameter, and $2c/b^2$ is the polydispersity index (close to 0 is monodisperse; 1.0 is fully polydisperse). The Z-ave and PDI are reliable parameters if the distribution is unimodal accessible. The Z-ave range is ~ 0.5 nm – 5 mm.

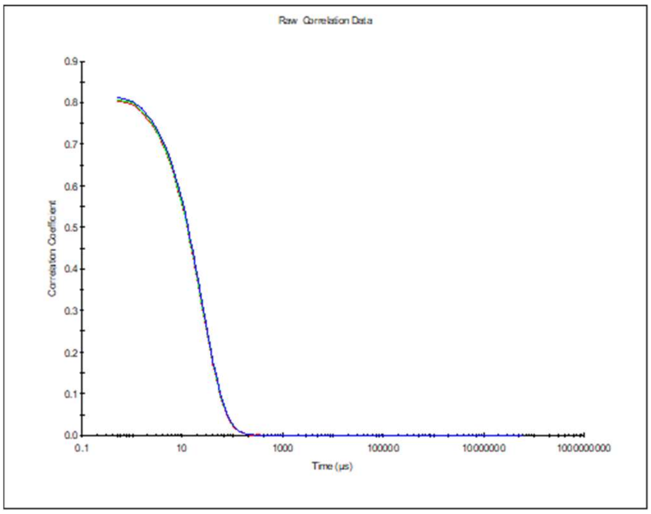

Figure 2-3: Raw correlation data. Smooth, single exponential decay function for a mono-size particle dispersion. The profile is typical for a population of small nanoparticles, i.e. onset of correlation decay occurs ≤ 10 µs.

It should also be noted that Mie theory can be used to generate size distributions for particles larger than the wavelength of the incident light.

DLS measurements were carried out on a Nanosizer ZS (Malvern Instruments; Worcestershire UK). Typically organic solutions were placed in glass or quartz cuvettes. Aqueous solutions were placed in disposable cuvettes. For low volumes of solutions, low volume glass or plastic cuvettes were used. The measurement temperature was 25 °C unless otherwise stated, and allowed to thermally equilibrate for 2 minutes prior to a measurement. A Helium-Neon 5 mW laser operating at 632.8 nm was used as the light source. For back scattering, the detector angle was set at 7° with respect to the incident beam. For forward scattering, an angle of 180° was used with respect to the incident beam. Unless otherwise stated, the back scattering angle was used. This results in an eight fold increase in intensity over forward scattering, which allows for greater sensitivity during measurements as the signal-to-noise ratio increased. A major limitation of the DLS experiment is that the scattering intensity of very small particles is “lost” in the presence of larger (more strongly scattering) particles, aggregates, etc. For example, a sphere with 100 nm diameter will scatter 10^6 times more light than a sphere with 10 nm diameter.

2.3. Electron Microscopy

When attempting to view very small objects at sufficient resolution, traditional light microscopy is limited in that the resolving power is dependent on the wavelength of the light source and, as a result, materials and particles in the sub-micron range do not yield sufficient information. In electron microscopy (EM), electrons are used as the illumination source, which allows the resolution of features at length scales smaller than the wavelength of visible light. The de Broglie relation (Eq 2-4) shows that the wavelength, λ, is inversely proportional to the momentum, p, of a particle/electron, and h is Planck's constant. This relationship allows for the wavelength of the electron to be changed by increasing the momentum of the electron. This allows the imaging of very small features approaching the sub-nm range.

Equation 2-4

$$\lambda = \frac{h}{p}$$

In general, electron microscopy is differentiated into scanning (SEM) and transmission (TEM) modes. The scanning mode focuses the electron beam to a fine spot which can be rastered over a sample. Therefore this technique is very useful for probing surface morphology. The transmission mode uses a beam of electrons which are shone through the sample. Scanning transmission electron microscopy (STEM) is a variant of TEM, whereby the incident electrons are focused to a fine spot (as in conventional SEM), and rastered over the sample. Most of the images of superparamagnetic iron oxides shown throughout the thesis were generated by STEM. Typically, a dispersion of nanoparticles is dried onto a copper grid coated with a thermoplastic resin known as Formvar, leaving a thin layer of nanoparticles on the grid. The grid is then placed inside a vacuum, where a beam of high voltage electrons (kV range) can be passed through the sample. The electrons interact with the sample and electrons are deflected or scattered throughout. Whilst most electrons pass through the sample, transmitted electrons are focused to form an image capable of being recorded or viewed.

A schematic representation of a STEM set-up is shown Figure 2-4. Positioned along the STEM are a series of lenses which act to focus the beam of electrons onto the sample. The electrons that are focused onto the sample interact with the sample, some deflected by the sample. The scattering intensity is approximately proportional to the square of the atomic number, so larger atoms such as heavy metals will deflect more electrons thus appearing darker than lower atomic numbered elements. Hence, real information with regards to size and shape of particles can be obtained.

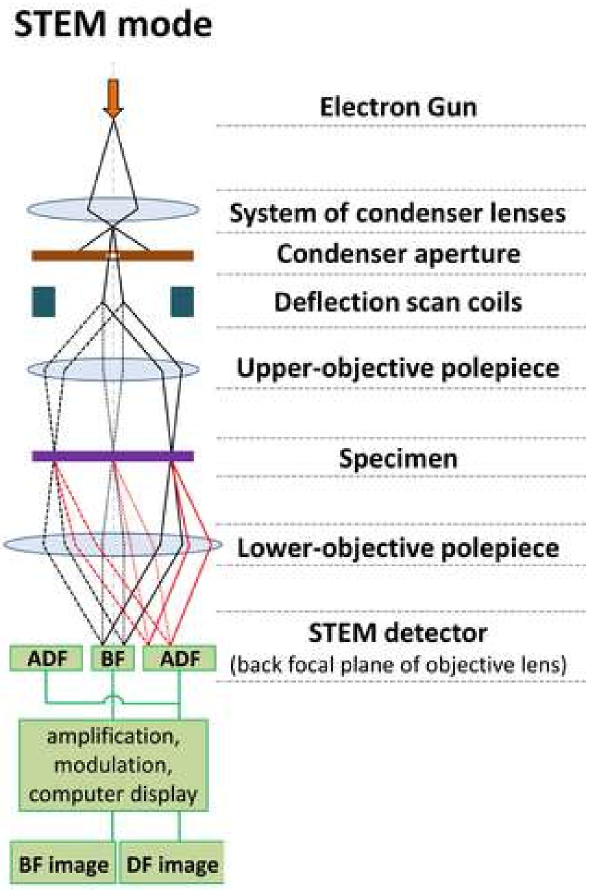

Figure 2-4: Schematic of motorized Duo STEM system in the S-5500 UHR in-lens FE-SEM indicating higher maximum scatter angle in HAADF mode and variable dark-field detection angles [105].

Typically, superparamagnetic iron oxide nanoparticle (NP) dispersions are diluted to a range appropriate for TEM (0.2 – 1 mM). One drop of diluted dispersion, typically in chloroform, was spotted on 3 mm diameter copper grid. The grid comprises a 400 square mesh coated in Formvar, with a thin layer of carbon evaporated onto the grid for extra stability and to render the sample conductive for the generation of electrons. The grids were supplied by Agar scientific and used as supplied.

Specimens for imaging must be very thin to allow the transmission of high energy electrons. Typical sample thickness is < 100 nm when possible, but in general, this requirement is a function of both electron energy and atomic number of the specimen. If the dimensions of a specimen are so small that the sample is essentially ‘electron transparent', then a dilute dispersion of the sample can be deposited on support grids and the solvent can be evaporated through open air drying. The disadvantage of this technique, however, is the potential introduction of artefacts during the drying process. Additional considerations are required when imaging objects only a few nanometres in size. For example, it is necessary to increase the magnification, but this limits the field of view, thus limiting the number of objects or structures that can be analysed in each image. The machine used was a Hitachi S-5500. The grids were placed in a topography grid holder and measured at an angle of 0° tilt with respect to the beam.

2.4. Differential Scanning Calorimetry

Differential scanning calorimetry (DSC) is a thermal analysis technique [106] for measuring thermodynamic processes that occur in materials. It was patented in 1966 by E. S. Watson and M. J. O'Neill [107]. A functional DSC system has three major components: the instrument itself, which contains the system electronics; the cell, which monitors differential heat flow and temperature; and a cooling accessory. A schematic showing a typical heat flux instrumental set-up is shown in Figure 2-5.

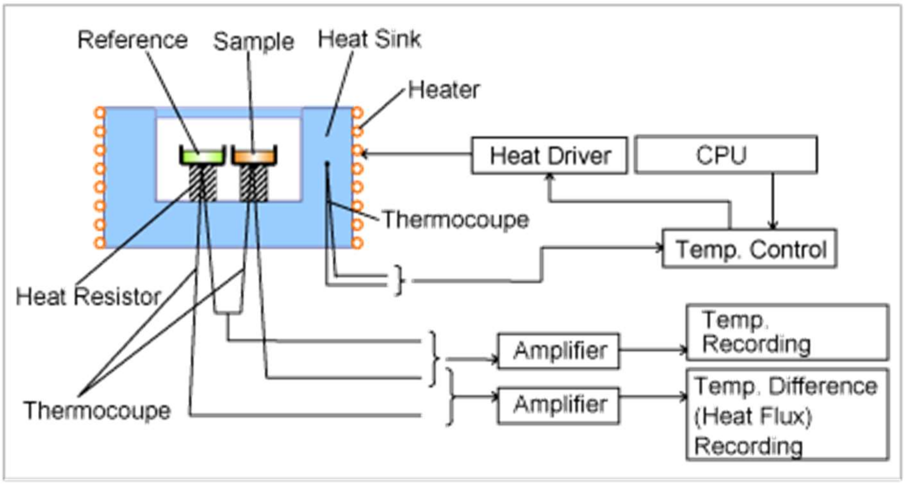

Figure 2-5: Schematic diagram of differential scanning calorimetry set-up.

The key aspect of the DSC technology is that both the sample and reference are maintained at the same temperature. During a thermal event or phase transition within the sample (phase changes, melting, oxidation, and other heat-related changes), heat flow depends on whether the process is exothermic or endothermic. For example, the melting of a solid is an endothermic process that requires heat, therefore for the sample to maintain the same temperature as the reference, additional heat must be supplied from the instrument. Conversely, exothermic processes such as crystallisation require less heat for the sample to maintain reference temperature. These processes are illustrated in Fig 2-6.

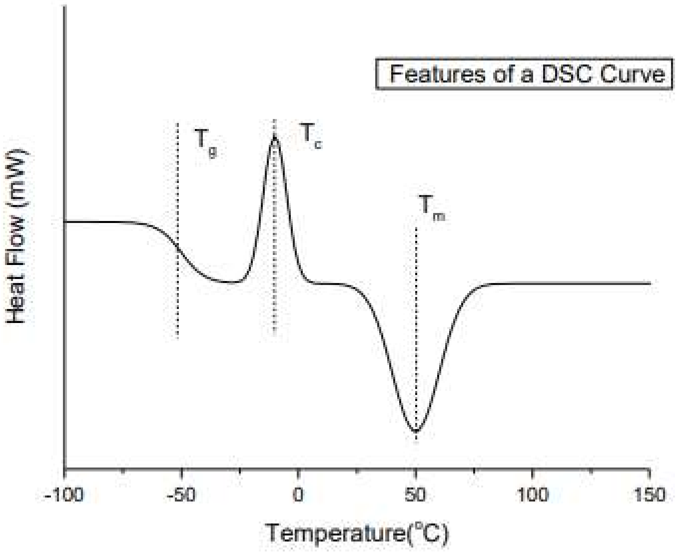

Figure 2-6: Typical features of a DSC curve, showing possible thermal transitions.

The heat flow is expressed as

Equation 2-5

$$\Delta H = \int Cp.dT$$

where ΔH is the enthalpy change between two states; C_p is the specific heat capacity; T is temperature. C_p can be difficult to measure; instead, a heat flux term, Q, can be used which describes the quantity of heat transferred per unit time and mass

Equation 2-6

$$Q/m = Cp.dT$$

There are several DSC modes, the most common of which are double furnace heat flow and singe furnace heat flux DSC. In heat flow the endotherms point up as heat must go to the sample to maintain the reference temperature. In heat flux it is the same event that causes the sample to absorb heat, and therefore initially cooler relative to the furnace, hence the endotherm points down (Fig 2-7).

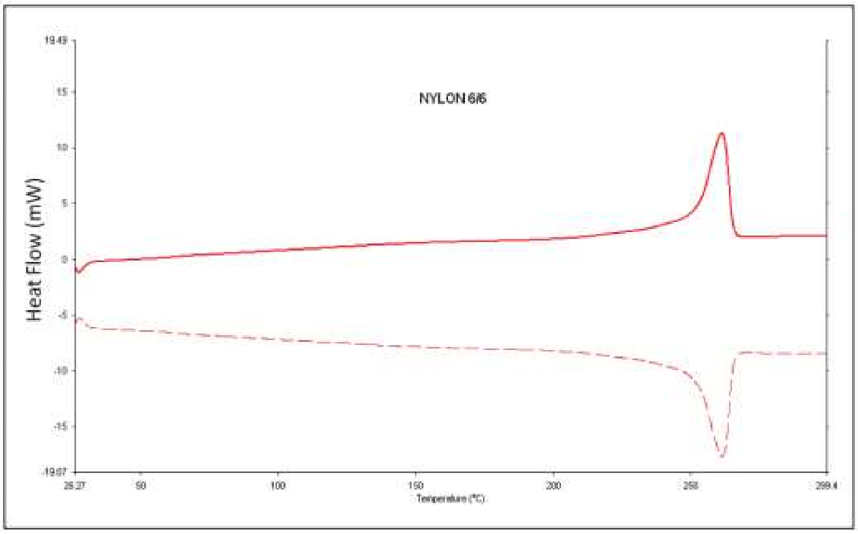

Figure 2-7: Comparison of curves for a nylon 6/6 sample from a double furnace heat flow DSC (solid line) and a single furnace heat flux DSC (dash line).

The aim of the DSC experiments was to show the thermal transitions within magnetic hydrogel nanocomposites (MNCHs) and couple these with the results obtained from the magnetic hyperthermia experiments (see section 2.5 for description of technique). Heat from MNCHs during magnetic hyperthermia experiments dissipates to the surroundings. Water is also leaving the sample, therefore the DSC experiment was "open pan", so that the sample conditions for the two measurements were consistent.

2.5. AC Magnetic Hyperthermia

AC magnetic hyperthermia (MH) is a physical phenomenon whereby electromagnetic energy is converted to heat energy *via* magnetic materials, e.g. NPs [37]. The principles of magnetisation and heat generation are found in Chapter 1. NP suspensions with very narrow particle size distributions contain dispersed particles which, when placed in an alternating magnetic field, can be thought of as a global magnetic moment to magnetise in the direction of the applied field. Samples are placed in a copper coil which generates the magnetic field (Fig 2-8).

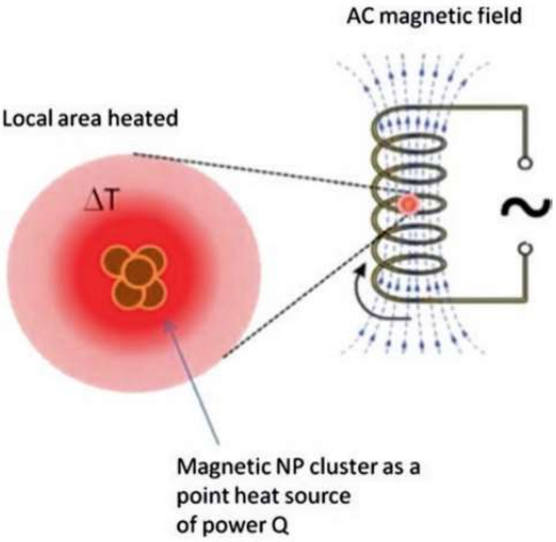

Figure 2-8: Illustration of AC field magnetic hyperthermia (MH) in a cluster of magnetic nanoparticles. Reproduced from [108].

Magnetic hyperthermia set-ups have evolved from simple induction devices to dedicated modular devices with switchable frequencies and intensities [109]. The set-up in Fig 2-9, the Nanotherics MagneTherm, contains the coil (9 or 17 turns). The coil can be combined with different capacitors, allowing adjustment of the magnitude of the field (6 – 12 k A m^{-1}) according to a resonant frequency (100 – 900 kHz).

Figure 2-9: Components of the Nanotherics MagneTherm system. A: Function generator and power supply. B: Coil and electronics. C: Oscilloscope.

Sample temperature can be monitored with thermocouples [110] or fiber optic probes. Thermocouples exploit the Seebeck effect, whereby the temperature difference between two strips of metal creates a voltage which can be converted back to a temperature reading by the software [111]. Whilst thermocouples are relatively inexpensive temperature measurement devices, they are prone to errors. Electromagnetic interference (EMI) from the magnetic field can induce currents in the thermocouple wires, which the software then interprets as a temperature fluctuation. As well as this, induction can result in heating of the wires themselves. Indirect disturbances, where the probe disturbs the field upon insertion, are also possible [111]. However, if the linear portion of the heating profile is sufficiently long, initial data points can be removed and the slope extracted with accuracy. We chose to use a fiber optic probe (Opsens, gallium arsenide) instead of a thermocouple so that non-specific effects associated with the magnetic field are eliminated.

The particular set-up used in the lab was non-adiabatic, i.e. subject to heat transfer between sample and surroundings. Despite efforts to minimise non-specific heating/cooling, the temperature measurement in non-adiabatic magnetic hyperthermia is extremely sensitive to the experimental conditions. For magnetic hyperthermia measurements, samples were equilibrated in a water at 32 °C (the temperature at which poly(*N*-Isopropylacrylamide)-based hydrogels begin to undergo phase changes). The temperature of the sample enclosure containing the coil was kept constant by circulating water through the system at 32 °C. During sample loading, some cooling does occur, but by applying the AC field at this point, the sample can be heated back to 32 °C, and then the data collection can start. We chose to sheath the fiber optic probe in a glass pipette with its tip sealed, so that nanoparticle suspension was not in direct contact with the probe. The probe was placed in the polystyrene insulation in such a fashion that it could be positioned reproducibly in a nanoparticle suspension or gel.

2.6. Vibrating-Sample Magnetometry

Vibrating-sample magnetometry (VSM) measures sample DC susceptibility and magnetisation [112]. Specifically, the saturation magnetisation, M_s, of a sample can be determined using this method. VSM was first reported in 1959 [113]. A typical scheme is shown in Fig 2-10. The vibrating component perturbs the otherwise stable magnetic field H, which generates an electrical field in the coils based on Faraday's Law of Induction [114]. Signal processing using a lock-in amplifier enables high signal-to-noise ratios to be obtained. The pickup coils are designed to ensure a linear response over the length of vibration and eliminate the signal from the applied DC field.

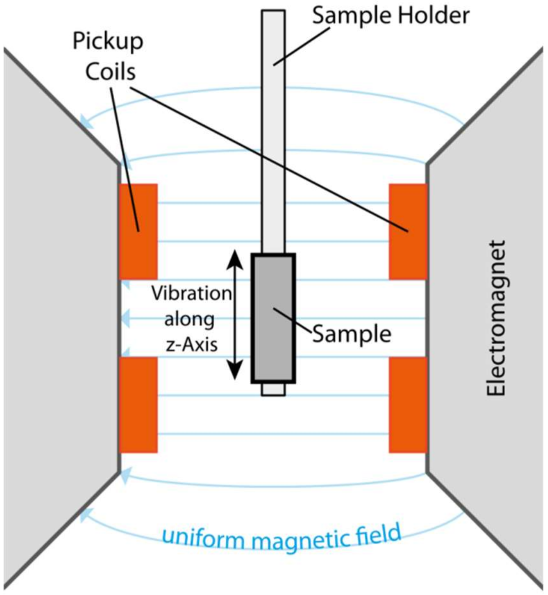

Figure 2-10: Scheme showing sample set-up of vibrating-sample magnetometer (VSM) [115]

Magnetization curves are measured in open circuit in applied magnetic fields of up to 14 T in a Quantum Design Physical Property Measurement System (PPMS). The NP sample is mixed with cyanoacrylate and fixed between gelcaps to produce a sample roughly 4 mm in diameter and 2 mm thick.

2.7. Attenuated Total Reflectance-Fourier Transform Infrared Spectroscopy

Attenuated Total Reflectance-Fourier Transform Infrared Spectroscopy (ATR-FTIR) combines the sampling technique of attenuated total reflectance with infrared spectroscopy. An infrared beam is directed onto an optically transparent internal reflectance element of higher refractive index than that of the contacting sample at an angle exceeding the critical angle (θ_c) for internal reflection. At the boundary between the crystal and the sample, the IR beam penetrates into the sample, typically at a depth of 3 μm (Fig 2-11) [116]. This is known as an evanescent wave which is the same frequency as the incident light but the intensity decays exponentially with distance from the crystal surface, according to the relation, $E = E_0.e^{-z/d_p}$, where d_p is the depth of penetration;

proportional to wavelength, λ , the incident angle, θ and the refractive index of the material, η (Eq 2-7).

Equation 2-7

$$d_p = \frac{\lambda}{2\pi\eta_{crystal}\left(\sin^2\theta - \left(\frac{\eta_{sample}}{\eta_{crystal}}\right)^2\right)^{\frac{1}{2}}}$$

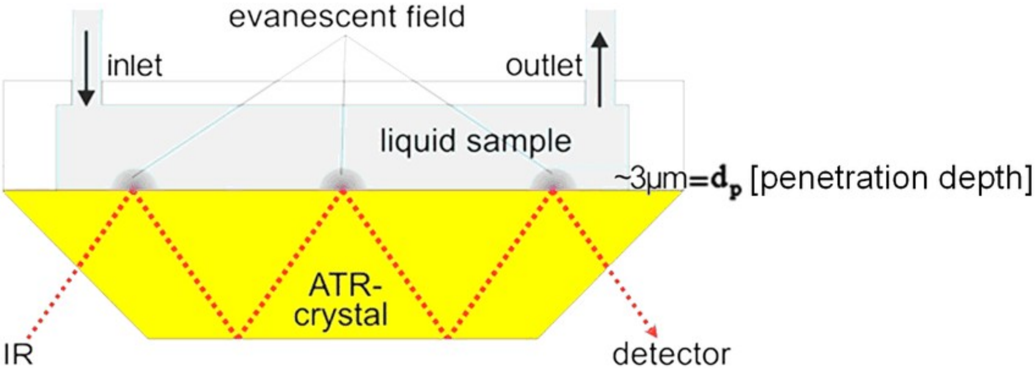

Figure 2-11: Schematic of the attenuated total reflectance of an infrared beam, where the ATR crystal is in contact with a liquid sample. Reproduced from [116].

The instrument used was a Spectrum100 FT-IR equipped with a ZnSe crystal Universal ATR attachment (PelkinElmer, Massachusetts, USA). Solid samples (typically in powder form) can be pressed flat against the crystal under applied force, whilst liquids form a natural contact. A background scan must be carried out in the first instance, as well as a blank (e.g. carrier solvent).

2.8. X-Ray Diffraction

X-Ray diffraction (XRD) is a technique used for determining the atomic and molecular structure of a crystal, in which the crystalline structure causes a beam of incident X-rays to diffract into many specific directions. Von Laue, in 1912 [117], discovered that crystalline substances act as three-dimensional diffraction gratings for X-ray wavelengths similar to the spacing of planes in a crystal lattice. The diffraction process is shown in Fig 2-12.

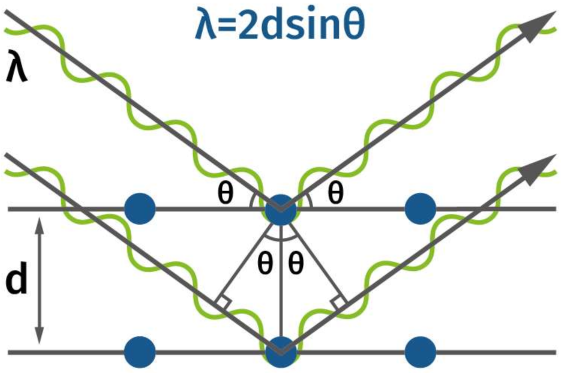

Figure 2-12: Schematic of X-Ray diffraction process.

By measuring the angles and intensities of these diffracted beams, a crystallographer can produce a three-dimensional picture of the density of electrons within the crystal. From this electron density, the mean positions of the atoms in the crystal can be determined, as well as their chemical bonds, their crystallographic disorder, and various other information.

The instrument (Siemens D500) uses the Bragg-Brentano parafocusing geometry. A point detector and sample are moved so that the detector is 2θ and the sample surface is θ relative to the incident X-ray beam. The sample must be spread evenly on the target, to ensure a sufficient number of diffraction events with respect to the geometry. The top surface of the holder is the reference height for the instrument and the sample must be level with this. The D500 operates at 40 kV and 30 mA at a wavelength of 0.1541 nm (CuKα radiation). The scan wavelength for this system was in 2θ mode with a scanning range from 10° to 100° with steps of 0.02° per second.

There are some limitations to the powder diffraction technique. A homogeneous and single phase material is best for identification of an unknown, and access to a standard reference file of inorganic compounds (d-spacings) is essential. The analysis requires only tenths of a gram of material which must be ground into a homogenous powder, so some manual effort is required. For mixed materials, detection limit is ~ 2% of sample. For unit cell determinations, indexing of patterns for non-isometric crystal systems is complicated. Peak overlay may occur and worsens for high angle reflections

2.9. Gel Permeation Chromatography

Gel permeation chromatography (GPC) is a type of size-exclusion chromatography (SEC) whereby the sample is dissolved in an organic solvent, such as tetrahydrofuran (THF). The aqueous analogue is referred to as gel filtration chromatography (GFC). Whilst the more common types (high performance liquid chromatography (HPLC), gas chromatography (GC), and thin layer chromatography TLC) work on the principle of retention (partitioning between a mobile and stationary phases), separation in SEC is based on the size of the molecule relative to the pore size

GPC analyses were carried out on a Waters HPLC system (dual pump; polystyrene-divinylbenzene column; UV and refractive index (RI) detectors. The mobile phase was THF; samples were dissolved in THF at 4 wt%, then injected onto the column *via* autosampler.

There are a limited number of peaks that can be resolved within the short time scale of the GPC run. Also, GPC requires an approximately 10% difference in molecular weight for a reasonable resolution of peaks to occur. In regards to polymers, the molecular masses of most of the chains will be too close for the GPC separation to show anything more than broad peaks. Another disadvantage of GPC for polymers is that filtrations must be performed before using the instrument to prevent dust and other particulates from ruining the columns and interfering with the detectors. Although useful for protecting the instrument, there is the possibility of the pre-filtration of the sample removing higher molecular weight sample before it can be loaded on the column. Another possibility to overcome these issues is the separation by field-flow fractionation.

Chapter 3 - Size Controlled Synthesis of Iron Oxide Nanoparticles

3.1 Introduction

One of the most interesting properties of ensembles of superparamagnetic iron oxide nanoparticles (NPs) is their ability to magnetise in the presence of a magnetic field generating a bulk moment, and then to completely lose this when the field is switched off. Furthermore, the magnetisation of the particles can be partially coherently driven by an alternating field, and the residual power left over from this process is dissipated as heat. The heat generated depends on physical properties of the NP, as well as strength and frequency of the AC field. A more detailed description of these factors is provided in Chapter 1.

The heat can be utilized to destroy cancer cells, either by injecting a suspension of nanoparticles directly into a tumour [118] or by functionalising the nanoparticle in such a way that it targets the cells in the tumour [119]. In magnetic hyperthermia, the heating can occur by any of three mechanisms: (i) eddy current heating due to the effects of induction from the application of an alternating pulsed magnetic field; (ii) frictional heating induced by the interaction between the NPs and the surrounding medium, and (iii) relaxation and hysteretic losses of the magnetic NPs.

As the key aspect of this thesis is the formation and use of magnetic hydrogel nanocomposites, the ability to generate nanoparticle suspensions with different heat outputs is of interest. In the case of hydrogel nanocomposites, it is especially of interest to generate large amounts of heat in short periods of time, e.g. towards a pulsatile release. The literature relating to these materials is reviewed in Chapter 1. The papers by Sun and Zeng in the early 2000s are still some of the most highly cited by those groups doing research on iron oxide nanoparticles. An overview of these papers is also provided in Chapter 1. They found that, starting with a seed particle, the particle size could be increased in stages by addition of precursor. Hence it was anticipated that multiple steps could produce NPs of sufficient size. The size of the particles can be controlled by adjusting the molar ratio of iron precursor to oleic acid and/or the number of steps. Oleic acid (OAc) is a molecule which has affinity for the iron oxide nanoparticle surface, binding as the carboxylate. According to Deacon and Phillips [120], the carboxylate ion can coordinate to the iron oxide surface in one of three ways: unidentate complex where one metal ion is binding with one carboxylic oxygen atom; a bidentate complex where one metal ion is binding with two carboxylate oxygens; or a bridging complex where two metal ions are binding with two carboxylate oxygens.

Despite the utility of this method for size-controlled synthesis of NPs, the coating of oleic acid renders the NPs hydrophobic when isolated from the reaction mixture. This non-polar layer does not make them suitable for applications in polar environments, i.e. biological applications. However, the coating of oleic acid can be displaced in favour of molecules which may render the nanoparticles dispersible in polar environments. The key to this is the anchoring moiety which allows a molecule to stabilise the NP surface. The carboxyl moiety of oleic acid can be displaced with moieties of higher affinity for the surface.

The major aims of this work were to synthesise NPs according to Sun's protocols, and characterise these materials sufficiently, so that their size-related magnetic properties could be better understood. Subsequently the particles should be phase transferred, by ligand exchange with a suitable low molecular mass species and these nanoparticles used in the formation of AC-field responsive composite gels, see Chapter 4.

3.2. Experimental

3.2.1. Materials and Methods

For the nanoparticle synthesis,[3] absolute ethanol, heptane, chloroform, benzyl ether (99%), 1,2-Tetradecanediol (97%), oleic acid (90%), oleylamine (>70%), iron(III) acetylacetonate were obtained from Sigma and used as received. The amounts of diol, oleic acid and oleylamine (OAm) weighed out were adjusted for purity, so that 9 mmol of oleylamine = (267.49 (g/mol) * 0.009 (mol)) / 0.7 (purity) = 3.44 g. For the ligand synthesis dimethylformamide (DMF), dicyclocarbodiimide (DCC), 4-Dimethylaminopyridine (DMAP) (> 99%), 3,4-Dihydroxybenzoic acid ("3,4-DHBA") (≥ 97.0 %), gallic acid ("3,4,5-THBA") (97.5 – 102.5%, titration) were obtained from Sigma and used as received. Jeffamine M-1000 (polyetheramine, "PEA") was obtained from Huntsman and used as received.

---

[3] Unless otherwise stated (in subsequent footnotes), all work described in this chapter was undertaken by Kevin Behan.

3.2.2. Synthesis of Nanoparticle Seeds (G0)

Iron(III) acetylacetonate ($Fe(acac)_3$) (1 g, 3 mmol), 1,2-Tetradecanediol (3.84 g, 15 mmol), oleic acid (2.82 g, 9 mmol), oleylamine (3.44 g, 9 mmol), and benzyl ether (30 mL) were weighed into a beaker. The beaker was placed in an oven until the diol completely melted and all components were miscible. The mixture was transferred to a 100 mL 3-neck round bottom flask (RBF) (preferably straight out of the oven) using a Pasteur pipette, then vigorously stirred under a flow of nitrogen at 80 °C for 15 minutes.[4] The mixture was then heated to 200 °C and held for 2 h. Under a blanket of nitrogen, the mixture was heated to reflux (~300 °C) for 1 h. After cooling the reaction mixture, 20 mL of heptane was added with stirring, to redisperse any aggregates which may have formed. The magnet was also washed with portions of heptane to recapture any material which was caught during the reaction. 20 mL portions of the suspension were mixed with ethanol and a black material precipitated, which was then magnetically separated. The black product was dissolved in heptane in the presence of oleic acid (~0.05 mL) and oleylamine (~0.05 mL). Centrifugation (6000 rpm, 10 min) was applied to remove any undispersed residue. The final volume of suspension was adjusted to 20 mL (this can be adjusted depending on requirements).

3.2.3. Seed-mediated Growth (G1 to G4)

All materials were prepared as for G0, and the temperature of the mixture held at 80 °C. After addition to the RBF, the seeds were pipetted into the flask and the mixture was heated to 120 °C and held there for 30 minutes to drive off the heptane. This was done under a nitrogen flow. The flask was then sealed and the synthetic protocol for G0 was followed. The work-up protocol for G0 was repeated for the subsequent generations.

3.2.4. Synthesis of Ligands

DMAP (0.5 mmol), PEA (5 mmol), and either 3,4-DHBA or gallic acid (5 mmol), were dissolved in 20 mL DMF and the mixture added to a 100 mL three-necked round bottom flask. The flask was placed on ice and purged with nitrogen over 1 hour. DCC (25 mmol)

---

[4] Stirring is essential to prevent bumping, as well as to ensure mixing during the synthesis.

was dissolved in 20 mL DMF and added dropwise from an addition funnel into the reaction mixture. The flask was removed from the ice and the reaction allowed to proceed overnight.

For the work-up the reaction mixture was filtered under vacuum to remove insoluble byproduct (dicyclohexylurea). DMF was removed by diluting 5 mL aliquots of the reaction mixture in 50 mL water, then extracting into chloroform. This was done several times to remove all of the DMF. Chloroform was removed under vacuum. Finally, the product was pipetted into dialysis tubing (MWCO 500 – 1000) and placed in a beaker of water. Water was changed after 2 hours, 4 hours, and the following day. The water was removed by azeotropic distillation using ethanol to form the azeotrope.

3.2.5. Characterisation of Suspensions

DLS measurements were performed at 25 °C ± 0.10 °C. The concentration range used for DLS was between 1 – 5 mM. Each sample measurement consisted of an average of 3 measurements (each measurement was an average of at least 10 sub runs of 10 seconds in length with the average being reported). In all cases, the RSD was below 1%. All sizes reported in this chapter are the Z-average, derived from the cumulants analysis, and referred to as dhyd, unless stated otherwise. All size intensity distributions presented were derived from the intensity weighted distribution analysis.

The core size and morphology of the particles were characterised using STEM (Hitachi S-5500) and TEM (Hitachi H-7650).[5] These techniques are described in Chapter 2. The solutions were diluted to approximately 0.2 – 1 mM with heptane. 5 μL of this solution was dropped onto a Formvar coated 400 mesh Copper grid or a Holey Carbon coated 400 mesh copper grid (Agar Scientific, Essex, UK.), and allowed to evaporate prior to imaging.

The Fe concentrations of the different dispersions were measured using flame atomic absorption.. NPs were digested using a standard acid digestion method. Typically, 100 - 200 μL of the dispersion was placed into a 50 mL conical flask. The solvent was evaporated and 1 mL of concentrated HCl (36% reagent grade) was added to the flask. This was heated until the volume of the solution was reduced to ~100 μL. 3 mL of deionised water was added to the flask and the solution was heated to boiling. This

---

[5] Brenton Cavanagh (RCSI) obtained the TEM images shown in Fig 3-11.

solution was allowed to cool, transferred to a volumetric flask and made up to the mark using 1 M nitric acid (dilution of min 65% reagent grade).

3.3. Results and Discussion

3.3.1. Size-controlled Synthesis of Superparamagnetic Iron Oxide Nanoparticles

Synthesis of iron oxide nanoparticles was done according to a procedure published by Sun *et al* [121]. A typical scheme is given below in Fig 3-1.

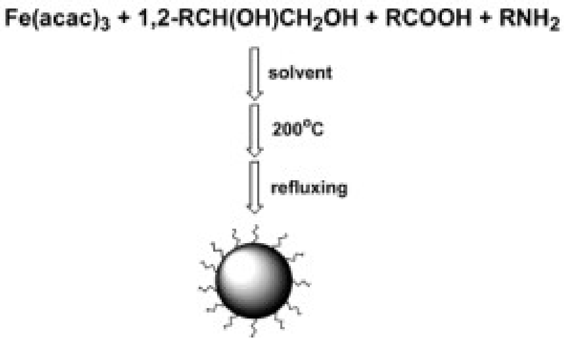

Figure 3-1: Scheme showing the synthesis of iron oxide nanoparticles, starting with iron(III) acetylacetonate as the metal precursor, 1,2-Tetradecanediol as reducing agent, oleic acid and oleylamine as surfactants. The decomposition reaction is carried out in benzyl ether at 200 °C, with annealing at 300 °C. Reproduced from [121].

The synthetic procedures and main observations are described in Section 3.2. Iron(III) acetylacetonate was reacted with 1,2-Tetradecanediol, in the presence of oleic acid and oleylamine as surfactants. The reaction solvent was benzyl ether, bp 298 °C. Post-synthesis, the reaction mixture was a sooty black colour, compared with the dark red colour of the precursor mixture. The work-up yielded a dark black pellet which responded to a neodymium magnet. For all synthetic procedures, the pellets obtained from the work-up were redispersed in heptane. These dispersions also responded to a neodymium magnet, i.e. ferrofluids were always formed. The clean dispersions were analysed by transmission electron microscopy (TEM).

TEM micrographs of representative samples of seeds (G0) and subsequent generations (G1 – G4) are shown in Figs 3-2 to 3-6. Each micrograph is accompanied by a statistical numerical analysis and a lognormal fit of the data, executed using OriginPro 9.1.

Statistical analysis was performed on each image using ImageJ (National Institutes of Health, US government). Histograms were constructed for all samples. The distributions were fitted to a log-normal particle size distribution with the probability density function P(x), of which d is the diameter and μ and σ are the mean and standard deviation of the ln(x), respectively. This model is shown in Equation 3-1.

$$P\ (x) = \frac{A}{\sqrt{2\pi}\sigma x}\ e^{\frac{-(\ln x-\mu)^2}{2\sigma^2}}$$

Equation 3- 1

Following successful fitting using this model, the particle mean and standard deviation were calculated using equations 3-2 and 3-3.

$$D_{TEM} = e^{\mu+(\sigma^2/2)}$$

Equation 3- 2

$$\sigma_{TEM} = D_{TEM} \ * \ \sqrt{\left(e^{\sigma^2} - 1\right)}$$

Equation 3- 3

Figure 3-2 shows a representative TEM image of the prepared seeds, according to Sun's method. In this case the reaction mixture was heated to 200 °C and held for two hours. Following this, the reaction was heated to boiling (298 °C) and held for one hour. The particles shown in Fig 3-2 tend to be monodisperse, well-formed and quasi-spherical. The approximate concentration of the heptane suspensions prior to depositing on the holey carbon grids was 0.5 – 1 mg/mL.

Working with the ImageJ program, analysis of the image allowed calculation of an average size of 7.5 nm, with a standard deviation of 1.6 nm. The mean diameter was 1.5 nm greater than that for the seeds reported by Sun and colleagues. The resulting data was used to construct a histogram and it was shown that the lognormal fit yielded similar mean and standard deviation values (7.3 ± 1.2 nm) in comparison to the core diameters measured using ImageJ .

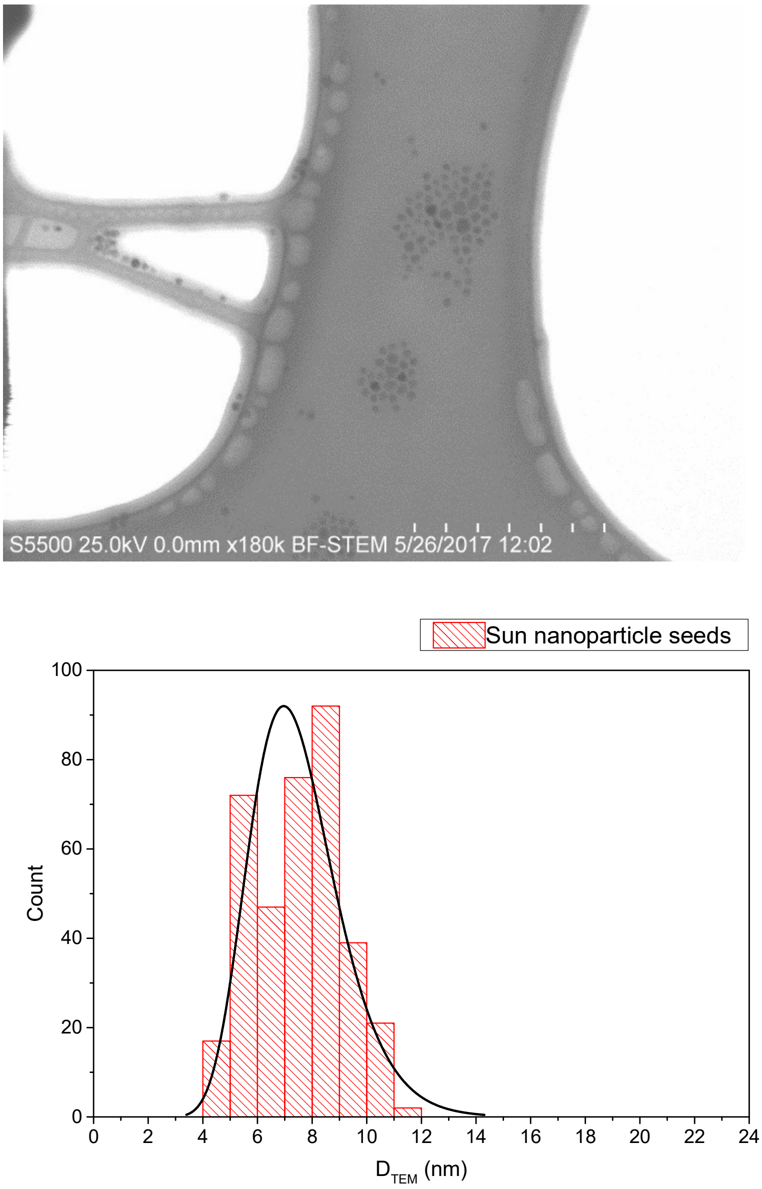

Figure 3-2: TEM image of iron oxide nanoparticle seeds (G0), synthesised according to Sun *et al*. The image is representative, i.e. several images were used to generate a sufficient sample size (366 particles measured using ImageJ analysis). The mean value was 7.5 ± 1.6 nm. The lognormal fit based on the histogram gave a mean of 7.3 ± 1.2 nm.

The seeds (G0) were added to the mixture for the next synthetic step. The decomposition and reflux times were reduced to 1 and 0.5 hours, respectively. The addition of 3 mmol of iron precursor, together with the seeds, resulted in nanoparticles (G1) with D_{TEM} of 8.7 ± 1.2 nm. Therefore, the mean D_{TEM} increased by 1.2 nm. This suggests seed mediated growth is predominant, as opposed to secondary nucleation. Starting with G1 as seeds, in a subsequent step the mean D_{TEM} increased by 3 nm to 11.7 ± 1.8 nm (G2). A further step resulted in nanoparticles with mean D_{TEM} of 14.2 ± 1.6 nm (G3), an increase of 2.5 nm. G3 seeds resulted in nanoparticles with mean D_{TEM} of 15.0 ± 2.0 (G4), an increase of 0.8 nm. Particle diameters were also calculated from the log-normal fit (Equations 3-2 and 3-3). Seeds (G0) were 7.3 ± 1.2 nm; G1 was 8.6 ± 1.1 nm; G2 was 11.6 ± 1.2; G3 was 14.0 ± 1.2; and G4 was 14.9 ± 1.2. This demonstrates the suitability of the log-normal model for analysing this data.

The data indicate that addition of previously synthesised seeds in the subsequent steps results in larger particles, maintaining a spherical shape and monodispersity. The low polydispersities, together with the larger than expected experimental diameters of G2 to G4, as compared to the expectations from the Sun study, suggest a reduction in the number of nanoparticles going into each synthetic step, which results in a larger particle size increase, due to more monomer available per particle. This assumes a heterogenous nucleation mechanism, whereby the existing population of seeds grows through diffusion of monomer onto the seed surface, rendering the nanoparticle number constant.

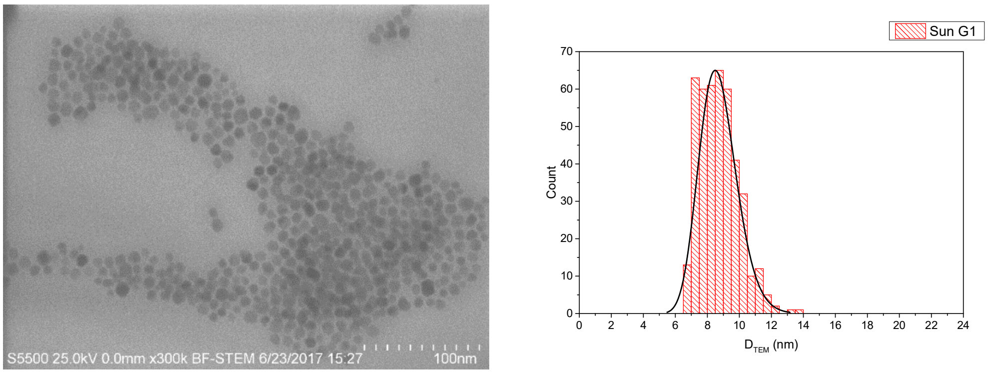

Figure 3-3: TEM image of first generation iron oxide nanoparticles (G1), synthesised according to Sun *et al*. The mean value was 8.7 ± 1.2 nm. The lognormal fit based on the histogram gave a mean of 8.6 ± 1.1 nm.

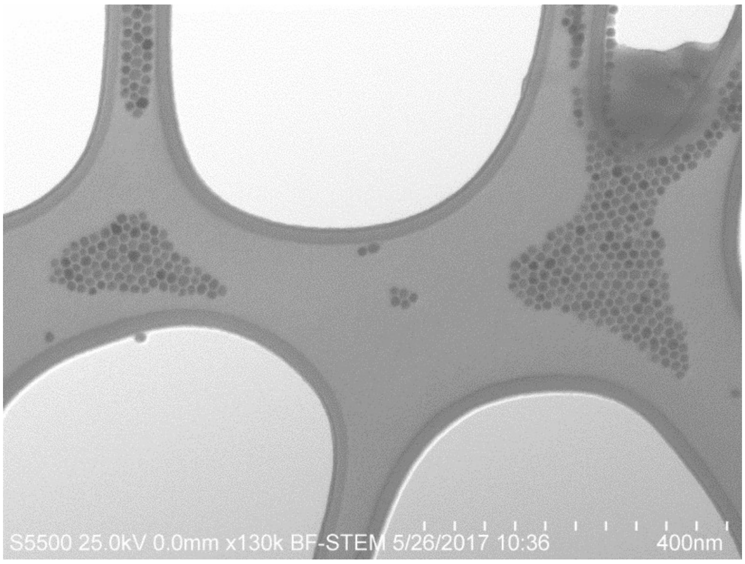

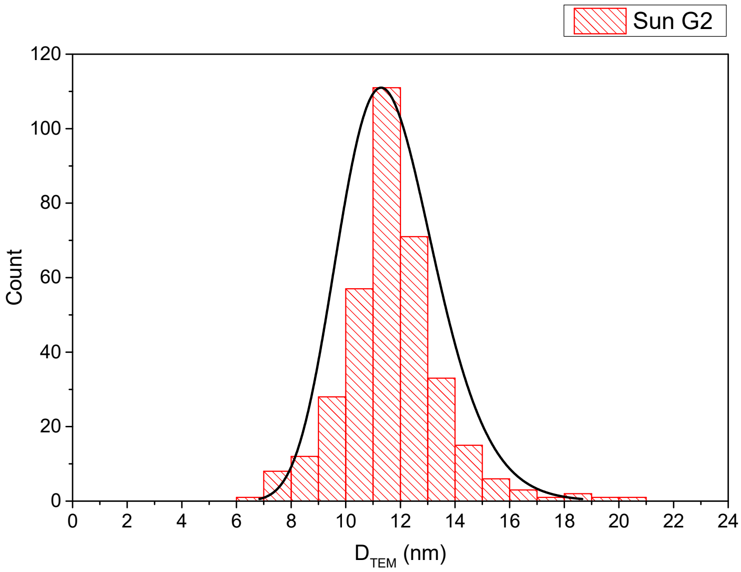

Figure 3-4: TEM image of second generation iron oxide nanoparticles (G2), synthesised according to Sun *et al*. The mean value was 11.7 ± 1.8 nm. The lognormal fit based on the histogram gave a mean of 11.6 ± 1.2 nm.

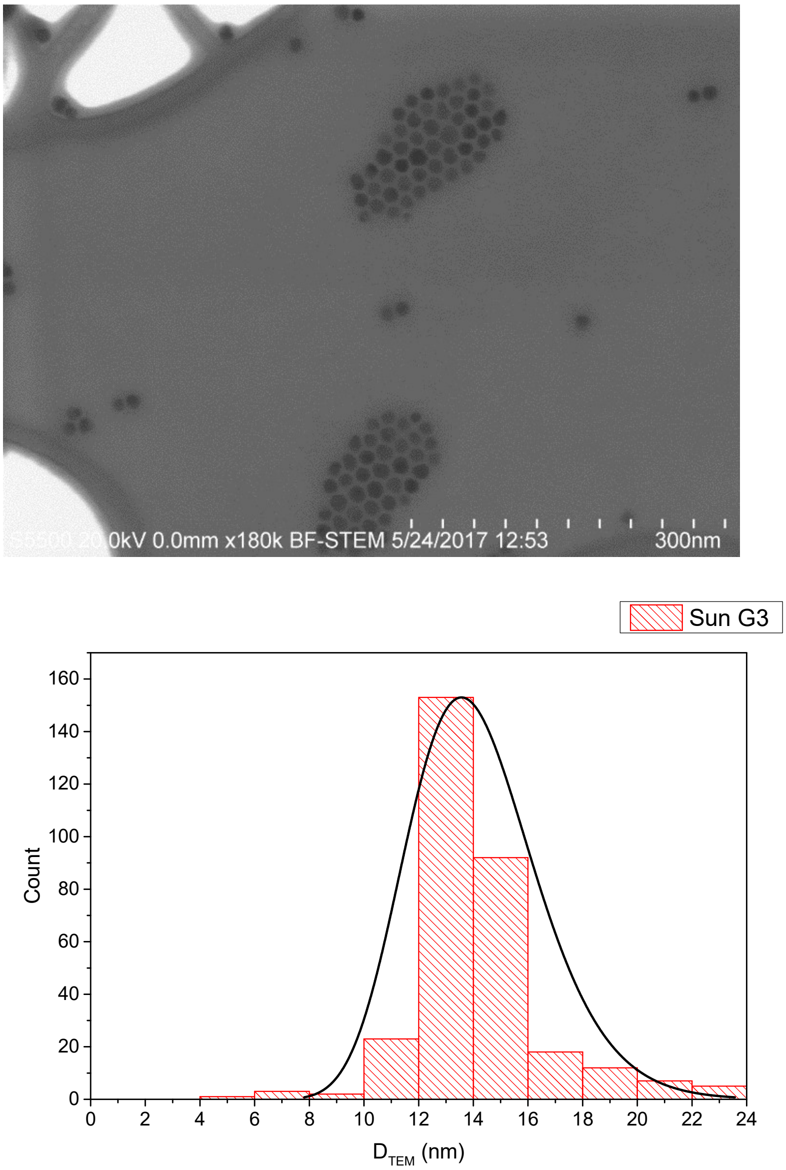

Figure 3-5: TEM image of third generation iron oxide nanoparticles (G3), synthesised according to Sun *et al*. The image is representative, i.e. several images were used to generate a sufficient sample size (317 particles measured using ImageJ analysis). The mean value was 14.2 ± 1.6 nm. The lognormal fit based on the histogram gave a mean of 14.0 ± 1.2 nm.

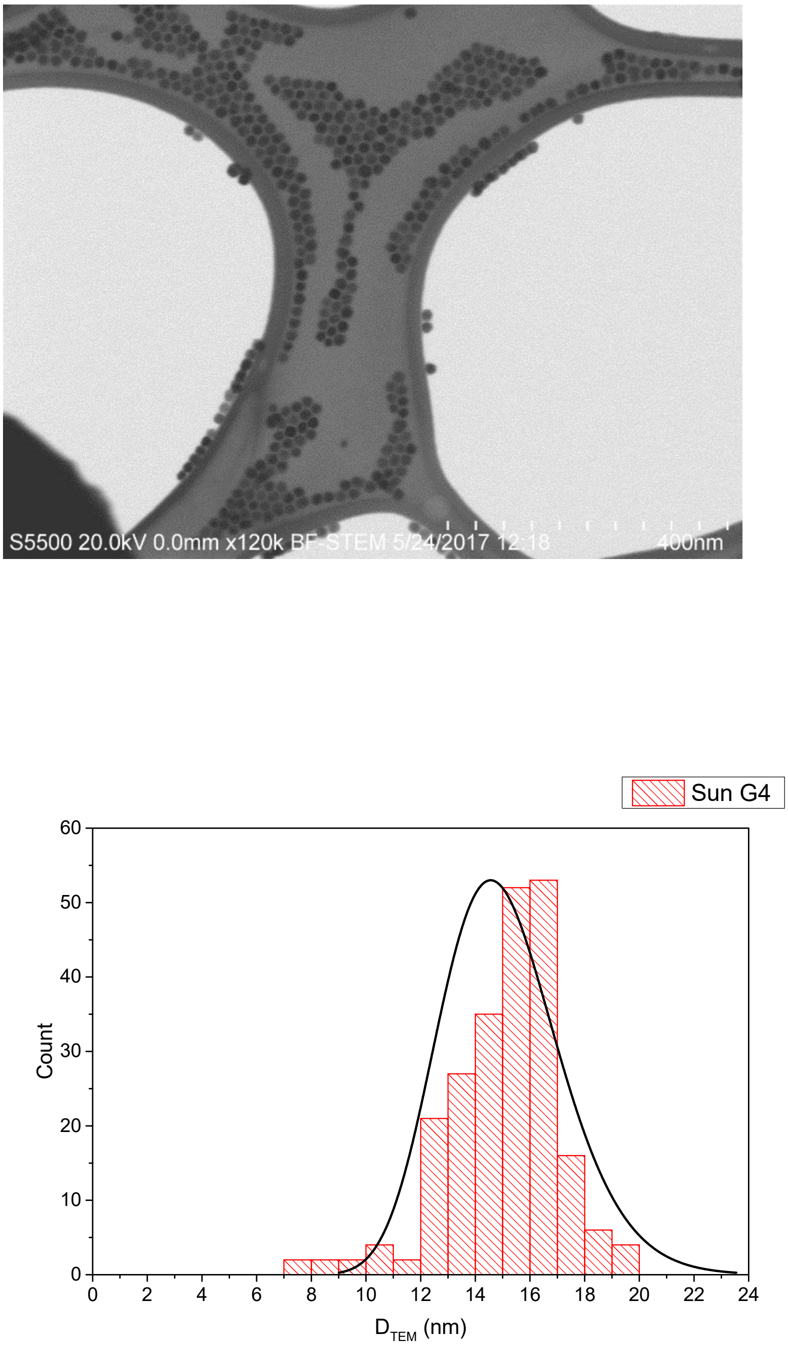

Figure 3-6: TEM image of fourth generation iron oxide nanoparticles (G4), synthesised according to Sun *et al*. The mean value was 15.0 ± 2.0 nm. The lognormal fit based on the histogram gave a mean of 14.9 ± 1.2 nm.

In the original procedure the synthesis times for the seeds (G0) are different to the times for the subsequent steps. Sun does not make clear the reasons for this change. It is not known how fast the resulting monomers diffuse and react at the particle surface, but it is reasonable to suggest that, in the presence of the seeds, it is fast enough to preclude nucleation, given that the starting precursor concentration is the same as in the initial step.

Sun's paper discusses the molar ratio of OAc/OAm to Fe precursor, and its effect on nanoparticle size. The purity of the technical grade oleic acid (90%) and oleylamine (70%) used by Sun may be a factor as they did not specify whether the amount quoted (9 mmol) was based on 90% oleic acid and 70% oleylamine content, i.e. it may be the case that significant amounts of impurities were present in the reaction mixture. Therefore, it is recommended that a synthesis using high purity oleic acid and oleylamine is carried out, to see if this affects outcomes such as size, shape, and batch-to-batch reproducibility.

Sun also showed that the choice of solvent determines the size of the seeds produced. Refluxing in phenyl ether (b.p. 259 °C) yielded seeds with a diameter of 4 nm, compared with 6 nm using benzyl ether (b.p. 298 °C). Considering that the first step in the synthesis is carried out at 200 °C, it can be hypothesised that the reflux temperature is critical in determining final seed size, suggesting that growth (and not nucleation) is size limiting. The concept of seed-mediated growth, whereby nucleation is confined to the seed surfaces in later steps, allows a better understanding of the stepwise growth. The newly-formed monomers, a result of the iron precursor decomposition, react on the surface of the seeds. As noted above, if this is fast, or if the concentration of monomer is low, homogenous nucleation can be avoided.

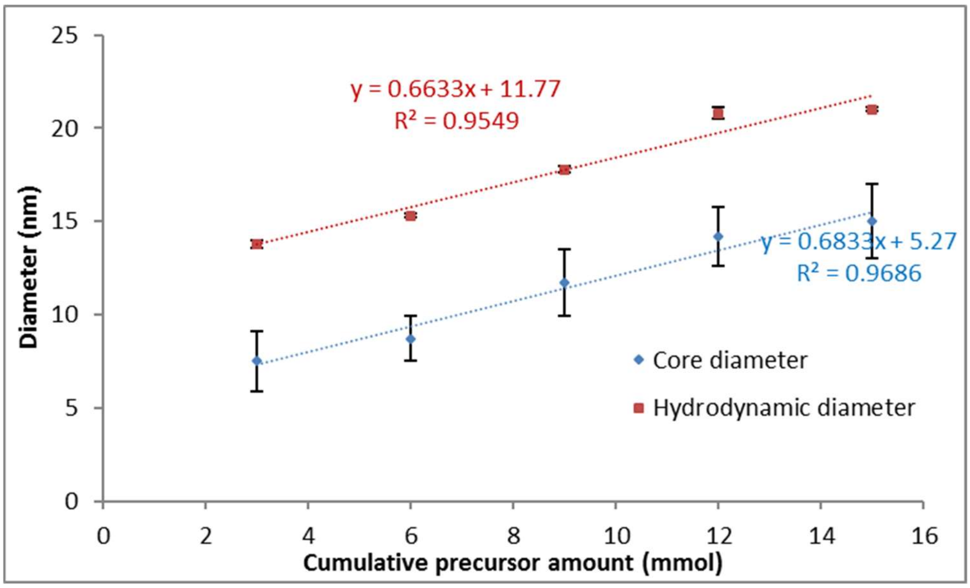

Figure 3-7: Effect of precursor on nanoparticle size, as determined by TEM (core) and DLS (hydrodynamic diameter). Both sets of data were obtained using dispersions of iron oxide nanoparticles in heptane.

Plotting the core (TEM) and hydrodynamic (DLS) diameters as a function of the total amount of precursor for the five synthetic steps, the relationship is found to be approximately linear (Fig 3-7). The increase in core size for G4 is possibly smaller than might be expected. This is observed in the data from both TEM and DLS.

Taking the increase in D_{TEM} from Table 3-7 the stepwise fractional increases in volume (assuming monodisperse spheres) from G0-G1, G1-G2, G2-G3 and G3-G4 are 1.56, 2.43, 1.79, 1.18, respectively. This emphasises the tailing off for G4, but more importantly it demonstrates that the yield for G1-G2 cannot be quantitative, i.e. some particles must be lost. Quantitative analysis was attempted for this set of samples, however, material was lost during the preparation (some of the samples crashed out) and this was not immediately noticed. So, this issue was revisited for a fresh NP series, see below.

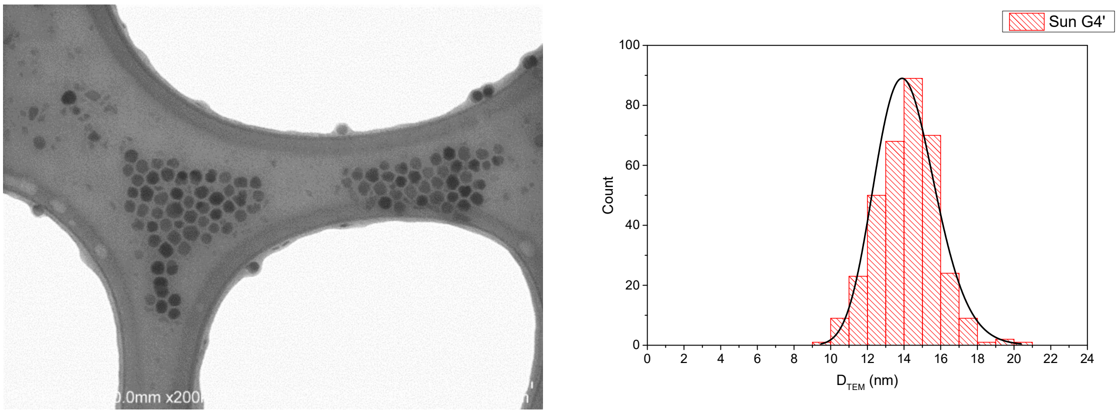

Figure 3-8: Left: TEM image of fourth generation iron oxide nanoparticles, synthesised according to Sun *et al*. A change to the method was an extended decomposition step (2h versus 1h), as well as extended reflux (1h versus 0.5h), for all growth steps. This sample was referred to as G4', versus G4 for the sample generated using Sun's published conditions. Both samples derived from the same batch of seeds. The image is representative, i.e. several images were used to generate a sufficient sample size. Right: 347 particles measured using ImageJ analysis. The mean value was 14.2 ± 1.7nm. The lognormal fit based on the histogram gave a mean of 14.1 ± 1.1 nm.

The core and hydrodynamic diameters for the seeds, G1 – G4, and of a new sample G4', are listed in Table 3-2. To generate G4', the synthesis times for G1 through to G4 were increased by a factor of two. Comparing the core size of G4 to G4', the dependence of size on synthesis conditions is apparent, with an average size of 15 nm for G4 versus 14.2 nm for G4', as determined by TEM (Fig 3-8). Interestingly, the average size of G4' is the same as that for G3, which was synthesised using the standard conditions described in Sun's paper. G4' is expected to have a larger size, as both the decomposition and reflux times for G1 through to G4 are doubled. Assuming no errors in preparation, it can be hypothesised that there are a higher number of particles in the sample G4'. Moreover, sample G4' (10.4 mg/mL) has been determined to contain more iron than G4 (7.8 mg/mL). While the work-up efficiency may vary, longer reaction times appear to increase the yield of stable, monodisperse nanoparticles.

3.3.2. Particle size as determined by Dynamic Light Scattering

The hydrodynamic diameters and polydispersity indices for the heptane dispersions (G0 to G4), as determined by DLS, are listed in Table 3-2. All of the suspensions were relatively monodisperse, typically with PDI <0.07, indicative of a unimodal size distribution. For each suspension, the washing protocol involved precipitation in ethanol, followed by resuspension in heptane and addition of OAc/OAm surfactants (total 100 μL). The total volume of suspension was 20 mL. The measured hydrodynamic size of each representative sample was on average 6.4 nm greater than the TEM core size. This indicates a ligand layer thickness of 3.2 nm, which is comparable to that described in another paper published by Sun's group, which estimated one monolayer of C18 to be 3-4 nm [122]. Granata et al also estimated a length of 1.97 nm for the oleic acid molecule [123]. A similar difference in dhyd (also in heptane) and D_{TEM} of 1.9 nm was obtained by Meledandri et al [124]. This is indicative of the difference in synthetic conditions employed in each work. Meledandri and co-workers conducted all reactions in phenyl ether, refluxing for 15 minutes (268 °C), compared with the conditions employed in this work, i.e. benzyl ether as solvent (298 °C), typical reaction time of 60 minutes (see experimental section 3.2.). The implication (of Sun's work but not Granata's) is that the greater hydrodynamic shell thickness reflects a layer of oleic acid plus a solvation layer of heptane molecules. However, some caution must be exercised with this interpretation; DLS measurements are sensitive to factors such as concentration, and these factors affect different optical setups (as used in the identified studies) in different ways. There is no indication from electron microscopy of any aggregation. This could be confirmed by fast-field cycling NMR relaxometry, a technique applied by our group for MNP suspensions [124]. However, at the time of this study the instrument was not available.

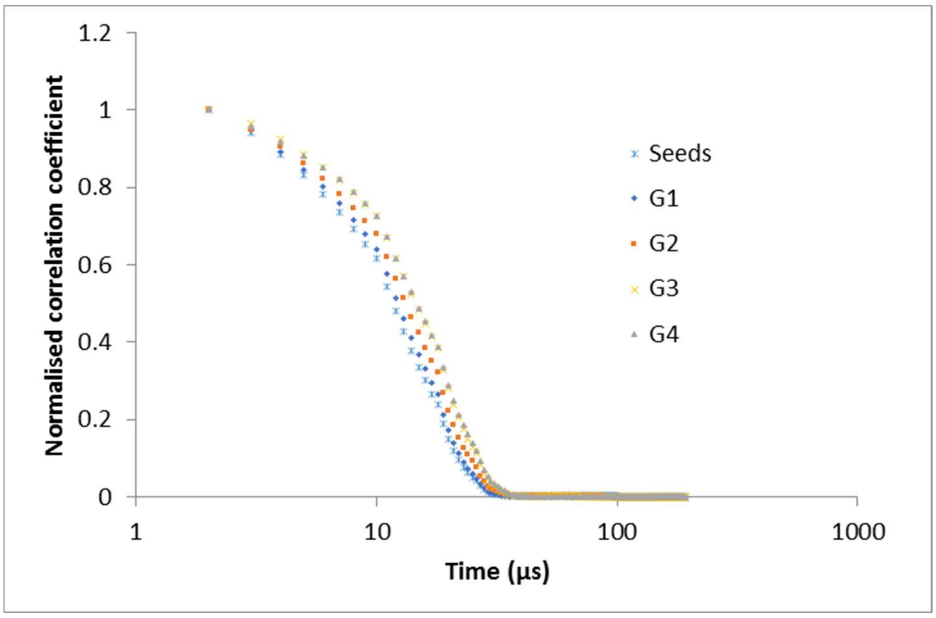

Figure 3-9 Overlay of normalised correlograms for all suspensions of C18-coated nanoparticles dispersed in heptane. As particle diameter increases, correlogram shifts to the right, indicating longer diffusion times.

The normalised correlograms for G0 through to G4 are overlaid in Fig 3-9. The correlogram for G0 is furthest to the left, indicating that the onset of correlation decay is fastest for those particles. Conversely, the onset of correlation decay increases with particle size, and the correlogram shifts to the right. The data shows the absence of aggregates, as well as a gradual increase in τ_{DIFF} for each subsequent generation. The slope of the decay in all cases is similar, indicating that all suspensions are monodisperse, or at least have similar polydispersity. The experimental (D_{TEM}) and theoretical core diameters, hydrodynamic diameter (dhyd) and PDI of the suspensions G0 to G4, as well as G4', are summarised in Table 3-1.

Table 3-1: D_{TEM} and dhyd of iron oxide nanoparticles seeds; G1 – G4; and G4'.

Sample ID	**D_{TEM} (nm)**	**Theoretical diameter, D (nm)** [6]	**dhyd (nm)**	**PDI**
G0	7.5 ± 1.6	-	13.8 ± 0.2	0.07
G1	8.7 ± 1.2	9.4	15.3 ± 0.1	0.05
G2	11.7 ± 1.8	10.8	17.8 ± 0.2	0.07
G3	14.2 ± 1.6	11.9	20.8 ± 0.3	0.13
G4	15.0 ± 2.0	12.8	21.0 ± 0.1	0.05
G4'	14.2 ± 1.7	-	20.3 ± 0.1	0.03

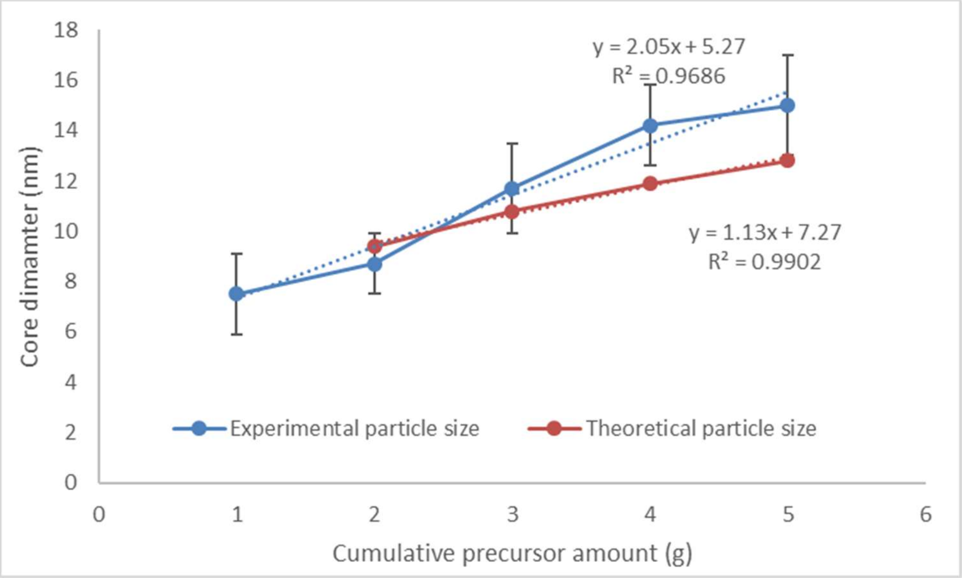

Figure 3-10: Experimental versus theoretical particle size (calculated from measured D_{TEM}). The nanoparticle dispersions were in heptane.

The experimental and theoretical particle sizes are displayed in Fig 3-10. The mean values calculated from the experimental data begin to diverge from the theoretical values, at the third synthetic step (3 g of precursor). The theoretical data is calculated from the experimental core diameter for G0, as determined by TEM. Again, this data assumes the persistence of all particles formed during the first synthetic step through to subsequent syntheses. This tends not to be the case, as in reality not all particles survive. For G3 and

---

[6] The theoretical diameter is calculated by taking the determined seed diameter (D_{TEM} 7.5 ± 1.6 nm) and, assuming full conversion of the iron precursor, extrapolating to a size which is equivalent to the theoretical increase in volume. A heterogeneous nucleation mechanism is assumed in such a case, which would result in the same number of particles, albeit larger in size.

G4, the mean experimental values were higher than the theoretical values (by a factor of 1.19 and 1.17, respectively), albeit in some cases the D_{TEM} standard deviations overlap with the experimental data.

A repeat series of NP suspensions were prepared and the yields for each step were determined by FAA analysis of the non-centrifuged suspensions. In this case each suspension was placed on a neodymium magnetic for one hour to remove any large magnetically-attracted aggregates. The dispersed particle yields are summarised in Table 3-2. It can be seen that the yields are very similar for G0 to G2, then start to drop for G3 and G4. This may be due to some particles aggregating during the later steps.

Table 3-2: Repeat synthesis of G4’ nanoparticles. Experimental versus theoretical [Fe].

Sample	**Theoretical [Fe] (mg/mL)**	**Experimental [Fe] (mg/mL)**	**Step Yield (%)**	**D_{TEM} (nm)**
G0	8.3354	7.4451	89.32	7.5 ± 1.6
G1’	15.7805	14.2633	90.39	8.7 ± 1.2
G2’	22.5987	19.9843	88.43	11.7 ± 1.8
G3’	28.3197	22.1003	78.04	14.2 ± 1.6
G4’	30.4357	16.2226	53.30	15.0 ± 2.0

G0 and G4 were analysed by TEM (Fig 3-11). The D_{TEM} was 8.2 ± 0.9 nm for G0, and 13.7 ± 1.5 nm for G4’. This compares to 7.5 ± 1.6 nm for the previous batch of G0, and 14.2 ± 1.7 nm for the previous batch of G4’.

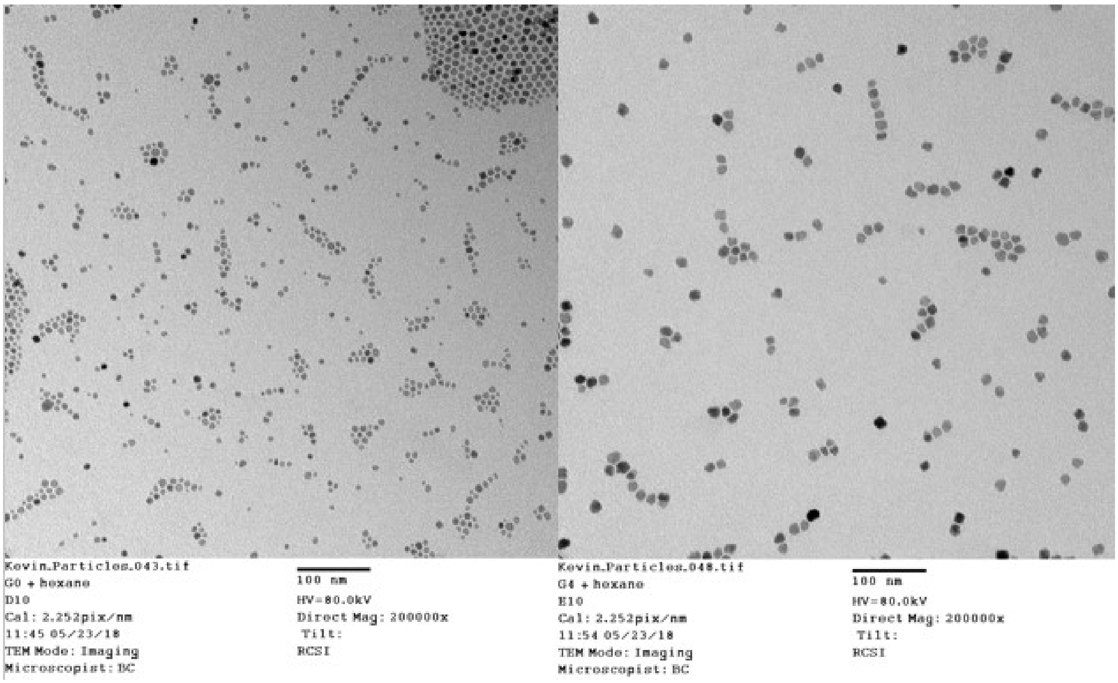

Figure 3-11: TEM images of repeat G0 and G4’ nanoparticle hexane suspensions. The D_{TEM} was 8.2 ± 0.9 nm for G0, and 13.7 ± 1.5 nm for G4’.

The estimated errors render the synthetic method reproducible with respect to size. For the remainder of the discussion, all experiments used the non-centrifuged suspensions from the original synthesis.

The TEM analysis of the G series and the yields of the G’ series were combined to calculate nominal particle numbers for the multi-step process (Table 3-3 and Fig 3-12). This is reasonable as the final sizes were very similar, however, the outcome should be viewed with some caution.

Table 3-3: Particle numbers with respect to particle size, D_{TEM}

Sample ID	**D_{TEM} (nm)**	**Experimental [Fe] (mg/mL)**	**Step Yield (%)**	**Particle number**
G0	7.5 ± 1.6	7.4451	89.32	6.5×10^{15}
G1’	8.7 ± 1.2	14.2633	90.39	8.0×10^{15}
G2’	11.7 ± 1.8	19.9843	88.43	4.6×10^{15}
G3’	14.2 ± 1.6	22.1003	78.04	2.9×10^{15}
G4’	15.0 ± 2.0	16.2226	53.30	1.8×10^{15}

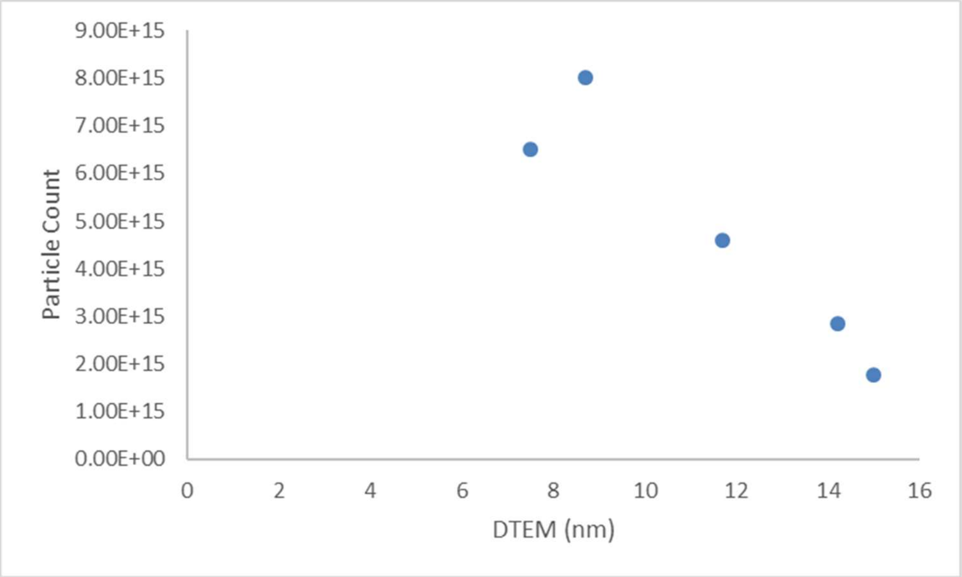

Figure 3-12: Graph of particle number with respect to the particle size, D_{TEM}.

Going from G0 to G1, and assuming monodisperse spheres, the number of NPs probably increases slightly. The difference might be due to errors, but it is unlikely given the good TEM data and low FAA errors. A tentative conclusion is that there may be some secondary homogenous nucleation when going from G0 to G1.

For the later stages, again assuming monodisperse spheres (and noting that the TEM % deviations do not change much down the series), the reduction in number suggests that NP losses are greater than any secondary homogenous nucleation. If the latter is low and constant then the losses are similar from step to step, which is encouraging. This raises two questions:

(i) Why are there losses?

This could de simply due to the workup. An attempt was made to maximise the dispersed yield. The fact that the drop is similar step to step suggests this has been achieved.

(ii) Why is G0 to G1 different from G1 to G2 and subsequent steps?

The amount of precursor, and its concentration, are unchanged step to step, while the number of NPs decreases slightly and the available surface area increases in each step. Also, the Fe concentration from the added precursor is constant. That might give a nanoparticle concentration range where secondary nucleation is suppressed. Similarly, it seems that reducing the surface area to volume ratio (with increasing NP size) does not suppress heterogeneous nucleation, taking things out of that kinetic regime.

3.3.3. Effect of Nanoparticle Size on Magnetic Properties in AC Field

To study their AC-field heating properties, the heptane dispersions of iron oxide nanoparticles, G0 through to G4, as well as G4', were placed in an AC magnetic field. Fig 3-13 shows the first 100 seconds of the heating profile for each suspension. A second order polynomial was fitted to each curve and the initial slope extracted as the linear term. This was corrected with the mass of iron, along with the heat capacities and masses of the respective components, and entering the values into the equation used by Gazeau et al [42]. A more detailed description can be found in Section 3.2. As described in Chapter 1, the heating of magnetic nanoparticles in AC fields can be described by a relation known as the specific absorption rate (SAR), Eq. 3-4. It states that the heating over time is dependent on the mass of magnetic material in the suspension, together with the sum of the heat capacities of the various components. The initial slope of heating is factored in.

$$\mathrm{SAR} = \frac{1}{m_e}\left(\sum_i c_i m_i \frac{dT}{dt}\right)$$

Equation 3- 4

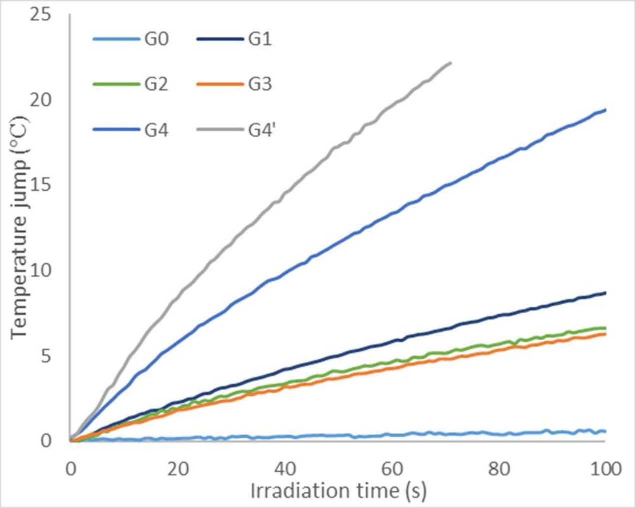

Figure 3-13 Uncorrected heating profiles of nanoparticle suspensions in heptane. Following the work-up procedure, each sample was dispersed in heptane, to a final volume of 20 mL. In each case, 1 mL of suspension was exposed to the AC field (476.6 kHz, 9.8 kA/m). For each measurement, the fiber optic probe was placed just below the meniscus of the suspension.

Table 3-4: SAR values measured for heptane suspensions of different generation NPs.

Sample ID	**Mean NP diameter (nm)**	**SAR (W/g)**
G0	7.5	1.92
G1	8.7	10.9
G2	11.7	11.8
G3	14.2	14.5
G4	15.0	49.4
G4’	14.2	63.7

The uncorrected magnetic hyperthermia data in Fig 3-13 was normalised using the SAR value for each suspension. The calculated SAR values are listed in Table 3-4. These were plotted against the mean nanoparticle diameters for G0, G1, G2, G3, G4, and G4’ (Fig 3-14). Some interesting size-dependent properties were observed. The lowest SAR was calculated for G0 (1.92 W/g). A size increase of 1.2 nm sees a 5-fold increase in the SAR for G1 (10.9 W/g), increasing to 11.8 W/g for G2, and 14.5 W/g for G3. There is a 3-fold increase observed for the G3 to G4 transition (14.5 to 49.4 W/g), despite a size increase of only 0.8 nm. The relatively small increase in the measured nanoparticle size would suggest a fundamental change in the morphology and/or crystallinity of the particle, influencing the magnetic properties. The magnetic moments of truly superparamagnetic nanoparticles fluctuate thermally, as there is no energetic barrier towards an easy axis, i.e. they have spontaneous magnetisation. This might explain why nanoparticles below a certain size have negligible heating, even in the presence of the AC field, as there is little or no energy barrier to overcome. It may be the case that, during the transition from G3 to G4, anisotropy increases and the hysteresis contribution becomes important. If the intensity of the AC field is such that the direction of magnetisation is no longer along the easy axis, then this energy required to drive magnetisation along a hard axis will be dissipated as heat, perhaps explaining the significant increase in heat output for G4 nanoparticles.

G4’ had the highest SAR (63.7 W/g). Considering the reaction conditions for the synthesis of G4’, it is expected that the average particle size would be larger than G4. In fact, G4’ had the same average size as G3 (14.2 nm), yet the SAR value was almost 4.5 times greater. Typically, the annealing step described in Sun’s paper lasts 30 minutes, but for

G4' in this work 60 minutes was used. This may increase crystallinity in all particles from G2' to G4' and would explain the significant increase in the SAR value for G4'.

The saturation magnetisation of iron oxide nanoparticles is dependent on several factors, including the crystallinity. At the nanoparticle surface, where it tends to be relatively disordered, there is a reduced magnetisation. As the particle size increases and relative surface area decreases, the ratio of ordered to disordered stoichiometric units is increased, resulting in higher crystallinity and hence an increased M_S.

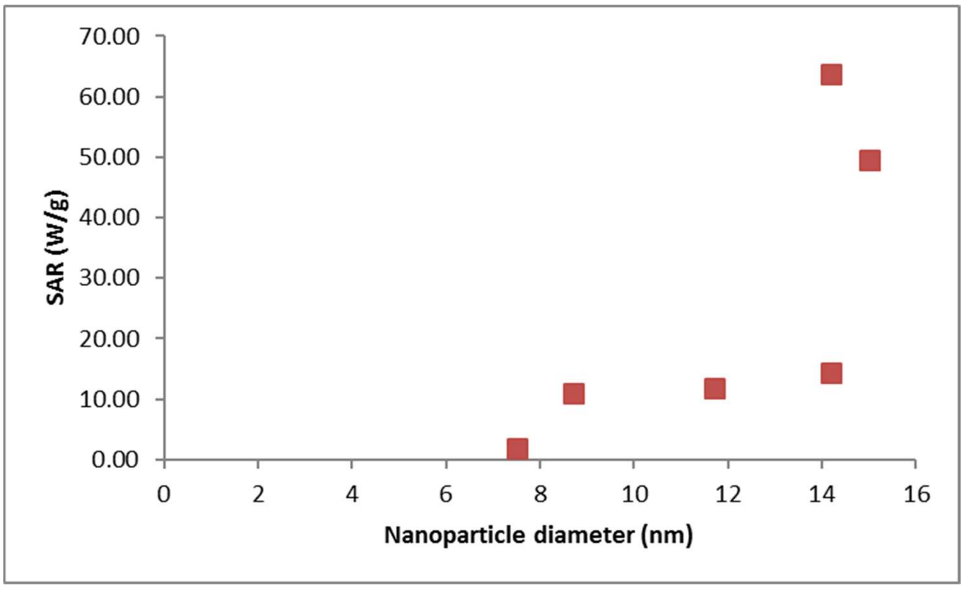

Figure 3-14: SAR as a function of iron oxide nanoparticle diameter, as summarised in Table 3-3. SAR was calculated according to the formula used by Gazeau et al [42]. Nanoparticle dispersions were in heptane.

The relationship between saturation magnetisation (M_S), coercivity (H_C), blocking temperature (T_B) and SAR is not fully understood. De Sousa et al reported "no clear relation between SAR values either with magnetic core size or with distribution standard deviation" [125]. Further, no obvious correlation was observed between the core or hydrodynamic diameters. A general upward trend is observed in De Sousa's data when the SAR is plotted against the saturation magnetisation. However, this parameter alone is not sufficient to explain the effect of the particle size on the heating characteristic. Several authors discuss magnetothermal properties of iron oxide nanoparticles in the context of magnetocrystalline anisotropy, K [126, 127]. Lee et al discuss an optimal range of K which corresponds to the Neel component, and the size D which corresponds to both Neel and Brownian components for high SAR iron oxides (1000 to 4000 W/g). They suggest that size alone does not correlate with SAR. Based on the data in Fig 3-14 (G3 v G4') this also appears to be the case, and underlines the need for a thorough characterisation, to include size, saturation magnetisation and magnetocrystalline anisotropy.

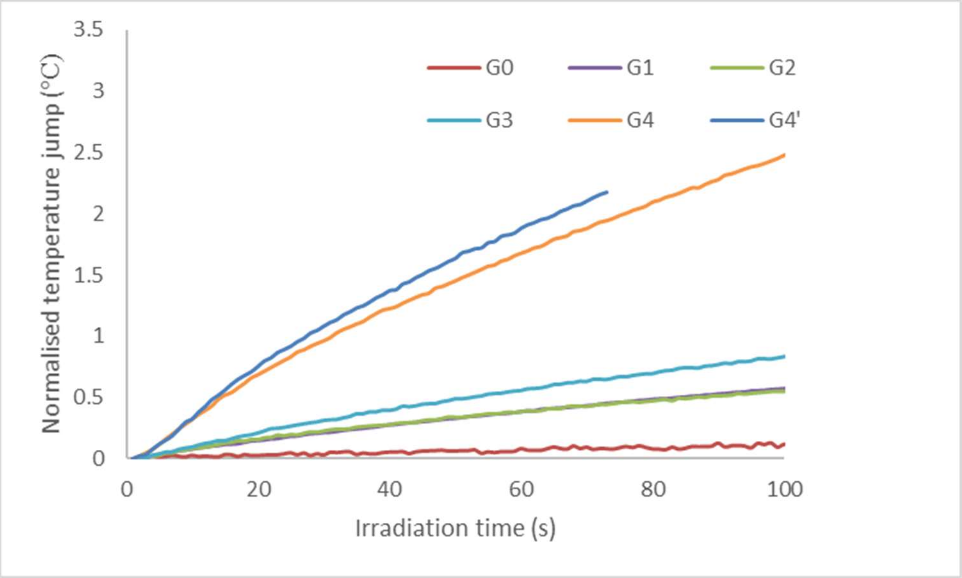

Figure 3-15 Normalised temperature data taken from Fig 10, using [Fe] (mg/mL). The nanoparticle suspensions were in heptane. The heating curves for G1 (purple) and G2 (green) overlap.

Data from the heating curves as depicted in Fig 3-13 were normalised with the iron concentration (mg/mL), determined by FAA in each nanoparticle suspension. Normalised temperature curves were then constructed (Fig 3-15). The seeds (G0) produce the least amount of heat, probably as the energy boundary for magnetisation is lowest. G2 has a core size of 11.7 nm, which is 3 nm larger than G1 (8.7 nm), yet both the SAR values (10.9 W/g for G1 and 11.8 W/g for G2) are similar. When normalised against the iron concentration the magnetic hyperthermia heating profiles for these two suspensions overlap strongly. It would be interesting to know the saturation magnetisation values for these two samples, and to see how this correlates with the other data. However, except for G4 and G4', full magnetometric characterisation of all samples was not possible. Finally, the choice of ligand for stabilisation in aqueous medium is another factor which may affect the SAR. This will be discussed in the following section.

3.3.4. Synthesis of PEA-catechols

Nanoparticles produced using the Sun method have a coating of C18 surfactants and, whilst these particles are monodisperse and stable in organic solvents, they are not suitable for applications in polar environments. The layer of oleic acid and oleylamine can be displaced by a ligand whose anchoring group has greater affinity for the nanoparticle surface. The carboxyl groups of oleic acid can be displaced by amines, silanes, phosphonates, and catechols [128]. Catechols were chosen for this study as they have a high affinity for iron oxides, to the extent that the binding can be considered irreversible [129]. It is possible, using DCC coupling, to link the acid moiety of a hydroxybenzoic acid to an amine-bearing block copolymer. Phase transfer of the G4' nanoparticles was carried out using a catechol-functionalised PEA. The structures of the catechol-functionalised polymers are shown in Fig 3-16 below. These are referred to as PEA-3,4 (PEA coupled to 3,4-DHBA) and PEA-3,4,5 (PEA coupled to gallic acid).

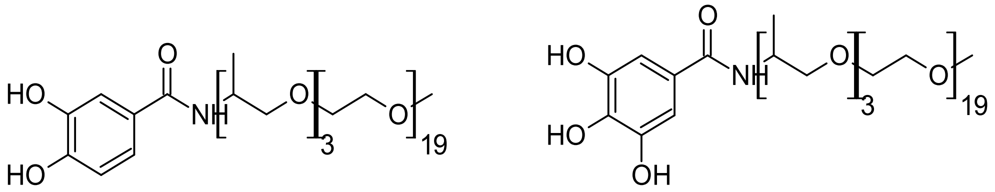

Figure 3-16: Molecular structures of PEA-3,4 (left) and PEA-3,4,5 (right).

When first attempting a synthesis of catechol-functionalised polymers using methoxy-PEGs, the yields of the ester were low (typically < 20%). Amines, whilst normally reacting with carboxylic acids to form stable carboxylate salts, can be made to form amides by first activating the carboxylic acid towards nucleophilic attack. Starting with a polyetheramine, formation of the amide was typically > 90%. As well as this, the resulting amides are more stable than esters, which could be advantageous for biological applications. Fig 3-18 shows a 1H NMR spectrum for a PEA-catechol. The resonance d confirms formation of the amide bond.

The synthesis is outlined in the scheme (Fig 3-17), as shown in the paper by Montalbetti and Falque [130]. For every 2 moles of carboxylic acid going into the reaction, one mole reacts with the DCC to form an intermediate. The other mole of carboxylic acid reacts with the intermediate to form an anhydride, with dicyclohexylurea as leaving group. The anhydride is then free to react with the amine, forming the functionalised polymer and carboxylic acid as leaving group. This means that for every mole of polymer to be functionalised, at least two moles of carboxylic acid must be used. To avoid this, a mixed anhydride approach is possible, as opposed to the symmetric anhydride route used in this work. However, assuming the acid is readily available and cheap, then the symmetric anhydride route is justifiable.

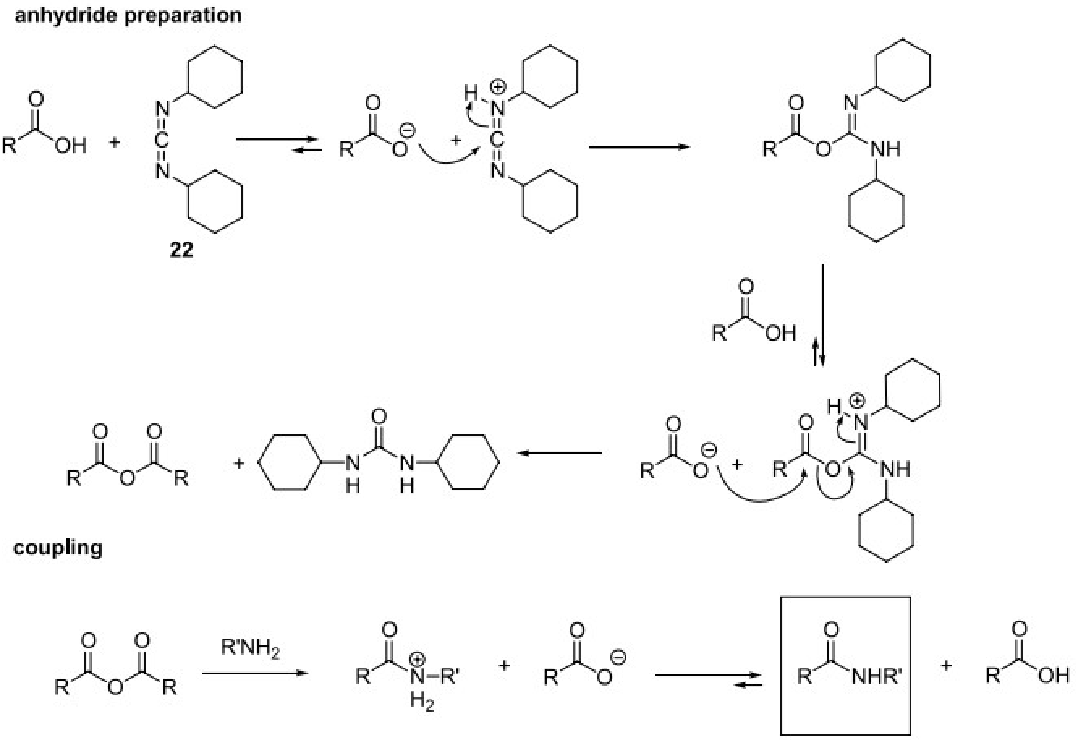

Figure 3-17: General scheme for the DCC coupling of a carboxylic acid to an amine. Reproduced from [130].

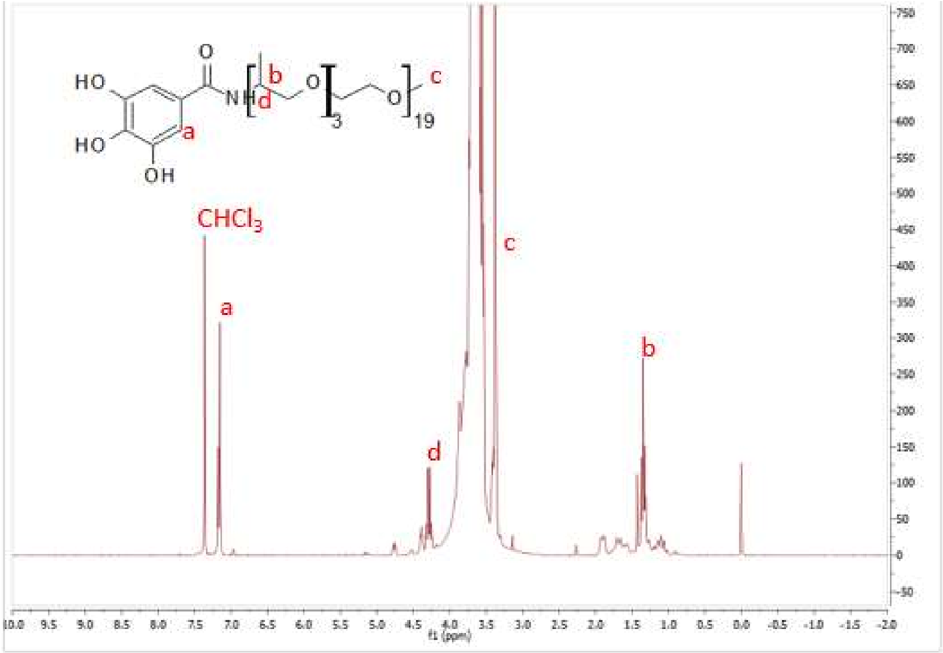

Figure 3-18: ^{1}H-NMR spectrum at 400 MHz of PEA-catechol

3.3.4. Effect of the Head Group (3,4,5-THBA acid versus 3,4-DHBA)

DCC coupling was used to synthesise two catechol-functionalised polyetheramines. In separate experiments, aliquots of G4 nanoparticles dispersed in heptane were first precipitated with ethanol and the supernatants separated by magnetic decantation. The remaining precipitates were treated with chloroform solutions of each ligand. The amount of ligand was calculated as 100 times the excess of the amount required to form a monolayer on the surface of the nanoparticle. This is based on a paper which calculated (using TGA data) the footprint of an oleic acid molecule on the iron oxide nanoparticle surface to be 38 Å^2 [131]. This approach was used consistently, but a good purification method is recommended. Samples dispersed in ethanol (approx. 1 mL) were taken for DLS measurements. After one day of shaking, the ethanol dispersions of iron oxide nanoparticles treated with PEA-3,4,5 had a hydrodynamic diameter of 35.3 nm and PDI 0.289, indicating the presence of aggregates (see Fig 3-19). The overlaid correlograms in show these aggregates as correlation decays at longer analysis times. The mechanism of ligand exchange in this case is competitive binding, where the catechol group has a greater affinity for the nanoparticle surface, compared with the carboxyl group of oleic acid. The latter tends to adsorb and desorb dynamically, so that at any one time the nanoparticle is stabilised. Introduction of a catechol will occupy a binding site, preventing the oleic acid from readsorbing. After one day this process is apparently not complete and the presence of oleic acid on the nanoparticle surface reduces the stability of the nanoparticles in ethanol. This was especially evident when the vial containing the ligand exchange reaction was placed on a neodymium magnet, and the partially aggregated nanoparticles were drawn towards the magnetic field. After two days of shaking the nanoparticles were stable to the magnetic field, and the hydrodynamic diameter was reduced from 35.3 to 26.1 nm, with the PDI going from 0.289 to 0.171. This indicated that the ligand exchange had progressed, in that more of the new ligand had displaced the oleic acid originally bound to the nanoparticle surface, further stabilising the nanoparticles in ethanol. Although the PDI had decreased, the new value would still be considered polydisperse suspension, with values of 0.1 and less accepted as monodisperse. The suspension was left shaking to see if the values decreased further, with no significant change to either the hydrodynamic diameter or PDI between Days 2 and 5, indicating that the process was complete during Day 2.

Based on these results, the aliquot of G4 nanoparticles treated with PEA-3,4 was shaken for two days. The nanoparticles were precipitated in diethyl ether and redispersed in ethanol. Moreover, the sample did not undergo filtration or centrifugation. This dispersion had a hydrodynamic diameter of 23.4 nm and PDI 0.054. Such a value indicates that the nanoparticle suspension is extremely monodisperse and comparable to the suspension pre-ligand exchange. Comparing these values to those of the G4 heptane dispersions (dhyd = 21 nm; PDI = 0.055), strongly suggests full particle dispersion in ethanol. As noted above field-cycling NMR could be used to confirm dispersion, this instrument was not available at the time of the study. Considering that the DLS experiment is based on particle diffusion, the increased size could be due to a larger solvation layer of ethanol molecules associating with the polymer chain, compared with the solvation layer of heptane molecules around the C18 layer of the originally synthesised nanoparticles. To test this further, both G4 and G4' nanoparticles were treated with PEA-3,4, and the correlation data compared to that of the heptane dispersions. The data is shown in Table 3-5.

Table 3-5: Evolution of DLS data during ligand exchange. The PEA-coated nanoparticles were dispersed in ethanol.

Sample ID	**dhyd (nm)**	**PDI**
PEA-3,4,5 Day 1	35.3	0.289
PEA-3,4,5 Day 2	26.1	0.171
PEA-3,4,5 Day 3	26.5	0.178
PEA-3,4,5 Day 5	26.3	0.182
PEA-3,4 Day 2	23.4	0.054

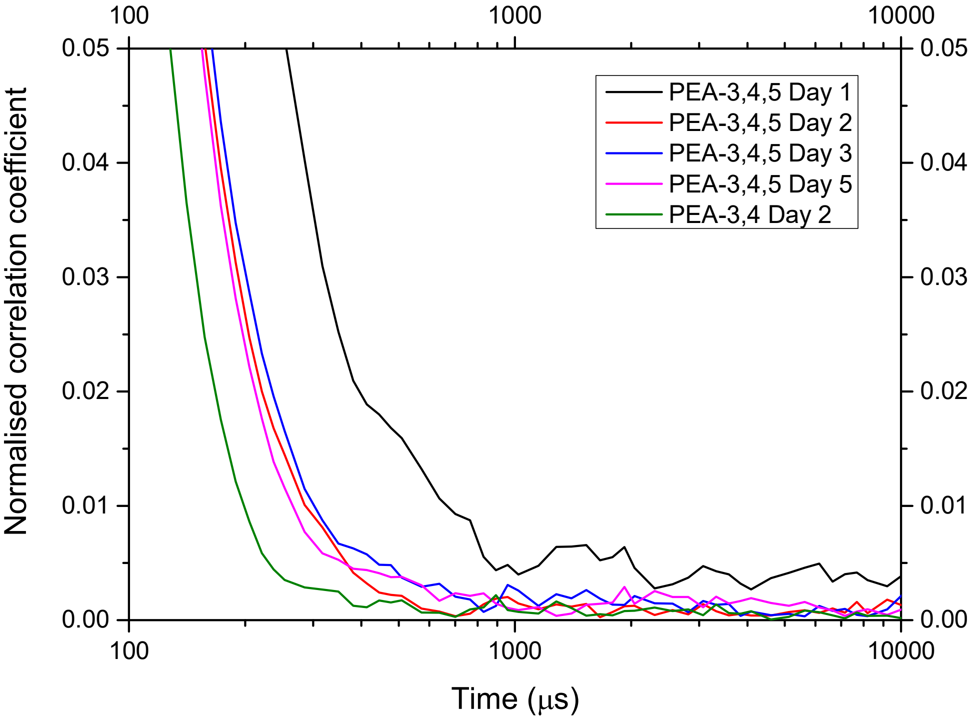

Figure 3-19: Overlaid correlograms of the ethanol dispersions of nanoparticles stabilised with PEA-3,4,5 and PEA-3,4, respectively. The evolution of the hydrodynamic size and PDI were monitored over time.

3.3.6. Phase Transfer of Iron Oxide Nanoparticles: Comparing G4 and G4'

The normalised correlograms for both G4 and G4', pre- and post-phase transfer, are shown in Fig 3-20. The heptane dispersions of G4 and G4' have overlapping correlograms, indicating similar diffusion behaviour. The diffusion coefficients were 53.4 and 55.2 μm^2/s, respectively. The slightly higher value for the G4' nanoparticles is indicative of its smaller size (14.2 nm compared with 15.0 nm for G4). The post-ligand exchange ethanol dispersions of G4 and G4' had diffusion coefficients of 17.0 and 17.8 μm^2/s, respectively. The correlograms for these suspensions show a shift to the right, reflecting the significantly longer diffusion times. Moreover, the correlograms overlay almost perfectly, which shows that the effect of the new ligand on the nanoparticle's diffusion is reproducible, and that the increase in the hydrodynamic diameter reflects the change in solvation. Most importantly, it is clear that the ethanol suspensions are monodisperse and there are no aggregates formed.

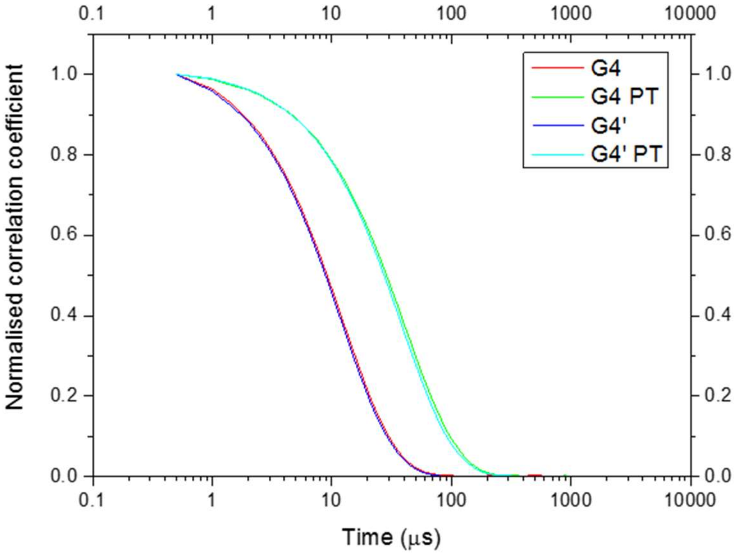

Figure 3-20: Normalised correlation coefficients of G4 and G4' heptane dispersions (left overlay), compared with G4 and G4' phase transferred dispersions in ethanol (right overlay). "PT" refers to phase transfer, i.e. the nanoparticles after they have undergone a ligand exchange process.

PEA-3,4, due to its apparent superior performance as a phase transfer agent, was used for the remaining experiments described in this chapter. It can be seen from the data in Table 3-6 that the polymeric ligand increases the diffusion coefficient considerably (from 17.0 to 53.4 μ2/s for G4; from 17.8 to 55.2 μ2/s for G4').

Table 3-6: Effect of ligand exchange on hydrodynamic size.

Sample ID	**dhyd (nm)**	**PDI**	**Diffusion coefficient (μ^2/s)**
G4	21.0	0.055	53.4
G4’	20.3	0.033	55.2
G4 PT	23.4	0.054	17.0
G4’ PT	22.4	0.019	17.8

3.3.6. Quantification of the Ligand Exchange

One of the most common problems encountered with the phase transfer of nanoparticles is material losses through aggregation during the ligand exchange process. It was decided to carry out the ligand exchange in chloroform, as both oleic acid and PEA-3,4 are soluble in this solvent. It was found that as the PEA-3,4 starts to replace oleic acid at the nanoparticle surface, the colloidal stability is maintained, and the formation of aggregates appears to be reduced. Based on the amount of iron determined in G4 and G4’ (Table 7), the ligand exchange efficiency was approximately 92%. This shows that the chloroform process is viable, with an excellent yield.

Table 3-7: Iron concentration of G4 and G4’ suspensions, determined by flame atomic absorption.

Sample ID	**[Fe] (mg/mL)**
G4	7.73
G4 PT	7.11
G4’	10.20
G4’ PT	9.38

3.3.7. Particle Size of Hydrophilic Nanoparticles as determined by Transmission Electron Microscopy

To further characterise the ligand exchange process, both G4 and G4' were coated with PEA-3,4 and examined by TEM. Ethanol dispersions were blotted onto holey carbon films and imaged in bright field (Fig 3-21). The self-assembly observed for the hydrophobic nanoparticles coated with oleic acid can also be seen for the phase transferred nanoparticles coated with PEA-3,4. Using the ImageJ program, 389 particles were counted in the image corresponding to the G4 sample. The histogram and lognormal distribution are shown in Fig 3-22.

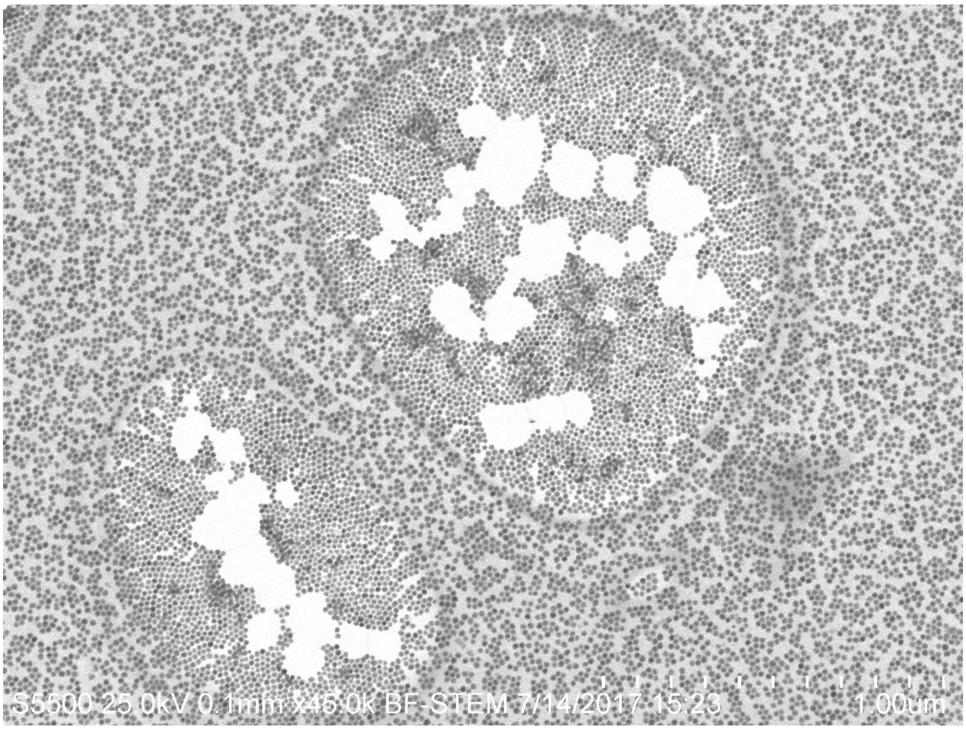

Figure 3-21: TEM image of iron oxide nanoparticles (G4) coated with PEA-3,4. The ethanol dispersion was deposited on holey carbon film and imaged in bright field.

The mean nanoparticle diameter was 15.3 nm for both the normal and lognormal distributions, with standard deviations of 1.2 and 1.1 nm, respectively. Comparing the mean diameter to that of the original hydrophobic dispersion, there is an increase of 0.3 nm, which is within the error of the measurement. This would indicate no changes in the size and morphology of the nanoparticles during the ligand exchange process, as expected given the high yield. However, this finding is important as the phenomenon of surface etching, described in a recent perspective, can have a significant impact [129].

Furthermore, the interaction of the head group with the iron oxide nanoparticle surface can influence the magnetic properties of the nanoparticle. Some reports [132] describe the realignment of surface spins and increases in saturation magnetisation. The fact that no obvious changes to the particle morphology were observed is encouraging.

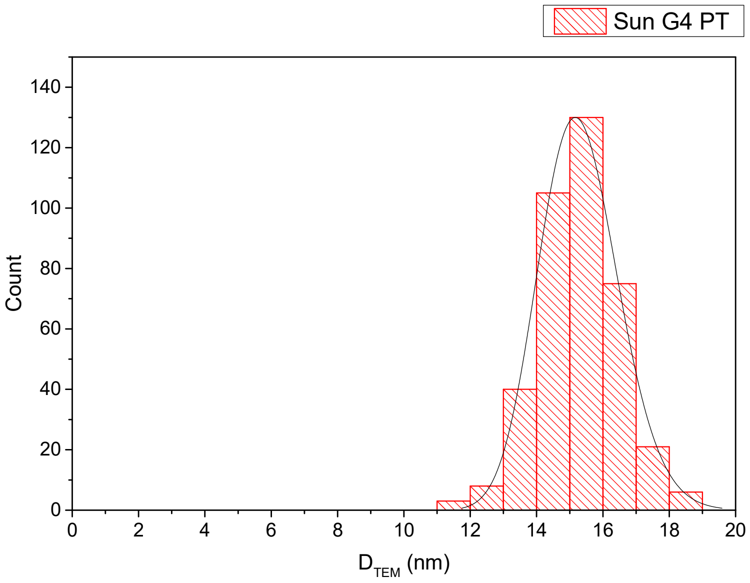

Figure 3-22: Lognormal distribution of 389 particles measured using the ImageJ program. The lognormal fit based on the histogram gave a mean nanoparticle diameter of 15.3 ±1.1 nm. The mean nanoparticle diameter from the normal distribution was 15.3 ±1.2 nm.

The TEM bright field image of G4' nanoparticles coated with PEA-3,4 is shown in Fig 3-23. As was observed in the TEM image of the G4 sample, the nanoparticles self-assemble as the ethanol dispersion of nanoparticles dries on the holey carbon film. The lognormal distribution of 1459 particles measured using the ImageJ program is shown in Fig 3-24. The lognormal fit based on the histogram gave a mean nanoparticle diameter of 14.0 ± 1.1 nm. The mean nanoparticle diameter from the normal distribution was 14.1 ± 1.4 nm. Again, this is identical to the mean nanoparticle diameter found for the same nanoparticles prior to ligand exchange.

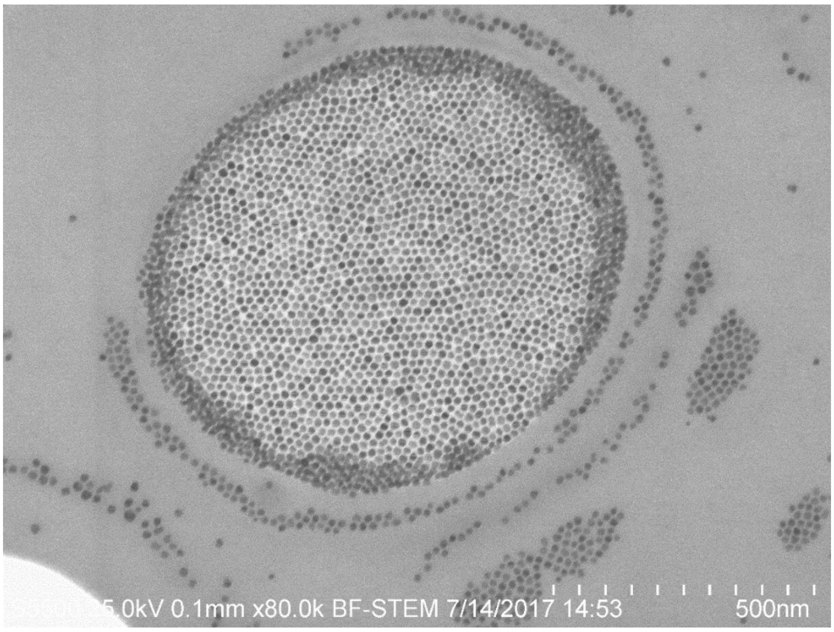

Figure 3-23: TEM image of iron oxide nanoparticles (G4) coated with PEA-3,4. The ethanol dispersion was deposited on holey carbon film.

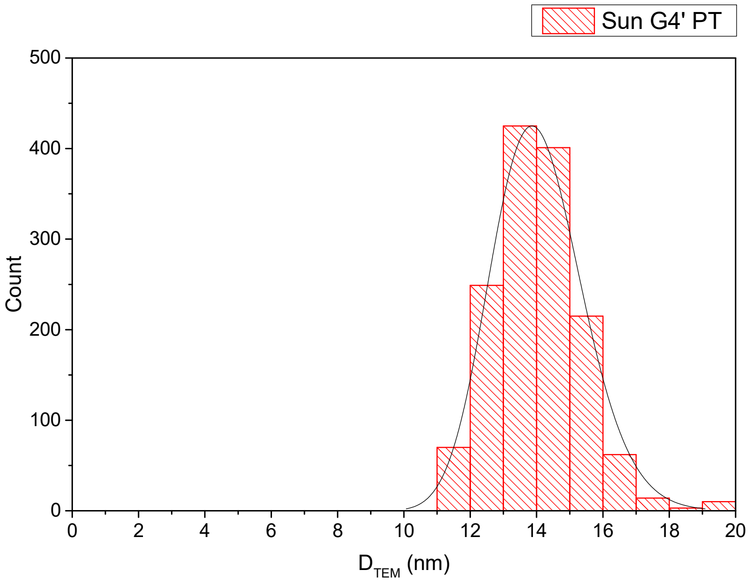

Figure 3-24: Lognormal distribution of 1459 particles measured using the ImageJ program. The lognormal fit based on the histogram gave a mean nanoparticle diameter of 14.0 ± 1.1 nm. The mean nanoparticle diameter from the normal distribution was 14.1 ± 1.4 nm.

3.3.8. Magnetic Properties of post-Ligand Exchange G4 and G4' Nanoparticles

To study the effect of ligand exchange on the magnetometric properties of G4 and G4' nanoparticles, their dispersions were prepared for DC magnetometry. The magnetic hysteresis (M-H) curves are shown in Figs 3-25 and 3-26. The saturation magnetisation values of dried G4 nanoparticles pre- and post-ligand exchange were 59.5 and 65.6

Am^2/kg, respectively. This shows that the interaction of catechol-bearing ligands with the nanoparticle surface, compared with the carboxyl-bearing oleic acid, increases the saturation magnetisation of the G4 nanoparticles by 10%. Interestingly, the G4' post-ligand exchange nanoparticles had a saturation magnetisation of 53.6 Am^2/kg (this sample could not be run prior to phase transfer). This is a decrease of 12 Am^2/kg, compared with the G4 nanoparticles. Note that the SAR value (in heptane) was higher for G4', Table 3-8.

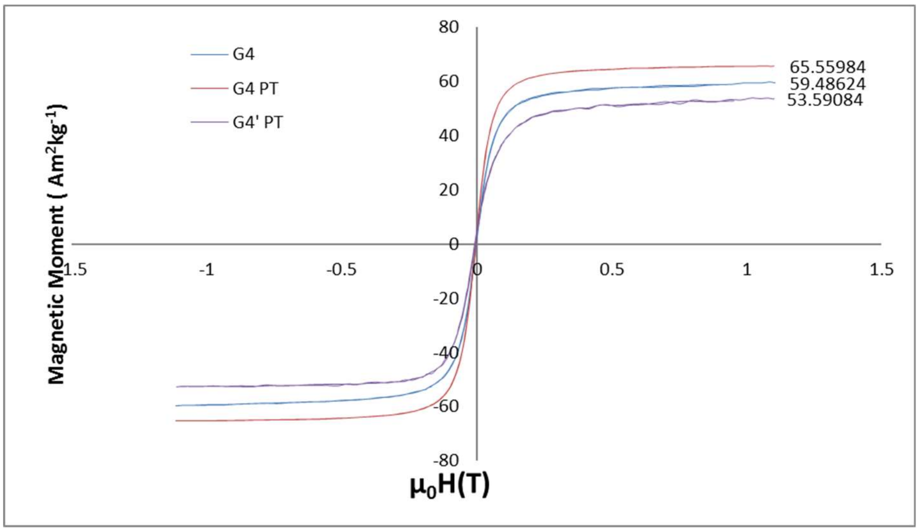

Figure 3-25: DC magnetometry of G4 and G4' dried nanoparticle suspensions, showing the effect of ligand exchange on saturation magnetisation.

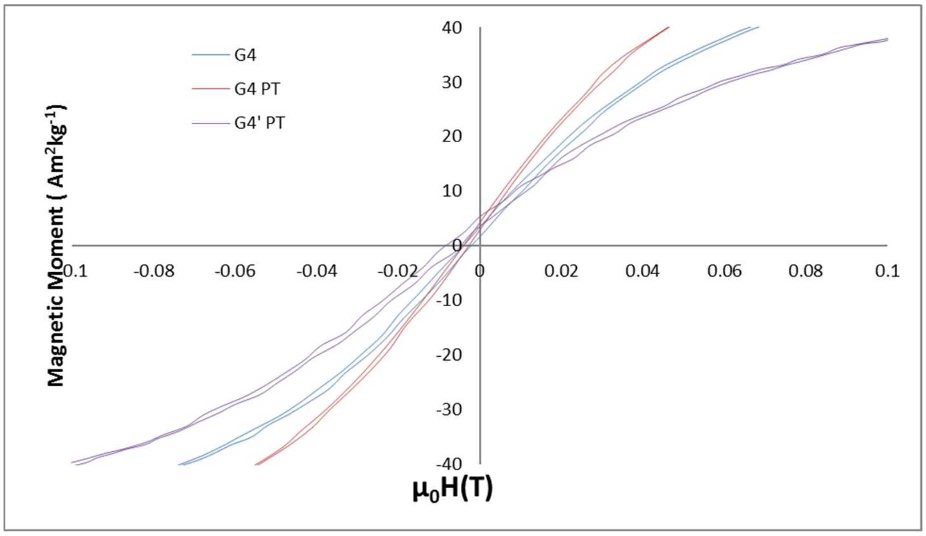

Figure 3-26: Reduced scale magnetometry response, showing hysteresis.

The suggested (but not reproduced) increase in M_S matches observations in a paper published by Nagesha and colleagues [132]. They observed an increase in the remanence

(M_R), saturation magnetisation (M_S), and blocking temperature (T_B) of the particles after dopamine functionalization, even though TEM and XRD studies revealed no change in the particles' size and/or structure, as in our case.

The effect of ligand exchange on the magnetic properties is shown as a change in the saturation magnetisation (Fig 3-25). Upon initial examination, the M-H curves would suggest that the nanoparticles are superparamagnetic, but further analysis shows some minor hysteresis (Fig 3-26). The remanent magnetisation was approximately 2.4 Am^2/kg and the coercivity was 0.01 T.

The heating profiles of G4 and G4' (pre- and post-ligand exchange) are shown in Fig 3-27. Using Eq 3-1, the initial slopes of the curves can be used to calculate the SAR. The SAR values are listed in Table 3-7. Following exchange of the oleic acid for PEA-3,4, there is a significant decrease in the SAR value for both samples. The G4 sample decreased by 36.4 W/g, whilst G4' decreased by 25.9 W/g. It is not entirely understood why the SAR drops and the Ms increases slightly following ligand exchange on the G4 nanoparticles.

The G4' samples heats by 10 °C in the first 25 seconds of AC field application. Such a temperature jump could be useful if using these nanoparticles as mediators for thermoablation of tumours, i.e. introduction of a nanoparticle suspension into a specific tumour volume, at the same nanoparticle concentration, could theoretically increase the local temperature beyond the typical range for thermoablation (42 – 45 °C). Although the real situation is more complicated; interactions between the nanoparticles and gradual dissolution mediated by the *in vivo* environment, can reduce the heat load obtainable [133].

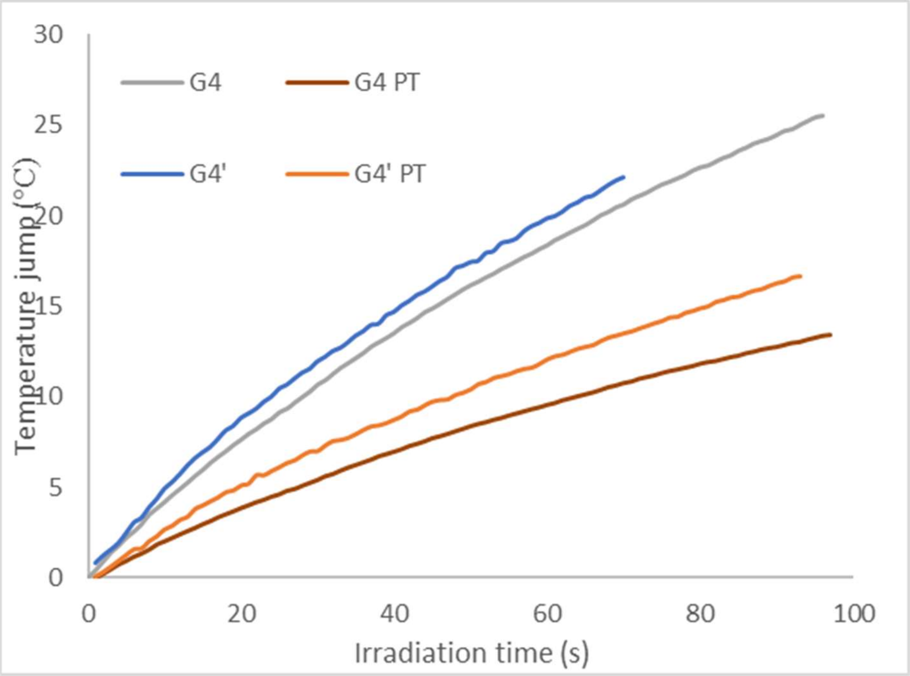

Figure 3-27: Heating profiles for G4 and G4', pre- and post-ligand exchange, irradiated in an AC magnetic field of 476.6 kHz, 9.8 kA/m. The nanoparticles are transferred from heptane to ethanol.

Table 3-8: Comparison of SAR values: pre- and post-ligand exchange.

Sample ID	**SAR (W/g)**
G4	49.4
G4'	63.7
G4 PT	13.1
G4' PT	37.8

3.4. Conclusions

A viable seed-mediated approach to preparing iron oxide nanoparticle suspensions with good hyperthermic properties, which can be reproduced and which should be scaleable has been demonstrated. The stepwise change in nanoparticle size and magnetic properties was consistent with the observations of Sun and colleagues. It was found that SAR is not simple dependent on nanoparticle size, given that changes in reaction conditions can result in suspension with similar particle sizes having dramatically different SAR values. Moreover, increases in saturation magnetisation do not necessarily lead to increases in

SAR. It appears that there are other factors at play, which together determine the heating efficiency. That could be the subject of further study, however our goal was the development of a robust synthesis and phase transfer protocol.

The exchange of hydrophobic ligands with a novel catechol-functionalised polyether in almost quantitative yield was demonstrated. These functionalised nanoparticles could be useful as mediators for thermoablation, or as components in a range of magnetic nanocomposites. In the next chapter their application in the formation of magnetically responsive composite hydrogels is described.

Chapter 4 - Magnetic nanocomposite hydrogels: magnetothermal and swelling response in AC fields

4.1. Introduction

In Chapter 3 the synthesis of size-controlled iron oxide nanoparticles and the ability to influence magnetic properties was described. Superparamagnetic iron oxide nanoparticles (NPs) have been shown to generate considerable heat in AC fields, and this heat can be used to actuate thermoresponsive materials, typically for application in cancer treatment, drug delivery, tissue engineering, or combinations thereof [134-136]. Hence Chapter 3 paved the way for a study of functional nanocomposite hydrogels containing superparamagnetic iron oxide nanoparticles.

Nanocomposite hydrogels may be defined as cross-linked stimuli-responsive polymer networks swollen with water in the presence of nanoparticles [137]. Tanaka was the first to recognise the stimuli-responsive behaviour of acrylamide-based gels [138]. These gel systems are the most well studied of the thermoresponsive polymers, with observed response to changes in temperature, pH, solvent composition, light, pressure, electric, and magnetic fields [139]. The initial studies were of poly(acrylamide) crosslinked with bis-acrylamide, but other crosslinked acrylamides such as poly(NIPAAm) were shown to have a sharper transition, due to the hydrophobic isopropyl moiety [140]. This chapter describes magnetic nanocomposite hydrogels (MNCH), an emerging class of material in which the unique properties of the individual components can be combined to generate a functional, magnetothermally-responsive nanocomposite. Heating and/or actuation of these networks using external stimuli has been a topic of interest for several years, as has been reviewed by Satarkar *et al* [141]. A key aspect of MNCHs is that the heat source is a magnetic nanoparticle whose magnetic moment is flipped by an AC magnetic field. As the field switches to zero the residual power is dissipated as heat. The heat causes a global increase in the temperature of the nanocomposite, triggering a gross deformation in the polymer network. The deformation is induced by a phase separation whereby water molecules desorb. The temperature at which this behaviour occurs is known as the lower critical solution temperature (LCST) for freely moving polymer chains and the volume phase transition temperature (VPTT) for crosslinked polymer chains. A more detailed description of the VPTT is given in Chapter 1. Assuming a homogenous distribution of nanoparticles in the polymer matrix, the net heat produced by all NPs is transferred to the surroundings, i.e. the polymer network. Assuming non-adiabatic conditions, heat will also transfer beyond the boundaries of the sample. Most of the literature assumes that the nanoparticles are evenly distributed, but this has not been shown conclusively. The distribution of nanoparticles has implications for the performance of MNCHs in clinical settings. The overall aim was to complete a more detailed physico-chemical investigation into the effect of the network architecture and MNP load on the stimulated de-swelling process.

The preliminary objectives of this work were:

- Fabricate MNCHs with homogeneous distribution of nanoparticles
- Compare the magnetic properties of the MNCHs with the equivalent MNP suspensions
- Evaluate how the nanocomposites behave when heated internally by AC-field irradiation or by raising the bulk temperature whilst monitoring with differential scanning calorimetry (DSC).

The magnetic nanocomposite hydrogels discussed in this chapter contain iron oxide nanoparticles, approximately 14 nm in diameter, at different nanoparticle concentrations. The monomers, NIPAAm and AAm, form copolymers which can be crosslinked by polyethylene diacrylate into thermoresponsive networks. Such copolymers are classed as statistical [142].These networks typically undergo a volume phase transition around 33 °C. This is analogous to the LCST observed for free polymer chains [143]. The polymer network is charge neutral, and the iron oxide nanoparticles are coated with neutral diblock copolymers (polyethylene and polypropylene blocks) [140]. The interaction of this layer with the surrounding solvent determines the nanoparticle diffusivity, and in turn the magnetic behaviour.

As noted above an additional aim of this work was to gain a deeper understanding of how the physical chemistry of the gel-nanoparticle composite system affects heat generation. As will be shown later, the mixing of the nanoparticles with monomers, as well as the addition of APS and TEMED, affect the dynamics of the nanoparticles (both translationally and in term of the magnetic moments) and consequently the heat output of the gels in an AC field. Additionally, the ratio of components forming the gel network may also have implications for the heat output, especially during deswelling. The structure of hydrogels and effects on swelling behaviour have been described by the Flory-Rehner theory [144]. This combines thermodynamic and elasticity theory to explain how cross-linked polymers immersed in a suitable solvent will swell to equilibrium with the surroundings, subject to a thermodynamic force of mixing, as well as a retracting force owing to the crosslinked network of polymer chains. These two forces cancel out at equilibrium. The Gibbs free energy describes the combination of forces thus,

$$\Delta G_{total} = \Delta G_{elastic} + \Delta G_{mixing}$$

Equation 4-1

The ΔG_{mixing} term describes the compatibility of the polymer with the molecules of the surrounding fluid, as described by the polymer-solvent interaction parameter, χ_1 [145]. Diffusion through the pore volume between macromolecular chains is the primary mechanism of release of a drug molecule from a hydrogel network. Crosslinking density determines the molecular weight between cross-links, which in turn determines the pore size and swelling/deswelling ratio. The swelling ratio is defined as "the fractional increase in the weight of the hydrogel due to water absorption" [146], and can be written as

$$\frac{Ws - Wd}{Wd}$$

Equation 4-2

Conversely, the deswelling can be defined as the fractional decrease in the weight of the hydrogel due to water desorption. Increased crosslinking density reduces pore volume, which is expected to influence the extent of water diffusion and hence desorption from the gel network.

The magnetothermal deswelling experiments described in this chapter are dynamic, in that the temperature is changing over time. It should be noted that swelling/deswelling ratios are typically calculated based on a static temperature, i.e. equilibrium values. It is known that when a hydrogel is heated, the network responds to minimise the effect. It follows that any swelling/deswelling ratio calculated at a given temperature during the magnetic hyperthermia experiments is an approximation, as the network is essentially playing "catch up". A suitable theoretical model might reflect the dynamic temperature effect.

A Web of Science search of "poly(*N*-isopropylacrylamide-co-acrylamide)" gives 107 results. The most cited of these, "Thermosensitive poly(*N*-isopropylacrylamide-co-acrylamide) hydrogels: Synthesis, swelling and interaction with ionic surfactants" [97], was published in 2006 and has 107 citations. Adding the search term "magnetic hyperthermia" gives 9 results, the most cited of these being "Stimuli-Responsive Magnetic Nanomicelles as Multifunctional Heat and Cargo Delivery Vehicles" [147], published in 2013 with 55 citations. This paper describes the use of a block copolymer comprising poly(NIPPAm-co-AAm) and caprolactone (CL), generating micelles with characteristic shell and core responses to external stimuli that can be employed for controlled drug release. The next most cited paper, "Thermo-responsive copolymer coated $MnFe_2O_4$ magnetic nanoparticles for hyperthermia therapy and controlled drug delivery" [148], was published in 2012 with 36 citations. The authors describe the use of poly(NIPPAm-co-AAm) as a coating for $MnFe_2O_4$ nanoparticles. Doxorubicin was loaded into the polymer coating at 25 °C, whilst the LCST was found to be 39 °C, above which drug was released. It should be noted that in both cases the nanocomposites were not bulk gels, as described in this thesis. In fact, there are no examples in the literature of bulk gels composed of poly(NIPAAm-co-AAm), which are then used in conjunction with magnetic hyperthermia.

As previously described in Chapter 1, Satarkar *et al.* utilised NIPAAm as the sole monomer and the fabricated magnetic nanocomposites showed a response in AC fields [77]. However, in this thesis it is shown that further tuning of the response is possible by substituting NIPAAm with AAm in defined amounts. The first detailed analysis of the kinetics of deswelling is also described.

Finally, a detailed microscopic picture of stimulated water deswelling may be predictive of the mechanisms of release of hydrophilic low molecular mass species from nanocomposite gels. Indeed, gaining insight into water dynamics is probably a first necessary step towards that longer-term goal.

4.2. Experimental

4.2.1. Materials and Methods

N-Isopropylacrylamide (≥ 97%), acrylamide ((≥ 99%), ammonium persulfate (APS) (98%), tetramethylethylenediamine (TEMED) (99%), and PEG-diacrylate (M_n = 700) were purchased from Sigma-Aldrich. All were used without further purification, except *N*-Isopropylacrylamide, which was recrystallised from warm heptane.

4.2.2. Synthesis of 14 nm Iron Oxide NPs

14 nm iron oxide nanoparticles (known as "G4' NPs") were prepared according to the procedure in Chapter 3, section 3.2, which was adapted from a method published by Sun *et al* [33]. Nanoparticle seeds were first generated and then grown step-wise. Following the fifth synthetic step, the isolated heptane dispersions were found to have D_{TEM} of 14.2 ± 1.7 nm (ImageJ). After precipitating the G4' NPs in ethanol, a 5 mL solution of a catechol-bearing ligand (see section 3.2 of Chapter 3 for synthesis of the ligand) dissolved in chloroform (approx. 200 mg/mL) was added to the precipitate. Sonication was applied to disperse any aggregates present, and the suspension was allowed to shake overnight. D_{TEM} of the ligand-exchanged G4' NPs was 14.0 ± 1.1 nm. The structure of this molecule is found in Fig 3-16 of Chapter 3, page 20. The saturation magnetisation (M_s) of the G4' NPs was 53.6 Am^2/kg, and the specific absorption rate (SAR) was 37.8 W/g.

4.2.3. Preparation of Magnetic Nanocomposite Hydrogels

To study the effect of different parameters on the magnetothermal response, MNCHs were prepared as listed in Table 4-1.

Table 4-1: MNCH formulations; component volumes and concentrations.

MNCH ID	**NIPAAm stock[7] (µL)**	**[NIPAAm] sample (mM)**	**AAm stock[8] (µL)**	**[AAm] sample (mM)**	**G4' NP stock[9] (µL)**	**[Fe] sample (mM)**	**PEG 700 diacrylate stock[10] (µL)**	**[PEG 700 diacrylate] sample (mM)**
1	400	0.88	25	0.07	125	19.3	100	0.049
2	368	0.81	50	0.14	125	19.3	100	0.049
3	304	0.67	100	0.28	125	19.3	100	0.049
4	400	0.88	25	0.07	250	38.6	100	0.049
5	368	0.81	50	0.14	250	38.6	100	0.049
6	304	0.67	100	0.28	250	38.6	100	0.049
7	400	0.88	25	0.07	500	77.2	100	0.049
8	368	0.81	50	0.14	500	77.2	100	0.049
9	304	0.67	100	0.28	500	77.2	100	0.049
10	368	0.81	50	0.14	125	19.3	100	0.049
11	368	0.81	50	0.14	125	19.3	200	0.097
12	368	0.81	50	0.14	125	19.3	300	0.194
13	368	0.81	50	0.14	250	38.6	100	0.049
14	368	0.81	50	0.14	250	38.6	200	0.097
15	368	0.81	50	0.14	250	38.6	300	0.194
16	368	0.81	50	0.14	500	77.2	100	0.049
17	368	0.81	50	0.14	500	77.2	200	0.097
18	368	0.81	50	0.14	500x	77.2	300	0.194

For a given NP concentration, in samples 1 - 9 the ratio of *N*-Isopropylacrylamide (NIPAAm) to acrylamide (AAm) was varied, with the total moles of NIPAAm and AAm kept constant. The amount of PEG diacrylate crosslinker was kept constant at 5% of total moles of NIPAAm and AAm co-monomers, so that the crosslink density of the network was unchanged. To study the effect of the crosslink density on the network response, for a given NP concentration, the PEG 700 diacrylate concentration was varied whilst keeping the molar ratio of NIPAAm:AAm constant (see samples 10–18).

---

[7] [NIPAAm] stock in EtOH = 2.2 mM

[8] [AAm] stock in EtOH = 2.8 mM

[9] G4' NP stock, [Fe] = 154 mM

[10] [PEG 700 diacrylate] stock in water = 0.49 mM

The MNCHs were polymerised by radical polymerisation using 10% w/v APS (50 µL) as the radical source, and TEMED (5 µL) as catalyst (see scheme, Fig 1-11, Chapter 1). Prior to addition of TEMED, all other components were mixed and ethanol evaporated under a stream of nitrogen to reduce all volumes to 0.9 mL. Samples were then placed on ice. Upon addition of TEMED, samples were made up to a final volume of 1 ml with ethanol and vortex mixed. The samples were then allowed to polymerise overnight. The following day the MNCH samples were placed in dialysis membrane to wash out unreacted monomer. The minimum amount of dialysis tubing was employed to contain the 1 cm^3 sample and placed in 2 L of DI water. The molecular weight cut off (MWCO) of the dialysis tubing was 13 kDa. The water was changed at 2 and at 4h. Samples were then left to dialyse overnight. Prior to magnetic hyperthermia, all MNCHs were equilibrated in DI water at 32 °C.

4.2.4. Transmission Electron Microscopy

To image dispersed G4' nanoparticles in the crosslinked polymer network, samples were fixed in 10% neutral buffered formalin for 20 min prior to treatment. The samples were then stained with 1% osmium tetroxide for 1 h, followed by dehydration using ascending grades of methanol (50 to 100%). They were subsequently immersed in a 1:1100% Methanol/London resin (LR) white and finally in pure LR white for one hour at room temperature. The samples were then embedded in LR white and ultrathin sections were generated using an EM UC6 ultramicrotome (Leica) and mounted on copper grids prior to examination in a Hitachi H-7650 electron microscope operating at 100 kV.

4.2.5. Magnetic Hyperthermia

To test the magnetothermal response of the MNCHs in AC magnetic field, the samples were placed in a Magnetherm (Nanotherics, UK) 17-turn copper coil. Field strength, H, was 9.9 kA/m and frequency, f, was 476.6 kHz. Prior to irradiation in the AC field, the system was adjusted to resonance. MNCHs were placed in a plastic vial with a fiber optic temperature probe (Opsens, Canada) placed in the MNCH. The MNCHs were irradiated for a total of 2400 seconds and temperature was monitored during each measurement.

To study the network response, the samples were removed, blotted and weighed at 600 s. The sample was then re-swollen (to the same total mass) and re-equilibrated at 32 ºC and then irradiated for 1200 s. This process was the repeated for 1800 and subsequently for 2400 s irradiation time measurements. This lengthy procedure was necessary, as consistent data could only be produced by avoiding variable partial re-swelling and differences in starting temperature. Reproducibility of gel deformation was tested in samples containing 19.2 mM Fe, by measuring the deswelling ratio in triplicate. The upper acceptable limit of the relative standard deviation was set at 5%.

4.2.6. Differential Scanning Calorimetry

Thermal properties of MNCHs were investigated using a TA Q200 differential scanning calorimeter, placing the sample in an open pan. Heating programs were based on the temperature changes observed during magnetic hyperthermia experiments. The reference was also an open pan, the rationale being that the magnetic hyperthermia set-up was an open system.

4.3. Results and Discussion

4.3.1 Synthesis of Superparamagnetic Iron Oxide Nanoparticles

Figure 4-1 shows a TEM image of the phase transferred iron oxide nanoparticles (designated as G4'). A statistical analysis of the nanoparticles was carried out using ImageJ software, the histogram data having a lognormal distribution (Fig 4-2). In Chapter 3 it was shown that the process of ligand exchange had no effect on the nanoparticle core size, which remained at 14 nm. Following phase transfer, the saturation magnetisation of the nanoparticles increased from 59.5 to 65.6 Am^2/kg. This has been ascribed to an interaction of the catechol with the iron oxide nanoparticle surface, causing a realignment of canted spins in the outer layers [149, 150].

Table 4-4: Hydrodynamic diameter of G4', pre- and post-ligand exchange. G4' nanoparticles were dispersed in heptane and G4' PT nanoparticles were dispersed in ethanol.

Sample ID	**Solvent**	**dhyd (nm)**	**PDI**
G4'	Heptane	20.3	0.033
G4' PT	Ethanol	22.4	0.019

In Chapter 3, dynamic light scattering (DLS) showed that the nanoparticles were fully dispersed in ethanol following ligand exchange. Table 4-4 shows the increase in the dhyd after exchange of the oleic acid coating for catechol-based ligand referred to as PEA-3,4. “PEA” stands for polyetheramine; “3,4” refers to 3,4-Dihydroxybenzoic acid which has been coupled to the PEA via an amidation reaction (Chapter 3, section 3.2). Assuming an iron oxide core diameter of 14 nm, the oleic acid layer in heptane causes the particle to diffuse at a rate equivalent to a sphere 20.3 nm in diameter. This increases to 22.4 nm after phase transfer with PEA-3,4. The diblock copolymer tail of PEA-3,4 has a number average molecular weight of 1000 g/mol. It is reasonable to think of the polymer coating as another layer. However, the specific interaction of coating and dispersing solvent is responsible for the particle’s diffusivity, and will determine the polymer conformation.

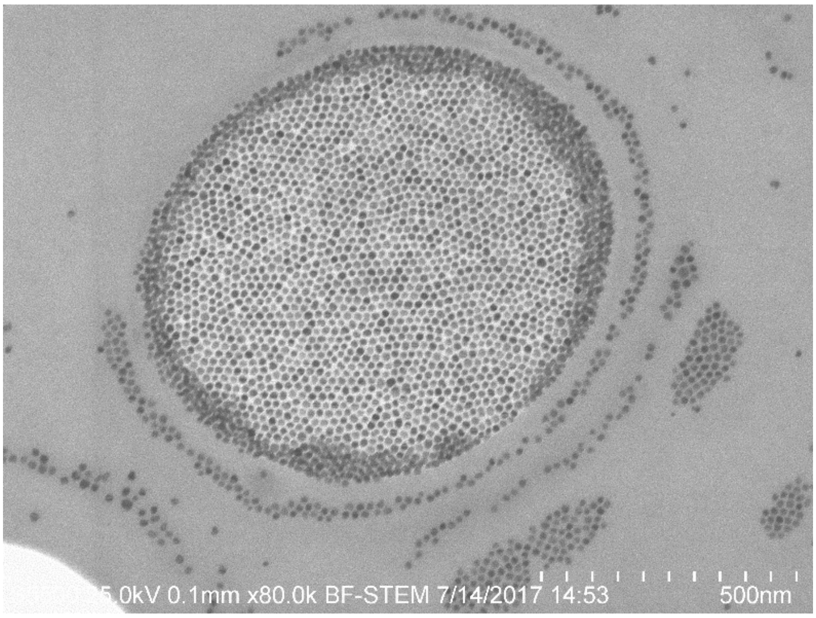

Figure 4-1: Bright field TEM image of iron oxide nanoparticles (G4’) coated with PEA-3,4. The ethanol dispersion was deposited on holey carbon film.

The bright field TEM image in Fig 4-1 shows the nanoparticles after ligand exchange. ImageJ was used to generate statistics on the nanoparticle size distribution. The lognormal fit based on the histogram (Fig 4-2) gave a mean nanoparticle diameter of 14.0 ± 1.1 nm. The mean nanoparticle diameter from the normal distribution was 14.1 ± 1.4 nm. What is especially interesting about this image and the size data is that the stability of the nanoparticles is maintained after the ligand exchange process.

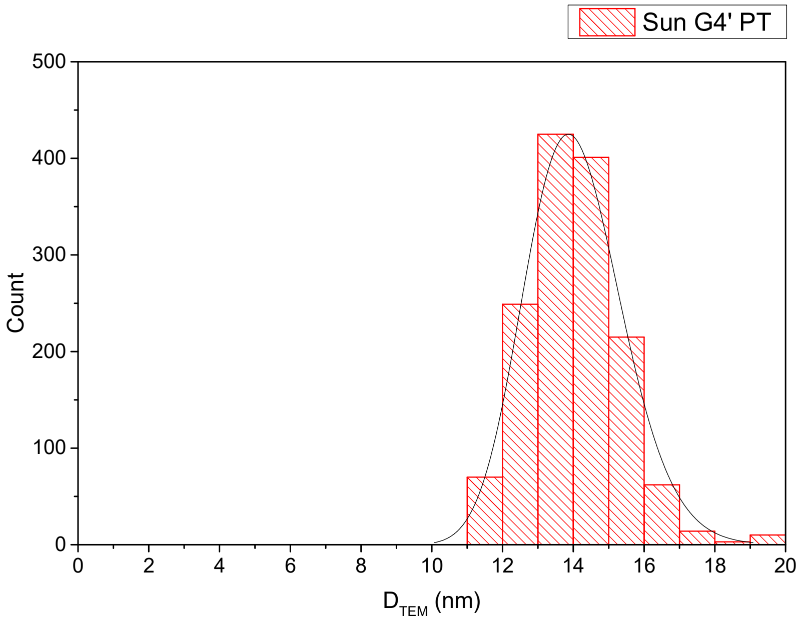

Figure 4-2: Lognormal fit of the histogram of 1459 iron oxide nanoparticles (G4') coated with PEA-3,4 measured using the ImageJ program.

4.3.2. G4' Nanoparticles and Gel Components: Effect on SAR

The specific absorption rate (SAR) is used to describe the heating ability of a superparamagnetic material in an AC field. We sought to understand the influence of the G4' iron oxide nanoparticle's diffusivity on the SAR. Therefore, it is of interest to understand the change in SAR when magnetic nanoparticles are transferred into new environments (such as that encountered in magnetic nanocomposite hydrogels and their precursor solutions).

To investigate the effect of different environments on the heating of nanoparticles in AC fields, aliquots of phase transferred G4' nanoparticle suspension (500 µL) were mixed separately with either ethanol, monomer stock, or incorporated into gels *via* polymerisation. In all cases, the final sample volume was 1000 µL, the samples were homogeneous (to the eye), and the iron concentration was approximately 77.2 mM. The suspensions were exposed to an alternating magnetic field of 9.9 kA/m at 476.6 kHz. It can be seen in Fig 4-3 that mixing of G4' nanoparticles with monomers results in a change in the initial slope and therefore the SAR of the nanoparticles. The reasons for this are presently unclear but may relate to changes in viscosity and/or partial aggregation of the nanoparticles. The nanoparticles still produce significant heat, as will be discussed later.

The crosslinking of poly(NIPAAm-*co*-AAm) results in incorporation of the PEA-3,4-coated G4’ nanoparticles, producing stable, visually homogenous gels. Previous efforts with trisodium citrate coatings resulted in ongoing diffusion of nanoparticles out of the gel matrix, which compromised composite response (results not shown). It was hypothesised that a polymer coating might fix nanoparticles within the gel matrix, *via* physical entanglements. The SAR value of the G4’ nanoparticles in ethanol was 39.9 W/g. Following introduction of the monomers, the value of the initial slope decreased by approximately 20%, corresponding to a SAR of 31.8 W/g. The SAR decreased by a further 10% following gelation, to 28.5 W/g. The total decrease in SAR of G4’ nanoparticles, going from ethanolic suspension to crosslinked network, was 28.6%. Moreover, the sol-gel transition appears to modify the transfer of heat energy through the sample.

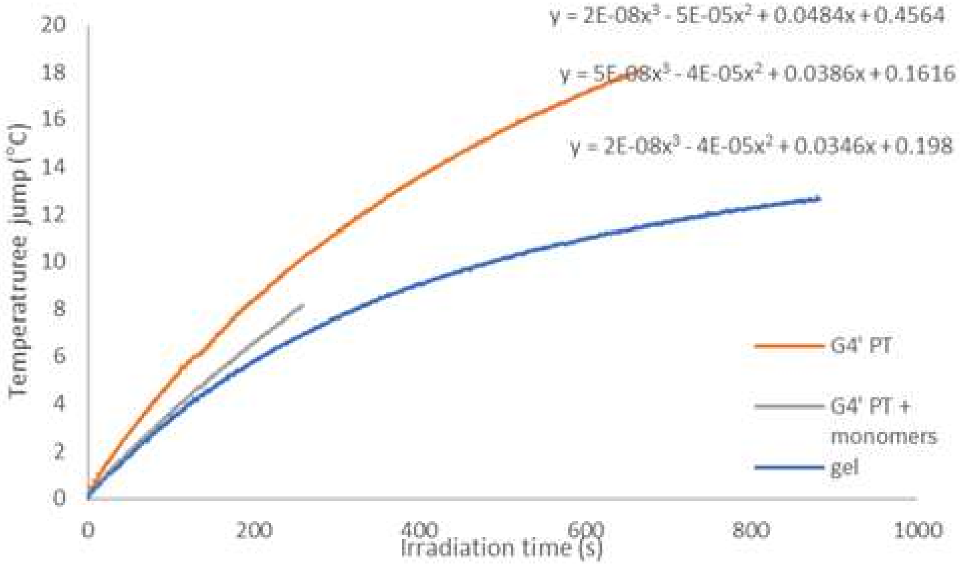

Figure 4-3: Effect of local environment on the heating profile of G4’ nanoparticles. 500 μL aliquots of G4’ stock in either ethanol, ethanol/monomers, or gel (crosslinked state). Total volume was 1000 μL. The suspensions were irradiated at H = 9.9 kA/m and f = 476.6 kHz. These parameters were used throughout the study.

To investigate further, DLS was used to probe the effect of monomers and other additives on the diffusion of G4’ nanoparticles in the same solvent. The solvent molecules are in such excess that the viscosity of the system is assumed to be unchanged. Typically, samples for DLS analysis are optically clear ([Fe] ≈ 17.9 mM). However, to measure the hydrodynamic size and polydispersity of a sample with a nanoparticle concentration that was relevant to the magnetic nanocomposite hydrogel studies, [Fe] = 77.2 mM. The dhyd of the G4' nanoparticles used in this sample was 29.9 nm, PDI 0.2. This could be the result of multiple scattering events brought about by high nanoparticle concentration. Following addition and mixing of the monomers the dhyd increased to 61.3 nm, PDI 0.22. The addition of the monomers may have caused aggregation and/or increased the viscosity of the suspension.

The dhyd value increased to 235.3 nm after addition of APS. Real-time measurement saw the dhyd increase approximately exponentially with time (Fig 4-4). The increase in d_{hyd} can be fitted with an exponential function. Upon addition of TEMED, the rate of polymerisation significantly increased and the dhyd data could no longer be fitted using the cumulants approach. Typically, an increase in the dhyd indicates aggregation, but on inspection of the sample, it could be seen that a gel had formed. The gel was dark reddish-brown in colour but optically clear, similar in appearance to a nanoparticle suspension of equivalent concentration (19.3 mM). Dropwise addition of ethyl ether to an equivalent volume of suspension destabilised the particles, resulting in a light-brown, opaque suspension which quickly agglomerated in the presence of a neodymium magnet, suggesting that any aggregation at this point is minor.

It is probable that the quasi-exponential increase in dhyd is related to the polymerisation of the monomers, which increases viscosity of the system. As viscosity increases, the particle diffusivity decreases. Closer to the point of gelation, it is likely that diffusion is suppressed, the data can no longer be fitted and DLS is no longer the appropriate technique.

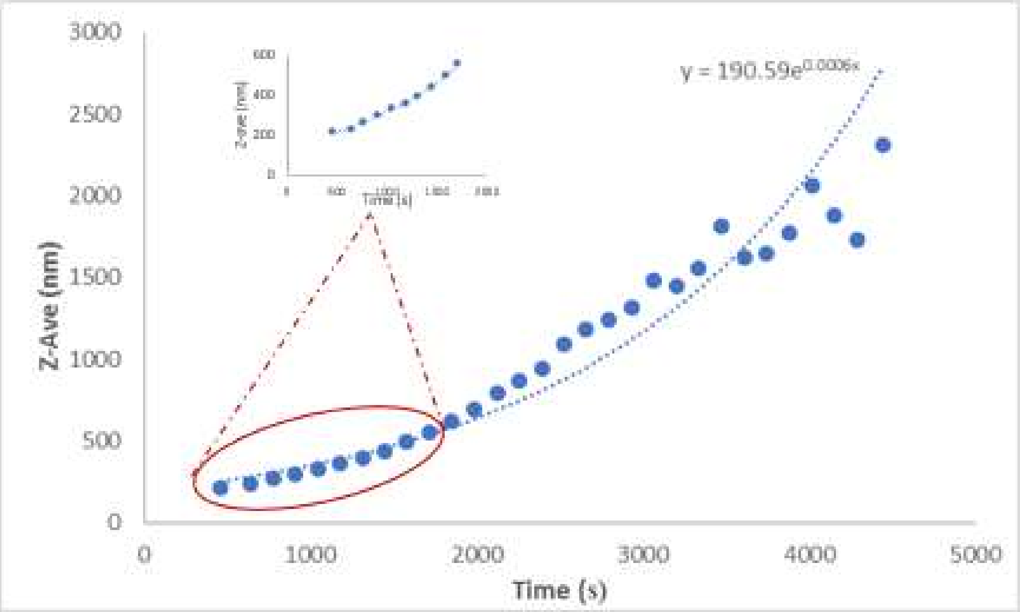

Figure 4-4: Hydrodynamic diameter as a function of time, following addition of APS and TEMED.

4.3.3. Fabrication of Magnetic Nanocomposite Hydrogels

Nanocomposite hydrogels containing G4’ iron oxide nanoparticles were fabricated using free radical thermal polymerisation. The effect of AAm, PEG700 diacrylate and G4’ nanoparticle concentration on the gel network response were studied. Nanoparticle-free controls were made using both thermal and photopolymerisation approaches. An attempt was made to fabricate nanoparticle-loaded gels by photopolymerisation, but it was found that even relatively low nanoparticle concentrations caused attenuation of UV light, to the extent that the polymerisation did not proceed adequately. Therefore, the thermal method of polymerisation was used in this study. Gels were cast in 1.5 mL centrifuge tubes. The resulting magnetic nanocomposite hydrogels were optically translucent at low nanoparticle concentrations but became progressively darker as the nanoparticle load increased (Fig 4-5). In this case both samples were doped with G4’ nanoparticles at intermediate concentration (250 µL; [Fe] = 38.6 mM). During swelling and deswelling of gels, the apparent nanoparticle concentration is dynamic. In the case of the deswollen sample, approximately the same number of nanoparticles occupies a smaller volume, effectively increasing [Fe] at that volume.

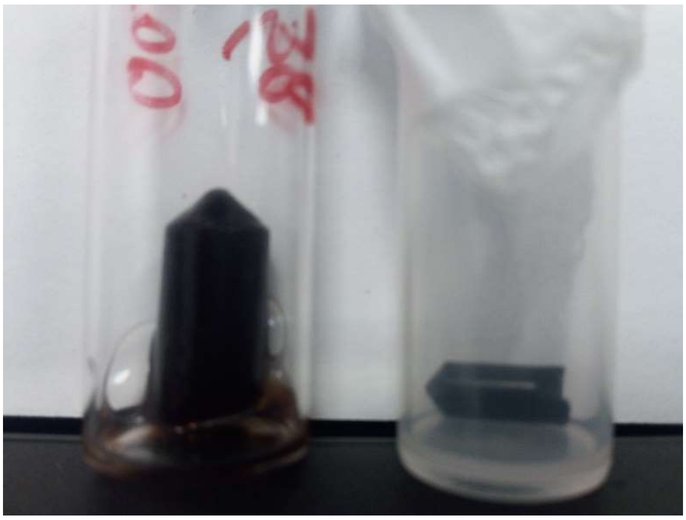

Figure 4-5: Photograph of magnetic nanocomposite hydrogels (MNCHs), [Fe] = 38.6 mM. The sample on the left is an equilibrated MNCH, whilst the sample on the right has been deswollen in an AC field. Note how the deswelling is isotropic.

4.3.4. The Effect of Gel Volume on SAR

As discussed in section 3.3.3 of Chapter 3, when a population of iron oxide nanoparticles is dispersed in a solvent and irradiated in an AC field, the initial slope of the temporal temperature response allows calculation of the SAR, with the initial response scaling with nanoparticle concentration. The SAR is then an intrinsic property of the nanoparticles, assuming they are fully dispersed. Fig 4-6 shows the initial response plotted against iron concentration for a set of nanocomposite hydrogels. As has been observed for the nanoparticle suspensions, the fit of the response in the MNCHs is linear. This confirms that, within the iron concentration range studied (19.3 to 77.2 mM), the heat produced is proportional to the number of nanoparticles in the gel. It can concluded that the aggregation state of the nanoparticles is unchanged, and the nanoparticles are dispersed in all cases. To confirm this, a section of gel with nanoparticle concentration [Fe] = 77.2 mM prepared by ultramicrotomy was imaged by TEM. The TEM images are presented in Figs 4-7 and 4-8.

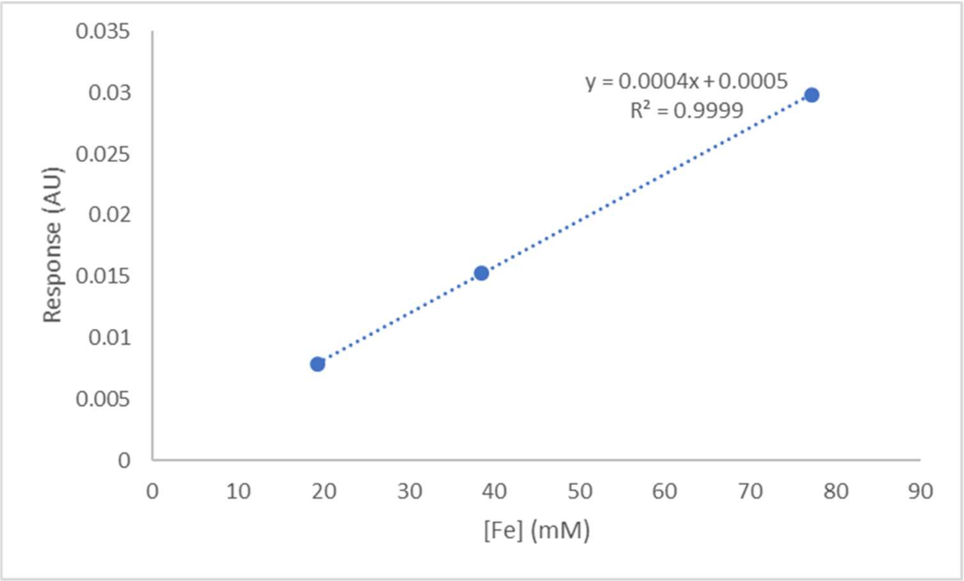

Figure 4-6: Effect of nanoparticle concentration in magnetic nanocomposite hydrogels (MNCHs) on the initial response of a fiber optic probe. The response has arbitrary units (AU).

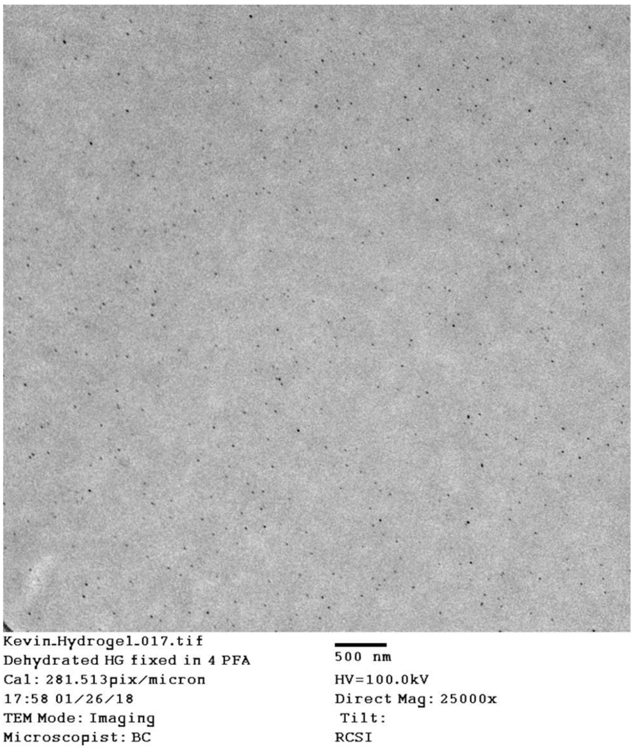

Figure 4-7: TEM image of G4’ NPs dispersed in poly(NIPAAm-co-AAm) gel network. Magnification 25000x. Section thickness was 80 nm.

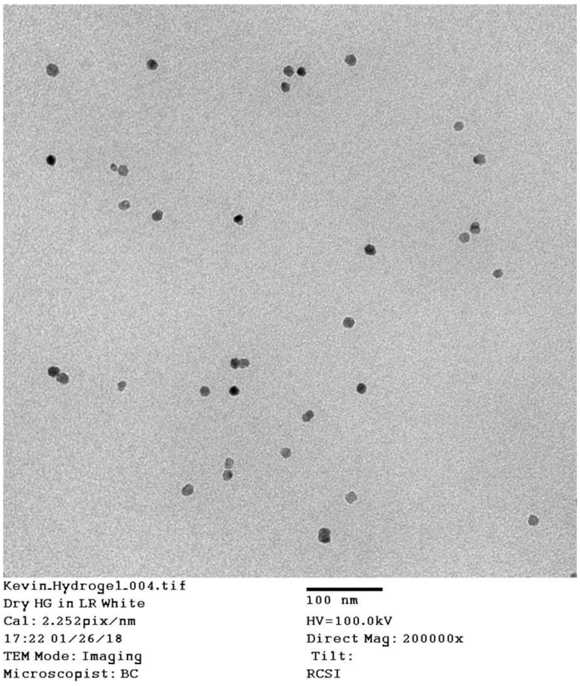

Figure 4-8: TEM image of G4' NPs dispersed in poly(NIPAAm-co-AAm) gel network. Magnification 200000x. Section thickness was 80 nm.

The images show that the nanoparticles are fully dispersed in the gel network. Based on a section thickness of approximately 70 nm, ImageJ analysis was used to calculate the area surrounding the nanoparticles in Fig 4-7. The volume calculated was 3.43×10^{7} nm^{3}, equivalent to 3.43×10^{-14} cm^{3}. Knowing that there are approximately 1.68×10^{15} nanoparticles in 1 cm^{3}, it was possible to estimate the number of particles in 3.43×10^{-14} cm^{3} (approximately 58 particles). This compares to 40 particles counted in Fig 4-7. This agreement is sufficiently good, in conjunction with the apparent homogeneity of the expanded image (Figure 4-7), to strongly suggest excellent particle dispersion in the gels.

4.3.5. Effect of Nanoparticles on Deswelling of MNCHs

Prior to studying magnetothermal deswelling, the effect of NP presence in gels was studied at 0.07 and 0.14 mM AAm. Gels were immersed in water at 45 °C to initiate the volume phase transition. As can be seen in Fig 4-9, the presence of NPs accelerates the rate of deswelling. Considering the images in Figs 4-7 and 4-8, the NPs are well dispersed, and one would not expect a significant effect on the deswelling rate. Reswelling of the pre-equilibrated samples in water at 21 °C (Fig 4-10) also shows an influence of the NPs on the reswelling kinetics.

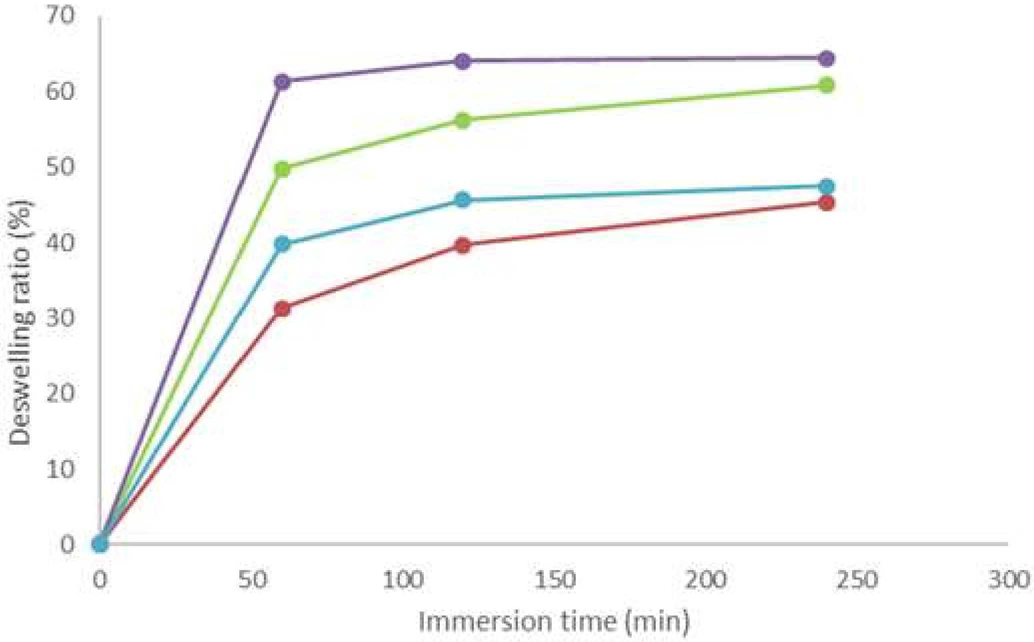

Figure 4-9: Effect of the presence of nanoparticles (green and purple data = with NP; red and blue data = without NP) in the deswelling of a nanocomposite hydrogel at 21 °C. Tested for two AAm concentrations (green and purple data = 0.07 mM; red and blue = 0.14 mM). "NP" refers to those gels containing nanoparticles. 125 µL of nanoparticle suspension was used.

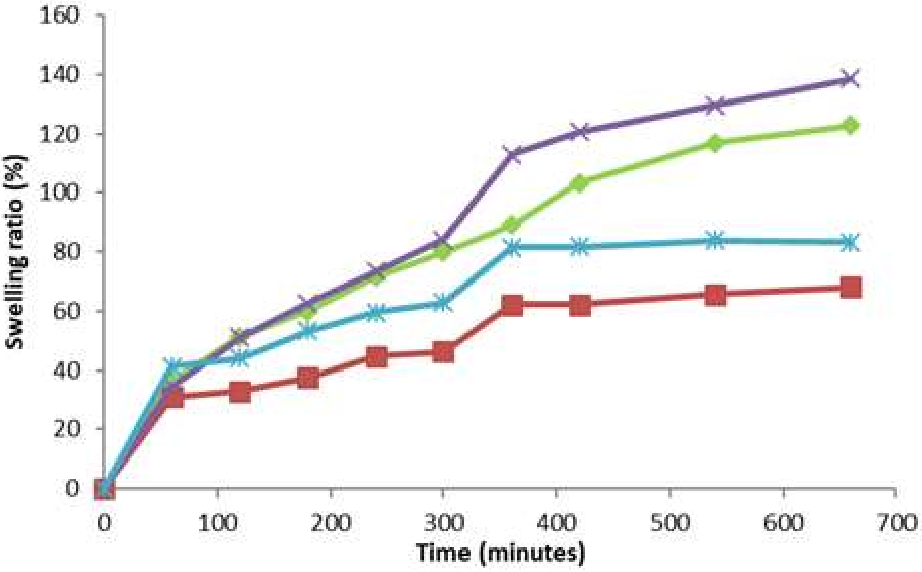

Figure 4-10: Effect of the presence of nanoparticles on the reswelling kinetics of nanocomposite hydrogels equilibrated at 45 °C for 300 minutes, then immersed in water at 21 °C (green and purple data = with NP; red and blue data = without NP). These were tested for two AAm concentrations (green and purple data = 0.07 mM; red and blue = 0.14 mM); 125 µL of nanoparticle suspension was used in the "NP" samples.

4.3.6. Effect of Acrylamide Comonomer on Deswelling and Thermal Events in Magnetic Nanocomposite Hydrogels

The preliminary work showed that the deswelling of a magnetic nanocomposite hydrogel in an AC field is a remotely induced gross deformation of the hydrogel network, which can be tuned by controlling the ratio of comonomers to be used, and hence the balance of hydrophilic and hydrophobic moieties. A parametric study was designed in order to study the deformations in detail (see section 4.2.3 for formulation table). Sample response was studied by thermometry, gravimetrically and by DSC. In the first set of experiments, the AAm content was varied at constant total AAm and NIPAAm content and constant G4' nanoparticle concentration, [Fe] = 19.3 mM. The amount of PEG700 diacrylate crosslinker used in the formulations was kept constant at 0.049 mM. After 2400 seconds of irradiation, the sample temperature had increased to 38.3 °C, from a starting temperature of 32 °C. For each irradiation time the weight loss was recorded and a deswelling ratio calculated. Fig 4-11 shows a plot of deswelling ratio of magnetic nanocomposite hydrogels over time. After 2400 s of irradiation, the deswelling ratios were 14.1, 10.8, and 8.6% for AAm contents of 0.07, 0.14, and 0.28 mM. This shows a systematic effect of the AAm, even at low iron concentrations. The decreased ratio is ascribed to the more hydrophilic AAm monomer allowing more water molecules to be absorbed into the polymer network.

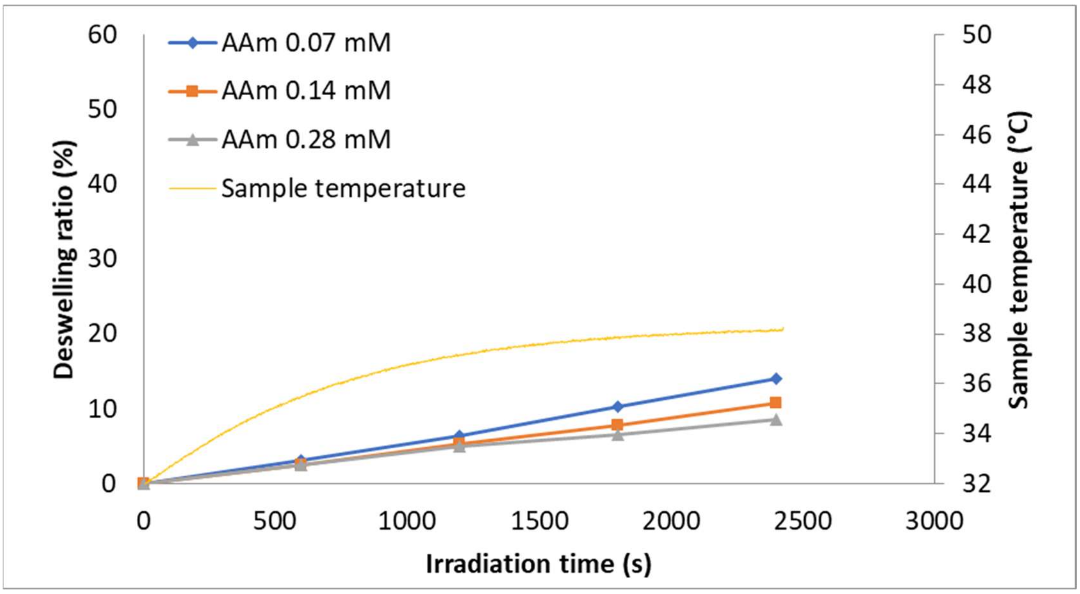

Figure 4-11: Deswelling ratio of magnetic nanocomposite hydrogels with AAm concentrations at 0.07, 0.14, and 0.28 mM (corresponding NIPAAm concentrations were 0.88, 0.81, and 0.67 mM, respectively), subjected to an AC magnetic field (H = 9.9 kA/m and f = 476.6 kHz). The G4' nanoparticle load was equivalent to [Fe] = 19.3 mM. The concentration of PEG 700 diacrylate crosslinker was set at 0.049 mM. Sample temperature is plotted on the secondary y-axis.

The deswelling ratios of all three samples begin to diverge between 600 and 1200 seconds, corresponding to a temperature range of 35 to 37 °C. The same samples were analysed by DSC (Fig 4-12). Whilst some endothermic transitions are observed between 32 and 34.5 °C, these are not obvious in the deswelling data from 0 to 600 seconds, which corresponds to the same temperature range. However, it is interesting that from 34.5 °C onwards the DSC data for the gels containing 0.07 and 0.14 mM AAm begins to shift upward, indicating exothermic behaviour, and this corresponds to the divergence of deswelling data between 600 and 1200 seconds of irradiation in the AC field.

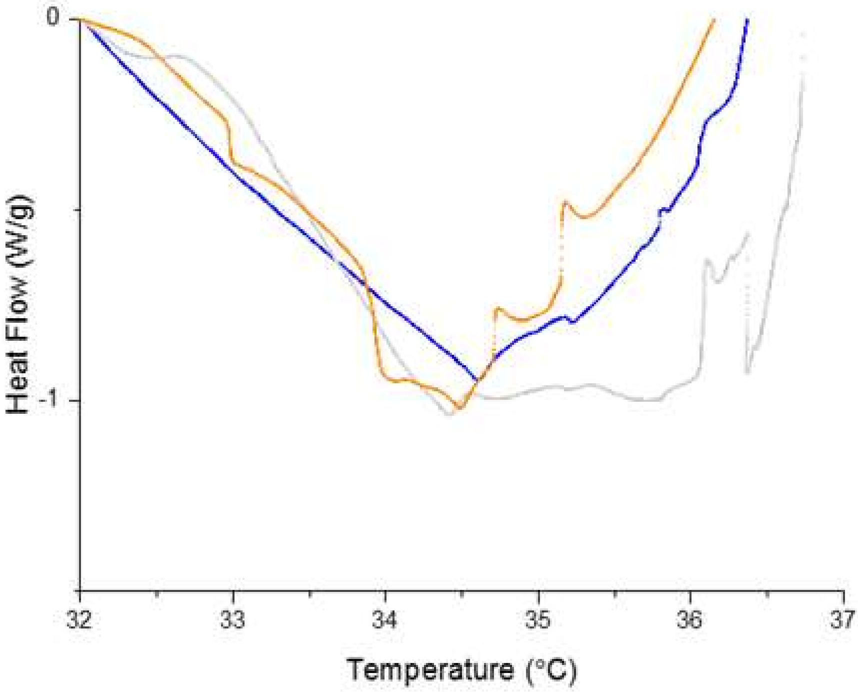

Figure 4-12: DSC thermogram of magnetic nanocomposite hydrogels containing containing NIPAAm (0.88, 0.81, and 0.67 mM), PEG700DA (0.097 mM), and G4' nanoparticles ([Fe] = 19.3 mM), subject to a temperature ramp consistent with that recorded during the magnetic hyperthermia experiment (Fig 4-11). The concentration of AAm is varied (blue = 0.07 mM; orange = 0.14 mM; grey = 0.28 mM).

On increasing the nanoparticle concentration to [Fe] = 38.6 mM, the gels reach a higher final temperature of approximately 42 °C after 2400 seconds of irradiation (Fig 4-13), irrespective of AAm content. The final deswelling ratios were 33.2, 23.5, and 14.1% for 0.07, 0.14, and 0.28 mM AAm content.

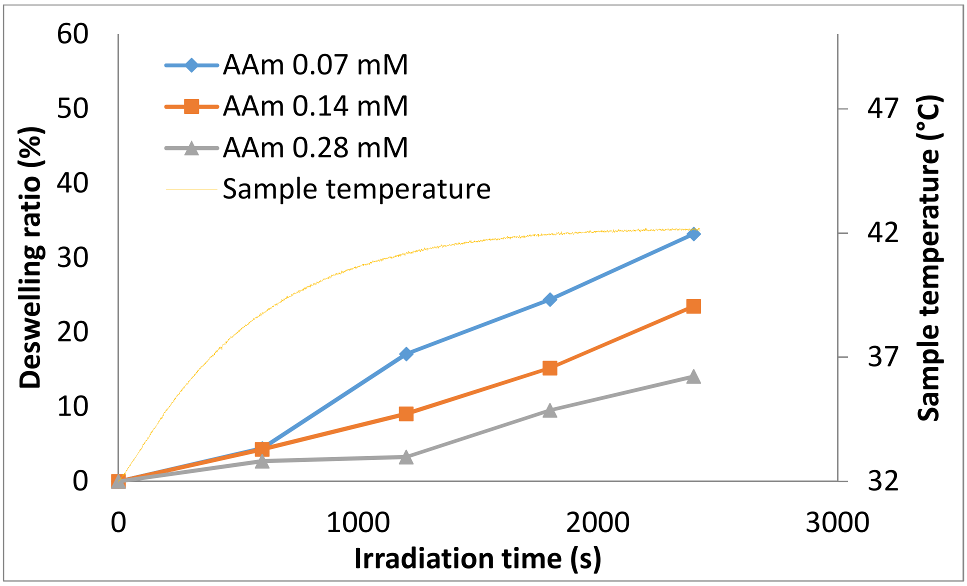

Figure 4-13: Deswelling ratio of magnetic nanocomposite hydrogels with AAm concentrations at 0.07, 0.14, and 0.28 mM (corresponding NIPAAm concentrations were 0.88, 0.81, and 0.67 mM, respectively), subjected to an AC magnetic field (H = 9.9 kA/m and f = 476.6 kHz). The G4' nanoparticle load was equivalent to [Fe] = 38.6 mM. The concentration of PEG 700 diacrylate crosslinker was set at 0.049 mM. Sample temperature is plotted on the secondary y-axis.

At lower AAm content, a step change in the deswelling ratio is observed between 38.6 and 41.1 °C (after 600 s). A possible explanation is that the initial amount of water bound by the network at that temperature is not enough to prevent aggregation of hydrophobic domains. When [AAm] = 0.28 mM the deswelling rate changes little, if at all, in this temperature range. However, between 41.1 and 42.1 °C (after 1200 s), all three gels deswell at approximately the same rate, indicating that a transition occurs between 38.6 and 41.1 °C.

Looking at the corresponding DSC data (Fig 4-14), the rate of heat transfer for all three samples is similar between 32 and 34 °C. A sharp endothermic peak is observed around the same temperature (38.6 °C), once again at this temperature, or perhaps slightly above it, the deswelling data begins to diverge. Also, the rate of deswelling for the sample containing 0.28 mM AAm is greatest, whilst the heat flow is lowest. This is what is expected for the polymer network containing the least amount of AAm, i.e. fewer water molecules associated with the network may mean less energy required to desorb those water molecules. A similar endothermic transition is observed for the sample containing 0.28 mM AAm, except that it occurs at 40 °C. This is mirrored by the deswelling data, as the rate of deswelling for that sample undergoes a step change at approximately 40 °C. This suggests that the more AAm-dense network has more water molecules associated, therefore more heat energy is required to desorb sufficient water and bring about the phase separation. The steady exothermic climb observed in all samples starting at 38 – 40 °C likely represents the hydrophobic collapse of the network, which is thermodynamically favourable. At that point less heat is required to maintain the sample at the same temperature as the reference. The sample containing 0.14 mM AAm is anomalous, in that the endothermic transition would be expected to occur somewhere between 38.6 and 40 °C, but actually occurs slightly higher than 40 °C. The deswelling data for that sample shows a step change at 41 °C. It may be the case that beyond a minimum amount of AAm, the endothermic transition moves to higher temperature and any additional AAm makes no further measurable effect.

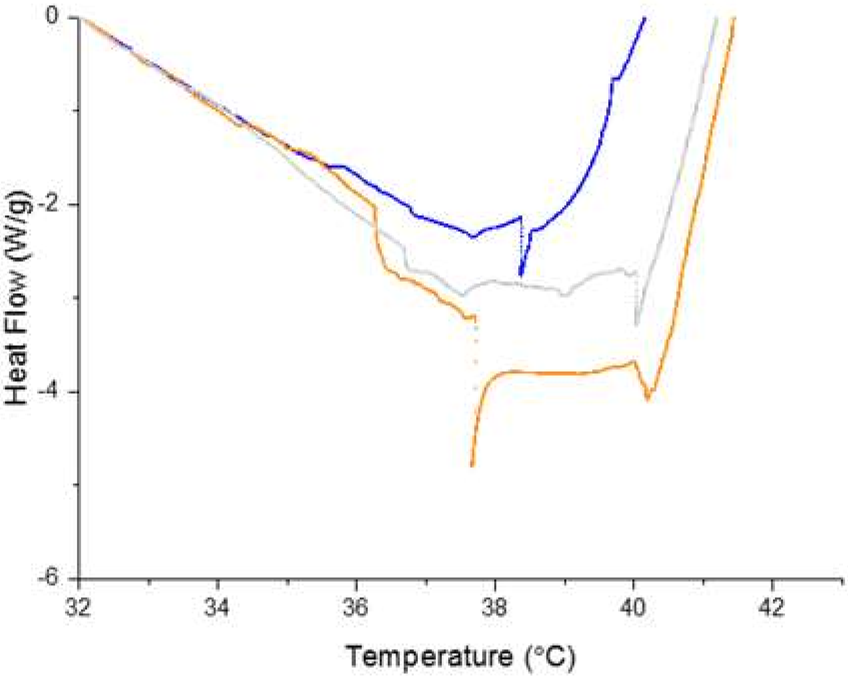

Figure 4-14: DSC thermogram of magnetic nanocomposite hydrogels containing NIPAAm (0.88, 0.81, and 0.67 mM), PEG700DA (0.097 mM), and G4' nanoparticles ([Fe] = 38.6 mM), subject to a temperature ramp consistent with that recorded during the magnetic hyperthermia experiment (Fig 4-13). The concentration of AAm is varied (blue = 0.07 mM; orange = 0.14 mM; grey = 0.28 mM).

When the iron concentration was increased to 77.2 mM, the effect of AAm content on the deswelling was more pronounced (Fig 4-15). At 0.07 and 0.14 mM it was apparent that there was markedly different response with the change in AAm content. In this case at 600 s the temperature was 43.4 °C and the deswelling ratios were 38.8, 23.8, and 4.9% with increasing AAm content. Compared with the sets of deswelling data in Figs 4-12 and 4-14, these samples lose significantly more water, due to increased nanoparticle concentration generating more heat on irradiation. This implies that even below the bulk VPTT, the extent of water loss increases with nanoparticle concentration, therefore it may not be necessary to reach the VPTT when assessing nanocomposite hydrogels as drug delivery devices. It is interesting that the samples containing 0.14 and 0.28 mM AAm have the same deswelling ratio after 2400 seconds of irradiation in the AC field.

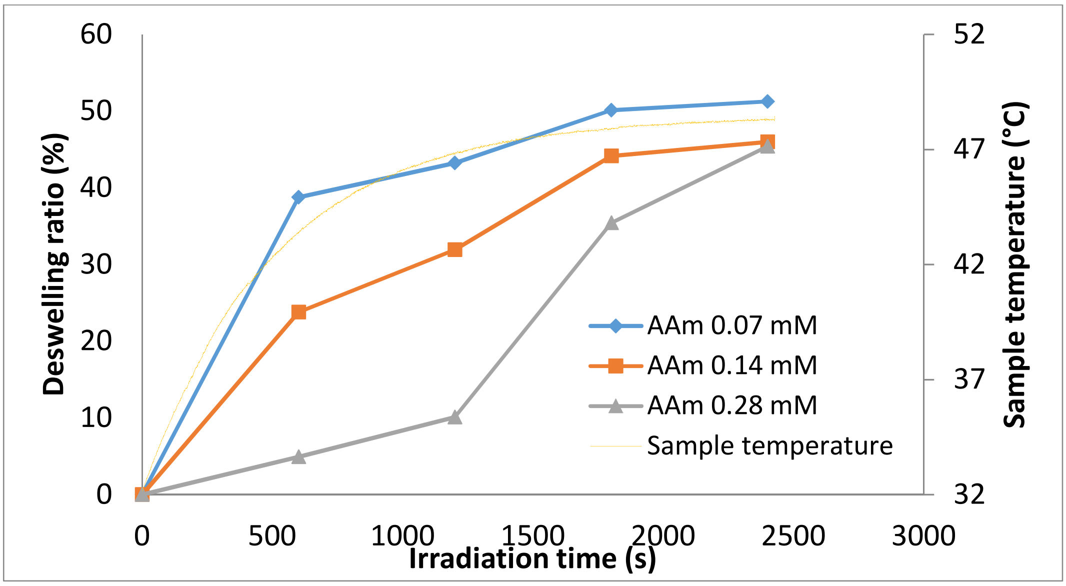

Figure 4-15: Deswelling ratio of magnetic nanocomposite hydrogels with AAm concentrations at 0.07, 0.14, and 0.28 mM (corresponding NIPAAm concentrations were 0.88, 0.81, and 0.67 mM, respectively), subjected to an AC magnetic field (H = 9.9 kA/m and f = 476.6 kHz). The G4' nanoparticle load was equivalent to [Fe] = 77.2 mM. The concentration of PEG 700 diacrylate crosslinker was set at 0.049 mM. Sample temperature is plotted on the secondary y-axis.

The DSC data for the AAm-variable gels containing 77.2 mM Fe can be seen in Fig 4-16. At approximately 41 °C the endotherm (downward slope) transforms to an exotherm (upward climb), representing the VPTT. Although the endotherm transitions to an exotherm at the same temperature for all three samples, the total heat flow in each sample is different, i.e. the sample containing the least amount of AAm requires the least amount of heat to keep up with the reference. As before this may be because there are fewer water molecules associated with the polymer network to begin with. Again, the anomalous thermal behaviour of the gel containing 0.14 mM is observed. Some endothermic transitions normally associated with the LCST/VPTT of NIPAAm are observed at 32 and 34 °C for the gel containing 0.14 mM AAm, and 38.5 and 39 °C for the gel containing 0.28 mM AAm. It is difficult to link these to the corresponding deswelling data, as after 600 seconds of irradiation the sample temperature has already reached 44 °C, which is on the exothermic rise in the DSC data.

Overall, the responses are consistent with the mol% of AAm present in the crosslinked polymer network determining the network's ability to retain water during a temperature increase. The driving force for deswelling is hydrogen bonding becoming thermodynamically unfavourable. The response of NIPAAm to temperature increase dominates the kinetics of deswelling, but the water content of the gels is controlled by the amount of AAm. Despite forming copolymer networks, the individual properties of each monomer contribute to the resulting swollen network.

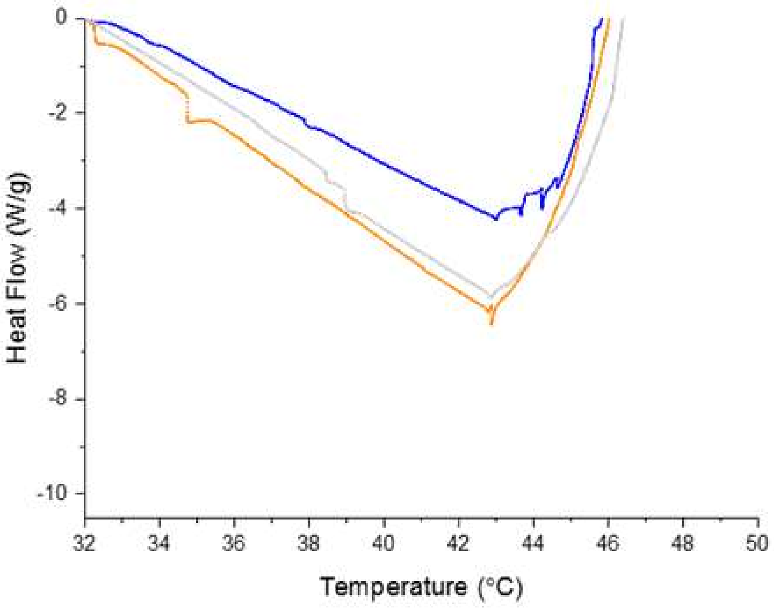

Figure 4-16: DSC thermogram of magnetic nanocomposite hydrogels containing NIPAAm (0.88, 0.81, and 0.67 mM), PEG700DA (0.097 mM), and G4' nanoparticles ([Fe] = 77.2 mM), subject to a temperature ramp consistent with that recorded during the magnetic hyperthermia experiment (Fig 4-15). The concentration of AAm is varied (blue = 0.07 mM; orange = 0.14 mM; grey = 0.28 mM).

4.3.7. Effect of PEG Diacrylate Crosslinker on Deswelling and Thermal Events in Magnetic Nanocomposite Hydrogels

Keeping the AAm and NIPAAm content constant (0.14 and 0.81 mM, respectively), the effect of the PEG diacrylate crosslinker on the magnetically-mediated deswelling kinetics and thermal behaviour was studied by gravimetry and DSC. Fig 4-17 shows the deswelling ratio versus irradiation time of gels containing 19.3 mM iron. The temperature reached *c.* 38 °C, as in the earlier series at the same Fe concentration. The deswelling ratios at 38 °C were 10.0, 10.8, and 10.8% for increasing PEG content. Hence, despite variation of PEG crosslinker content the deswelling kinetics are almost identical. This might be expected from the previous findings, as the AAm content is kept constant. This suggests that, within this temperature range, the crosslink density does not have an influence; the extent of water loss being the same for all samples. The linearity of the data would suggest that no major transitions have occurred up as far as 38 °C.

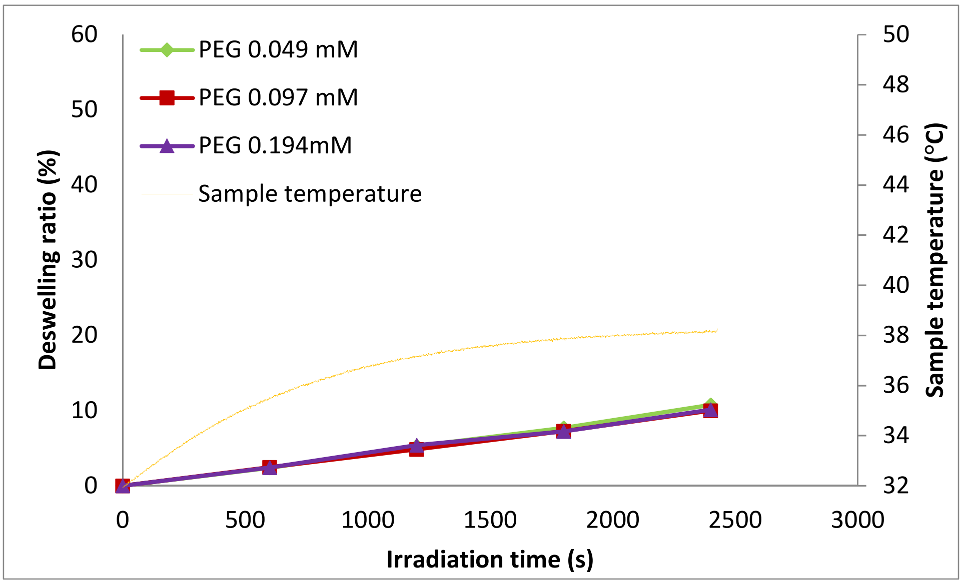

Figure 4-17: Deswelling ratio of magnetic nanocomposite hydrogels with varying PEG 700 diacrylate crosslinker, subject to an AC magnetic field (H = 9.9 kA/m and f = 476.6 kHz). The G4' nanoparticle load was equivalent to [Fe] = 19.3 mM. AAm and NIPAAm concentrations were 0.14 and 0.81, respectively. Sample temperature is plotted on the secondary y-axis.

Fig 4-18 shows DSC of the same set of gels. It is difficult to interpret this data with respect to the deswelling data. As already mentioned, there are no distinctive features in the deswelling data and the exo- to endo-thermic switch observed at 35-35 ºC was complete within 300 s.

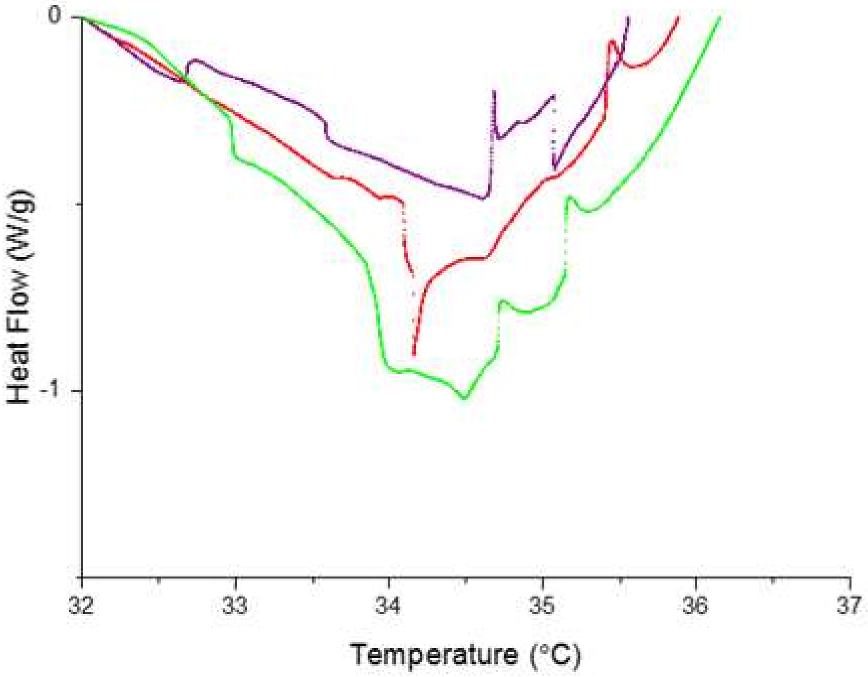

Figure 4-18: DSC thermogram of magnetic nanocomposite hydrogels containing AAm (0.14 mM), NIPAAm (0.81 mM) and G4’ nanoparticles ([Fe] = 19.3 mM), subject to a temperature ramp consistent with that recorded during the magnetic hyperthermia experiment (Fig 4-17). The concentration of PEG 700 diacrylate is varied (green = 0.049 mM; red = 0.097 mM; purple = 0.194 mM).

When the iron concentration was increased to 38.6 mM, the swelling ratios were 23.5, 21.3, and 24.2% (Fig 4-19). By increasing the nanoparticle load, the sample reached a final temperature of 42 °C, as in the previous series at this Fe concentration. There is a step change in the slope of the deswelling ratio for all three samples at 41 °C, irrespective of the crosslink density. After a further 600 seconds of irradiation, the temperature increased by 0.9 °C. Again, the baseline shifts in the exothermic direction at this temperature. Between 41.0 and 41.9 °C, there is a change for all PEG contents, which we tentatively assign to the bulk VPTT, resulting in an accelerated, and similar, rate of deswelling. This is appears to be a common feature in all samples that are heated beyond 41 °C. We suggest that the minor differences apparent for 0.097 mM PEG sample are not significant.

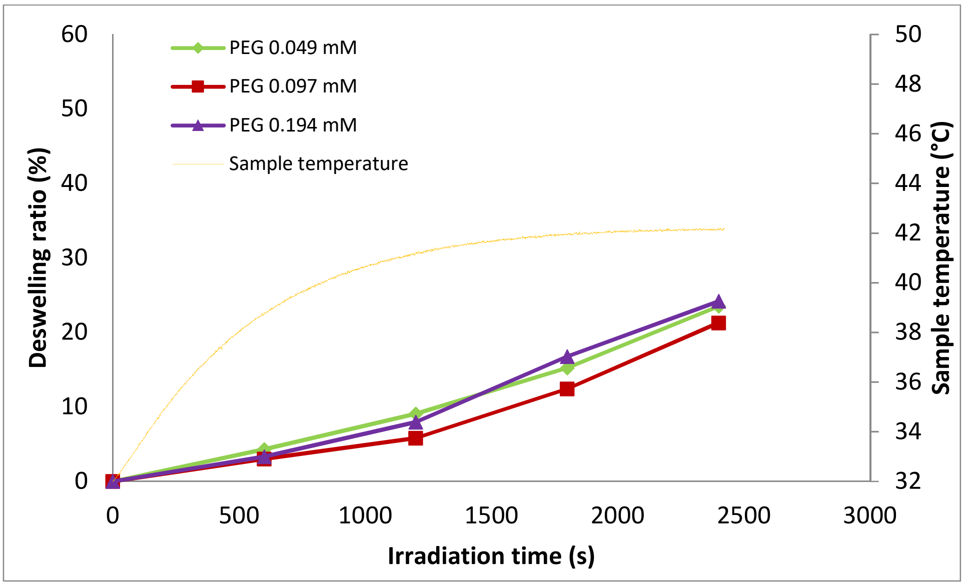

Figure 4-19: Deswelling ratio of magnetic nanocomposite hydrogels with varying PEG 700 diacrylate crosslinker, subject to an AC magnetic field (H = 9.9 kA/m and f = 476.6 kHz). The G4' nanoparticle load was equivalent to [Fe] = 38.6 mM. AAm and NIPAAm concentrations were 0.14 and 0.81, respectively. Sample temperature is plotted on the secondary y-axis.

The DSC data in Fig 4-20 shows that irrespective of the crosslink density the heat transfer is initially the same for all samples, suggesting that the AAm content (which is kept constant) is indeed a factor. The gel containing 0.194 mM PEG undergoes a transition at 36 °C, but this cannot be linked to the deswelling data, as at that temperature the rate of deswelling is the same for all samples. Again, the transition at ca. 41 °C corresponds to the step change in the deswelling rate for all samples.

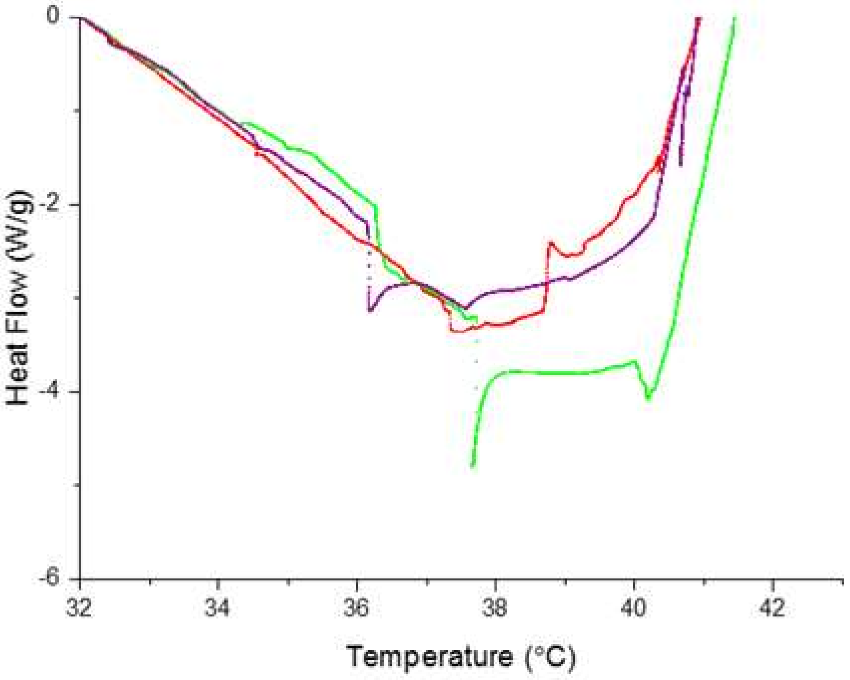

Figure 4-20: DSC thermogram of magnetic nanocomposite hydrogels containing AAm (0.14 mM), NIPAAm (0.81 mM), and G4' nanoparticles ([Fe] = 38.6 mM), subject to a temperature ramp consistent with that recorded during the magnetic hyperthermia experiment (Fig 4-19). The concentration of PEG 700 diacrylate is varied (green = 0.049 mM; red = 0.097 mM; purple = 0.194 mM).

When the nanoparticle load is further increased ([Fe] = 77.2 mM), the gel heated to a maximum of 48 °C (Fig 4-21), similar to the previous series. The final deswelling ratios were 45.6, 45.6, and 20.7% for increasing PEG content. The sample containing 0.194 mM PEG shows the smallest deswelling ratio change. Although the other two concentrations have different overall swelling kinetics, they show no measureable difference in the deswelling ratio after 2400 seconds of irradiation. It is interesting that there is no measureable difference in the initial rate of deswelling for the samples containing 0.097 and 0.194 mM PEG. Then, during the subsequent 600 seconds, a very dramatic increase in the deswelling of the network containing 0.097 mM PEG was observed. This is unexpected for two reasons; at 0.097 mM PEG, the network is more densely crosslinked and should deswell to a lesser extent overall. Secondly, the increased PEG content should result in more water being bound by the polymer network.

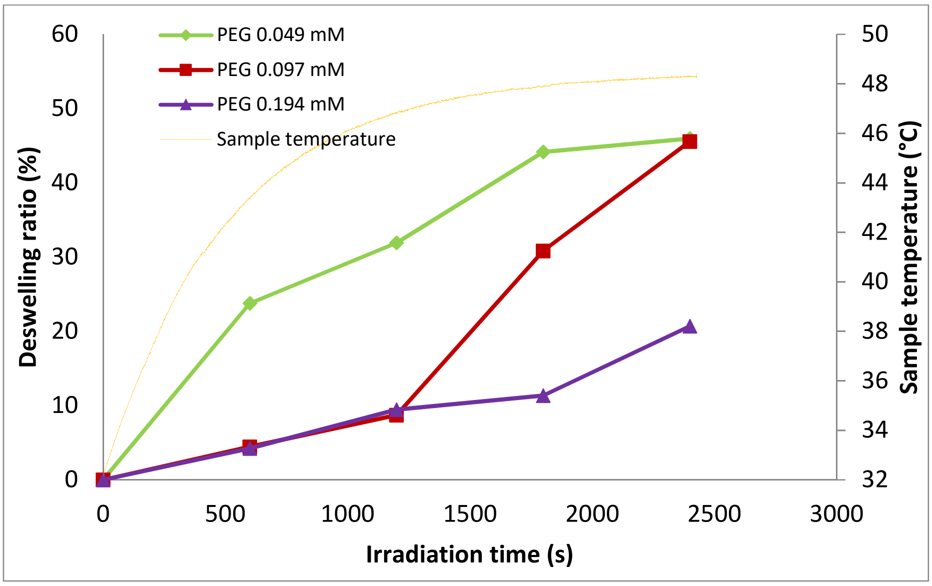

Figure 4-21: Deswelling ratio of magnetic nanocomposite hydrogels with varying PEG 700 diacrylate crosslinker, subject to an AC magnetic field (H = 9.9 kA/m and f = 476.6 kHz). The G4' nanoparticle load was equivalent to [Fe] = 77.2 mM. AAm and NIPAAm concentrations were 0.14 and 0.81, respectively. Sample temperature is plotted on the secondary y-axis.

A step change at 1200 seconds in the deswelling data for all samples is represented in the DSC data (Fig 4-22), as a step change in the baseline exotherm at approximately 46 – 47 °C for all three sample. What is interesting is that the heat flow is quite similar for all samples, yet the deswelling data is markedly different. This suggests that at higher temperatures, crosslink density becomes a strong influence on the deswelling. As might be expected, the least amount of deswelling is observed for the sample with highest crosslink density.

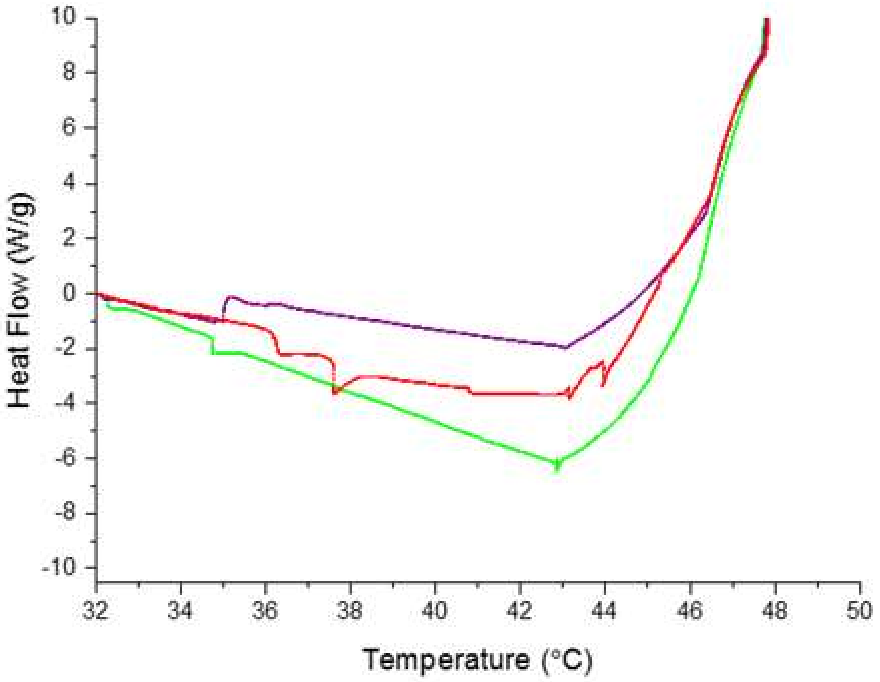

Figure 4-22: DSC thermogram of magnetic nanocomposite hydrogels containing AAm (0.14 mM), NIPAAm (0.81 mM), and G4' nanoparticles ([Fe] = 77.2 mM), subject to a temperature ramp consistent with that recorded during the magnetic hyperthermia experiment (Fig 4-21). The concentration of PEG 700 diacrylate is varied (green = 0.049 mM; red = 0.097 mM; purple = 0.194 mM).

4.4. Conclusions

The experimental observations from the nanocomposite hydrogels magnetothermal deswelling study can be summarised as follows:

i. The gels deswell naturally, even in the absence of the magnetic field, and this effect is accelerated by the presence of the iron oxide nanoparticles.

ii. AC-field irradiation accelerates the deswelling process for nanoparticle containing gels only.

iii. The bulk gel temperature change on irradiation is reduced, as compared to suspensions at the same concentration, with the response determined primarily by the MNP concentration, irrespective of the gel formulation.

iv. The AC-field induced deswelling rate and extent are also a function of the nanoparticle concentration, but are highly sensitive to the gel formulation.

v. There and many spurious features present in the DSC traces, however, the onset of temperature (and hence irradiation time) dependent changes in the stimulated deswelling profiles can be linked to thermal events (an endo- to exothermic-switch on increasing the temperature above 41 °C) for all samples studied with sufficient MNP loading to reach this temperature. We ascribe this to hydrophobic collapse mediated by the association of isopropyl moieties within the poly(NIPAAm-co-AAm) network.

vi. The effect of increasing the AAm/NIPAAm ratio for fixed PEG content is to decrease the % deswelling and the total water loss, in particular at higher nanoparticle concentration and hence temperature load. This reflects the increased hydrophilicity of the networks both at equilibrium and during the irradiation. The effect of increasing the PEG content, for fixed acrylamide content, is to decrease the % deswelling and the total water loss, again due to the hydrophilicity of PEG (and the increased crosslink density).

The work in this chapter has shown how varying the AAm/NIPAAm ratio in the nanocomposite can modulate magnetothermal deswelling and water release. Further steps should include more detailed measurements of the time dependence (denser data sampling) to enable a model be developed for the deswelling kinetics. Secondly, the correlation between water release and the release of model drugs, whether these be hydrophilic, hydrophobic, or amphiphilic could be examined. The release of a hydrophilic drug may not correlate with the water release, due to specific interactions of the drug molecule with the polymer network and/or polymer-coated nanoparticles.

Chapter 5 - Generation of superparamagnetic iron oxide nanoparticles for nanocomposite preparation by a top-down approach

5.1. Introduction

Nanoparticles are increasingly used in many industries, e.g. chemical, pharmaceutical, ceramic, and microelectronic industries [151]. The bottom-up methods for the synthesis of nanoparticles from molecular precursors are well established [152, 153] and have been described in Chapters 1 and 3. Using the thermal decomposition approach to nanoparticle synthesis from metallo-organic precursors, it is possible to control the size and magnetic properties of iron oxide NPs [154] and to control the amount of heat released when exposed to AC magnetic fields, which could be useful in a clinical setting [40]. However, the translation of iron oxide nanoparticles (NPs) is not without challenge. Specifically, the expense of pre-clinical trials to validate the safety of a material is the first major hurdle in product development [155]. Studies using generally-recognised-as-safe (GRAS) materials have a greater chance of clinical translation [156]. One way to generate GRAS magnetic iron oxide nanoparticles is to take a pre-certified iron oxide powder and attempt a size reduction process.

High-energy ball milling (HEBM) is a common modality for size reduction of bulk materials. A sub-class of HEBM, stirred media milling (SMM), has been used as a top-down approach for the production of ultrafine particles [157], and also as a route towards nanoparticles [158]. Stehr reported first examples of grinding using SMM, on the size reduction of coal slurries [159-161]. Since then the technique has been used in the production of paints [162], ceramics [163], and pharmaceuticals [164]. With respect to pharmaceuticals, the dissolution rate of hydrophobic drugs can be increased by reducing the size of particles down to the nanoscale [165]. The breakage of particles results in new surfaces and the free energy increase must be utilised to avoid aggregation of the newly formed particles. This is achieved by the addition of stabilisers which serve to minimise the free energy increase associated with new surfaces, these can operate electrostatically, sterically, or electrosterically [164]. Size reduction confers other advantages such as content uniformity, uniform flow, improved stability, and improved bioavailability [166]. SMM uses free-movable grinding media [167], typically hard and durable, e.g. silicon nitride (Si_3N_4), tungsten carbide (WC), and yttria-stabilised zirconia (Y_2O_3-Zr_2O_3)

(abbreviated YSZ). Zirconia is 8 on the Mohs scale of hardness, whilst doping with yttria at 5% (w/w) increases the hardness to > 9. The yttria dopant modifies the crystal structure such that wear resistance and chemical inertness are increased significantly [168]. For context, it should be noted that diamond has a Mohs hardness of 10 [169]. The utility of SMM as a route to ultrafine particles and nanoparticles can be understood within the context of the specific energy, i.e. the energy that is imparted to the stirrer, milling media and the material of interest [170]. The specific energy can be calculated using the following equation:

$$E_{m,M} = \frac{\int_0^t (P - P_0)}{m_P}$$

Equation 5-1

Where P is the power output of the mill, P_0 is the output when the mill is empty, and m_P is the mass of material in kg [170]. The remaining energy is dissipated as heat by friction processes. Material can be stressed by grinding media in three ways;

(i) Media accelerated from the stirrer shaft towards the grinding chamber wall, which affords them kinetic energy;
(ii) Pressing against the grinding wall due to centrifugal acceleration;
(iii) Moving tangentially at high velocity and colliding with grinding media which have a lower velocity.

Kwade determined that the third scenario is the most important as it results in sufficient stress events in which enough stress energy is available for grinding [171]. The number of stress events for each particle can be expressed by the stress number *SN*, which is determined by the number of bead contacts (N_c); the probability that a particle is caught and sufficiently stressed at a bead contact (P_s); and the number of particles inside the mill (N_p):

$$SN = \frac{Nc.Ps}{Np}$$

Equation 5-2

The number of bead contacts increases as the bead diameter decreases. For very small bead diameters (0.1 to 0.2 mm), the grinding result depends on the hardness of the grinding media. Kwade observed no progression in product fineness when using glass beads in the 0.1 to 0.2 mm range [167]. Li *et al.* used YSZ beads with sizes of 50 – 800 μm. They found that only beads of 50 – 100 μm in size led to sub-100 nm griseofulvin particles [172]. Despite the relatively low stress energies applied to a material, the very high stress number expected when using 100 μm media of sufficient hardness results in significant fracture. Therefore 100 μm YSZ was used as the media in the milling experiments described in this chapter.

There is only one example in the literature of SMM being used to generate iron oxide nanofluids. Manikandan *et al.* milled α-Fe_2O_3 in both water and ethylene glycol/water, which in both cases generated stable suspensions, without the need for a surfactant. This was achieved by controlling the suspension pH, affording electrostatic stabilisation of the resulting nanoparticles. The pre-milled material had a particle size range of 20 – 50 nm, which when added to water resulted in the formation of aggregates. These were milled using YSZ beads. 0.4 mm beads were used for "coarse grinding", and 0.2 mm beads were used for "fine grinding". Grinding of aggregates with 0.2 mm YSZ resulted in a particle size of 79 nm [173].

The questions then arise; what is the physical limit of grinding, and what determines it? The "*grinding limit*", as described by Knieke *et al.* [174], is where size reduction due to grinding reaches a plateau, despite increases in specific energy. There are two competing phenomena at play: breakage and agglomeration. The former depends on energy transfers, whilst the latter can be controlled by the addition of stabilisers. It follows that the grinding result depends on the suspension stability, and therefore the rheological properties. Knieke proposed two grinding limits; an *apparent grinding limit*, in which the viscosity of the suspension results in viscous-damping of the grinding media, removing some of the kinetic energy which would otherwise contribute to the breakage of particles. Interestingly, Knieke also showed that the effect of changing the milling chamber temperature from -5 °C up to 45 °C was negligible, the outcome presumably being due the inherent brittleness of oxides [175].

Under conditions where viscous damping does not occur, a *true grinding limit* can be obtained, which is limited by breakage itself. At a certain point in the process, a particle can no longer generate or store defects and therefore reaches a maximum strength. It should be noted that this limit is strongly influenced by material properties and hardly affected by process conditions. However, the breakage kinetics strongly depend on the process parameters and suspension conditions and hence grinding limit is not reached [175]. Based on the conclusions of Knieke, it likely that size control of nanoparticles generated by SMM may be possible by tuning the viscous damping effect.

The major goals of this work were to;
(i) Generate colloidal dispersions of NPs from a bulk material using stirred media milling, for use as a dye in 3D printing.
(ii) Study the reproducibility of the milling process. Can similar sized nanoparticles be generated batch-to-batch?
(iii) Study the effect of solvent viscosity on the size of the NPs generated *in situ*, i.e. can the solvent choice allow tunable size based on a viscous damping effect?
(iv) Study the effect of the stabiliser on the size of the NPs generated. How does the structure of the stabiliser and its interaction with the iron oxide surfaces determine final nanoparticle size?
(v) Study the effects of comminution on crystallinity and magnetic properties of generated NPs. Does the increased surface area lead to a change in the saturation magnetisation, compared with the value for the bulk material?

5.2. Experimental

5.2.2. Materials and Methods

Fe_3O_4, α-Fe_2O_3 and γ-Fe_2O_3 (denoted "BU-MAG") were purchased from Sigma-Aldrich. The same iron oxides were also obtained from Cathay Pigments, *via* Kromachem, UK. Ceramic beads composed of YSZ were obtained from Hosokawa Alpine, Germany. Oleic acid (Tech., $\geq$ 90%), oleylamine (Tech., $\geq$ 70%), ethanol, and anhydrous heptane (HPLC grade) were obtained from Sigma-Aldrich. A catechol-functionalised diblock copolymer, designated "PEA-3,4", was prepared as described in Chapter 3.

5.2.3. Generation of Superparamagnetic Iron Oxide Nanoparticles

All stirred media milling experiments were performed with a wet agitated horizontal media mill (Hosokawa Alpine AG, Augsburg, Germany). The temperature of the milling chamber was kept constant at 22.7 °C using circulating water, irrespective of the rotational frequency. Starting with a grinding chamber volume of 25 cm^3 YSZ equivalent to a volume of 20 mL was added to the chamber. BU-MAG (1 g), oleic acid (1 mL), oleylamine (1 mL), and ethanol (1 mL) were then added. The total filling volume of the chamber was slightly less than 25 cm^3. The rotor speed was 7000 rpm, running for a total of seven hours. The specific energy imparted to the product material (3 g maghemite powder) at 7000 rpm was estimated to be 940 MJ/kg. Hydrophobic nanoparticles were generated in heptane and oleic acid as stabiliser (denoted as NANO-MAG). Hydrophilic nanoparticles were generated in ethanol and PEA-3,4 as stabiliser. Both stabilisers were in equimolar amounts.

5.2.4. Characterisation

The morphology of the parent material (denoted BU-MAG) was characterised by a Hitachi S-5500 field emission scanning electron microscope (FE-SEM) (Tokyo, Japan). Using a spatula, the material was placed on a carbon black stub and non-adhering particulates were removed under compressed air. Particle size analysis was performed with a Malvern Mastersizer 2000 (Malvern Instruments Ltd., UK) laser diffraction system. Magnetic properties were determined using an in-house DC magnetometer (School of Physics, Trinity College Dublin). Heptane dispersions of NANO-MAG were imaged using a Hitachi S-5500 in bright field scanning transmission electron microscopy (BF-STEM) mode. Core diameters (D_{TEM}) were measured using the ImageJ program (version 1.45h; NIH, Bethesda, MD) and a log-normal fit of the data was obtained using Origin 9.1 software (OriginLab Corporation, Northampton, MA, USA). Hydrodynamic diameters were measured by dynamic light scattering with a Malvern Zetasizer Nano-ZS (Malvern Instruments Ltd., UK), the average of three measurements reported. Low angle x-ray diffractions of BU-MAG and NANO-MAG were performed with a Siemens D5000 X-ray diffractometer, using Co $K_{\alpha}1$ radiation (λ = 1.7889 Å) and a graphite monochromator. The diffraction pattern was scanned in steps of 0.02° (2θ) between 30° and 65°.

5.3. Results and Discussion

5.3.1. Characterisation of Bulk Maghemite Powder

A representative sample of BU-MAG is shown in Fig 5-1. The sample is interacting with a neodymium magnet, confirming its magnetic character. Tree-like projections of iron oxide powder interacting with the magnetic field can be seen. Visualisation of BU-MAG by SEM showed that the material was composed of particulates ≤ 70 µm (Fig 5-2c). Magnification at the surface of one such particulate shows that they are in fact aggregates of acicular crystallites, of average length 450 nm. (Fig 5-2b).

Figure 5-1: BU-MAG in glass vial, placed on neodymium magnet.

The acicular crystal habit is characterised by a needle-like appearance. The interactions between the acicular crystallites are thought to be combined Van der Waals and dipole interactions of the ferrimagnetic crystallites, resulting in the thatched appearance [176].

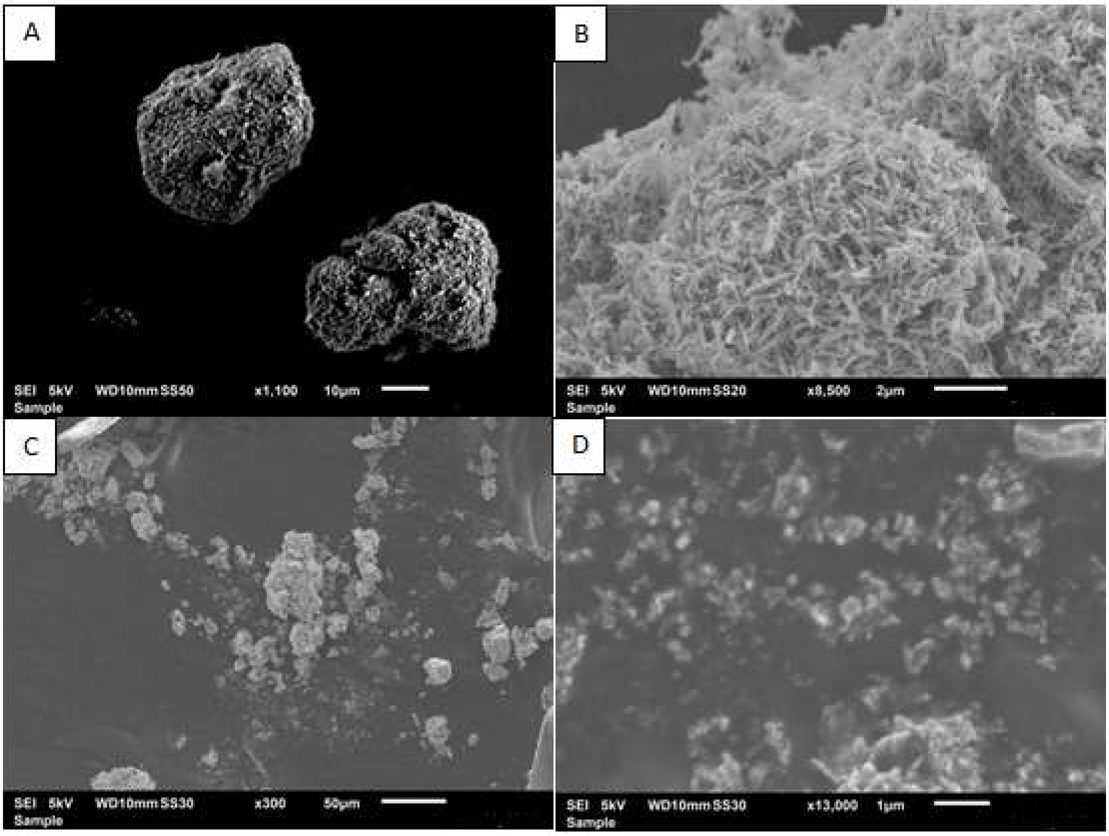

Figure 5-2: SEM images of representative sample of BU-MAG applied to carbon black film. A: Entire particulate; B: Particulate surface; C: Typical size range of particulates; D: Sub-micron particulates.

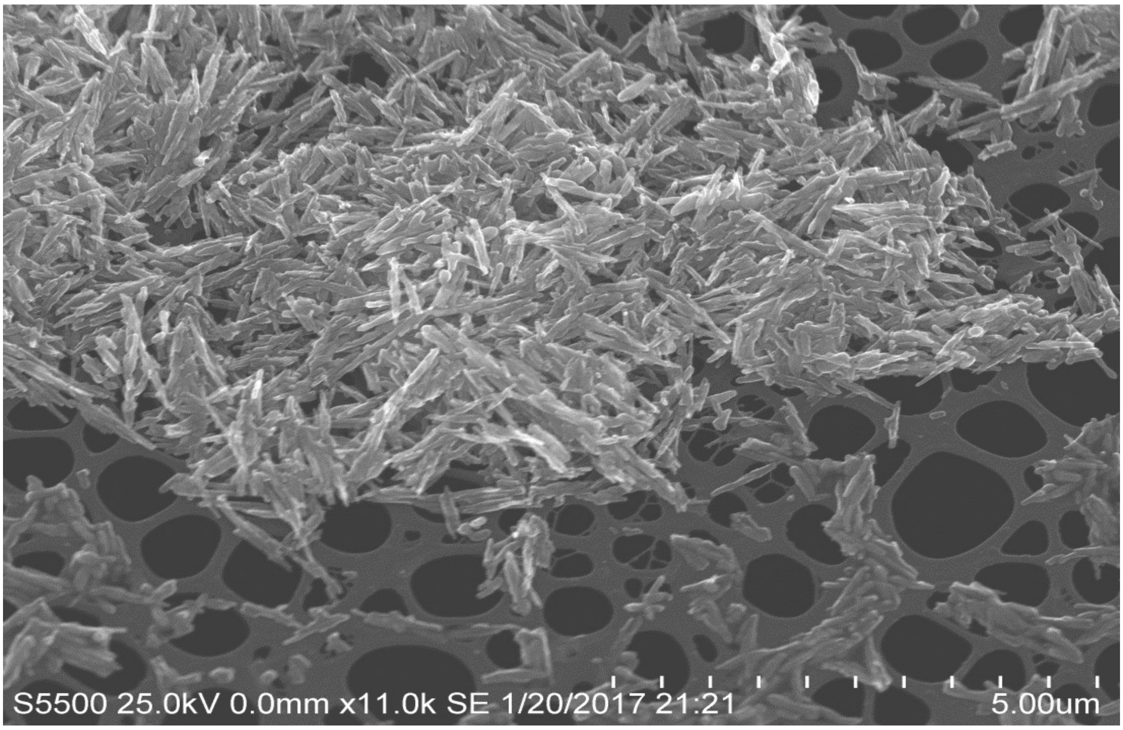

Figure 5-3: Sample of BU-MAG sonicated in water and deposited on grid. The tilt angle of the sample holder is adjusted to -30 °, to show the crystallites spread out across the holey carbon film.

A sample of BU-MAG was dispersed in water using a sonic probe and a portion of the product was imaged using SEM (Fig 5-3). The remaining sample was introduced to a Malvern Mastersizer 2000 laser diffraction system. The data indicated two distinct particle populations. The red line in Fig 5-4 shows the particle size distribution of the material without sonication, and the green line shows the distribution after one period of sonication. Initially the particle size ranges between 0.4 and 100 µm (red line), with two distinct populations having maxima at 2.5 and 25 µm, respectively.

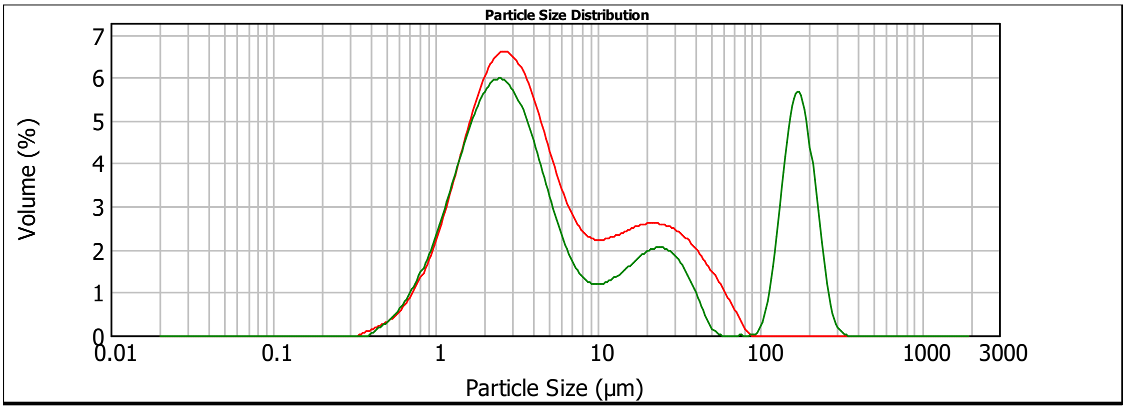

Figure 5-4: Particle size distribution of BU-MAG dispersed in water, as measured by laser diffraction. Red line is pre-sonication; green line is post-sonication.

The particles at the lower end of the scale are probably free crystallites, whilst the larger sizes are aggregates (as observed in the SEM images). Following sonication, a peak appears at approx. 150 µm (Fig 5-4, green line), compared with maximum 25 µm particle size without sonication. The percentage volume of this peak increases with repeated sonications (Fig 5-5), whilst the percentage volume decreases for the smaller particle sizes, with the peak maxima shifting to the left (1.5 and 15 µm, respectively).

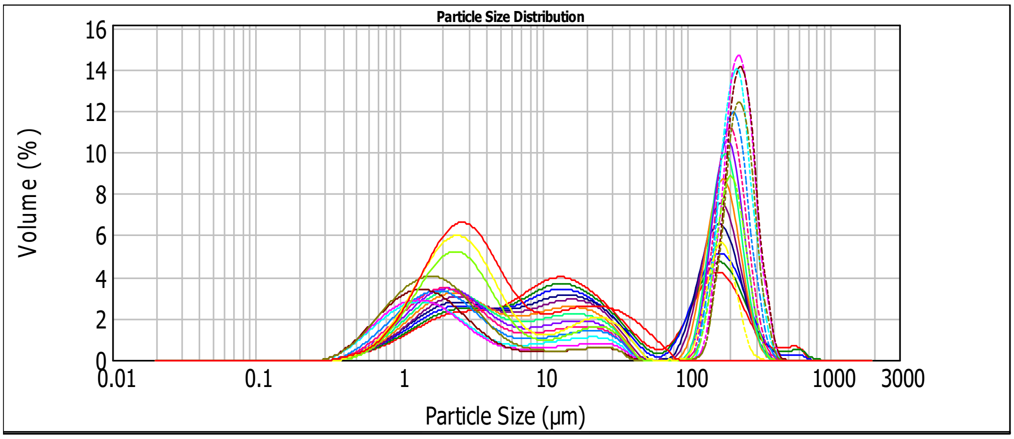

Figure 5-5: Evolution of the particle size distribution of BU-MAG sonicated in water.

In addition, the maximum of the new peak shifts to larger sizes. This indicates that the sonication cleaves crystallites away from the existing aggregates, whilst at the same time larger aggregates are formed. The acicular crystallite is the functional unit of the material as sold for magnetic data recording applications. According to the manufacturer it has a coercivity value, H_c = 325 Oe, and saturation magnetisation M_s = 74.5 emu/g. Berkowitz and Schuele reported that a length of 400 nm gives a maximum coercivity value, below which the material displays superparamagnetic behaviour (*ca.* 300 nm). [177]. Coercivity is reduced again for sizes larger than 400 nm, due to what Berkowitz and colleague describe as "non-coherent magnetisation", brought about by the emergence of multiple domains.

The observed hysteresis in BU-MAG (Fig 5-6) provides further evidence of the sample's ferromagnetic character. The saturation magnetisation as measured by DC magnetometry gave a value of 68.7 emu/g, which is an 8% drop in saturation magnetisation, compared with the value reported by the manufacturer (74.5 emu/g). The x- and y-axis intercept values are the coercivity and remanence, respectively. The coercivity of this sample was 0.031 T (cf 0.034 T) and the remanence was 28 emu/g (cf 30 emu/g).

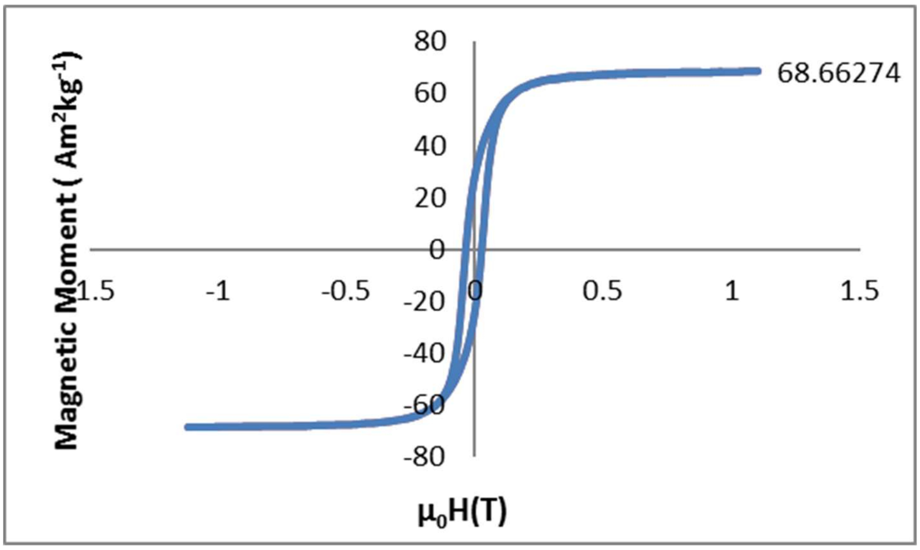

Figure 5-6: DC magnetometry of BU-MAG showing that the material is ferromagnetic.

It was found that, when BU-MAG was shaken in water, or in chloroform/oleic acid, a bright orange suspension results, following sedimentation of the magnetic material. In the absence of oleic acid, no suspension was formed in chloroform. This suggests that the orange material is electrostatically dispersed in water and steric interactions are sufficient to disperse it in chloroform. The suspensions were analysed by DLS, and the correlogram overlay in Fig 5-7 shows that both samples contain particles of similar dhyd (approximately 170 nm). This orange material could be a side product left over from the production process. According to the Cathay Pigments website, γ-Fe_2O_3 acicular crystallites are produced using a “unique lepidocrocite technology”. This may refer to thermal conversion of fcrocite (γ-FeOOH) to maghemite [178]. It should be noted that this material did not respond to a neodymium magnet, so could be unconverted lepidocrocite. Prior to the milling experiments, the orange material was separated from the maghemite.

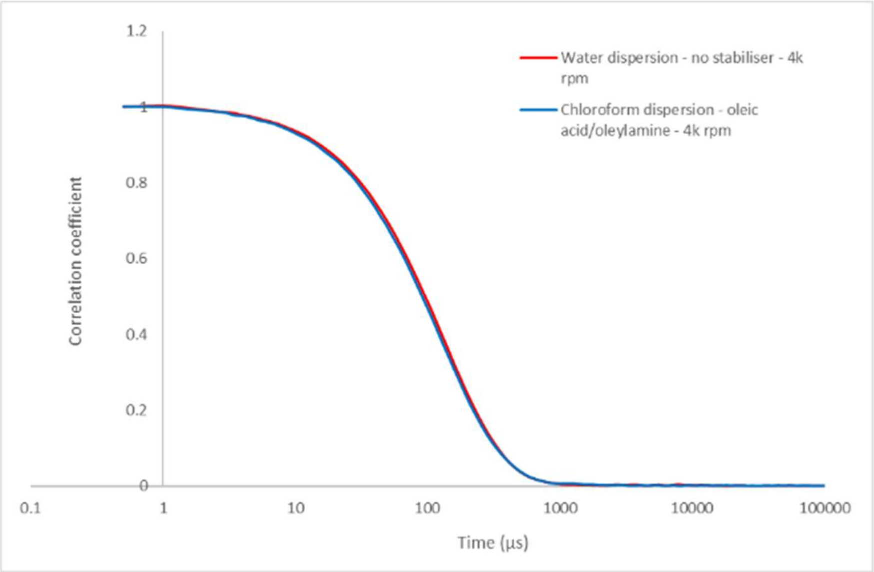

Figure 5-7: Overlay of normalized correlograms for water and chloroform suspensions of a non-magnetic material present in BU-MAG.

Initial milling experiments (the set up is shown in Fig 5-8) were conducted with a rotor speed of 10000 rpm. The results are shown in Fig 5-9. After 1 hour of milling, the material was comminuted to aggregates ≤ 10 µm (5-9a). After 2 hours of milling, aggregates were comminuted to individual crystallites (5-9c). After 7 hours, it appears that the crystallites had reaggregated (5-9d). This is characteristic of a system where the specific energy applied to the system is too high, and a reaggregation process competes with the breakage/dispersion process.

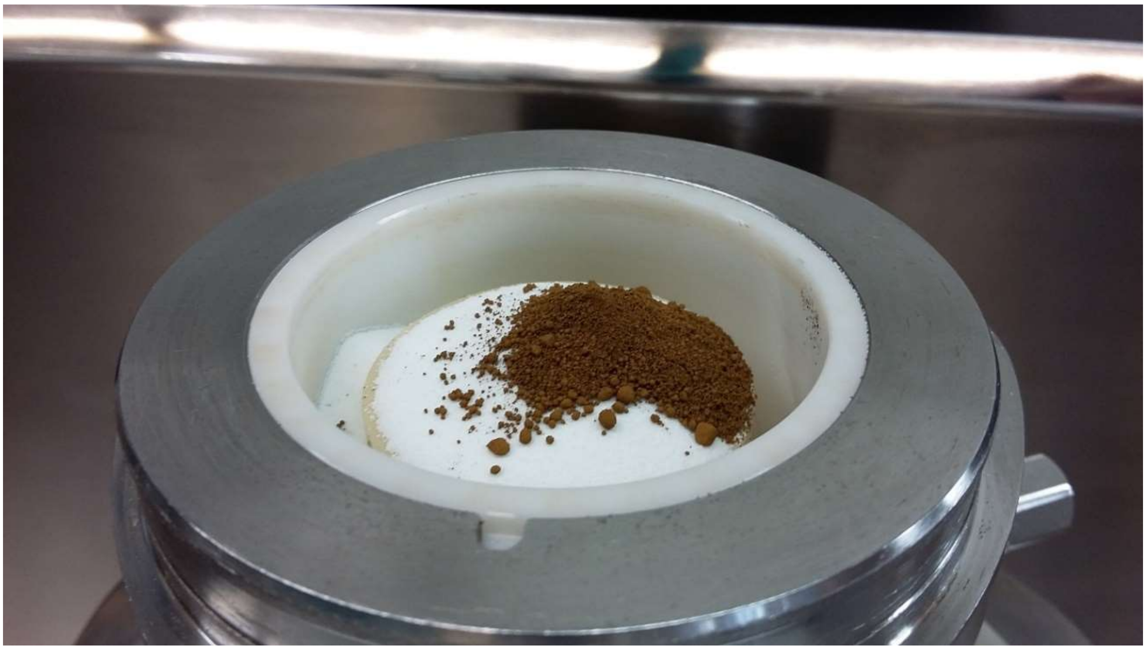

Figure 5-8: BU-MAG (brown powder) and yttria-stabilised zirconia (white beads), placed in the milling chamber of a Picoliq agitated media mill.

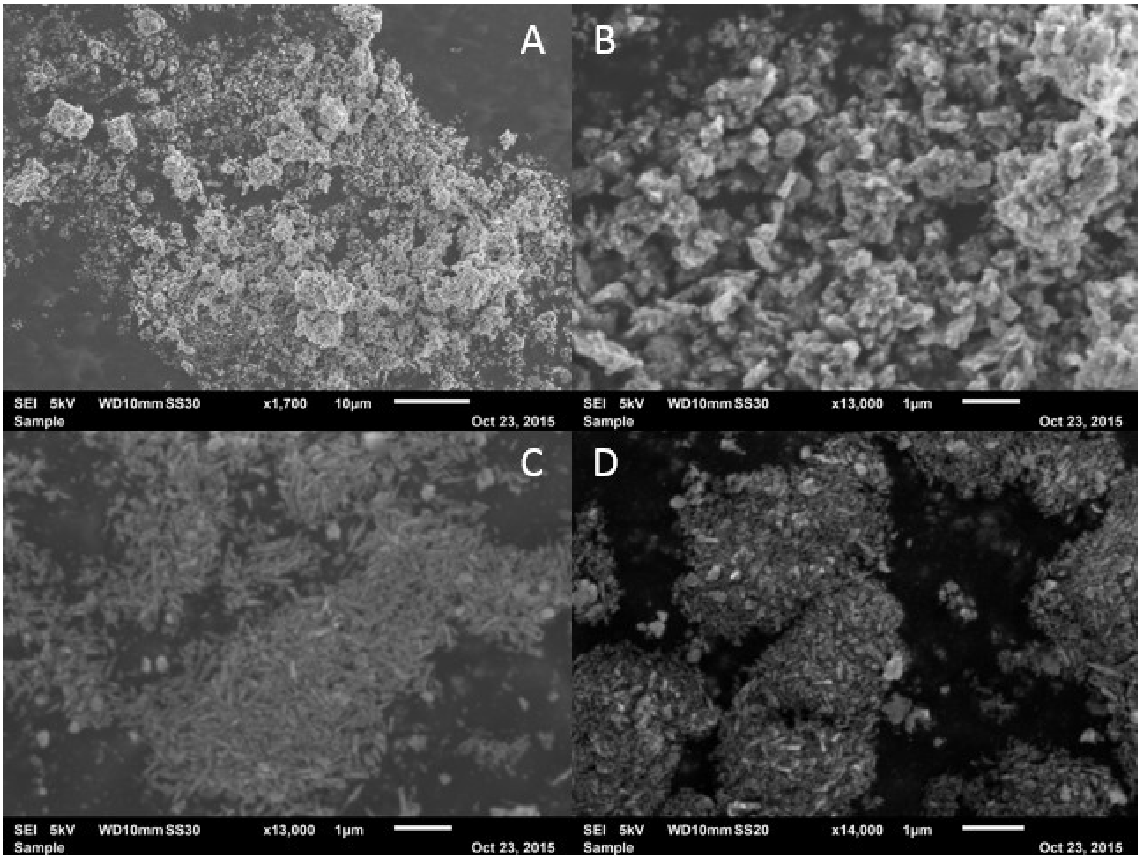

Figure 5-9: Stirred media milling (SMM) of BU-MAG. A and B – Comminution yielding particulates in the range 1 – 10 µm. C – Individual crystallites after milling for 2 hours.. D – Reaggregation.

To establish the presence of nanoparticles in the slurry, the charge was washed from the mill using heptane. Centrifugation yielded a dark, ruby-red dispersion (Fig 5-10). The normalised DLS correlograms for batches NANO-MAG-1 and NANO-MAG-2 are shown in Fig 5-11. Stability data for both batches are included. Both batches were milled at 10000 rpm, for 10 hours. Batch NANO-MAG-1had a dhyd of 22.3 ± 0.01 nm, PDI 0.08. The stability test was carried out the following day, giving a dhyd of 22.4 ± 0.06 nm, PDI 0.08. Batch NANO-MAG-2 had a dhyd of 22.0 nm, PDI 0.11, and the stability test gave a dhyd of 21.8 nm, PDI 0.11.

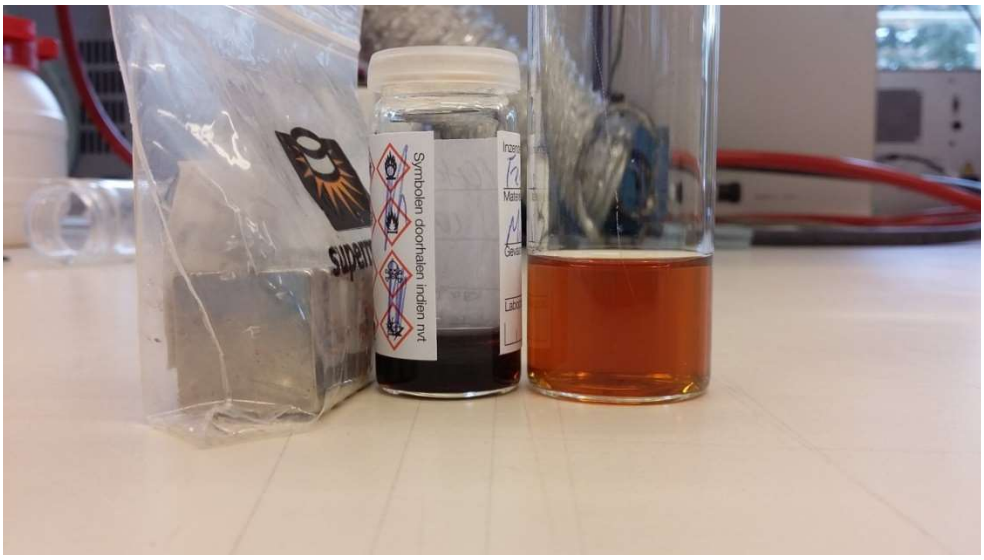

Figure 5-10: Dispersed NANO-MAG in heptane, following centrifugation of the heptane washings (centre), which were stable to a neodymium magnet (left). The vial on the right is a dilute heptane dispersion of NANO-MAG. dhyd of the dilute dispersion was 22.3 ± 0.01 nm, PDI 0.08.

The dhyd values indicate that the same size nanoparticles have been produced in subsequent batches, prepared a week apart. The overlapping of the normalised correlogram supports this hypothesis, i.e. the particles have the same diffusivity, and there are no large aggregates.

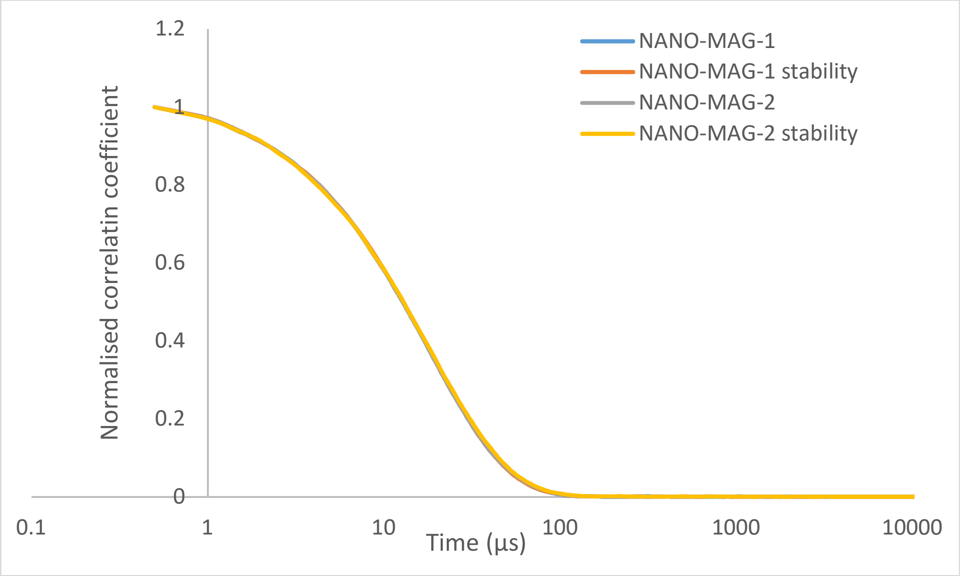

Figure 5-11: Two batches of NANO-MAG produced using the same conditions, showing overlapping correlograms (dispersions in heptane).

A sample of NANO-MAG-1 was blotted onto a TEM grid and viewed in bright field (BF) mode (Fig 5-12). Nanoparticle sizes were quantified using ImageJ, and a histogram of the sizes was constructed (Fig 5-13). Log-normal fitting gave a mean of 7.5 nm for the nanoparticle core size. The difference between the nanoparticle core size and the dhyd was larger than expected. Meledandri *et al* have reported a difference of 4.3 nm [124], whilst a difference of 7.25 nm was observed for NANO-MAG-1. Meledandri observed that a difference of 4.3 nm is also slightly larger than the value of 3.6 nm expected for a monolayer of oleic acid molecules [179], due to retention of oleic acid molecules secondary to the monolayer. They showed that, even when correcting for temperature, that the dhyd decreased as temperature increased, indicating liberation of oleic acid molecules.

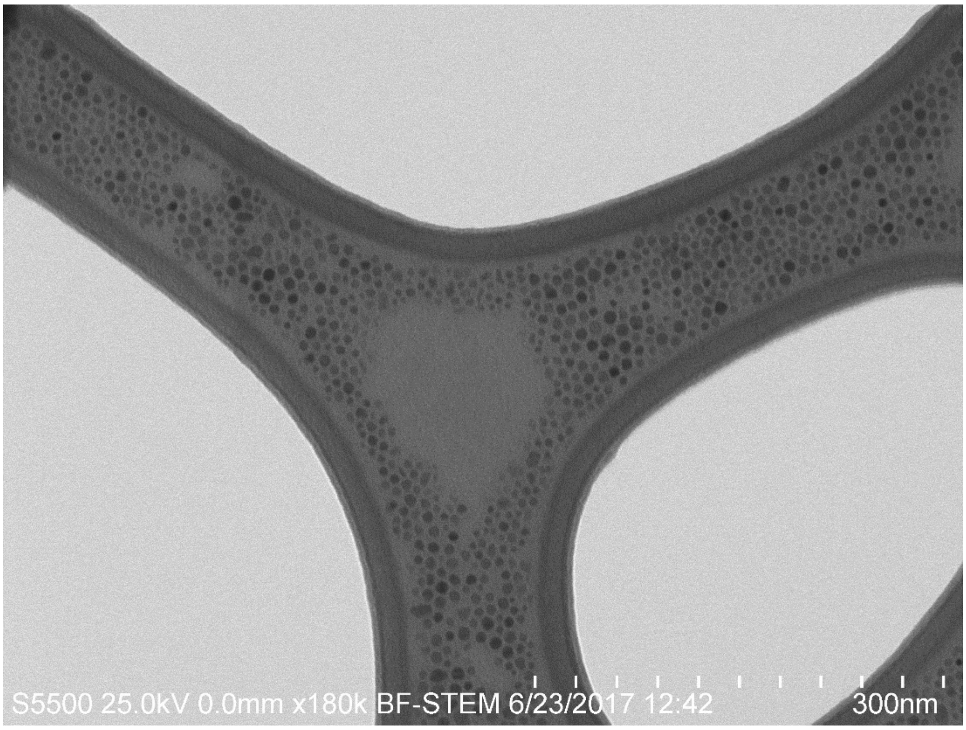

Figure 5-12: FESEM micrograph showing NANO-MAG-1 generated by SMM of BU-MAG. The heptane dispersion was blotted onto a TEM grid covered in holey carbon film.

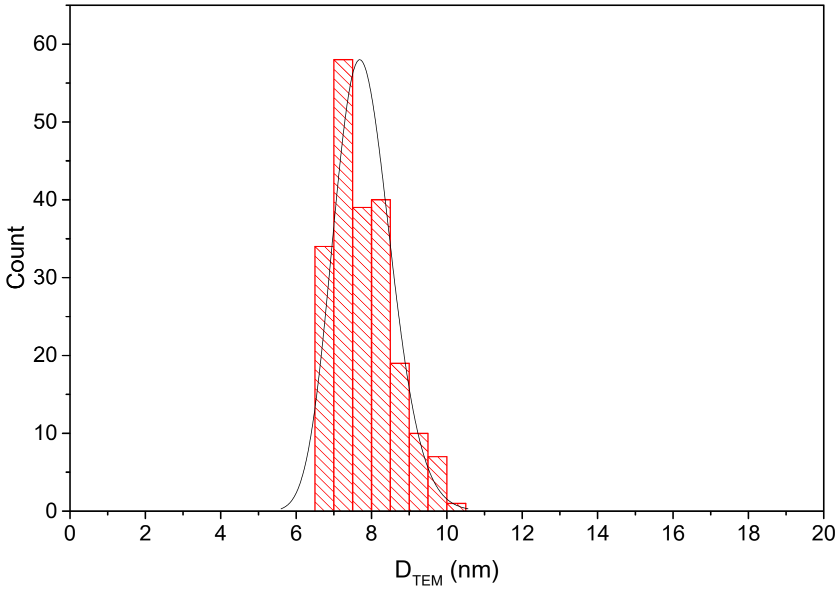

Figure 5-13: Histogram of D_{TEM} from a sample of NANO-MAG-1, generated by SMM at 10k rpm for10 h. Based on the lognormal fit, average nanoparticle diameter was estimated to be 7.3 ± 1.1 nm.

To further demonstrate the magnetic properties of the nanoparticles generated by SMM, a sample of the suspension was pipetted into a 50 mL glass vial containing acetone. The nanoparticles immediately destabilized, forming a brown-red precipitate that responded to a magnetic field (Fig 5-14). Removal of the supernatant and the addition of fresh heptane restored the dispersion, which was stable to a local magnetic field.

Figure 5-14: A sample of NANO-MAG-1, destabilized with acetone and collected using a neodymium magnet. Following removal of the magnet, the particles are readily redispersed

The original and milled samples of iron oxide were compared using x-ray diffraction (XRD). The bulk material diffracted significantly, in comparison to the nano iron oxide (Fig 5-15). Despite the peak broadening, the peaks are characteristic of magnetite and/or maghemite. The broadening shows that either the nanoparticle size was very small (in the nano range), and/or the sample has lost considerable crystallinity during the SMM process.

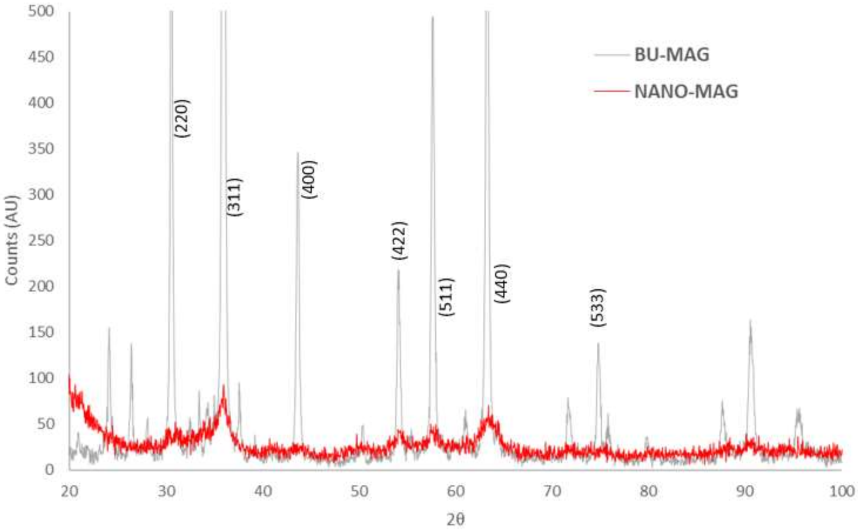

Figure 5-15: XRD overlay of BU-MAG and NANO-MAG.

5.3.2. Effect of Specific Energy: Comminution at the Nanoscale

As described in the previous section, NPs were generated at 10,000 rpm. However, the yield of dispersed nanoparticles from starting material was low (approximately 5%). It was hypothesised that the low yield was due to a high specific energy imparted to BU-MAG, causing the rate of reaggregation to increase with respect to the rate of comminution. Hence an experiment was undertaken whereby a sample of BU-MAG was milled at increasing rotational speeds i.e. specific energies. It was envisaged that this experiment would determine whether or not the nanoparticles observed by DLS and TEM were comminuted from the bulk.

The main goal was to identify rotor speeds that allow comminution of existing crystallites, with limited reaggregation. To study the effect of the specific energy on the nanoparticle size, the rotational frequency was varied, and the resulting samples were analysed by DLS. It was found that at 1000 rpm, no particles were detected by DLS. At 2000 rpm and higher, particles were detected. Hence, either the specific energy at 1000 rpm (50,400 kJ/kg) is not sufficient to generate nanoparticles from the bulk material, or existing particles caught in the bulk are not liberated. At 2000 rpm, nanoparticles with a dhyd of 41.1 nm and PDI 0.22 were detected by DLS. As the rotor speed was increased during the experiment, this affected the nanoparticle size, and polydispersity. A weak downward trend in the dhyd was observed up to 6000 rpm, for which a bimodal distribution emerges, giving dhyd = 60.1 ± 2.8 nm, PDI 0.42. Interestingly, approximately the same size is observed at 9000 rpm, with very similar data (58.4 ± 1.0 nm, PDI 0.44. The DLS size distributions also overlap. At 7000 rpm, the dhyd and PDI decrease to 29.9 nm and 0.21, respectively. A further hour of milling at 7000 rpm gave a sample with dhyd and PDI of 21.3 and 0.11, respectively. At higher rotor speed, the dhyd begins to increase again.

Table 5-1: The effect of the milling specific energy on both dhyd and PDI of BU-MAG in the presence of oleic acid and ethanol. Heptane dispersions were analysed by DLS.

Rotor speed (rpm)	Power (W)	Specific Energy (kJ/kg)	Cumulative Specific Energy (kJ/kg)	dhyd (nm)	PDI
2080	53	50400	50400	41.1 ± 0.1	0.22
3070	80	63600	114000	39.2 ± 0.1	0.19
4054	104	96000	210000	-	-
5033	133	124800	334800	37.2 ± 0.1	0.27
6016	159	159600	494400	60.1 ± 0.1	0.42
6986	186	223200	717600	29.9 ± 0.1	0.21
6986	186	223200	940800	21.3 ± 0.1	0.11
7966	211	253200	1194000	34.1 ± 0.2	0.19
8949	233	279600	1473600	58.4 ± 0.1	0.44
9918	262	314400	1788000	61.85 ± 0.1	0.49

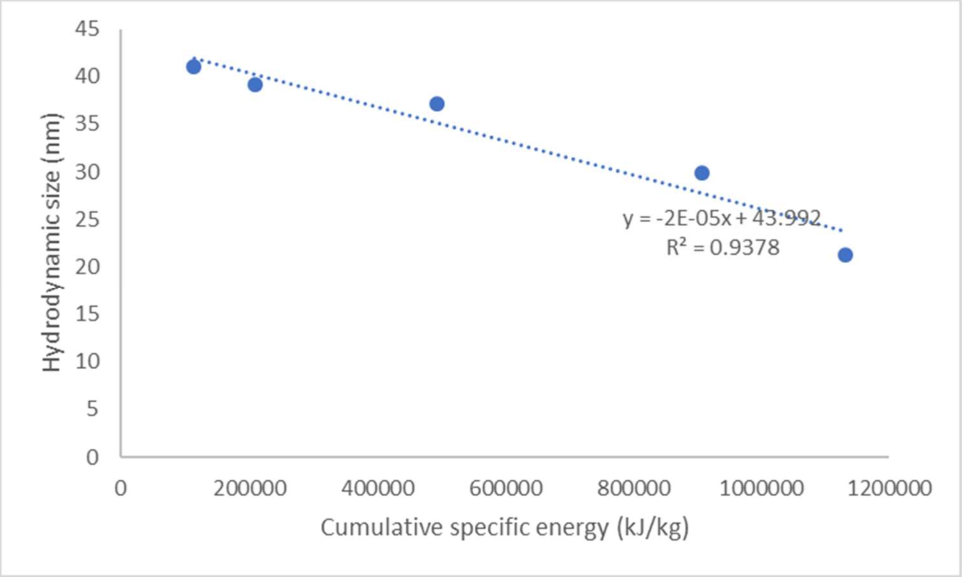

Figure 5-16: Hydrodynamic size as a function of the cumulative specific energy input. As more energy is put into the system, the heptane dispersions analysed by DLS show a downward trend in the hydrodynamic size.

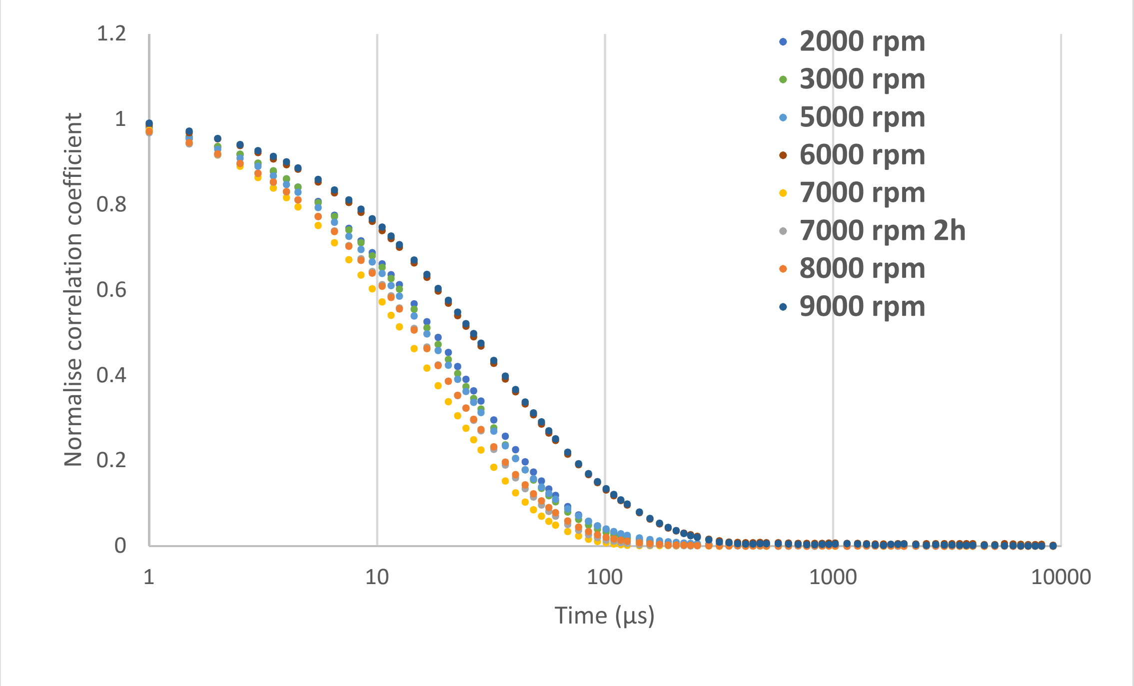

Figure 5-17: The effect of the rotational speed (specific energy) on the normalized DLS correlogram of maghemite nanoparticles produced by SMM of BU-MAG. Nanoparticle dispersions were in heptane.

A systematic change in the hydrodynamic size was observed when adjusting the rotational frequency of the mill from 2000 rpm through to 7000 rpm (Fig 5-16). Despite both dhyd and PDI being lower for the particles milled at 7000 rpm for 2 hours, the diffusion of the particles milled at 7000 rpm for 1 h indicates that these particles are smaller. The reason for the larger dhyd is probably due to some larger particles affecting the intensity-weighted dhyd, which highlights the importance of examining the correlogram when assessing effects of various parameters on the particle size. At 6000 and 9000 rpm there is significant reaggregation and a second peak in the intensity distribution is observed. In the case of these two rotational speeds, the particle sizes as calculated by Mie theory (from the scattering intensity), are 26.78 ± 0.7 and 26.76 ± 2.2 nm, respectively.

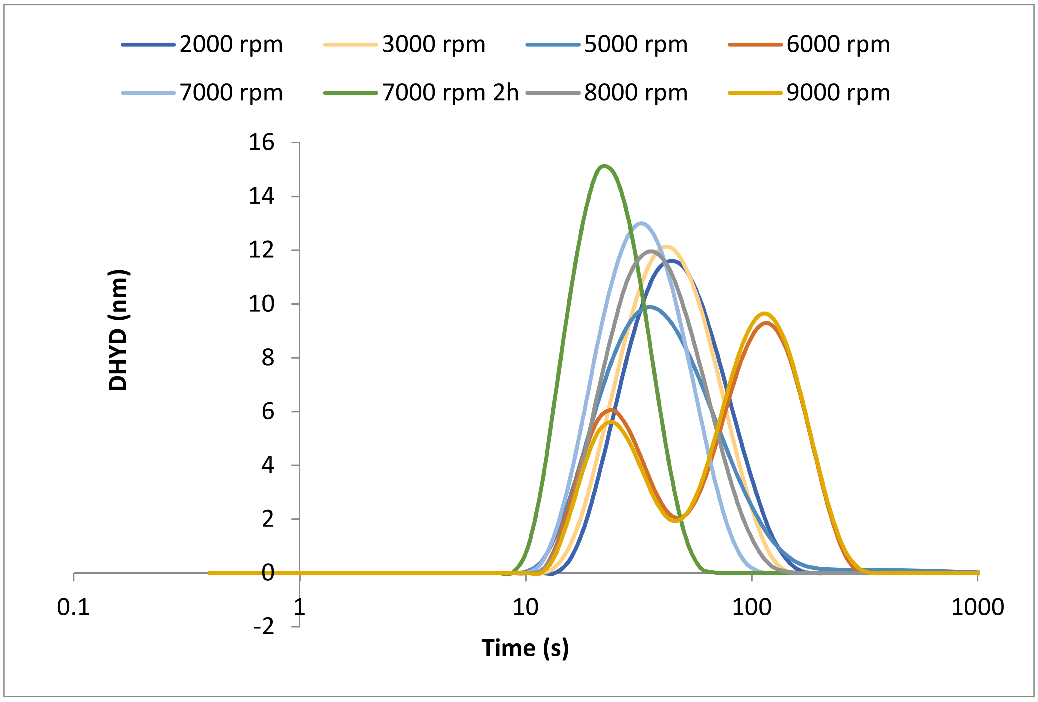

Figure 5-18: DLS intensity distributions of nanoparticles generated by SMM of BU-MAG. Dispersions were in heptane.

The DLS intensity data is shown in Fig 5-18. The distributions shift to lower size as rotor speed increases up to 7000 rpm, then shift to the right as the rotor speed is increased further. The bimodal distributions at 6000 (red) and 9000 (purple) rpm can be seen to overlap. The reasons for this phenomenon are not entirely clear, except that it may be energetically favoured. The correlation data was then normalised and plotted against time (Fig 5-17). Again, the profile shifts to lower size as the rotor speed increases towards 7000 rpm, then shifts to higher size at 8000 rpm and above. A tentative conclusion at this point is that comminution is taking place at the nanoscale, simultaneously reducing dhyd and PDI. The yield of dispersed particles was approximately 60% when milling at 7000 rpm. The yields at other speeds, apart from at 10000 rpm, were not determined. This warrants further work, as currently there is no established method of top-down size control with polydispersity.

5.3.3. Effect of the Liquid Medium on the Particle Size

To study potential viscous damping specific to the milling liquid, BU-MAG was milled in the presence of different solvents, to see if this had a significant effect on the hydrodynamic size. The DLS data are summarised in Table 5-2.

Table 5-2: Effect of viscosity on hydrodynamic size

Solvent	**dhyd (nm)**	**PDI**	**Viscosity @ 20 °C (cP)**
Ethanol	23.1	0.08	1.10
n-Propanol	26.0	0.16	2.26
Cumene	24.9	0.18	0.79
Heptane	22.4	0.12	0.41

The dhyd and PDI values indicate full dispersion and absence of larger aggregates. For all solvents apart from cumene, there appears to be an effect of the solvent viscosity on the hydrodynamic size (dhyd) of the generated NPs, which could be the result of viscoelastic damping. The NPs produced in ethanol have the same dhyd (within error) as the dhyd determined in the reproducibility experiments (Fig 5-11). The NPs generated in the presence of heptane and ethanol have similar dhyd and overlapping correlograms (Fig 5-19), despite the respective solvents having a viscosity difference of 0.69 cP. The same overlap of correlograms is observed for the NPs generated in n-Propanol and cumene, even though the difference in viscosities is greater in this case (1.47 cP). Knieke observed that a suspension of SnO_2 in ethanol had shear thinning behaviour between 10^0 and 10^3 [1/s], whilst the behaviour of ethylene glycol was very close to Newtonian over the same range [175]. Therefore, the viscosity value alone may not be enough to fully understand the effect of the solvent on the grinding result. In this respect, future work should include rheological analysis of the milling suspensions.

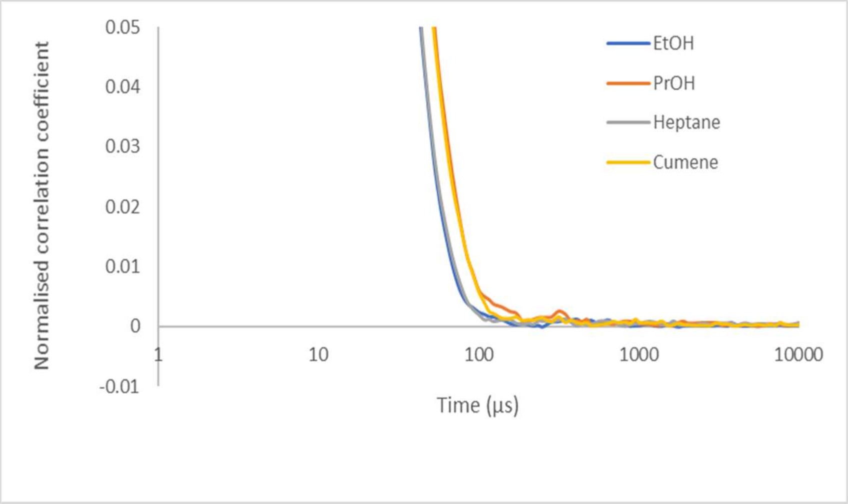

Figure 5-19: DLS correlogram of BU-MAG milled with oleic acid and dispersed in different milling liquids.

A second batch of maghemite, two separate batches of magnetite, and two separate batches of hematite, were obtained from the same supplier. Magnetite and hematite were also obtained from Sigma. In the case of magnetite, no particles were detected by DLS following milling. This may indicate that the bulk particles of magnetite are less easily comminuted due to the stronger magnetic interactions between crystallites, compared with maghemite. Either the specific energy is not sufficient to effect comminution, or comminution does take place and the fragments immediately reaggregate, on a timescale which is shorter than a newly formed surface being coated with a stabiliser. Correlograms from DLS measurements of the Cathay and Sigma samples are overlaid in Fig 5-20.

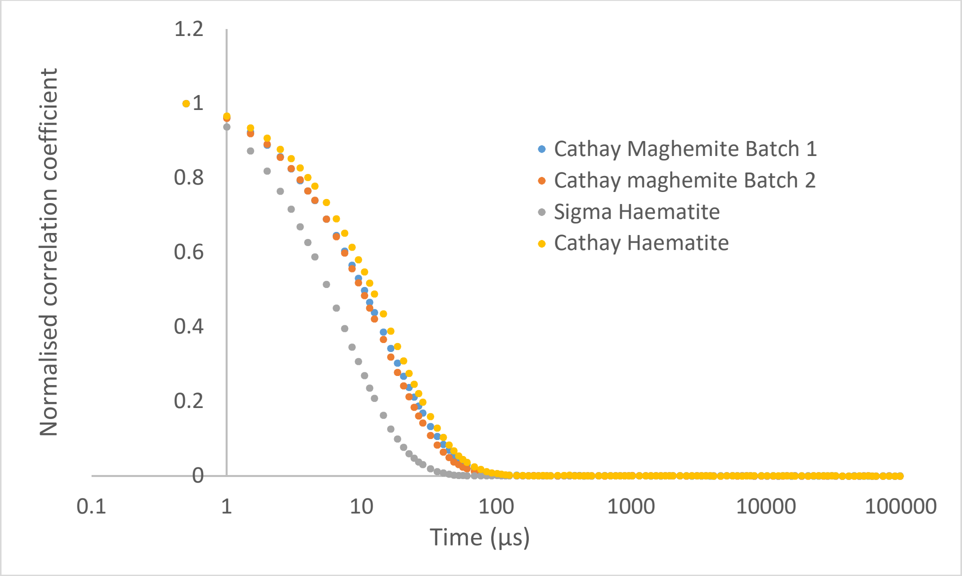

Figure 5-20: Comparison of correlograms for two batches of maghemite and hematite from Cathay Pigments; two batches of hematite from Sigma-Aldrich and Cathay Pigments, respectively. All samples for DLS were dispersed in heptane.

Table 5-3: DLS data for two batches of maghemite and hematite from Cathay Pigments; two batches of hematite from Sigma-Aldrich and Cathay Pigments, respectively. All samples milled in the presence of heptane and oleic acid.

Sample	**dhyd (nm)**	**PDI**
BU-MAG 1	23.2	0.10
BU-MAG 2	24.0	0.19
Sigma hematite	13.8	0.18
Cathay hematite	28.2	0.10

It can be seen from the values in Table 5-3 that both batches of BU-MAG have similar dhyd. The nanoparticles produced from the milling of Sigma and Cathay hematite give different dhyd 13.8 v 28.2 nm, respectively), which may indicate that the hematite provided by Sigma has a smaller initial particle size than the hematite from Cathay. Without more information it is difficult to be conclusive.

5.3.5. Effect of Stabiliser on Particle Size

To study the effect of the stabiliser on the particle size and morphology, BU-MAG was milled in the presence of oleic acid and PEA-3,4 in separate experiments. The amount of stabiliser for each experiment was calculated based on known footprints of carboxyl and catechol anchors, with respect to the surface area of a target nanoparticle size. PEA stands for polyetheramine, which is from the Jeffamine range of PEAs. The PEA used in this work was M-1000 ($M_n = 1000$). The amine was converted to the amide by DCC coupling to 3,4-Dihydroxybenzoic acid (3,4-DHBA). The catechol in this case binds strongly to the FeO surface (see Chapter 3 for a full description).

Table 5-4: Stirred media milling (SMM) of BU-MAG. The effect of stabiliser on nanoparticle size, for a given specific energy.

Sample ID	**dhyd (nm)**	**PDI**
Oleic acid/1500 rpm	23.2	0.10
Oleic acid/7000 rpm	21.5	0.12
PEA-3,4/1500 rpm	32.5	0.20
PEA-3,4/7000 rpm	36.3	0.18

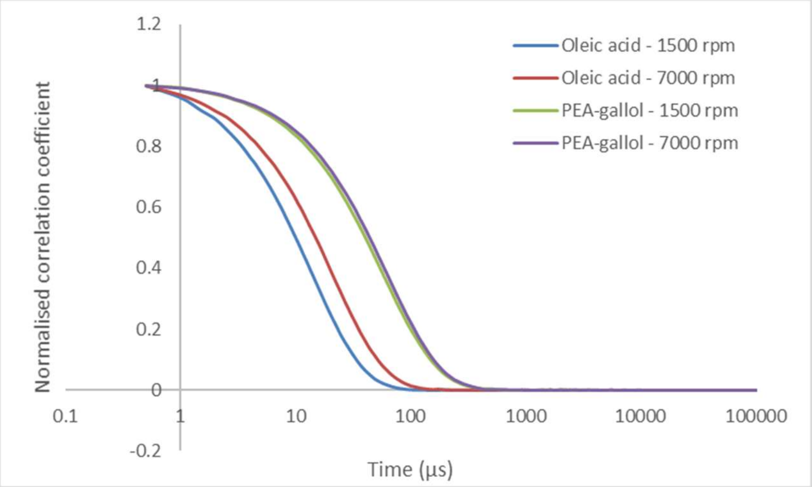

Figure 5-21: The effect of the stabiliser on the dhyd. Nanoparticles were generated from bulk iron oxide powders in chloroform, either in the presence of oleic acid or PEA-3,4 ("PEA-gallol"). Chloroform dispersions were analysed by DLS.

In the presence of oleic acid, nanoparticles were generated at 1500 rpm using a laboratory stirring plate. These particles had a slightly larger dhyd, compared with those generated on the Picoline mill at 7000 rpm This indicates that the specific energy applied to the material in the stirring plate experiment is less than the specific energy applied to the material in the Picoline mill. The particles generated in the presence of PEA-3,4 appear to have almost identical correlograms (Fig 5-21), but slightly different dhyd. There is a significant difference in size when comparing particles generated in the presence of either oleic acid or PEA-3,4. It can be hypothesized that the bulkier PEA-3,4 attenuates some of the specific energy and/or stabilizes the nanoparticles against further comminution. This suggests that the particle size is influenced by the molecular structure of the stabiliser, and is a useful route toward different size nanoparticles with different magnetic properties.

5.3.6. Effect of Milling Conditions on the Magnetic Properties

Based on the work of Berkowitz and Schuele, Lu et al produced a graph plotting the ratio of the size-related saturation magnetization and bulk magnetization values against the core diameter (Fig 5-25) [177]. Dividing the size-related magnetization (Ms(D)) of NANO-MAG-1 by the bulk magnetization (Ms0) of BU-MAG, a value of 0.23 was obtained. This value falls on Lu's graph, suggesting a surface layer of approximately 0.83 nm. The implication is that the drop in M_s is primarily due to particle size reduction, as opposed to changes in the crystallinity of the core. Further experiments are required to understand more fully the effect of SMM on the saturation magnetization of iron oxides. NANO-MAG-1 was exposed to DC field magnetometry, to compare the saturation magnetization to that of the bulk material.

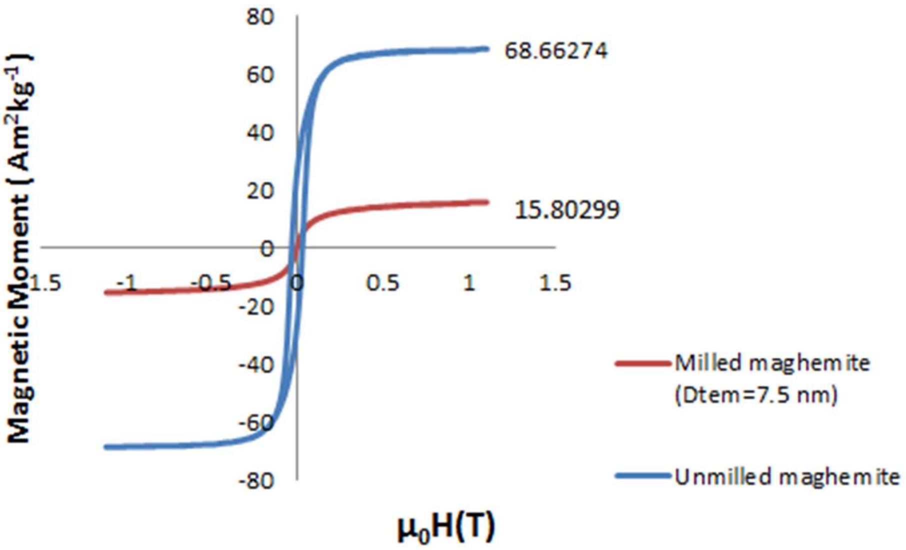

Figure 5-22: DC magnetometry analysis of milled and unmilled BU-MAG, showing strong reduction in saturation magnetization on milling.

From the data in Fig 5-22, it was hypothesized that the decrease in saturation magnetization (M_s) post-milling was due to a reduction in the crystallinity of the nanomaterial. The XRD data of the nanomaterial (Fig 5-15) shows characteristic peak broadening with reduction in particle size. In bulk maghemite, the non-crystalline surface layer is negligible, but as the particle size decreases the surface layer becomes more significant. It is also possible that the milling process itself could lead to amorphisation of crystallites. Amorphisation due to milling is generally due to the specific energy input being too great for a specific material. Samples milled at different rotor speeds, *i.e.* specific energies were compared, to see if this significantly affected the M_s value.

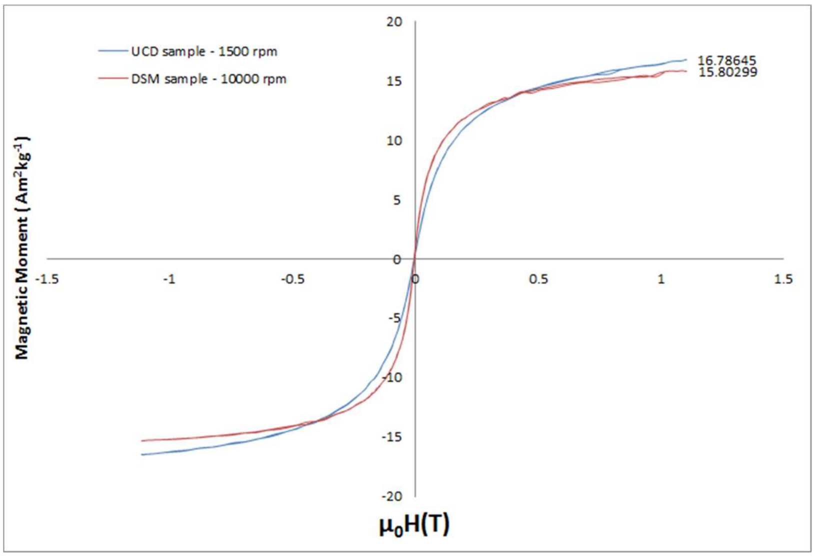

Figure 5-23: Saturation magnetization of nanomaterials generated at different specific energies. Comparing the speeds (1500 v 10000 rpm), the increase in Ms is not significant (1 emu/g).

Fig 5-23 compares the M_s of materials generated at two different specific energies. The difference in M_s is minor. Berkowitz and colleagues published a paper in the 1960s which describes the sharp drop in M_s as nanoparticle size decreases (Fig 5-24) [177].

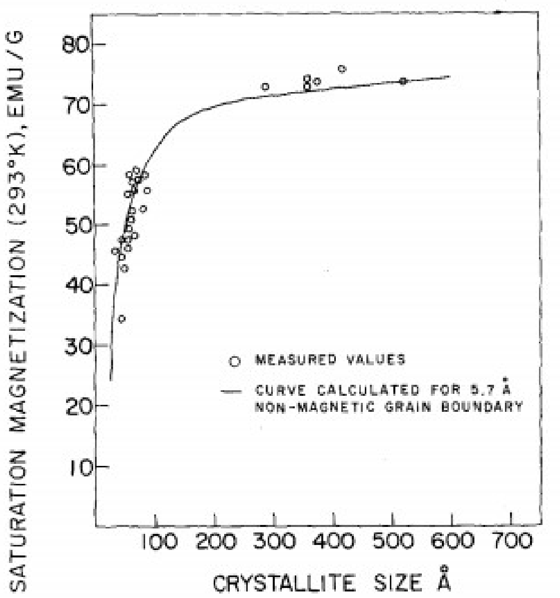

Figure 5-24: Evolution of the saturation magnetization as particle size decreases, described by Berkowitz *et al* [177].

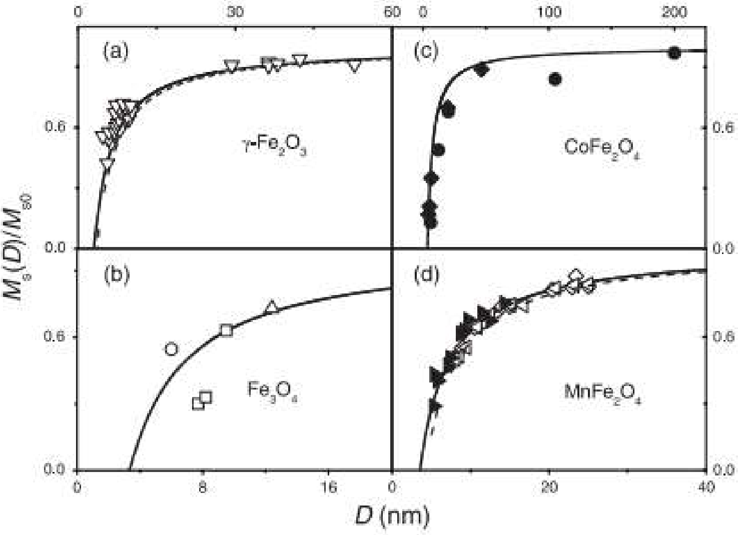

Figure 5-25: Evolution of the saturation magnetization as particle size decreases, as described by Lu et al [180]. The diagram top-left (a) shows the effect of size reduction on the M_s of maghemite.

5.4. Conclusions

This chapter describes a technique for the top-down generation of superparamagnetic iron oxide nanoparticles using stirred media milling, which is primarily used in the size reduction of hydrophobic pharmaceuticals as a means to enhance bioavailability. Knieke and colleagues have authored several papers describing the grinding limit of oxides, as prepared by stirred media milling. We proposed to apply this technique to the size reduction of iron oxide, i.e. maghemite, and generate colloidally stable dispersions of iron oxide nanoparticles. Starting with micron-scale powders obtained from a supplier of iron oxide-based pigments, it has been shown that the isolated NPs were less than 10 nm in size, polydispersity index (PDI) typically 0.05 – 0.1, and the NPs (as measured by transmission electron microscopy (TEM) and dynamic light scattering (DLS)) can be considered monodisperse. The nature of the technique, stirred media milling, may offer a means to generate NPs with heating properties that are superior to those generated using bottom-up approaches. It was found that the saturation magnetization dropped considerably during size reduction, which has been ascribed to the non-magnetic surface layer becoming more significant as size decreases. This could also be a reduction in the intrinsic crystallinity, or a combination of both of these factors. These nanoparticles were then used to prepare polymer nanocomposites, as described in Chapter 6.

Chapter 6 - Digital light processing of nanoparticle-doped elastomeric networks

6.1. Introduction

The thermoresponsiveness of iron oxide nanoparticle (NP)-doped poly(*N*-Isopropylacrylamide-*co*-acrylamide) (PNIPAAm-co-AAm) hydrogels in AC magnetic fields was described in Chapter 4. The magnetothermally-mediated deformations of these networks above the physiological temperature range make them potentially useful as devices for controlled release in drug delivery applications [181]. However, a major limitation associated with hydrogels, including those based on acrylamide, is the poor mechanical properties in the swollen state [182]. Synthetic elastomeric networks such as those based on oligomeric poly(trimethylene carbonate) (PTMC) have received a lot of interest due to their biocompatibility, biodegradability, and resorptivity, as well as their good mechanical properties [183]. Trimethylene carbonate is a 6-membered carbonate ester which can undergo ring-opening polymerisation to form the polymer PTMC (see Fig 6-6). The elastomer (elastic polymer) is amorphous and has a glass transition between -20 and -15 °C [184].

In contrast to the PNIPAAm-co-AAm hydrogels, PTMC-based networks are hydrophobic and do not swell in water [185]. They are thermally unresponsive within the physiological temperature range but undergo surface erosion through enzymatic degradation. The degradation rate can be tuned through control of polymer chain molecular weight, hence the utility of PTMC-based networks as drug delivery agents [186]. In designing this project it was hypothesised that the enzymatic degradation of PTMC networks, e.g. by lipase, could be influenced magnetothermally, by increasing the local temperature at the surface of a PTMC-based construct. Enzymatic activity of lipase reaches a maximum at around 40 °C, and this has been shown to increase to 45 °C on immobilising the lipase on a polyaniline–silver functionalized graphene oxide nanocomposite [187]. The same immobilised lipase retains activity at high temperatures when compared to free, non-immobilised enzyme (84% of its activity recovery as compared to 49% at 60 °C). The fabrication technique used to generate the PNIPAAm-co-AAm magnetic hydrogels was an *in situ* free-radical thermal polymerisation, in which iron oxide nanoparticles (NPs) dispersed in a pre-polymer solution were polymerised using the APS/TEMED redox system [188].

3D printing is an approach which can be used to fabricate polymer-based nanocomposites possessing spatially defined properties such as magnetisation and conductivity [189]. 3D printing is one of many types of additive manufacturing process first described by Hull in 1986 [190]. The original patent detailed programmable laser writing, i.e. classical stereolithography. Since then the technique has evolved to the use of digital mirror devices (DMDs), arrays of up to several million mirrors which can work independently in an on/off state, projecting a 2D pixel pattern onto a photocurable resin. This particular printing approach is known as digital light processing (DLP) [191]. A typical process flow for DLP of photocurable polymers is shown in Fig 6-1. Image slices are projected onto the polymer resin and as each layer polymerises, the platform moves up along the Z axis by a distance approximate to the chosen layer thickness, forming the designed build when the total number of layers have been printed [192]. Chemical, mechanical, and biological properties can be tuned according to the type and molecular weight of macromers and crosslinkers used. The use of nanoparticles can also influence the mechanical strength of a material[193]. Finally, the orientation in which an object is printed (flat, side-on, or end-on) can also influence the object's mechanical properties.

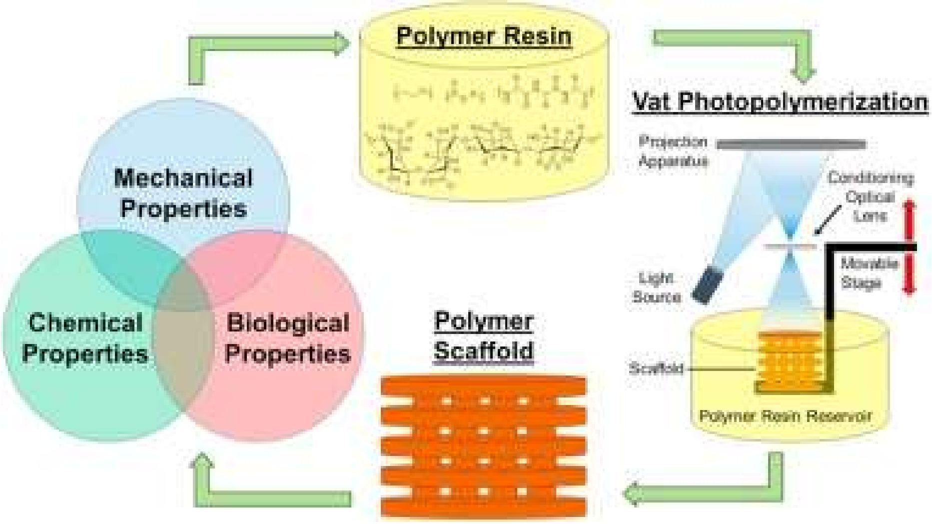

Figure 6-1: Process flow diagram of digital light processing (DLP) [192].

The thickness of a solidified layer (cure depth, C_d, in μm) is a function of the light irradiation dose E (mJ/cm^2) used in curing. A plot of the cure depth versus the irradiation dose is termed the working curve [194], and can be described by the equation,

$$C_d = D_p \ln(E/E_c)$$

Equation 6-1

In DLP, photocuring is characterised by the critical light irradiation dose, E_c (mJ/dm^2) and the penetration depth, D_p (µm), by convention along the Z axis. E_c is the minimum energy required for the formulation to reach the gel-point and start forming a solid layer. Equation 6-1 is a form of the Beer-Lambert law, which describes the decay of the intensity of light as it passes through a medium which shows some absorption. Resolution in the Z direction is especially important in DLP; the build forms through photocrosslinking of successive layers. Good interlayer bonding requires a significant overcure, e.g. a 50 µm layer would require an overcure of between 70 and 100 µm. This "stitching" prevents delamination of the layers. To exercise greater control over the curing process, inorganic and/or organic light absorbers can be used in the DLP resin as a means to control resolution in the Z direction.

This work sought to generate colloidally-stable suspensions of NPs, starting with high purity commercial biocompatible maghemite powder, as described in Chapter 5. According to the product leaflet, "*high purity material conforms the requirements of EC food legislation (EC-Directive 95/45/EEC). Apart from the requirements in EC directive, this product also fulfils the purity requirements of FDA regulations (title 21 section 73), which permitted as additives for foods, pharmaceuticals, drugs and cosmetics.*" A further advantage of using pharmaceutical grade iron oxide is that it can be milled down to nanosized particles which can then be used directly in the formulations. It was hypothesised that colloidally stable iron oxides with more isotropic scattering of light would result in more homogenous curing, compared with polydisperse iron oxides. The unmilled powder is the magnetic component in magnetic data recording, in the form of ferromagnetic acicular crystallites, whose ferromagnetic nature results in the formation of aggregates, which have been observed by SEM (see Chapter 5, Fig 5-2). An important requirement for this project was that the dye is biocompatible and hence the original rationale for doping with iron oxide. Iron oxide is commonly used as a light absorber in paints, i.e. a pigment, and hence is a good attenuator. Control of curing in the Z direction is achieved by using a "dye-initiator package", i.e. a dye and a photoinitiator.

Photoinitiators (PIs) are molecules which can generate radicals in the presence of light of specific wavelengths (Fig 6-2). PIs can be used in various polymerisations, most notably in free radical and cationic processes which have significant impact in the production of medical materials, coatings, etc [195]. The peak absorbance of the dye should not be greater than that of the initiator, otherwise there would be insufficient energy available for the initiator to form radicals [196].

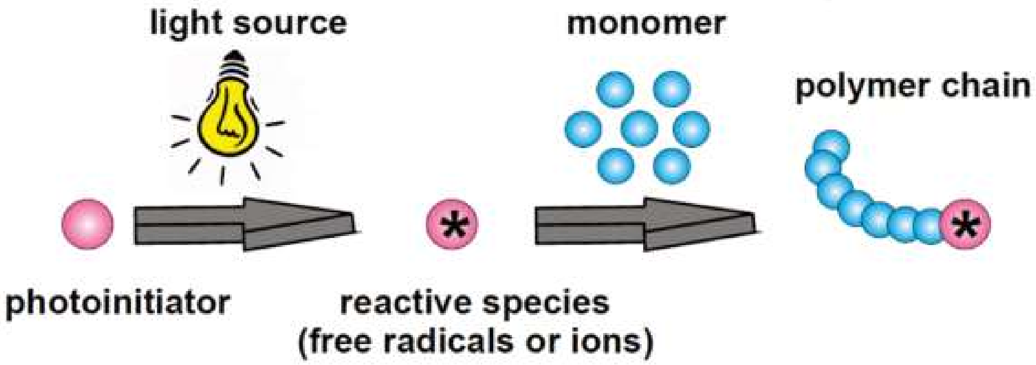

Figure 6-2: General scheme of photoinitiated polymerisation. Reproduced from [195].

PIs are classed as either Type I or Type II, depending on the mechanism of radical generation. Upon irradiation with light energy Type I PIs undergo unimolecular bond cleavage to yield free radicals, whilst Type II PIs undergo a bimolecular reaction, where the excited state of the photoinitiator interacts with a second molecule (a co-initiator) to generate free radicals [197]. (2,4,6-Trimethylbenzoyl)diphenylphosphine oxide, marketed as Irgacure 819, is the PI used in this work. It is an acylphosphine oxide that undergoes homolytic cleavage at the carbonyl-phosphorous bond, and is therefore a Type I PI. The radicals shown in Fig 6-3 can attack the vinyl double bonds of macromers, resulting in polymerisation and crosslinking.

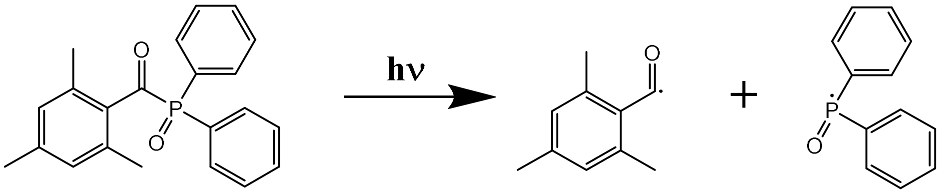

Figure 6-3: Chemical structure of (2,4,6-Trimethylbenzoyl)diphenylphosphine oxide (Irgacure 819) and its radicals following light irradiation.

The synthesis of PTMC macromer is described in sections 6.2 and 6.3, in summary, upon reaction with 2-Isocyanatoethyl methacrylate (2-Iso), a PTMC urethane macromer with pendant methacrylate groups is formed. A general scheme for the reaction of 2-Iso with a diol is shown in Fig 6-4.

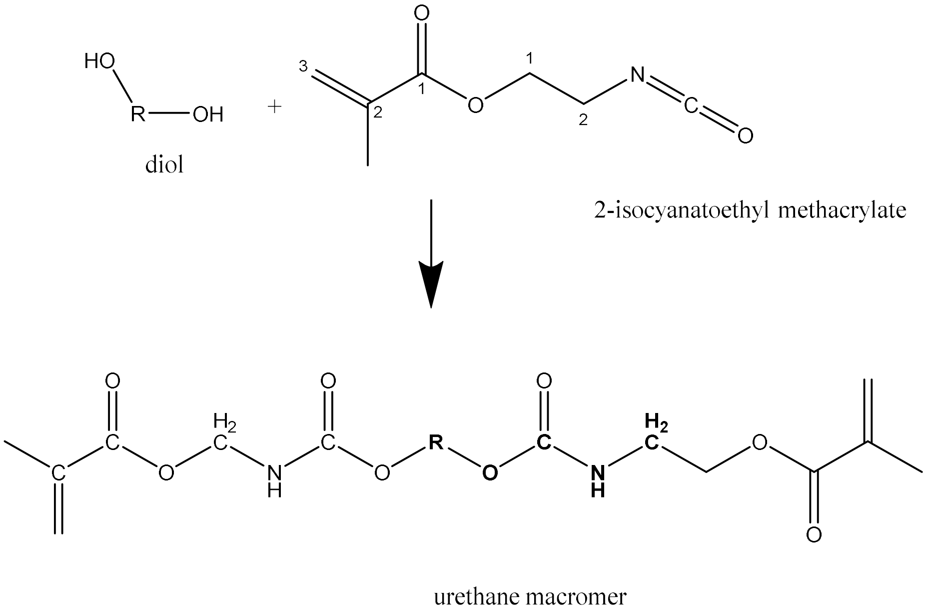

Figure 6-4: General scheme for the reaction of a diol with 2-Isocyanatoethyl methacrylate (2-Iso) to form a urethane.

With respect to the photochemistry taking place during DLP, an advantage of forming urethane macromers is that these can pre-organise through hydrogen bonding, which has been shown to enhance the rate of polymerisation [198]. In order to prevent spontaneous crosslinking of PTMC macromers, inhibitors such as 2-Methoxyphenol work as radical scavengers (Fig 6-5). The primary radicals react with O_2 to form peroxide radicals ($RO_2^{\cdot}$), which are then scavenged by MeHQ.

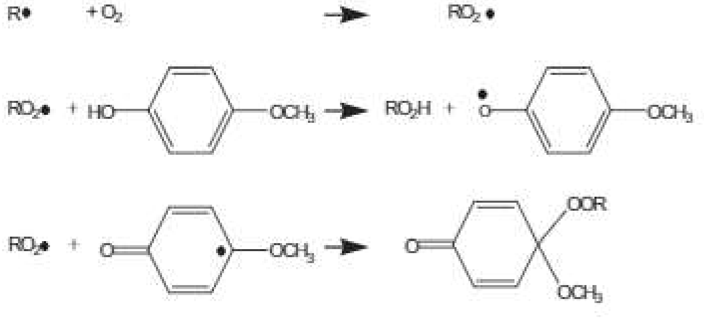

Figure 6-5: Radical scavenging by 4-Methoxyphenol. Reproduced from [199].

The major goals of this work were to:

1. Synthesise and characterise PTMC oligomers from TMC monomer. The choice of PTMC as the polymer is due to its biodegradability and biocompatible breakdown products *in vivo*.
2. Generate photocrosslinked PTMC networks using DLP. The reason for using DLP is that it can generate constructs with high fidelity, as well as being faster (compared with SLA).
3. Study the effect of formulation components (crosslinker, dye, etc) on the photopolymerisation. This is important as it determines the mechanical properties of the final construct.
4. Study DLP fidelity when using PTMC macromers. Fidelity of the final construct should be relevant to the design in the .stil file.
5. Study effect of build orientation on the mechanical properties of the final PTMC constructs. The direction of the build determines the number of layers to be printed, which may affect the mechanical properties of the construct.

A secondary aim of this work was to formulate nanocomposites which respond to an AC magnetic field. Unfortunately, due to low light power output of the lamp in the Rapidshape S60, the more interesting question of magnetothermally-influenced enzymatic degradation could not be addressed sufficiently. However, future work is proposed in section 6.4.

6.2. Experimental

6.2.1. Materials and Methods

Trimethylene carbonate was obtained from WuXi AppTec, China. Hexanediol, stannous octoate, Deuterated chloroform ($CDCl_3$), 2-Isocyanatoethyl methacrylate and 4-Methoxyphenol were obtained from Sigma-Aldrich.

Triethylene glycol dimethacrylate, anisole, ethanol, propylene carbonate, and oleic acid were purchased from Sigma-Aldrich and used without further purification. Irgacure 819 was obtained from Ciba Speciality Chemicals, Switzerland.

NPs were obtained *in situ* by stirred media milling (see Chapter 5 for full procedure). Briefly, an ethanolic slurry of iron oxide bulk powder was milled in the presence of 100 µm yttria-stabilised zirconia milling beads and excess PEA-3,4 stabiliser[11]. The generated NP suspensions were formulated with PTMC macromer for DLP experiments.

^{1}H-NMR of synthesised materials was performed on a Bruker 400 MHz instrument. Typically 10 mg of sample was dissolved in 0.7 mL $CDCl_3$. For end-group analysis, approximately 80 mg of sample was used so that the signals representing the end groups were quantifiable. Determination of molecular weights was by gel permeation chromatography (GPC). The GPC setup consisted of a Waters 2414 Refractive Index Detector (RID), Waters 2487 Dual λ Absorbance Detector and a Waters 717 Plus Autosampler. Polystyrene standards ranging from 50 - 20000 g/mol were used. Samples were dissolved in THF at 4 wt% and filtered across a 0.45 µm PTFE membrane, prior to injection onto an Agilent PLgel MIXED-E GPC column. FTIR spectra were obtained with a Perkin Elmer Spectrum One.

6.2.2. Polymer Synthesis

Bifunctional oligomers were synthesised on a 60 g scale, by ring-opening polymerisation of trimethylene carbonate for 72 h at 130 °C, under a nitrogen atmosphere, with stannous octoate as the catalyst (Fig 6-6).

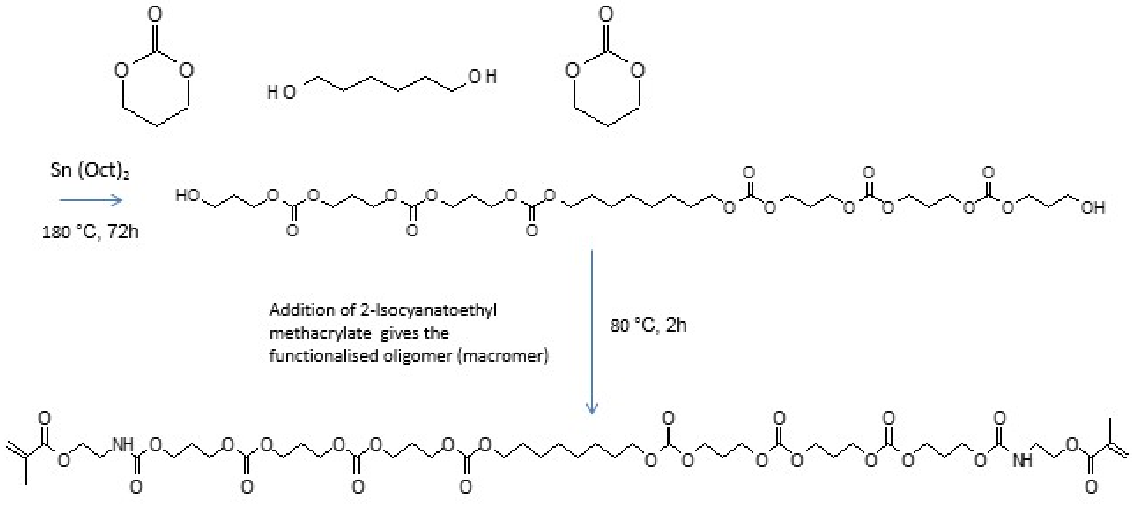

Addition of 2-Isocyanatoethyl methacrylate gives the functionalised oligomer (macromer)

Figure 6-6: Reaction scheme showing synthesis of PTMC-OH oligomers and PTMC-MAc macromers.

---

[11] “PEA-3,4” refers to a diblock copolymer (Jeffamine M1000, molar mass 1 kDa) linked with 3,4-Dihydroxybenzoic acid (via DCC coupling chemistry). See Chapter 2 for synthetic protocol.

Hexanediol was used as a chain extender to prepare the two-armed oligomer. The molecular weight arm length was controlled by adjusting the monomer to initiator ratio. ^{1}H-nuclear magnetic resonance spectroscopy (in $CDCl_3$, Bruker 400 MHz) was used to determine TMC conversion and oligomer molecular weights, by end group analysis.

PTMC oligomers were functionalised by reacting the terminal hydroxyl groups with 2-Isocyanatoethyl methacrylate in the bulk, forming the polyurethane. The reaction proceeded under a nitrogen atmosphere for 2 h at 80 °C. The reaction was then allowed to cool, followed by bubbling of air through the reaction mixture for 1 min. To minimise free isocyanate, the amount of 2-Iso used was calculated to be 99 mol% of the available OH groups in the oligomers. ^{1}H-NMR was used to determine the degrees of functionalisation of the macromers. ATR-FTIR (see Chapter 2 for description of technique) was used to confirm that all of the 2-Iso was used up during synthesis by monitoring the spectrum *c.* 2260 cm^{-1} where the NCO stretch is expected.

6.2.3. Formulations for DLP

To formulate liquid polymerisable PTMC-MAc formulations, the macromer was diluted in anisole and the solution then doped with varying amounts of NPs. Anisole is relatively non-toxic and therefore suitable as a non-reactive diluent for DLP formulations. All formulations used in the study are presented in Tables 6-1 and 6-2.

Table 6-1 shows the variation of NPs added to the DLP formulation. Table 6-2 shows the variation of triethyleneglycol dimethacrylate in a formulation containing 0.1 wt% FeO. Mixing of the formulations was achieved with a dual asymmetric centrifuge (DAC), which combines centrifugal forces to create zones of high shear, allowing homogenous mixing as well as degassing of samples. Viscosity measurements were performed at 25 °C using a Brookfield CAP 1000. The cone (Brookfield Cone 05) was rotated at 750 rpm. To prevent premature crosslinking, 0.2 wt% 4-Methoxyphenol was used as polymerisation inhibitor.

Table 6-1: Formulations used to study effect of FeO concentration on curing in DLP.

PTMC-MAc macromer (wt%)	**Total anisole (wt%)**	**γ-Fe_2O_3 nanomaterial (wt%) ***	**Irgacure 819 photoinitiator (wt%) ***	**4-Methoxyphenol inhibitor (wt%) ***
78.4	21	0	0.4	0.2
78.3	21	0.1	0.4	0.2
78.2	21	0.2	0.4	0.2
77.9	21	0.5	0.4	0.2
77.4	21	1.0	0.4	0.2

* Stock solution in anisole

Table 6-2: Formulations used to study effect of additional crosslinker on tensile properties of 3D printed samples.

PTMC-MAc macromer (wt%)	**Total anisole (wt%)**	**γ-Fe_2O_3 nanomaterial (wt%) ***	**TEGDMA crosslinker (wt%) ***	**Irgacure 819 photoinitiator (wt%) ***	**4-Methoxyphenol inhibitor (wt%) ***
78.3	21	0.1	0	0.4	0.2
74.3	21	0.1	4	0.4	0.2

* Stock solution in anisole

6.2.4. Network Characterisation

PTMC networks with varying build orientation, filler type, and filler loading were placed in a 50:50 mixture of propylene carbonate (PC) and ethanol (EtOH), to wash out unreacted components. The medium was changed once every 24 hours, over 3 days. Samples were then dried to constant weight in a vacuum oven prior to tensile testing.

A second set of PTMC networks with varying nano FeO loading were extracted as above, except that the ratio of ethanol to propylene carbonate was increased from 50:50 to 100:0 over 3 days, followed by oven drying. Gel contents were determined in triplicate from the mass of the dry network after extraction (m_{dry}) and the macromer mass initially present in the formulation (m_0). Mechanical properties were determined 3-fold in tensile tests using a Hounsfield universal testing machine.

6.2.5. Digital Light Processing

To fabricate PTMC networks by DLP, stock formulations comprising PTMC-MAc macromer, non-reactive diluent anisole, Irgacure 819 photoinitiator, and 4-Methoxyphenol inhibitor were formulated. NPs in anisole suspension were added to achieve 0.1, 0.2, 0.5, and 1 wt%, based on the iron concentration as determined by FAA. Tensile test specimens were designed on Netfabb computer software. The designs were built using a Rapidshape S60 DLP apparatus. The output wavelength and intensity were 405 nm and 6 W/m^2, respectively. Using a build platform step height of 50 µm, layers of formulation were sequentially photo-crosslinked by exposure to the projected light.

6.3. Results and Discussion

6.3.1. ^{1}H-NMR End-group Analysis of Oligomers and Macromers

PTMC oligomers were synthesised by the ring-opening polymerisation of trimethylene carbonate monomer (55 g scale), using hexanediol as initiator. Approximately 90 mg of PTMC oligomer was dissolved in $CDCl_3$ for ^{1}H-NMR analysis. The ratio of initiator to monomer was chosen so that the oligomeric chains had a number average molecular weight of approximately 1000 g/mol, equivalent to 8 repeat units of TMC, as confirmed by end group ^{1}H-NMR analysis. Whilst TMC is available as a white powder, the resulting oligomers were colourless and viscous, with a treacle-like consistency.

The -CH_2OH end group resonances were first identified by reacting PTMC-OH with trifluoroacetic anhydride (Fig 6-7), forming trifluoroacetate ester.

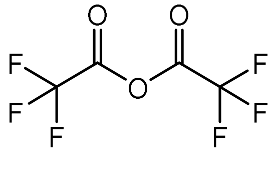

Figure 6-7: Chemical structure of trifluoroacetic anhydride

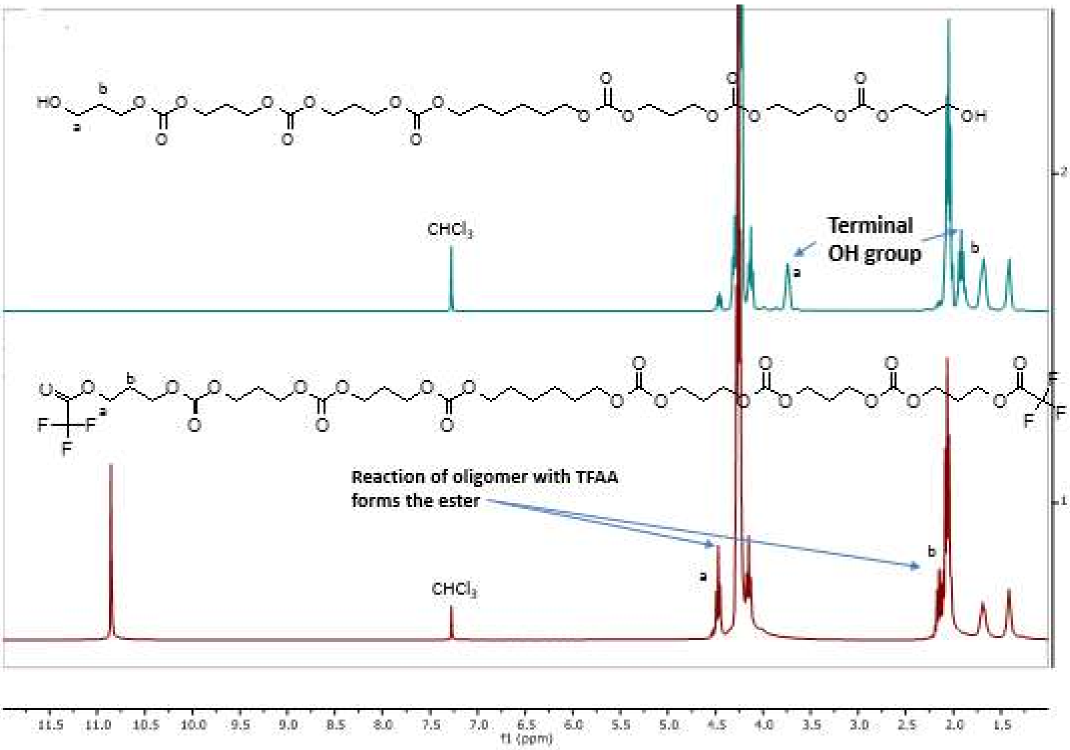

Figure 6-8: Comparison of ^{1}H-NMR spectra for PTMC-OH (top) and PTMC trifluoroacetate ester (bottom).

The ^{1}H-NMR spectra for the PTMC-OH oligomer (top, blue) and PTMC trifluoroacetate ester (bottom, red) are shown in Fig 6-8. Upon addition of TFAA, the resonances at 1.85 and 3.75 ppm, corresponding to the two methylene groups closest to the terminal OH, are shifted downfield to 2.25 and 4.50 ppm, respectively. A signal which can be assigned to free TFA appears at approximately 10.8 ppm, confirming reaction of TFAA with the alcohol. This is a useful means to identify the -OH end group and also to determine the degree of functionalisation when the end group has reacted. After identification of the original end-group chemical shift, the integrated area can be compared to that of the new end-group, and the ratio of the integrals used to determine functionalisation. After locating the methylene group adjacent to the terminal OH, the PTMC-MAc macromer was analysed by ^{1}H-NMR. The degree of functionalisation of the bifunctional macromers was determined from the peak areas corresponding to the $–CH_2OH$ end group resonances (3.75 ppm) in the oligomer, and the $–CH_2$-N- end group resonances (3.5 ppm) in the macromer. A high degree of functionalisation was inferred from the absence of a signal corresponding to the $–CH_2OH$ end groups. The appearance of methacrylate resonances (*c.* 5.65 and 6.20 ppm) were further confirmation of functionalisation.

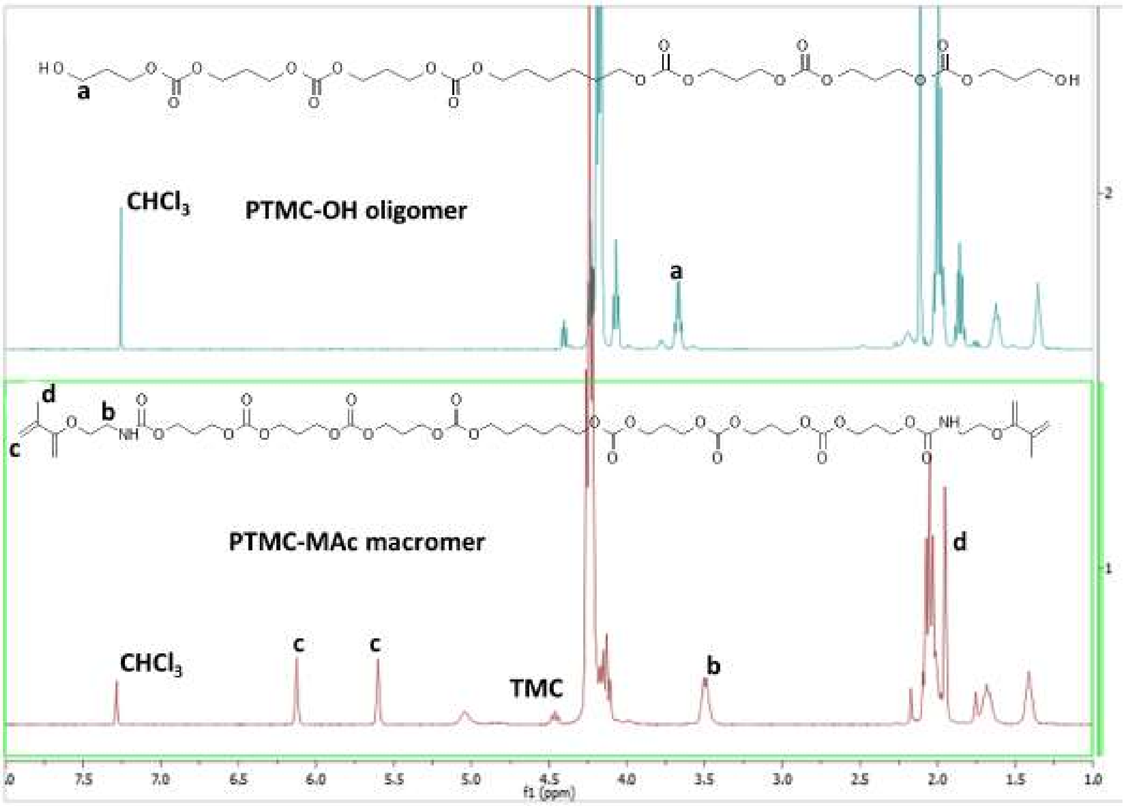

Figure 6-9: ^{1}H-NMR spectrum of PTMC-OH oligomer (top) and PTMC-MAc macromer (bottom). The chemical structures show 3 repeat units either side of the alkyl chain.

The monomer conversions and the arm lengths of the synthesised PTMC oligomers were derived from ^{1}H-NMR spectra (Fig 6-9). The TMC conversion of 98% was determined from the ratio of the peak areas corresponding to the monomer $–CH_2$-O- resonances (4.45 ppm) and the oligomer $–CH_2$-O- resonances (4.25 ppm). The degree of polymerisation (DP) was determined from the ratio of the peak areas corresponding to the $–CH_2OH$ end group resonances (3.75 ppm) and the $–CH_2$-O- resonances (4.25 ppm) in the repeat unit, giving a value of DP ~ 8. Using this value, the number-average molecular weight (M_n) was determined to be 1170 g/mol.

Functionalisation of the oligomers was carried out by addition of 2-Iso. The isocyanate reacts exothermically with the alcohol to form a urethane, and the resulting functionalised oligomer (macromer) can be classed as a poly(carbonate-urethane) methacrylate. This is the preferred route of methacrylation as, although methacryloyl chloride is a significantly cheaper alternative which forms poly(carbonate-ester), the reaction of the chloride with a polyol yields hydrogen chloride which must be scavenged with excess triethylamine. The resulting polymer requires purification to remove excess triethylamine and its hydrochloride salt. Hence the interest in using the isocyanate, which yields no side products when forming the urethane.

Isocyanates can react with water, forming an amine and carbon dioxide, hence the requirement that the synthesis of the oligomer and addition of the isocyanate are done in anhydrous conditions. No carbon dioxide bubbles were observed during or after the synthesis, indicating the absence of water. The number of moles of 2-Iso in the reaction was 99% of OH groups on the PTMC oligomers. This is to ensure that there is no residual 2-Iso post-synthesis.

6.3.2. FTIR-ATR Analysis

After functionalisation, the macromer was analysed by FTIR-ATR. The FTIR-ATR transmittance spectrum of PTMC-MAc is shown in Fig 6-10. The carbonyl stretch corresponding to the carbonate can be seen at 1739 cm^{-1}. The alkyl chain C-H stretch is at 2950 cm^{-1}. No feature corresponding to the NCO stretch, which is expected at 2260 cm^{-1}, was observed, suggesting that there was no residual 2-Iso present in the macromer product.

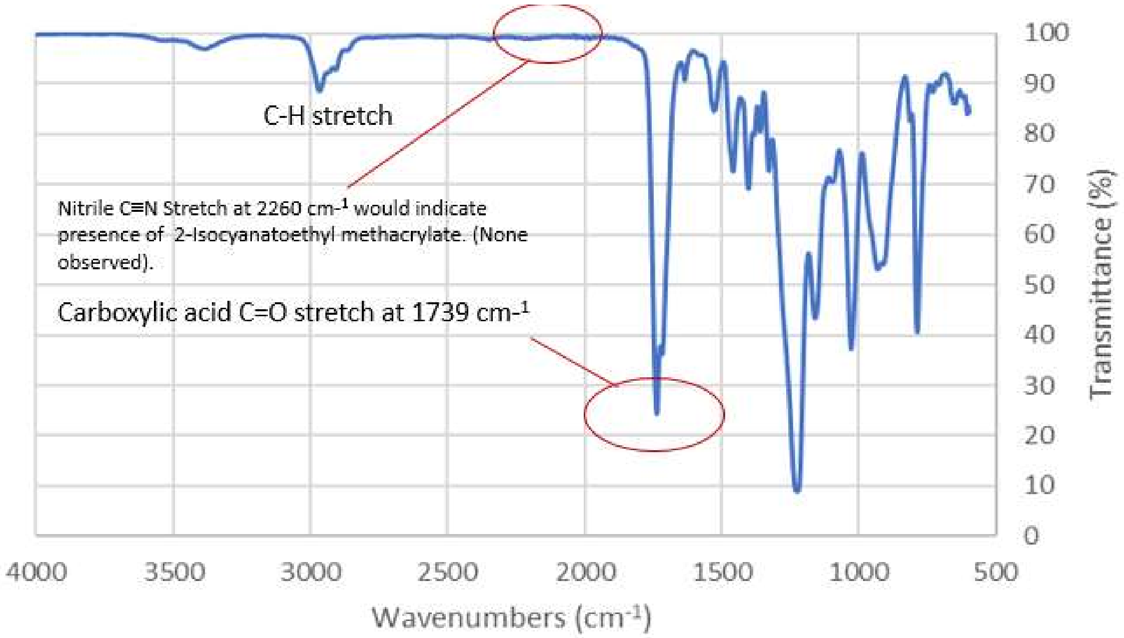

Figure 6-10: FTIR-ATR spectrum of PTMC-MAc, showing the absence of a nitrile stretch at 2260 cm^{-1}, indicating that all 2-Isocyanatoethyl methacrylate reacted.

6.3.3. GPC Analysis

The GPC chromatograms for both oligomer and macromer are overlaid in Fig 6-11, plotted as the normalised (by weight) refractive index response as a function of time. The modal peaks of the oligomer had similar elution times (approximately 15 minutes). Smaller oligomeric/macromeric chains are observed at later times.

Using polystyrene universal calibration standards, the M_n, M_w, and Đ values for oligomers and macromers were estimated (Table 6-3). The M_n increases after functionalisation of the oligomer with 2-Isocyanatoethyl methacrylate, increasing from 1424 to 1609 g/mol. M_w also increased, from 2671 to 3208 g/mol. The dispersity, Đ, was calculated using M_w/M_n, and found to be relatively unchanged following conversion of oligomer to macromer; increasing from 1.88 to 1.99.

Table 6-3: Characterisation of PTMC-OH and PTMC-MAc by size exclusion chromatography.

Sample ID	**RT (min)**	**M_n**	**M_w**	**Đ**
PTMC-OH	13.917	1424	2671	1.88
PTMC-MAc	14.353	1609	3208	1.99

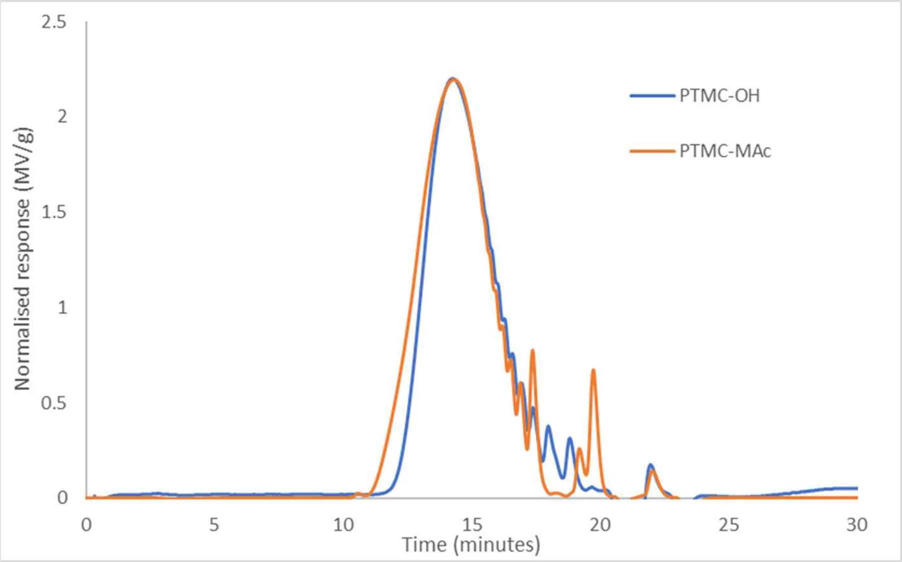

Figure 6-11: Overlay of GPC chromatograms comparing the PTMC-OH oligomer and PTMC-MAc macromer eluted in THF. The data from the refractive index detector is normalised according to the sample mass. The normalised signals are plotted against time.

The M_n of the oligomer appears to be affected by the initial amount of monomer. A small-scale synthesis (5 g TMC) yielded oligomers composed of 9.0 units of TMC and M_n = 1243, whilst a 20 g synthesis yielded oligomers composed of 8.2 units of TMC and M_n = 1162. The lower M_n of the batches synthesised using 20 and 55 g TMC (1162 and 1170 g/mol, respectively) indicate that the nature of the polymerisation, i.e. bulk polymerisation, can result in a lower DP. This may be due to the decreased mobility of chains and monomers as the viscosity of the reaction mixture increases, preventing free monomers adding onto existing chains, resulting in increasingly smaller chains. The MP (molecular weight of the highest peak) values corresponding to each peak observed for PTMC-OH in Fig 6-11 are plotted against retention time, showing that the retention time of a molecule in the poly(styrene-co-divinylbenzene) [200] network increases exponentially with decreasing molecular weight (Fig 6-12).

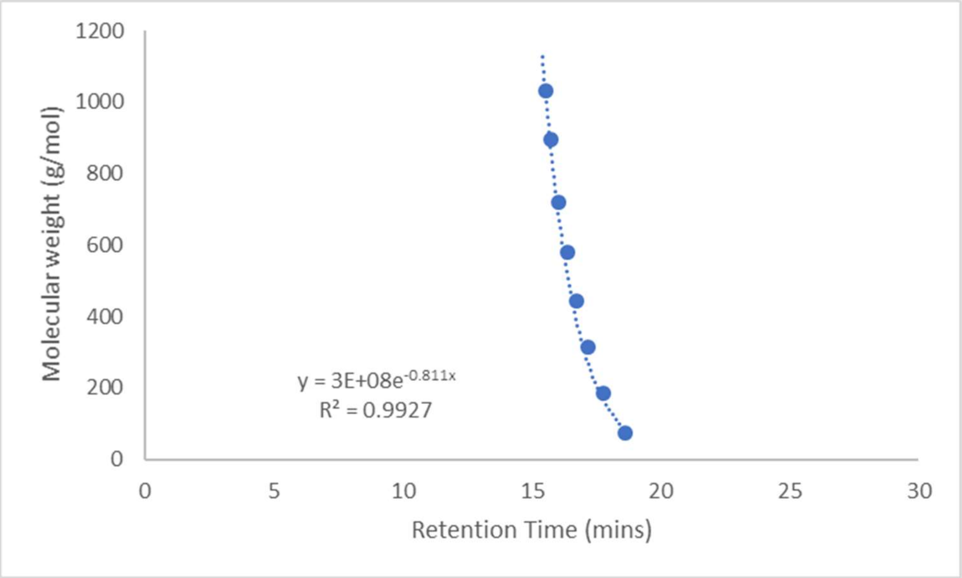

Figure 6-12: Relationship between molecular weight and retention, under GPC analysis, of oligomeric species.

Conversely, the higher M_n of the small-scale synthesis could be due to the smaller initial mass of monomer combined with the smaller reaction flask (50 mL). This would result in a greater proportion of the reaction mixture being in direct contact with the oil bath, which might decrease the overall viscosity of the system and lead to increased monomer and chain mobility. Polymers are typically purified by precipitation in cold solvents (e.g. ethanol, propanol, hexane, etc) [186]. This works well for mid- to high-molecular weight polymers, but low molecular weights are more difficult to purify by this method due to polymer not precipitating out, resulting in significant losses. Therefore, the bulk method was chosen for the synthesis of the low MW PTMC oligomers.

Functionalisation of the oligomers with 2-Isocyanatoethylmethacrylate is expected to increase the molecular weight by 300 g/mol. Taking the M_n values in Table 6-3, the calculated increase was 185 g/mol. GPC cannot be used to compare polymers of different chemical composition. Functionalisation such as that with 2-Isocyanatoethyl methacrylate can lead to significant differences in apparent molecular weight, depending on the solvent [200]. However, the peak shape and retention times of the oligomer and macromer are similar, albeit there is a slight decrease in the retention time of the macromer. The shorter polymer chains in both cases appear as shoulders off the main peak, showing that they have a longer retention time in the column. In this case the shorter chains remained in the macromer formulation and the polydispersity was still relatively low (1.37).

The viscosity of the macromer formulation is a critical parameter for DLP. At 21% anisole for a 10 g sample, the viscosity was 1.8 Pa.s. Based on a typical range of 1 – 2 Pa.s, this viscosity was deemed appropriate for the DLP fabrication. Addition of FeO up to 0.5 wt% had no significant effect on viscosity at the same shear rate.

6.3.4. Generation of Iron Oxide Nanoparticles

The DLS correlograms of NPs generated in the presence of PEA-3,4 (dispersed in anisole) and oleic acid (dispersed in heptane), respectively, are shown in Fig 6-13. The dhyd of the NP-PEA-3,4 was 36 ± 0.64 nm, and the PDI was 0.18.

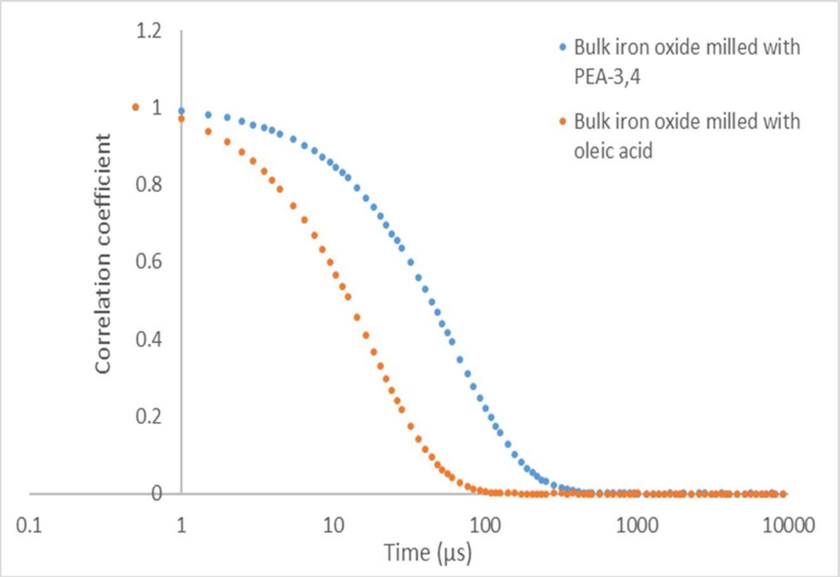

Figure 6-13: Normalised correlation coefficient for an anisole dispersion of NPs, stabilised by a catechol-functionalised polyetheramine, PEA-3,4. The nanoparticles were generated during a bead milling comminution process. The dhyd of the NP-PEA-3,4 was 36 ± 0.64 nm, and the PDI was 0.18. The correlation coefficient for nanoparticles stabilised by oleic acid in heptane is included for comparison.

The novel stabilising ligand based on a catechol (synthesis of the ligand can be found in Chapter 3, Section 3.3.4, pp 20-21) was employed *in situ*, stabilising the nanomaterial as it forms from comminution of the bulk FeO powder. The resulting nanomaterial, NP-PEA-3,4, freely dispersed in anisole. As shown in Fig 6-13, the nanoparticles produced in the presence of the polymeric ligand have longer diffusion correlation times, and hence larger dhyd (approximately 36 nm), as compared with those particles generated in the presence of oleic acid (approximately 22 nm). It can also be observed that there is no aggregation in either sample (no features observed at longer times), showing the utility of the bead milling technique for *in situ* nanoparticle generation and stabilisation.

6.3.5. Formulation Studies

Both PTMC-OH oligomer and PTMC-MAc macromer were mixed with various amounts of anisole (non-reactive diluent), and the viscosity of these mixtures was determined in triplicate using cone and plate viscometry (Brookfield CAP 1000). The viscosity was determined at 17, 21, and 25 wt% anisole. Results for oligomer and macromer are shown in Fig 6-14. The viscosity was determined at 25 °C, under a constant shear rate of 50 s^{-1}. The data are summarised in Table 6-4.

Table 6-4: Mean viscosities of oligomer and macromer as function of anisole wt%.

Sample ID	**Anisole (wt%)**	**Mean viscosity (Pa.s)**	**Standard deviation (Pa.s)**
PTMC-OH_A17	17	0.89	0.02
PTMC-OH_A21	21	0.55	0.08
PTMC-OH_A25	25	0.21	0.01
PTMC-MAc_A17	17	2.35	0.01
PTMC-MAc_A17	21	1.83	0.01
PTMC-MAc_A17	25	0.84	0.01

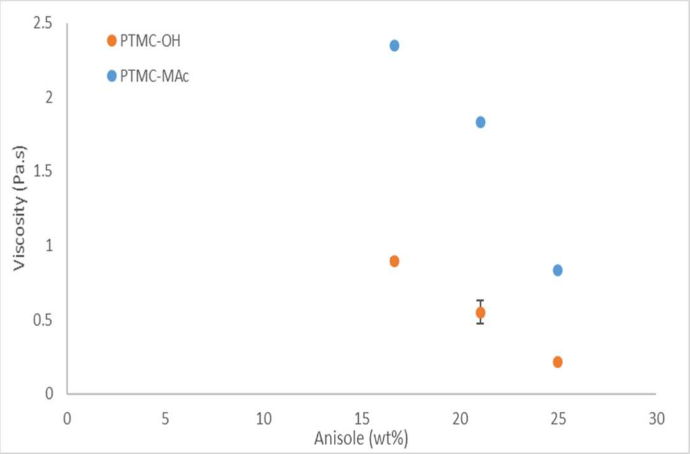

Figure 6-14. Viscosity at 25 ºC of PTMC-OH oligomers and PTMC-MAc macromers as a function of anisole diluent concentration. The shear rate used was 50 s^{-1}.

It is shown that, for a given amount of anisole the viscosity of PTMC-MAc macromer was more than twice that of PTMC-OH, we ascribe this to hydrogen bonding between PTMC-MAc molecules, where MAc represents a urethane methacrylate. The slope of the decrease in viscosity as anisole content increases is greater for PTMC-MAc, suggesting that the hydrogen bonding is diminished with increasing anisole. PTMC-MAc macromer, Irgacure 819, and triethyleneglycol dimethacrylate (TEGDMA) were all soluble in anisole, and the PEA-3,4-coated NPs were fully dispersed.

6.3.5. Fabrication of Tensile Test Samples by DLP

The overall goal of this work was to combine PTMC networks with colloidal dispersions obtained by stirred media milling, and to study the effect of the NP load on both photopolymerisation and mechanical properties. In the first instance, the photopolymerisation of formulations containing unmilled FeO ("bulk"), milled FeO ("nano"), and blank (containing no FeO) was studied. Fig 6-15 shows working curves plotting the incident light energy against the curing depth of the respective formulations. Comparing the values for each set of data (Table 6-5) shows that curing of the blank formulation requires a lower critical energy (E_c) (763 mJ/dm^2) than the formulations containing FeO, i.e. $E_{c,\,\text{blank}} < E_{c,\,\text{FeO}}$. The formulations containing bulk FeO and nano FeO have critical energies of 1727 and 1904 mJ/dm^2, respectively.

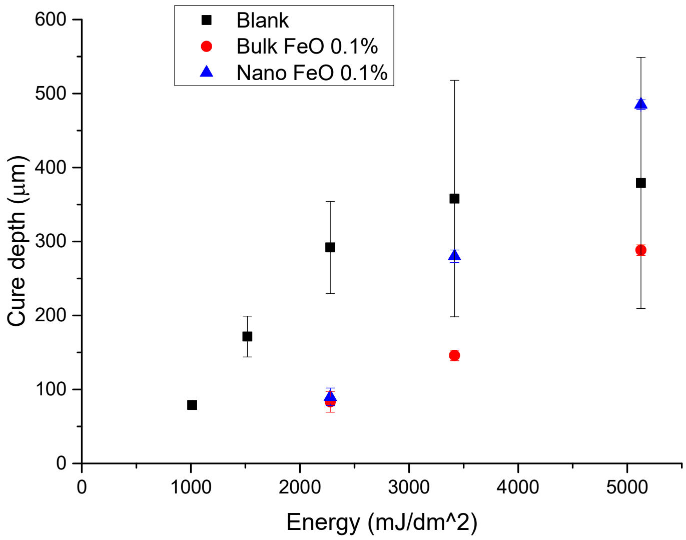

Figure 6-15: The effect of energy dose on cure depth in formulations containing blank, milled (nano) FeO, and non-milled (bulk) FeO, respectively.

Table 6-5: Effect of dopant type on cure depth.

Energy Dose **(mJ/dm^2)**	**Blank cure depth** **(µm)**	**0.1% nano** **FeO cure depth** **(µm)**	**0.1% bulk** **FeO cure depth** **(µm)**
1013	79 ± 3	-	-
1519	172 ± 28	-	-
2278	292 ± 62	90 ± 14	83 ± 12
3417	358 ± 160	280 ± 7	146 ± 9
5126	379 ± 170	485 ± 7	288 ± 6

Table 6-6: Penetration depth (D_p) and critical energy (E_c) of blank and doped formulations. D_p is the slope of the linear portion of the working curve (for a specific formulation); E_c is the intercept on the x-axis.

Sample	**D_p** **(µm)**	**E_c** **(mJ/dm^2)**
Blank	605	763
Nano FeO	1122	1904
Bulk FeO	582	1727

The critical energy, E_c, of the formulation containing 0.1 wt% nano FeO was 1904 mJ/dm^2, compared to 763 mJ/dm^2 for the blank formulation (Table 6-6). Therefore, it can be concluded that the inorganic component of the 0.1 wt% nano FeO-containing formulation attenuates more light energy due to scattering by the FeO particles present in the formulation. It follows that the formulation has a higher critical energy requirement in order to generate radicals for photocrosslinking of PTMC-MAc chains. Interestingly, the penetration depth D_p of the nano FeO formulation (1122 µm) was larger than that found for the blank formulation (605 µm). A possible interpretation is that the NPs dispersed in the formulation at 0.1 wt% allow more incident light to be transmitted by elastic scattering after the critical energy has been reached. Perhaps unexpectedly, the bulk FeO formulation had a slightly smaller critical energy requirement (1727 mJ/dm^2), compared with the nano FeO. A possible explanation is that, although the larger particles in the bulk formulation are expected to scatter more light than a 7 nm nanoparticle, there is a much greater number of 7 nm particles in the nano FeO formulation, than particles in the bulk FeO. There was greater variability in the curing of the blank formulations, as can be seen in Table 6-5. The inconsistent curing in the blank formulation is not easily explained, but the main conclusion to be drawn is that the presence of a dye allows better control of the cure depth. The effect of nano FeO concentration on the photopolymerisation of DLP-fabricated PTMC networks was studied and the working curves for each formulation are shown in Fig 6-16.

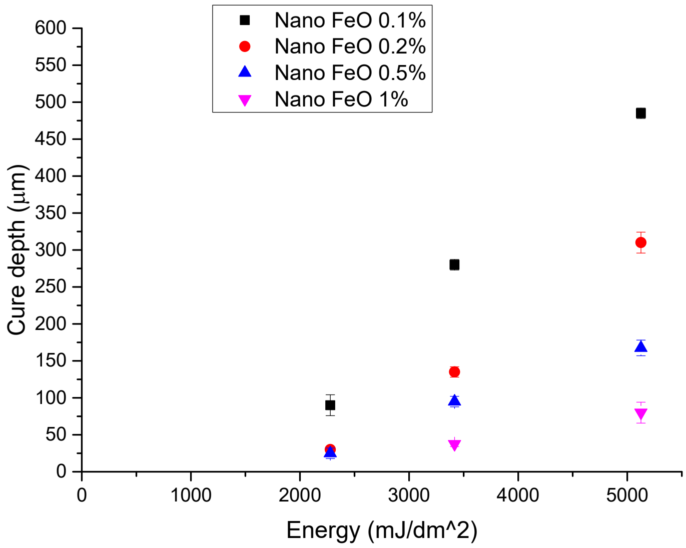

Figure 6-16: The effect of FeO nanoparticle concentration on cure depth and penetration depth.

Table 6-7: Effect of nano FeO dopant concentration on cure depth

Energy Dose (mJ/dm^2)	**0.1% nano FeO cure depth (µm)**	**0.2% nano FeO cure depth (µm)**	**0.5% nano FeO cure depth (µm)**	**1% nano FeO cure depth (µm)**
1013	-	-	-	-
1519	-	-	-	-
2278	90 ± 14	30 ± 0	25 ± 7	-
3417	280 ± 7	135 ± 7	95 ± 7	38 ± 4
5126	485 ± 7	310 ± 14	168 ± 11	80 ± 14

It was found that as the FeO nanoparticle concentration in the formulation is increased, both D_p and C_d decrease in an approximately linear fashion; the absorption of light energy by dispersed nanoparticles becomes the dominant factor, compared with the lower nanoparticle concentration samples. The relationship between incident light energy and penetration depth follows that of the Beer-Lambert law, where the penetration of light into the formulation drops off across the path length, as described by Lambert, and is inversely proportional to the molar extinction coefficient [201]. The penetration depth values as determined by profilometry are listed in Table 6-9.

Table 6-8: Effect of nano FeO concentration on penetration depth (D_p) and critical energy (E_c)

Nano FeO concentration (wt%)	**D_p (µm)**	**E_c (mJ/dm^2)**
0.1	1122	1904
0.2	795	2160
0.5	405	1981
1	241	2389

Beer's contribution to the law was to state that the absorbance is dependent on the concentration of attenuating species, i.e. NPs. Plotting penetration depth against nanoparticle concentration (Fig 6-17) shows that, as the nanoparticle concentration is increased, the penetration depth decreases exponentially.

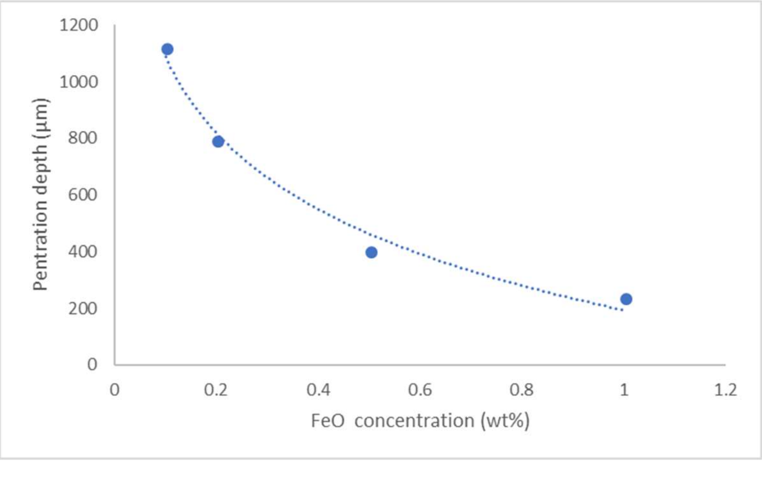

Figure 6-17: Effect of FeO concentration on the penetration depth, with exponential fit.

In conclusion, it has been shown that the presence of NPs in a PTMC-based formulation acts as an attenuator of incident light, i.e. a dye, which may allow better control of curing characteristics.

6.3.6. Dimensional Analysis of 3D Printed Tensile Bars

To test the effect of dye additive on the spatial fidelity of an object built by DLP, tensile bars were built using formulations containing various amounts of NPs. The tensile bars were built in three orientations, to test for any effect of the nature of interlayer bonding on the mechanical properties of the builds. The tensile sample design was from an in-house database of .stl files. The file was loaded in Netfabb Standard 2018.0 software (Fig 6-19), and builds were fabricated according to the original dimensions.

Build dimensions of 3D printed tensile bars were measured before and after PC/EtOH extraction of the finished builds, using a vernier caliper, and compared with the file dimensions. To study potential filler effects, the FeO concentration in the builds was varied between 0.1 and 0.5 wt%. The effect of the nanoparticle concentration on the appearance of the 3D printed tensile bar is shown in Fig 6-14 The build is still translucent at 0.1 wt% FeO, but a 5-fold increase of the nanoparticle load results in a build that is considerably darker. These nanoparticle loadings and their effect on the DLP photochemistry were discussed in Section 6.3.5.

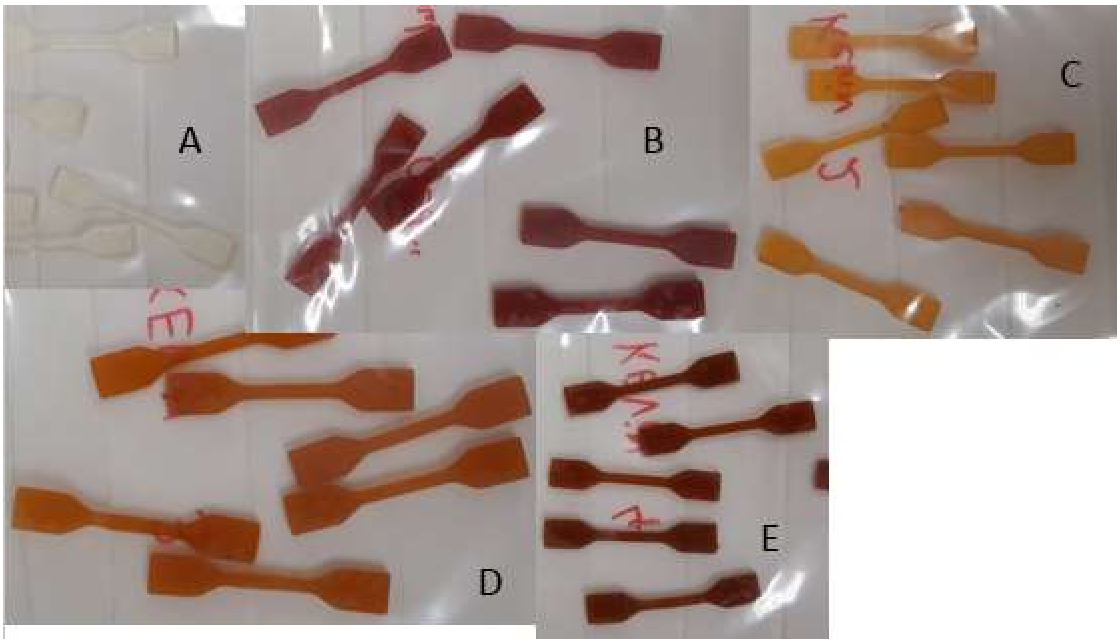

Figure 6-18: Tensile bars composed of crosslinked PTMC. Blank (A), Bulk FeO (B), 0.1 wt% nano FeO (C), 0.2 wt% nano FeO (D), and 0.5 wt% nano FeO (E).

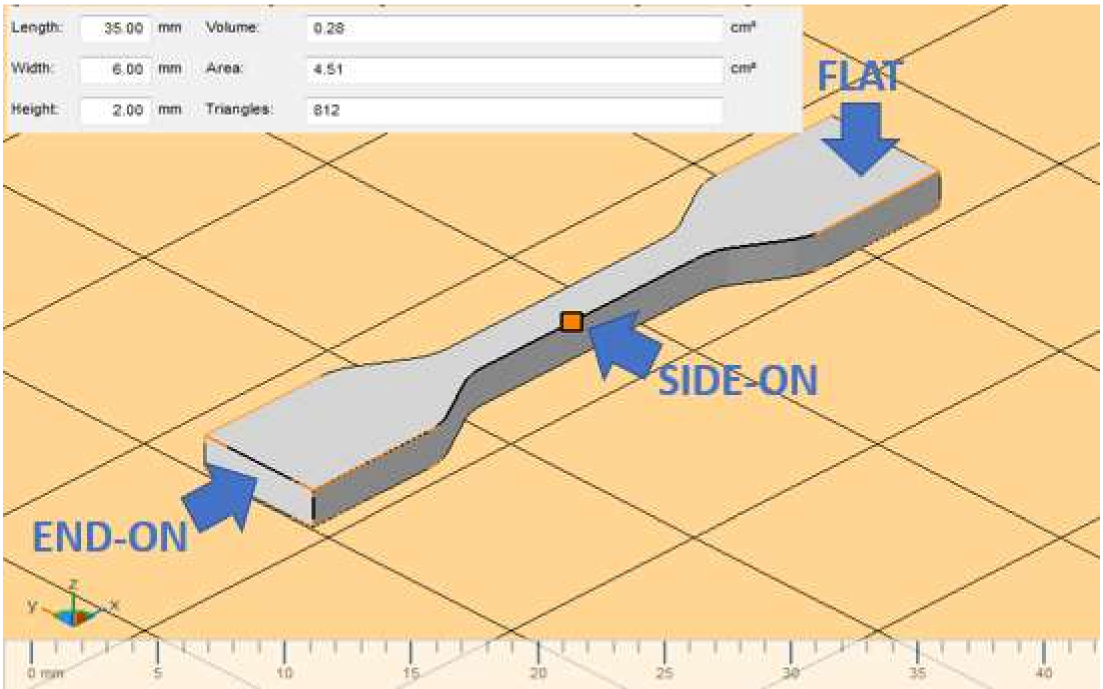

Length: 35.00 mm Volume: 0.28 cm³

Width: 6.00 mm Area: 4.51 cm²

Height: 2.00 mm Triangles: 812

Figure 6-19: Screenshot of Autodesk Netfabb Standard 2018.0 software with tensile bar design and dimensions (inset).

Table 6-9: Dimensions of pre-extract tensile bars, n = 3.

Sample ID	**Length (mm)**	**Length fidelity* (%)**	**Width (mm)**	**Width fidelity* (%)**	**Height (mm)**	**Height fidelity* (%)**
Blank	30.8 ± 0.1	88.0	5.4 ± 0.1	90.0	2.0 ± 0.1	100
FeO nano 0.1%	30.9 ± 0.2	88.2	5.2 ± 0.1	87.8	1.8 ± 0.1	90.0
FeO nano 0.2%	31.3 ± 0.3	89.4	5.4 ± 0.1	90.6	1.8 ± 0.1	91.7
FeO nano 0.5%	31.2 ± 0.6	89.2	5.3 ± 0.1	88.3	1.9 ± 0.1	93.3
FeO nano 0.1%/TEGDMA 4%	31.8 ± 0.4	91.0	5.5 ± 0.1	91.7	1.8 ± 0.1	91.7
Bulk 0.1%	31.3 ± 0.1	89.4	5.6 ± 0.1	93.3	1.8 ± 0.1	90.0

* Fidelity is the observed mean value for length, width or height; expressed as a percentage of the file value.

After 3D printing, the tensile bars were rinsed with 2-Propanol and post-cured in a UV oven. The dimensions of the builds, measured in triplicate, are listed in Table 6-10. The mean value measured for each sample was compared to the file dimensions (35, 6, and 2 mm, respectively) and the fidelity expressed as a percentage. Build fidelity ranged between 88 and 93%. When compared with the sample FeO nano 0.1%, the presence of the crosslinker TEGDMA at 4 wt% (“FeO nano 0.1%/TEGDMA 4%”) increased fidelity in all planes. The increased fidelity is likely mediated by the additional crosslinks in the network.

After PC/EtOH extraction of the samples, the dimensions were measured again (Table 6-10). Overall, shrinking was less than 5% and found to be variable across replicates. The gel (non-extractable, crosslinked network) contents of each build were determined by extracting the sol (unreacted monomer, etc) fraction, and determining the mass of each fraction gravimetrically. The average gel content was found to be 96% (Table 6-11). This shows that almost all of the PTMC reacted to form the polymer network. It can also be concluded that, assuming sufficient energy interacts with the formulation, any dopant present did not interfere with the crosslinking reaction.

Table 6-10: Dimensions of tensile bars extracted with PC/EtOH, n = 3.

Sample ID	**Length (mm)**	**Width (mm)**	**Height (mm)**
Blank	30.5 ± 0.1	5.2 ± 0.2	1.8 ± 0.2
FeO nano 0.1%	30.3 ± 0.2	5.2 ± 0.1	1.7 ± 0.1
FeO nano 0.2%	30.4 ± 0.6	5.2 ± 0.2	1.8 ± 0.1
FeO nano 0.5%	30.4 ± 0.2	5.2 ± 0.1	1.8 ± 0.1
FeO nano 0.1%/TEGDMA 4%	31.0 ± 0.4	5.4 ± 0.1	1.8 ± 0.1
Bulk 0.1%	30.9 ± 0.3	5.3 ± 0.1	1.7 ± 0.1

Table 6-11: Sol and gel fractions of tensile bars fabricated by DLP, n = 3.

Sample ID	**Gel (g)**	**Sol (g)**	**Sol/gel (g)**	**Gel (%)**
FeO nano 0.1%	0.24 ± 0.01	0.009 ± 0.001	0.25 ± 0.01	96
FeO nano 0.2%	0.24 ± 0.01	0.006 ± 0.001	0.25 ± 0.01	96
FeO nano 0.5%	0.24 ± 0.02	0.009 ± 0.001	0.25 ± 0.02	96
FeO nano 0.1%/ TEGDMA 4%	0.25 ± 0.01	0.008 ± 0.001	0.26 ± 0.01	96

The high gel contents show almost complete conversion of macromers into a crosslinked network, which is consistent with the low shrinkage following PC/EtOH extraction. The error in the build as compared to the file dimensions should be factored in when attempting to print accurately, i.e. the part can be designed with slightly larger dimensions than the target build dimensions, so that the shrinkage is accounted for and the final part has the target dimensions. Despite the observed errors, as well as the inconsistent curing observed for the blank formulation, there were no significant differences in the dimensions for all samples (irrespective of the formulation). To further examine potential differences in network formation across formulations, the tensile bars were subjected to mechanical testing.

6.3.7. Effect of Build Orientation on Mechanical Properties of 3D Printed Tensile Bars

Prior to tensile testing, samples containing bulk FeO, nano FeO and FeO blanks were built flat, side-on, and end-on (Fig 6-18), extracted in PC/EtOH (50:50), and dried in a vacuum oven. The potential influence of build orientation on the mechanical properties of PTMC tensile bars was studied. A schematic representation of the forces acting on a tensile bar during a tensile test is shown in Fig 6-20, where the tension force F is generated at the clamped ends of the sample by the crosshead displacement of the testing machine. The area under which the tension force acts is the tensile stress experienced by the sample. L_0 is the original gauge length which increases by ($L_1 - L_0$) during elongation.

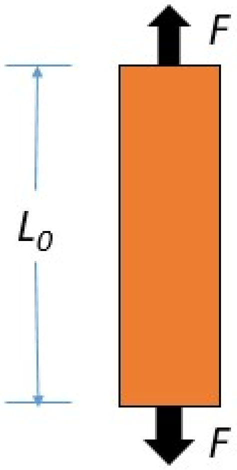

Figure 6-20: Scheme of the tension force F applied during tensile testing.

The data recorded is presented in Fig 6-21, and the elastic modulus values listed in Table 6-12. The elastic moduli measured for all samples was in the range 10 – 100 kPa which is typical of elastomeric materials. It should be noted that in some cases the samples were quite fragile and broke prior to testing, hence for those samples only one replicate could be tested (albeit the extracted elastic moduli for these samples were within the expected range).

Table 6-12: Effect of build orientation on elastic modulus. n = 3 (except for data marked with asterisk)

Sample Name	Blank Flat (BF)	Blank Side (BS)	Blank End (BE)	Nano Flat (NF)	Nano Side (NS)	Nano End (NE)	Bulk Flat (BUF)	Bulk Side (BUS)	Bulk End (BUE)
YM (kPa) (SD)	45 (8)	78 *	84 *	51 (12)	93 (6)	82 (6)	62 (3)	83 (10)	81 (5)

*Only one replicate could be measured due to sample breakage prior to measurement.

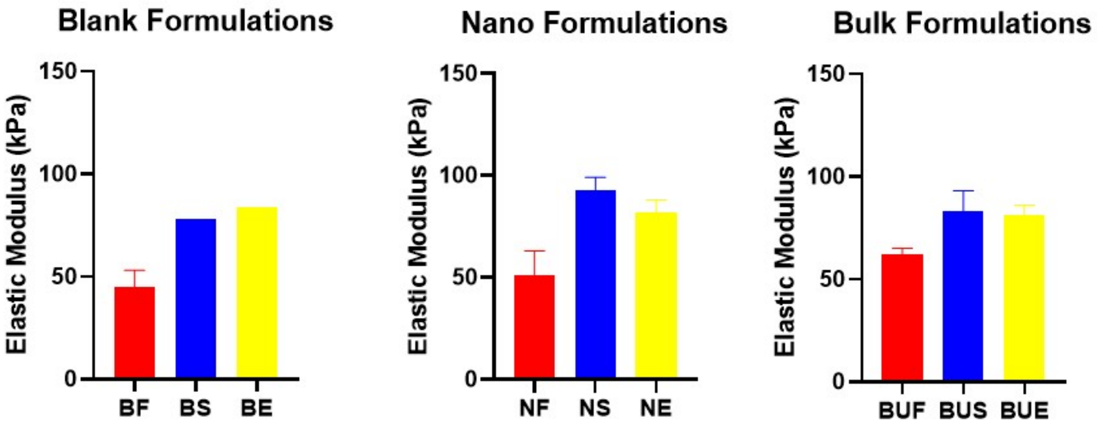

Figure 6-21: Effect of build orientation (flat/side/end, indicated as F, S and E, respectively) on elastic modulus, for a given filler type (blank/nano/bulk, indicated as B, N and BU, respectively).

The effect of build orientation on the elastic modulus is shown in Fig 6-21. For all filler types, the elastic modulus of the tensile bar built in the flat orientation is lower than those built in the other two orientations. However, the data for all filler types shows that the flat orientation consistently results in a lower elastic modulus, which is related to the direction of the layers with respect to the tensile force being applied. According to a review by Dizon *et al*, “the best tensile properties are obtained when filaments are oriented longitudinally and parallel to the loading direction, and the worst tensile properties are obtained when the samples are loaded along the build direction due to weak interlayer bonding.” [202]. The increase in elastic modulus for those samples built side-on and end-on is related to the orientation of the layers with respect to the applied force. As well as this, it might be expected that the number of layers contributes to the mechanical properties of the build. A combination of layer area and layer number determines the optimal mechanical properties [203]. The number of layers sent to the Rapidshare machine was 40 for flat, 120 for side-on, and 700 for end-on (all based on 50 µm layer thickness). From a manufacturing point of view, the quickest build is in the flat orientation, and this is probably preferred for elastomeric networks which will stretch longitudinally under tension [202]. The flat orientation is a likely complromise for applications requiring higher modulus, as its manufacturing time is less excessive. It can be concluded that both build orientation and the type of filler present in the formulation affect the elastic modulus.

6.3.8. Effect of Extraction Method on Mechanical Properties of 3D Printed Tensile Bars

Two extraction methods were tested. Extraction method (ExM)1 used PC/EtOH at 50:50 for 3 days, changing once per day. For ExM2 , the ratio of EtOH to PC was 50:50 on Day 1, 75:25 on Day 2, and 100:0 on Day 3. Fig 6-22 shows representative data for the tensile test of samples containing nano FeO at 0.1 to 0.5 wt%. The data is summarised in Table 6-13 and compared with the data from the original extraction method. It can be seen that by increasing the ratio of ethanol in the extraction medium, the mechanical properties were significantly altered. The elasticity of the network is greater (elastic modulus decreases) in those samples prepared using the alternative extraction method. This suggests that the presence of residual propylene carbonate increases the stiffness of the PTMC network. Upon addition of TEGDMA crosslinker at 4 wt%, the elastic modulus increased by 20% when using ExM1. The increase was 61% using ExM2. For both extraction methods, the elastic modulus of the samples containing TEGDMA crosslinker was almost identical (73 and 74 kPa, respectively). This indicates that the presence of TEGDMA dominates the stiffness irrespective of residual propylene carbonate content in the PTMC network.

Table 6-13: Effect of extraction method (ExM) on elastic modulus at different nanoparticle concentrations.

Sample Name	**ExM1 elastic modulus (kPa)**	**ExM2 elastic modulus (kPa)**
0.1 wt% nano FeO	61 ± 1	46 ± 1
0.2 wt% nano FeO	69 ± 6	49 ± 5
0.5 wt% nano FeO	54 ± 20	45 ± 5
0.1 wt% nano FeO 4 wt% TEGDMA	73 ± 7	74 ± 6

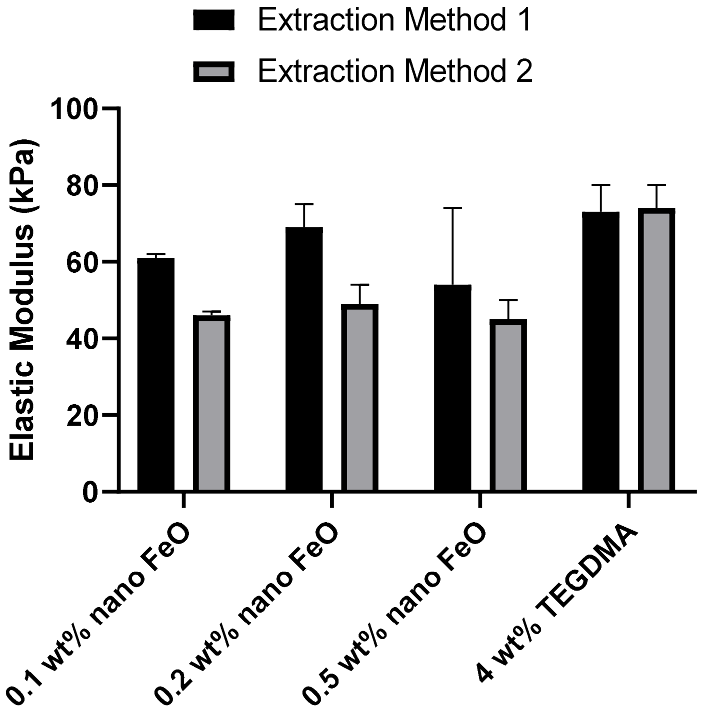

Figure 6-22: Effect of extraction method on the elastic modulus of tensile samples with varying amounts of nano FeO. At 0.1 wt% nano FeO, the effect of additional crosslinker (4 wt% TEGDMA) is also plotted.

6.4. Conclusions

PTMC-MAc macromers with a molecular weight of approximately 1300 g/mol were synthesised and fully characterised. These were then formulated with polymer-coated NPs. Compared with the blank formulation, the presence of NPs at increasing concentrations attenuates light energy, requiring higher critical energies to achieve equivalent cure depths. Interestingly, the penetration depth was higher at 0.1 wt% FeO, compared with the blank. when the nanoparticle concentration increases to 0.2% and higher, both penetration and cure depths decrease.

The elastic modulus was found to be lowest in the flat orientation for all filler types. At loadings between 0.1 and 0.5 wt% of NPs, no significant effect on the elastic modulus was observed. The addition of TEGDMA crosslinker at 4 wt% increased the elastic modulus of PTMC networks and was the dominant feature irrespective of extraction method.

Future work should focus further on the effect of FeO doping on the properties of the builds from three perspectives:

1. Build resolution. The tensile sample design is flat and more complicated structures could be attempted, e.g. knee meniscus.

2. Mechanical properties. It has been shown that the presence of nanoparticles in a polymer network can result in enhanced properties, compared with the native polymer [204]. Therefore, the loading (if any) at which the presence of nanoscale FeO begins to affect mechanical properties of the network is of interest. Moreover, the dispersion state of the nanoscale component may also confer distinct properties on the composite.

3. Magnetic properties. The next generation of printers can provide sufficient energy to print structures with FeO loadings in the 5 to 10% range (as achieved with the magnetic hydrogel nanocomposites described in Chapter 4). Therefore, the work should focus on printing magneto-responsive composites with high intensity DLP machines. In the case of PTMC, the rate of enzymatic degradation could be modified through the use of superparamagnetic NPs. As these NPs can produce heat in an AC magnetic field, they could be used to effect local temperature changes at the surface of the PTMC construct, which could in turn affect the enzymatic activity and therefore the rate of enzymatic degradation.

Chapter 7 - Thesis Conclusions and Further Work

The thesis contains seven chapters. Four of these contain the experimental results and discussion. These were:

- Size-controlled synthesis of iron oxide nanoparticles (Chapter 3)
- Magnetic nanocomposite hydrogels: magnetothermal and swelling response in AC fields (Chapter 4)
- Generation of superparamagnetic iron oxide nanoparticles for nanocomposite preparation by a top-down approach (Chapter 5)
- Digital light processing of nanoparticle-doped elastomeric networks (Chapter 6)

The third and fourth chapters together form a physico-chemical study of the macroscopic deswelling response in acrylamide-based polymer networks (soft polymer magnetic nanocomposites), due to heat being generated by the NPs in an AC field. This experimental work was conducted primarily in the research laboratories of the NMR and Nanomaterials Group (DCU and laterally UCD). The aims were to generate monodisperse nanoparticle (NP) suspensions with sufficient AC field induced heating following nano-compositing for use in nanocomposite hydrogel systems.

The fifth and sixth chapters combine to form a study of the photo-induced polymerisation of poly(trimethylene carbonate) and the effect of dispersed NPs on photopolymerisation kinetics. Mechanical properties (of these hard polymer magnetic nanocomposites) as a function of both NP content and DLP build direction were described. This experimental work was conducted primarily in the research laboratories of DSM in Limburg, The Netherlands. The aim was to produce a DLP formulation with nanoparticulate dye incorporated primarily for DLP attenuation, but with a view to magnetic response in later generations.

7.1. Comparison of Approaches to NP Generation

Both approaches use magnetic iron oxide nanoparticles as potential heat mediators in nanocomposite hydrogels, and for the latter case as attenuators for DLP. Considering the nanoparticle preparation first:

For the soft nanocomposites a seed-mediated approach first reported by Sun *et al* was employed, and the stepwise change in nanoparticle size and properties agreed with Sun's observations. Magnetic hyperthermia measurements of different size NPs were used to determine values of the specific absorption rate (SAR) for each step. It was found that the SAR is not simply related to NP size, given that specific reaction conditions can result in identical particle sizes having dramatically different SAR values, albeit the SAR always increases monotonically. Moreover, increases in saturation magnetisation do not necessarily lead to increases in SAR. The optimised NPs were phase transferred using a catechol-functionalised polymer, with a high efficiency of ligand exchange. The core nanoparticle diameter and polydispersity were unaffected. However, it was found that the heating of the polymer-coated NPs in ethanol was less than that of the oleic acid-coated NPs in heptane. The further decrease in heating observed when the NPs were mixed with acrylamide monomers was also interesting; this demonstrates the sensitivity of NP heat production to the surroundings, which is probably related to reduced particle diffusion. It is known that dhyd can change drastically when NPs are placed *in vivo* affecting their heating, so considering the biological milieu, it is perhaps impossible to avoid those factors resulting in slowed diffusion of the NPs. Hence, high SAR materials are recommended for use as discrete NP heat mediators.

The major advantage of Sun's bottom-up approach to nanoparticle synthesis is size control, albeit it requires five synthetic steps to achieve a particle diameter of 14 nm. From a commercialisation perspective, this is not an efficient production process. A much more facile route to NPs with high SAR would be advantageous. The major challenge of the Sun method for synthesis of iron oxide NPs is batch-to-batch reproducibility. To achieve a nanoparticle size that allows sufficient heat generation in AC fields (*ca.* 14 nm), five synthetic steps are required and minor differences step to step tend to accumulate. Future work should demonstrate reproducibility and/or reduce the number of synthetic steps, or investigate other routes to similarly sized NPs.

The top-down approach to NP synthesis described in the second part of the thesis is much less demanding from a production perspective. The material is loaded into a mill and the size reduction step can run unattended. Stirred media milling of bulk iron oxide powder resulted in colloidally stable NP suspensions. The saturation magnetisation was found to decrease upon size reduction, which was ascribed to the non-magnetic surface layer becoming more significant. The final NPs were found to have a diameter of 7 nm and not to heat significantly. However, preliminary data suggests that the type of solvent used during milling may also affect the final nanoparticle size, and perhaps magnetic response, through viscous damping. Future experiments using stirred media milling should investigate the possibility of size control and retention of magnetisation by viscous damping. Based on this concept, the viscosity of a given solvent may allow tuning of the nanoparticle size. This could then allow the generation of nanoparticle suspensions with suitable properties from bulk powders.

Turning to the nano-compositing; for both approaches to magnetic nanocomposites an *in situ* method was used to generate the nanocomposite material, whereby the NPs are blended with either monomers or macromers, followed by polymerisation. For the nanocomposite hydrogels described in Chapter 4, vortex mixing was sufficient to achieve dispersion of NPs on the nanoscale. For the more viscous formulations described in Chapter 6, centrifugal mixing was required to disperse the NPs. In both cases, the mixing process can be considered facile and reproducible and hence homogeneous materials can be produced.

7.2. Soft Polymer Magnetic Nano-composites

In the case of the soft polymer nanocomposites; the physico-chemical approach to studying network dynamics in magnetically responsive hydrogels, shown in the first part of the thesis, advances knowledge in the field. Previous work has focused on macroscopic drug release, without any attempt to understand the interplay between magnetic heating and polymer composition and hydration.

When the NPs are incorporated into magnetic nanocomposite hydrogels, the surface coating determines the interaction of the NPs with the polymer network. Early experiments using citrate coatings resulted in uncontrolled NP diffusion away from the network, whilst the catechol-functionalised polymer showed no such diffusion. It was initially concluded that the NPs must be effectively anchored within the polymer network, or at least that their diffusion was greatly reduced. The NP concentration was found to affect the rate of temperature increase, which in turn influences the rate of the deswelling response. For a given NP concentration, it was also shown that the deswelling response could be tuned by adjusting the formulation. This tunable behaviour provides a basis for the study of release of molecules other than water from these networks, while the kinetics of deswelling provide new insights into the macroscopic response. This work is ongoing in the NMR and Nanomaterials Group based at UCD. To advance this work it will be necessary to collect data more finely spaced in time, to distinguish between kinetic models. One challenge will be the time required to capture such data; as samples must be re-equilibrated each time, typically overnight. Multiple samples could be generated to increase throughput; DLP could be a suitable method for producing multiple samples. A better understanding of the deswelling process would contribute to understanding of release mechanisms for drug molecules, growth factors, etc. The study presented has established the methodology for the proposed future studies.

Despite the interesting compositionally modulate-able thermo-response of NIPAAm-based hydrogel networks, the major issue found when working with them was their mechanical weakness. In order to obtain good data, great care was required when handling the gel during data collection. Such a material would not be suitable for implantation and would likely degenerate during motion of a patient. Robust mechanical stability is essential for the development of implantable nanocomposite hydrogel devices.

7.3. Hard Polymer Magnetic Nano-composites

For the hard polymer nanocomposites, the optimised (top-down) NPs from stirred media milling were used as attenuators for DLP printing of tensile bars. It was shown that the size of the particles (bulk versus milled) affected the amount of light energy ($\lambda = 405$ nm) available to generate radicals during DLP; these were found to induce photopolymerisation and crosslinking of trimethylene carbonate macromers, which could be printed as discrete layers. The orientation of the build (and therefore the area and number of layers) was found to have an effect on the Young's Modulus of the printed tensile bars.

The final PTMC-based nanocomposites were found to have good mechanical properties. They are rubbery with low elastic modulus and can undergo significant strain, hence the widespread use of this polymer in biodegradable medical devices. It has been shown that these materials can be 3D printed using DLP. The lack of thermoresponse in PTMC-based networks does not preclude their use as magnetothermally-mediated drug delivery devices, as it may be possible to develop a delivery system based on enzyme-mediated surface erosion.

Using a DLP instrument with a higher intensity light source would allow 3D printing of an object that can generate heat in AC fields. With respect to PTMC which undergoes enzymatic surface erosion, the potential for controlling the surface temperature, *i.e.* at the interface between polymer and enzyme, could allow controlled degradation of a PTMC-based construct.

7.4. Final Comments

The studies presented here make it clear that the ideal magnetically responsive nanocomposite would incorporate inherent thermo-responsiveness, such as that in NIPAAm, coupled to the good mechanical properties of an elastomer such as PTMC, and which can be printed using an additive manufacturing approach (DLP, SLA *etc*). Such materials would provide unique opportunities to demonstrate the huge potential of 3D printing in manufacturing of medical devices with excellent morphological control. The future for magnetically stimulated devices for use in medicine is bright, if these technical issues can be addressed. It is hoped that the work and methodologies described in this thesis will help prove useful benchmarks in the evaluation of stimuli-responsive nanocomposites.

List of References

1. Issa, B., et al., *Magnetic nanoparticles: surface effects and properties related to biomedicine applications.* International Journal of Molecular Sciences, 2013. **14**(11): p. 21266-21305.
2. Pankhurst, Q.A., et al., *Applications of magnetic nanoparticles in biomedicine.* Journal of Physics D: Applied Physics, 2003. **36**(13): p. R167.
3. Gazeau, F. and C. Wilhelm, *Magnetic labeling, imaging and manipulation of endothelial progenitor cells using iron oxide nanoparticles.* Future Medicinal Chemistry, 2010. **2**(3): p. 397-408.
4. Mathew, D.S. and R.-S. Juang, *An overview of the structure and magnetism of spinel ferrite nanoparticles and their synthesis in microemulsions.* Chemical Engineering Journal, 2007. **129**(1-3): p. 51-65.
5. Meledandri, C., *NMR studies of membrane-bound nanoparticles and nanoparticle assemblies*. 2009, Dublin City University.
6. Rosensweig, R.E., *Ferrohydrodynamics*. 2013: Courier Corporation.
7. McConnell, H.M., *Ferromagnetism in solid free radicals.* The Journal of Chemical Physics, 1963. **39**(7): p. 1910-1910.
8. Furlani, E.P., *Magnetic biotransport: analysis and applications.* Materials, 2010. **3**(4): p. 2412-2446.
9. Buschow, K.H.J. and F.R. Boer, *Physics of Magnetism and Magnetic Materials*. Vol. 92. 2003: Springer.
10. Cullity, B.D. and C.D. Graham, *Introduction to magnetic materials*. 2011: John Wiley & Sons.
11. Cornell, R.M. and U. Schwertmann, *The iron oxides: structure, properties, reactions, occurrences and uses*. 2003: John Wiley & Sons.
12. Demortiere, A., et al., *Size-dependent properties of magnetic iron oxide nanocrystals.* Nanoscale, 2011. **3**(1): p. 225-232.
13. Phan, M.-H., et al., *Exchange bias effects in iron oxide-based nanoparticle systems.* Nanomaterials, 2016. **6**(11): p. 221.
14. Kittel, C., *Theory of the structure of ferromagnetic domains in films and small particles.* Physical Review, 1946. **70**(11-12): p. 965.
15. Lu, A.H., E. Salabas, and F. Schüth, *Magnetic nanoparticles: synthesis, protection, functionalization, and application.* Angewandte Chemie International Edition, 2007. **46**(8): p. 1222-1244.
16. García, P.F., et al., *High-gradient magnetic separation for technical scale protein recovery using low cost magnetic nanoparticles.* Separation and purification technology, 2015. **150**: p. 29-36.
17. Franzreb, M., et al., *Protein purification using magnetic adsorbent particles.* Applied microbiology and biotechnology, 2006. **70**(5): p. 505-516.
18. Roth, H.C., et al., *Immobilization of cellulase on magnetic nanocarriers.* ChemistryOpen, 2016. **5**(3): p. 183-187.
19. Rossi, L.M., et al., *Magnetic nanomaterials in catalysis: advanced catalysts for magnetic separation and beyond.* Green Chemistry, 2014. **16**(6): p. 2906-2933.
20. Liu, J., et al., *Shape-controlled iron oxide nanocrystals: synthesis, magnetic properties and energy conversion applications.* CrystEngComm, 2016. **18**(34): p. 6303-6326.
21. Tian, L.-L., et al., *γ-Fe_2O_3 nanocrystalline microspheres with hybrid behavior of battery-supercapacitor for superior lithium storage.* ACS applied materials interfaces2015. **7**(47): p. 26284-26290.

22. Liu, G., et al., *Applications and potential toxicity of magnetic iron oxide nanoparticles.* Small, 2013. **9**(9-10): p. 1533-1545.
23. Bauer, L.M., et al., *High-performance iron oxide nanoparticles for magnetic particle imaging–guided hyperthermia (hMPI).* Nanoscale, 2016. **8**(24): p. 12162-12169.
24. Nel, A.E., et al., *Understanding biophysicochemical interactions at the nano–bio interface.* Nature Materials, 2009. **8**(7): p. 543.
25. Xu, Z., Y. Hou, and S. Sun, *Magnetic core/shell Fe3O4/Au and Fe3O4/Au/Ag nanoparticles with tunable plasmonic properties.* Journal of the American Chemical Society, 2007. **129**(28): p. 8698-8699.
26. Fan, Z., et al., *Theranostic nanomedicine for cancer detection and treatment.* Journal of Food and Drug Analysis, 2014. **22**(1): p. 3-17.
27. Revia, R.A. and M. Zhang, *Magnetite nanoparticles for cancer diagnosis, treatment, and treatment monitoring: recent advances.* Materials Today, 2016. **19**(3): p. 157-168.
28. Su, S.S. and I. Chang, *Review of Production Routes of Nanomaterials*, in *Commercialization of Nanotechnologies–A Case Study Approach*. 2018, Springer. p. 15-29.
29. Massart, R., *Preparation of aqueous magnetic liquids in alkaline and acidic media.* IEEE Transactions on Magnetics, 1981. **17**(2): p. 1247-1248.
30. Massart, R., et al., *Preparation and properties of monodisperse magnetic fluids.* Journal of Magnetism and Magnetic Materials, 1995. **149**(1-2): p. 1-5.
31. Rockenberger, J., E.C. Scher, and A.P. Alivisatos, *A new nonhydrolytic single-precursor approach to surfactant-capped nanocrystals of transition metal oxides.* Journal of the American Chemical Society, 1999. **121**(49): p. 11595-11596.
32. Sun, S. and H. Zeng, *Size-controlled synthesis of magnetite nanoparticles.* Journal of the American Chemical Society, 2002. **124**(28): p. 8204-8205.
33. Sun, S., et al., *Monodisperse* MFe_2O_4 *(M= Fe, Co, Mn) nanoparticles.* Journal of the American Chemical Society, 2004. **126**(1): p. 273-279.
34. Krishnan, K.M., et al., *Nanomagnetism and spin electronics: materials, microstructure and novel properties.* Journal of Materials Science, 2006. **41**(3): p. 793-815.
35. Rosensweig, R.E., *Heating magnetic fluid with alternating magnetic field.* Journal of magnetism and magnetic materials, 2002. **252**: p. 370-374.
36. Laurent, S., et al., *Magnetic iron oxide nanoparticles: synthesis, stabilization, vectorization, physicochemical characterizations, and biological applications.* Chemical Reviews, 2008. **108**(6): p. 2064-2110.
37. Abenojar, E.C., et al., *Structural effects on the magnetic hyperthermia properties of iron oxide nanoparticles.* Progress in Natural Science: Materials International, 2016. **26**(5): p. 440-448.
38. Singh, V., V. Banerjee, and M. Sharma, *Dynamics of magnetic nanoparticle suspensions.* Journal of Physics D: Applied Physics, 2009. **42**(24): p. 245006.
39. Gupta, A.K. and M. Gupta, *Synthesis and surface engineering of iron oxide nanoparticles for biomedical applications.* Biomaterials, 2005. **26**(18): p. 3995-4021.
40. Laurent, S., et al., *Magnetic fluid hyperthermia: focus on superparamagnetic iron oxide nanoparticles.* Advances in Colloid and Interface Science, 2011. **166**(1-2): p. 8-23.
41. Reissis, Y., et al., *The effect of temperature on the viability of human mesenchymal stem cells.* Stem Cell Research & Therapy, 2013. **4**(6): p. 139.

42. Lartigue, L.n., et al., *Cooperative organization in iron oxide multi-core nanoparticles potentiates their efficiency as heating mediators and MRI contrast agents.* ACS Nano, 2012. **6**(12): p. 10935-10949.
43. Deatsch, A.E. and B.A. Evans, *Heating efficiency in magnetic nanoparticle hyperthermia.* Journal of Magnetism and Magnetic Materials, 2014. **354**: p. 163-172.
44. Fortin, J.-P., et al., *Size-sorted anionic iron oxide nanomagnets as colloidal mediators for magnetic hyperthermia.* Journal of the American Chemical Society, 2007. **129**(9): p. 2628-2635.
45. Tong, S., et al., *Size-dependent heating of magnetic iron oxide nanoparticles.* ACS Nano, 2017. **11**(7): p. 6808-6816.
46. Hawkins, A.M., N.S. Satarkar, and J.Z. Hilt, *Nanocomposite degradable hydrogels: demonstration of remote controlled degradation and drug release.* Pharmaceutical Research, 2009. **26**(3): p. 667-673.
47. Ortolani, A., et al., *The prospective opportunities offered by magnetic scaffolds for bone tissue engineering: A review.* Joints, 2016. **4**(4): p. 228.
48. Gilchrist, R., et al., *Selective inductive heating of lymph nodes.* Annals of Surgery, 1957. **146**(4): p. 596.
49. MEDAL, R., et al., *Controlled radio-frequency generator for production of localized heat in intact animal: Mechanism and construction.* AMA Archives of Surgery, 1959. **79**(3): p. 427-431.
50. Shingleton, W.W., *Selective heating and cooling of tissue in cancer chemotherapy.* Annals of Surgery, 1962. **156**(3): p. 408.
51. Gilchrist, R., et al., *Effects of electromagnetic heating on internal viscera a preliminary to the treatment of human tumors.* Annals of Surgery, 1965. **161**(6): p. 890.
52. Rand, R.W., et al., *Thermomagnetic surgery for cancer.* Applied biochemistry and biotechnology, 1981. **6**(4): p. 265-272.
53. Rand, R.W., et al., *Thermo-magnetic surgery for experimental renal cancer.* The Journal of urology, 1982. **128**(3): p. 618-620.
54. Jordan, A., et al., *Cellular uptake of magnetic fluid particles and their effects on human adenocarcinoma cells exposed to AC magnetic fields in vitro.* International journal of hyperthermia, 1996. **12**(6): p. 705-722.
55. Kozissnik, B., et al., *Magnetic fluid hyperthermia: advances, challenges, and opportunity.* International Journal of Hyperthermia, 2013. **29**(8): p. 706-714.
56. Antman-Passig, M. and O. Shefi, *Remote magnetic orientation of 3D collagen hydrogels for directed neuronal regeneration.* Nano Letters, 2016. **16**(4): p. 2567-2573.
57. Margolis, G., B. Polyak, and S. Cohen, *Magnetic Induction of Multiscale Anisotropy in Macroporous Alginate Scaffolds.* Nano Letters, 2018.
58. Souza, G.R., et al., *Three-dimensional tissue culture based on magnetic cell levitation.* Nature Nanotechnology, 2010. **5**(4): p. 291.
59. Camargo, P.H.C., K.G. Satyanarayana, and F. Wypych, *Nanocomposites: synthesis, structure, properties and new application opportunities.* Materials Research, 2009. **12**(1): p. 1-39.
60. Kalia, S., et al., *Magnetic polymer nanocomposites for environmental and biomedical applications.* Colloid and Polymer Science, 2014. **292**(9): p. 2025-2052.
61. Paul, D. and L.M. Robeson, *Polymer nanotechnology: nanocomposites.* Polymer, 2008. **49**(15): p. 3187-3204.
62. Ullah, F., et al., *Classification, processing and application of hydrogels: A review.* Materials Science and Engineering: C, 2015. **57**: p. 414-433.

63. Seiffert, S. and J. Sprakel, *Physical chemistry of supramolecular polymer networks.* Chemical Society Reviews, 2012. **41**(2): p. 909-930.
64. Zhang, Y., Y. Li, and W. Liu, *Dipole–Dipole and H-Bonding Interactions Significantly Enhance the Multifaceted Mechanical Properties of Thermoresponsive Shape Memory Hydrogels.* Advanced Functional Materials, 2015. **25**(3): p. 471-480.
65. Deng, C., et al., *Biodegradable polymeric micelles for targeted and controlled anticancer drug delivery: promises, progress and prospects.* Nano Today, 2012. **7**(5): p. 467-480.
66. Jătariu, A.N., et al., *Covalent and ionic co-cross-linking—An original way to prepare chitosan–gelatin hydrogels for biomedical applications.* Journal of Biomedical Materials Research Part A, 2011. **98**(3): p. 342-350.
67. Melchels, F.P.W., *Preparation of advanced porous structures by stereolithography for application in tissue engineering*. 2010: University of Twente [Host].
68. Gauvin, R., et al., *Microfabrication of complex porous tissue engineering scaffolds using 3D projection stereolithography.* Biomaterials, 2012. **33**(15): p. 3824-3834.
69. Kost, J., J. Wolfrum, and R. Langer, *Magnetically enhanced insulin release in diabetic rats.* Journal of Biomedical Materials Research, 1987. **21**(12): p. 1367-1373.
70. Langer, R., *Biomaterials in drug delivery and tissue engineering: one laboratory's experience.* Accounts of Chemical Research, 2000. **33**(2): p. 94-101.
71. Lu, Z., et al., *Magnetic switch of permeability for polyelectrolyte microcapsules embedded with Co@ Au nanoparticles.* Langmuir, 2005. **21**(5): p. 2042-2050.
72. De Paoli, V.M., et al., *Effect of an oscillating magnetic field on the release properties of magnetic collagen gels.* Langmuir, 2006. **22**(13): p. 5894-5899.
73. Peppas, N.A., et al., *Hydrogels in biology and medicine: from molecular principles to bionanotechnology.* Advanced Materials, 2006. **18**(11): p. 1345-1360.
74. Hu, S.-H., et al., *Controlled pulsatile drug release from a ferrogel by a high-frequency magnetic field.* Macromolecules, 2007. **40**(19): p. 6786-6788.
75. Hu, S.-H., et al., *Magnetic-sensitive silica nanospheres for controlled drug release.* Langmuir, 2008. **24**(1): p. 239-244.
76. Ma, T., et al., *A novel method to in situ synthesis of magnetic poly (N-isopropylacrylamide-co-acrylic acid) nanogels.* Colloid and Polymer Science, 2016. **294**(8): p. 1251-1257.
77. Satarkar, N.S. and J.Z. Hilt, *Magnetic hydrogel nanocomposites for remote controlled pulsatile drug release.* Journal of Controlled Release, 2008. **130**(3): p. 246-251.
78. Keurentjes, J.T., et al., *Externally Triggered Glass Transition Switch for Localized On-Demand Drug Delivery.* Angewandte Chemie International Edition, 2009. **48**(52): p. 9867-9870.
79. Ozay, O., et al., *Removal of toxic metal ions with magnetic hydrogels.* Water Research, 2009. **43**(17): p. 4403-4411.
80. Satarkar, N.S., et al., *Magnetic hydrogel nanocomposites as remote controlled microfluidic valves.* Lab on a Chip, 2009. **9**(12): p. 1773-1779.
81. Meenach, S.A., et al., *Characterization of PEG–iron oxide hydrogel nanocomposites for dual hyperthermia and paclitaxel delivery.* Journal of Biomaterials Science, Polymer Edition, 2013. **24**(9): p. 1112-1126.
82. Zhou, M., et al., *Magnetic biocomposites for remote melting.* Biomacromolecules, 2015. **16**(8): p. 2308-2315.

83. Coffel, J. and E. Nuxoll, *Magnetic nanoparticle/polymer composites for medical implant infection control.* Journal of Materials Chemistry B, 2015. **3**(38): p. 7538-7545.
84. Kim, H., et al., *Magnetic field-responsive release of transforming growth factor beta 1 from heparin-modified alginate ferrogels.* Carbohydrate Polymers, 2016. **151**: p. 467-473.
85. Le Renard, P.-E., et al., *The in vivo performance of magnetic particle-loaded injectable, in situ gelling, carriers for the delivery of local hyperthermia.* Biomaterials, 2010. **31**(4): p. 691-705.
86. Le Renard, P.-E., et al., *Magnetic and in vitro heating properties of implants formed in situ from injectable formulations and containing superparamagnetic iron oxide nanoparticles (SPIONs) embedded in silica microparticles for magnetically induced local hyperthermia.* Journal of Magnetism and Magnetic Materials, 2011. **323**(8): p. 1054-1063.
87. Hu, K., et al., *A novel magnetic hydrogel with aligned magnetic colloidal assemblies showing controllable enhancement of magnetothermal effect in the presence of alternating magnetic field.* Advanced Materials, 2015. **27**(15): p. 2507-2514.
88. Saric, M., H. Dietsch, and P. Schurtenberger, *In situ polymerisation as a route towards transparent nanocomposites: Time-resolved light and neutron scattering experiments.* Colloids Surfaces A: Physicochemical and Engineering Aspects, 2006. **291**(1-3): p. 110-116.
89. Satarkar, N.S., et al., *Remote actuation of hydrogel nanocomposites: heating analysis, modeling, and simulations.* AIChE Journal, 2011. **57**(4): p. 852-860.
90. Safronov, A.P., et al., *Polyacrylamide ferrogels with magnetite or strontium hexaferrite: Next step in the development of soft biomimetic matter for biosensor applications.* Sensors, 2018. **18**(1): p. 257.
91. Campbell, S.B., M. Patenaude, and T.J.B. Hoare, *Injectable superparamagnets: highly elastic and degradable poly (N-isopropylacrylamide)–superparamagnetic iron oxide nanoparticle (SPION) composite hydrogels.* 2013. **14**(3): p. 644-653.
92. Alarcon, C.d.l.H., S. Pennadam, and C. Alexander, *Stimuli responsive polymers for biomedical applications.* Chemical Society Reviews, 2005. **34**(3): p. 276-285.
93. Brazel, C.S. and N.A. Peppas, *Pulsatile local delivery of thrombolytic and antithrombotic agents using poly (N-isopropylacrylamide-co-methacrylic acid) hydrogels.* Journal of controlled release, 1996. **39**(1): p. 57-64.
94. Brazel, C.S., *Magnetothermally-responsive nanomaterials: combining magnetic nanostructures and thermally-sensitive polymers for triggered drug release.* Pharmaceutical Research, 2009. **26**(3): p. 644-656.
95. Ankareddi, I., et al. *Temperature controlled grafted polymer network incorporated with magnetic nanoparticles to control drug release induced by an external magnetothermal trigger*. in *NSTI Nanotech*. 2007.
96. Chen, Y.-M., et al., *Thermoresponsive dual-phase transition and 3D self-assembly of poly (N-isopropylacrylamide) tethered to silicate platelets.* Chemistry of Materials, 2009. **21**(17): p. 4071-4079.
97. Caykara, T., S. Kiper, and G. Demirel, *Thermosensitive poly (N-isopropylacrylamide-co-acrylamide) hydrogels: synthesis, swelling and interaction with ionic surfactants.* European Polymer Journal, 2006. **42**(2): p. 348-355.
98. Van Leeuwen, A., et al., *In vivo behaviour of a biodegradable poly (trimethylene carbonate) barrier membrane: a histological study in rats.* Journal of Materials Science: Materials in Medicine, 2012. **23**(8): p. 1951-1959.

99. Knecht, L.D., et al., *Nanoparticle-mediated remote control of enzymatic activity.* ACS Nano, 2012. **6**(10): p. 9079-9086.
100. Ji, Z., et al., *Multimaterials 3D Printing for Free Assembly Manufacturing of Magnetic Driving Soft Actuator.* Advanced Materials Interfaces, 2017. **4**(22): p. 1700629.
101. Cooperstein, I., et al., *Hybrid Materials for Functional 3D Printing.* 2018: p. 1800996.
102. Rayleigh, J.W.S.B., *On the scattering of light by small particles*. 1871.
103. Mie, G., *Beiträge zur Optik trüber Medien, speziell kolloidaler Metallösungen.* Annalen der physik, 1908. **330**(3): p. 377-445.
104. Instruments, M., *Dynamic light scattering: an introduction in 30 minutes.* Technical Note Malvern, MRK656-01, 2012: p. 1-8.
105. Wikipedia. *Scanning transmission electron microscopy*. 11 May 2019 22:18 UTC [cited 2019 12/06]; Available from: https://en.wikipedia.org/w/index.php?title=Scanning_transmission_electron_microscopy&oldid=896638169.
106. Chatwal, G.R. and S.K. Anand, *Instrumental methods of chemical analysis*. 1979: Himalaya publishing house Mumbai:.
107. Watson, E.S. and M.J. O'Neill, *Differential microcalorimeter*. 1966, Google Patents.
108. Bandyopadhyay, A., T. Das, and S. Yeasmin, *Nanoparticles in Lung Cancer Therapy-Recent Trends*. 2015: Springer.
109. Garaio, E., et al., *A multifrequency eletromagnetic applicator with an integrated AC magnetometer for magnetic hyperthermia experiments.* Measurement Science and Technology, 2014. **25**(11): p. 115702.
110. Kim, D.-H., et al., *Heat generation of aqueously dispersed CoFe2O4 nanoparticles as heating agents for magnetically activated drug delivery and hyperthermia.* Journal of Magnetism and Magnetic Materials, 2008. **320**(19): p. 2390-2396.
111. Wren, J. and D. Loyd, *Thermocouples.* Encyclopedia of Medical Devices and Instrumentation, 2006.
112. Hoon, S., *An inexpensive, sensitive vibrating sample magnetometer.* European Journal of Physics, 1983. **4**(2): p. 61.
113. Foner, S., *Versatile and sensitive vibrating-sample magnetometer.* Review of Scientific Instruments, 1959. **30**(7): p. 548-557.
114. Jiles, D., *Introduction to magnetism and magnetic materials*. 2015: CRC press.
115. Wikipedia. *Vibrating-sample magnetometer.* [cited 2019 04/04]; Available from: https://en.wikipedia.org/wiki/Vibrating-sample_magnetometer#/media/File:VSM_en.svg.
116. Adigüzel, Y., *ATR-FTIR spectroscopy of membrane-bound Ras protein.* 2008.
117. von Laue, M., *Concerning the detection of X-ray interferences.* Nobel lecture, 1915. **13**.
118. Hergt, R. and S. Dutz, *Magnetic particle hyperthermia—biophysical limitations of a visionary tumour therapy.* Journal of Magnetism and Magnetic Materials, 2007. **311**(1): p. 187-192.
119. Sonvico, F., et al., *Folate-conjugated iron oxide nanoparticles for solid tumor targeting as potential specific magnetic hyperthermia mediators: synthesis, physicochemical characterization, and in vitro experiments.* Bioconjugate Chemistry, 2005. **16**(5): p. 1181-1188.
120. Deacon, G. and R. Phillips, *Relationships between the carbon-oxygen stretching frequencies of carboxylato complexes and the type of carboxylate coordination.* Coordination Chemistry Reviews, 1980. **33**(3): p. 227-250.

121. Sun, S., et al., *Monodisperse MFe_2O_4 (M= Fe, Co, Mn) nanoparticles.* J. Am. Chem. Soc, 2004. **126**(1): p. 273-279.
122. Xie, J., et al., *Linking hydrophilic macromolecules to monodisperse magnetite (Fe_3O_4) nanoparticles via trichloro-s-triazine.* Chemistry of Materials, 2006. **18**(23): p. 5401-5403.
123. Granata, C., et al., *Magnetic properties of iron oxide nanoparticles investigated by nanoSQUIDs.* The European Physical Journal B, 2013. **86**(6): p. 272.
124. Meledandri, C.J., et al., *Nonaqueous magnetic nanoparticle suspensions with controlled particle size and nuclear magnetic resonance properties.* Langmuir, 2008. **24**(24): p. 14159-14165.
125. De Sousa, M.E., et al., *Stability and relaxation mechanisms of citric acid coated magnetite nanoparticles for magnetic hyperthermia.* The Journal of Physical Chemistry C, 2013. **117**(10): p. 5436-5445.
126. Verde, E.L., et al., *Magnetic hyperthermia investigation of cobalt ferrite nanoparticles: Comparison between experiment, linear response theory, and dynamic hysteresis simulations.* Journal of Applied Physics, 2012. **111**(12): p. 123902.
127. Lee, J.-H., et al., *Exchange-coupled magnetic nanoparticles for efficient heat induction.* Nature Nanotechnology, 2011. **6**(7): p. 418-422.
128. Smolensky, E.D., et al., *Surface functionalization of magnetic iron oxide nanoparticles for MRI applications–effect of anchoring group and ligand exchange protocol.* Contrast Media and Molecular Imaging, 2011. **6**(4): p. 189-199.
129. Yuen, A.K., et al., *The interplay of catechol ligands with nanoparticulate iron oxides.* Dalton Transactions, 2012. **41**(9): p. 2545-2559.
130. Montalbetti, C.A. and V. Falque, *Amide bond formation and peptide coupling.* Tetrahedron, 2005. **61**(46): p. 10827-10852.
131. Wooding, A., et al., *Studies of the double surfactant layer stabilization of water-based magnetic fluids.* 1991. **144**(1): p. 236-242.
132. Nagesha, D.K., et al., *Functionalization-induced improvement in magnetic properties of Fe_3O_4 nanoparticles for biomedical applications.* Journal of Applied Physics, 2009. **105**(7): p. 07B317.
133. Feliu, N., et al., *In vivo degeneration and the fate of inorganic nanoparticles.* Chemical Society Reviews, 2016. **45**(9): p. 2440-2457.
134. Jordan, A., et al., *Magnetic fluid hyperthermia (MFH): Cancer treatment with AC magnetic field induced excitation of biocompatible superparamagnetic nanoparticles.* Journal of Magnetism and Magnetic Materials, 1999. **201**(1-3): p. 413-419.
135. Zhao, W., et al., *In situ synthesis of magnetic field-responsive hemicellulose hydrogels for drug delivery.* Biomacromolecules, 2015. **16**(8): p. 2522-2528.
136. Zhang, N., et al., *Magnetic nanocomposite hydrogel for potential cartilage tissue engineering: synthesis, characterization, and cytocompatibility with bone marrow derived mesenchymal stem cells.* 2015.
137. Ahmed, E.M., *Hydrogel: Preparation, characterization, and applications: A review.* Journal of advanced research, 2015. **6**(2): p. 105-121.
138. Tanaka, T., *Gels.* Scientific American, 1981. **244**(1): p. 124-S-17.
139. Qiu, Y. and K. Park, *Environment-sensitive hydrogels for drug delivery.* Advanced Drug Delivery Reviews, 2001. **53**(3): p. 321-339.
140. Hirokawa, Y. and T. Tanaka. *Volume phase transition in a non-ionic gel.* in *AIP Conference Proceedings*. 1984. Aip.

141. Satarkar, N.S., D. Biswal, and J.Z. Hilt, *Hydrogel nanocomposites: a review of applications as remote controlled biomaterials.* Soft Matter, 2010. **6**(11): p. 2364-2371.
142. Jean, B., L.-T. Lee, and B. Cabane, *Interactions of sodium dodecyl sulfate with acrylamide–N-isopropylacrylamide) statistical copolymer.* Colloid Polymer Science, 2000. **278**(8): p. 764-770.
143. Luo, B., et al., *Multi-functional thermosensitive composite microspheres with high magnetic susceptibility based on magnetite colloidal nanoparticle clusters.* 2009. **26**(3): p. 1674-1679.
144. Flory, P. and J. Rehner, *1943Statistical mechanics of cross-linked polymer networks. II. Swelling.* Journal of Chemical Physics.
145. Flory, P.J., *Principles of polymer chemistry*. 1953: Cornell University Press.
146. Park, H., et al., *Effect of swelling ratio of injectable hydrogel composites on chondrogenic differentiation of encapsulated rabbit marrow mesenchymal stem cells in vitro.* Biomacromolecules, 2009. **10**(3): p. 541-546.
147. Kim, D.-H., et al., *Stimuli-Responsive Magnetic Nanomicelles as Multifunctional Heat and Cargo Delivery Vehicles.* Langmuir, 2013. **29**(24): p. 7425-7432.
148. Shah, S.A., et al., *Thermo-responsive copolymer coated MnFe2O4 magnetic nanoparticles for hyperthermia therapy and controlled drug delivery.* Materials Chemistry and Physics, 2012. **137**(1): p. 365-371.
149. Daou, T., et al., *Coupling agent effect on magnetic properties of functionalized magnetite-based nanoparticles.* Chemistry of Materials, 2008. **20**(18): p. 5869-5875.
150. Nagesha, D.K., et al., *Functionalization-induced improvement in magnetic properties of Fe 3 O 4 nanoparticles for biomedical applications.* Journal of Applied Physics, 2009. **105**(7): p. 07B317.
151. Stark, W.J., et al., *Industrial applications of nanoparticles.* Chemical Society Reviews, 2015. **44**(16): p. 5793-5805.
152. Sun, S., et al., *Monodisperse* MFe_2O_4 *(M = Fe, Co, Mn) nanoparticles.* Journal of the American Chemical Society, 2004. **126**(1): p. 273-279.
153. Hyeon, T., *Chemical synthesis of magnetic nanoparticles.* Chemical Communications, 2003(8): p. 927-934.
154. Park, J., et al., *One-nanometer-scale size-controlled synthesis of monodisperse magnetic Iron oxide nanoparticles.* Angewandte Chemie, 2005. **117**(19): p. 2932-2937.
155. Prestwich, G.D., et al., *What is the greatest regulatory challenge in the translation of biomaterials to the clinic?* Science Translational Medicine, 2012. **4**(160): p. 160cm14-160cm14.
156. Webber, M.J., et al., *A perspective on the clinical translation of scaffolds for tissue engineering.* Annals of biomedical engineering, 2015. **43**(3): p. 641-656.
157. Romeis, S., J. Schmidt, and W. Peukert, *Mechanochemical aspects in wet stirred media milling.* International Journal of Mineral Processing, 2016. **156**: p. 24-31.
158. Sommer, M., et al., *Agglomeration and breakage of nanoparticles in stirred media mills—a comparison of different methods and models.* Chemical Engineering Science, 2006. **61**(1): p. 135-148.
159. Stehr, N., R. Mehta, and J. Herbst, *Comparison of energy requirements for conventional and stirred ball milling of coal-water slurries.* Coal Preparation, 1987. **4**(3-4): p. 209-226.
160. Stehr, N., *Wet coal grinding in agitation ball mills and conventional ball mills-grinding kinetics and energy consumption. Nasszerkleinerung von Kohle in Ruehrwerkskugelmehlen und konventionelle Kugelmuehlen-Zerkleinerungskinetik und Energiebedarf.* 1984.

161. Stehr, N., *Residence time distributions in a stirred ball mill and their effect on comminution.* Chemical Engineering Processing: Process Intensification, 1984. **18**(2): p. 73-83.
162. Bilgili, E., R. Hamey, and B. Scarlett, *Nano-milling of pigment agglomerates using a wet stirred media mill: Elucidation of the kinetics and breakage mechanisms.* Chemical Engineering Science, 2006. **61**(1): p. 149-157.
163. Adam, J., et al., *Milling of zirconia nanoparticles in a stirred media mill.* Journal of the American Ceramic Society, 2008. **91**(9): p. 2836-2843.
164. Malamatari, M., et al., *Pharmaceutical nanocrystals: production by wet milling and applications.* Drug Discovery Today, 2018. **23**(3): p. 534-547.
165. Peltonen, L. and J. Hirvonen, *Pharmaceutical nanocrystals by nanomilling: critical process parameters, particle fracturing and stabilization methods.* Journal of Pharmacy and Pharmacology, 2010. **62**(11): p. 1569-1579.
166. Patel, R.P., A.H. Baria, and N.A. Patel, *An overview of size reduction technologies in the field of pharmaceutical manufacturing.* Asian Journal of Pharmaceutics, 2014. **2**(4).
167. Kwade, A., *Wet comminution in stirred media mills—research and its practical application.* Powder Technology, 1999. **105**(1-3): p. 14-20.
168. Basu, B., *Toughening of yttria-stabilised tetragonal zirconia ceramics.* International Materials Reviews, 2005. **50**(4): p. 239-256.
169. Axinte, D., et al., *Abrasive waterjet cutting of polycrystalline diamond: A preliminary investigation.* International Journal of Machine Tools Manufacture, 2009. **49**(10): p. 797-803.
170. Kwade, A. and J. Schwedes, *Wet grinding in stirred media mills.* Handbook of Powder Technology, 2007. **12**: p. 251-382.
171. Kwade, A., *Determination of the most important grinding mechanism in stirred media mills by calculating stress intensity and stress number.* Powder Technology, 1999. **105**(1-3): p. 382-388.
172. Li, M., et al., *Sub-100 nm drug particle suspensions prepared via wet milling with low bead contamination through novel process intensification.* Chemical Engineering Science, 2015. **130**: p. 207-220.
173. Manikandan, S., N. Karthikeyan, and K. Rajan, *Viscosity of Fe2O3 nanoparticles dispersion in water and ethylene glycol-water mixture (nanofluids).* International Journal of Nanoparticles, 2013. **6**(1): p. 10-27.
174. Knieke, C., M. Sommer, and W. Peukert, *Identifying the apparent and true grinding limit.* Powder Technology, 2009. **195**(1): p. 25-30.
175. Knieke, C., S. Romeis, and W. Peukert, *Influence of process parameters on breakage kinetics and grinding limit at the nanoscale.* AIChE Journal, 2011. **57**(7): p. 1751-1758.
176. Tang, Y., Q. Chen, and R. Chen, *Magnetic field induced controllable self-assembly of maghemite nanocrystals: From 3D arrays to 1D nanochains.* Applied Surface Science, 2015. **347**: p. 202-207.
177. Berkowitz, A., W. Schuele, and P. Flanders, *Influence of Crystallite Size on the Magnetic Properties of Acicular* γ*-*Fe_2O_3 *Particles.* Journal of Applied Physics, 1968. **39**(2): p. 1261-1263.
181. Gandhi, A., et al., *Studies on thermoresponsive polymers: Phase behaviour, drug delivery and biomedical applications.* asian journal of pharmaceutical sciences, 2015. **10**(2): p. 99-107.
182. Zhang, J.T., et al., *Preparation and properties of poly (N-isopropylacrylamide)/poly (N-isopropylacrylamide) interpenetrating polymer networks for drug delivery.* Journal of Polymer Science Part A: Polymer Chemistry, 2004. **42**(5): p. 1249-1254.

183. Amsden, B., *Curable, biodegradable elastomers: emerging biomaterials for drug delivery and tissue engineering.* Soft Matter, 2007. **3**(11): p. 1335-1348.
184. Wach, R.A., et al., *Nerve guidance channels based on PLLA–PTMC biomaterial.* Journal of Applied Polymer Science, 2013. **127**(3): p. 2259-2268.
185. Schüller-Ravoo, S., et al., *Flexible and Elastic Scaffolds for Cartilage Tissue Engineering Prepared by Stereolithography Using Poly (trimethylene carbonate)-Based Resins.* Macromolecular bioscience, 2013. **13**(12): p. 1711-1719.
186. Zhang, Z., et al., *The in vivo and in vitro degradation behavior of poly (trimethylene carbonate).* Biomaterials, 2006. **27**(9): p. 1741-1748.
187. Asmat, S., Q. Husain, and A. Azam, *Lipase immobilization on facile synthesized polyaniline-coated silver-functionalized graphene oxide nanocomposites as novel biocatalysts: stability and activity insights.* RSC Advances, 2017. **7**(9): p. 5019-5029.
188. Caulfield, M.J., et al., *Degradation on polyacrylamides. Part I. Linear polyacrylamide.* Polymer, 2003. **44**(5): p. 1331-1337.
189. Nadgorny, M. and A. Ameli, *Functional Polymers and Nanocomposites for 3D Printing of Smart Structures and Devices.* ACS applied materials & interfaces, 2018.
190. Hull, C.W., *Apparatus for production of three-dimensional objects by stereolithography*. 1986, Google Patents.
191. Melchels, F.P., J. Feijen, and D.W. Grijpma, *A review on stereolithography and its applications in biomedical engineering.* Biomaterials, 2010. **31**(24): p. 6121-6130.
192. Mondschein, R.J., et al., *Polymer structure-property requirements for stereolithographic 3D printing of soft tissue engineering scaffolds.* Biomaterials, 2017.
193. Crosby, A.J. and J.Y. Lee, *Polymer nanocomposites: the "nano" effect on mechanical properties.* Polymer reviews, 2007. **47**(2): p. 217-229.
194. Melchels, F.P., J. Feijen, and D.W. Grijpma, *A poly (D, L-lactide) resin for the preparation of tissue engineering scaffolds by stereolithography.* Biomaterials, 2009. **30**(23): p. 3801-3809.
195. Yagci, Y., S. Jockusch, and N.J. Turro, *Photoinitiated polymerization: advances, challenges, and opportunities.* Macromolecules, 2010. **43**(15): p. 6245-6260.
196. Wallace, J., et al., *Validating continuous digital light processing (cDLP) additive manufacturing accuracy and tissue engineering utility of a dye-initiator package.* Biofabrication, 2014. **6**(1): p. 015003.
197. Aydin, M., et al., *Mechanistic study of photoinitiated free radical polymerization using thioxanthone thioacetic acid as one-component type II photoinitiator.* Macromolecules, 2005. **38**(10): p. 4133-4138.
198. Jansen, J.F., et al., *Fast monomers: factors affecting the inherent reactivity of acrylate monomers in photoinitiated acrylate polymerization.* Macromolecules, 2003. **36**(11): p. 3861-3873.
199. Becker, H. and H. Vogel, *The role of hydroquinone monomethyl ether in the stabilization of acrylic acid.* Chemical Engineering & Technology: Industrial Chemistry-Plant Equipment-Process Engineering-Biotechnology, 2006. **29**(10): p. 1227-1231.
200. Holding, S.R. and E. Meehan, *Molecular weight characterisation of synthetic polymers*. Vol. 83. 1995: iSmithers Rapra Publishing.
201. Jacobs, P.F., *Rapid prototyping & manufacturing: fundamentals of stereolithography*. 1992: Society of Manufacturing Engineers.

202. Dizon, J.R.C., et al., *Mechanical characterization of 3D-printed polymers.* Additive Manufacturing, 2017.
203. Dean, D., et al., *Continuous digital light processing (cDLP): Highly accurate additive manufacturing of tissue engineered bone scaffolds: This paper highlights the main issues regarding the application of Continuous Digital Light Processing (cDLP) for the production of highly accurate PPF scaffolds with layers as thin as 60 μm for bone tissue engineering.* Virtual and physical prototyping, 2012. **7**(1): p. 13-24.
204. Kumar, S.K. and R. Krishnamoorti, *Nanocomposites: Structure, Phase Behavior, and Properties.* Annual Review of Chemical and Biomolecular Engineering, 2010. **1**(1): p. 37-58.